# INSTITUTO POTOSINO DE INVESTIGACIÓN CIENTÍFICA Y TECNOLÓGICA, A.C.

# UNIVERSITÉ PARIS-SACLAY

## Doctorado en Nanociencias y Materiales

## Photocatalysts for Hydrogen Generation and Wastewater Treatment

Tesis que presenta: **I.Q. Ana Andrea Méndez Medrano**
Para obtener el grado de: **Doctora en Nanociencias y Materiales**

Co-Directores de la Tesis:

**Dr. José Luis Rodríguez López**
*División de Materiales Avanzados*
*Instituto Potosino de Investigación Científica y Tecnológica, A.C*

**Dra. Hynd Remita**
*Institut de Chimie Physique & CNRS*
*Université Paris-Saclay, Orsay, France.*

**Dra. Gladis Judith Labrada Delgado**
*Laboratorio Nacional de Investigaciones en Nanociencias y Nanotecnología*
*Instituto Potosino de Investigación Científica y Tecnológica, A.C*

**San Luis Potosí, SLP, 05 de Diciembre de 2024.**

THÈSE DE DOCTORAT

NNT : 2024UPASF074

# Photocatalysts for hydrogen generation and wastewater treatment

*Photocatalyseurs pour la production d'hydrogène et le traitement de l'eau*

**Thèse de doctorat de l'Université Paris-Saclay et de l'Instituto Potosino de Investigación Científica y Tecnológica A.C. (IPICYT)**

École doctorale n° 571: sciences chimiques : molécules, matériaux, instrumentation et biosystèmes (2MIB)
Spécialité de doctorat : Chimie.
Graduate School : Chimie. Référent: Faculté des sciences d'Orsay

Thèse préparée dans les unités de recherche **Institut de Chimie Physique (Université Paris-Saclay, CNRS)** et **División de Materiales Avanzados (IPICYT)** sous la direction de **Hynd REMITA**, Directrice de recherche, et de **José Luis RODRÍGUEZ LÓPEZ,** Directeur de recherche.

**Thèse soutenue à San Luis Potosí, le 05 décembre 2024, par**

**Ana Andrea MÉNDEZ MEDRANO**

## Composition du Jury

Membres du jury avec voix délibérative

| | |
|---|---|
| **Rodolfo ZANELLA SPECIA**<br>Professeur, ICAT-Universidad Nacional Autónoma de México | Rapporteur |
| **Souhir BOUJDAY**<br>Professeure, Laboratoire de Réactivité de Surface, Sorbonne Université | Rapporteure |
| **Ally AUKAULOO**<br>Professeur, ICMMO-Université Paris-Saclay | Examinateur |
| **Gladis Judith LABRADA DELGADO**<br>Professeure, LINAN-IPICYT | Examinatrice |
| **María Alejandra CARREÓN ÁLVAREZ**<br>Professeure, Centro Universitario de los Valles-Universidad de Guadalajara | Examinatrice |

université PARIS-SACLAY

ÉCOLE DOCTORALE
Sciences Chimiques : Molécules, Matériaux, Instrumentation et Biosystèmes (2MIB)

**Titre :** Photocatalyseurs pour la Production d'Hydrogène et le Traitement de l'Eau.

**Mots clés :** Génération d'hydrogène; carburants solaires; traitement de l'eau; nanoparticules métalliques; photocatalyse; cocatalyseurs ; résonance plasmonique de surface localisée.

**Résumé:** Le développement durable est essentiel pour relever les défis énergétiques et environnementaux. La photocatalyse constitue une alternative viable pour convertir et stocker l'énergie solaire sous forme de carburants tels que l'hydrogène ($H_2$), tout en contribuant à la réduction des émissions de dioxyde de carbone ($CO_2$) et à la dégradation des polluants dans l'air et l'eau. La conception de photocatalyseurs efficaces, rentables et stables est essentielle pour faire progresser les technologies de conversion de l'énergie solaire. Le dioxyde de titane ($TiO_2$) est le photocatalyseur le plus couramment utilisé, connu pour sa faible toxicité, son faible coût, sa bonne activité photocatalytique et sa stabilité chimique et biologique. Cependant, son utilisation est limitée par la recombinaison rapide et à taux élevé de la paire électron-trou (excitons) et par le fait qu'il ne peut être excité que sous irradiation UV en raison de son large gap énergétique (3,0–3,2 eV). Cette thèse de doctorat se concentre sur le développement de photocatalyseurs modifiés en surface avec des nanoparticules métalliques (NPs), qui présentent une synergie entre leurs propriétés optiques et électroniques, améliorant ainsi le processus photocatalytique. Des phénomènes tels que la résonance plasmonique de surface localisée (LSPR) dans certains métaux de transition (Au, Pd, Ag) et la formation de la barrière de Schottky permettent une plus grande absorption de la radiation dans le spectre visible et réduisent la recombinaison des excitons, augmentant ainsi l'activité photocatalytique. Dans ce projet, la surface du $TiO_2$ a été modifiée avec des NPs plasmoniques mono- et bi-métalliques, ainsi que des NPs d'oxyde métallique (Au, Pd, AuPd, NiFe, NiO), synthétisées par des méthodes chimiques ou par radiolyse. Ces NPs sont utilisée comme cotalyseurs pour la génération d'hydrogène vert par photocatalyse. Nous avons également démontré que la forme des NPs est cruciale lors de l'utilisation de NPs anisotropiques en forme de nanoétoiles d'or (AuNSs) dans le traitement des eaux contaminées, réduisant efficacement le composé toxique 4-nitrothiophénol (4-NTP) en 4-aminothiophénol (4-ATP) sous irradiation de lumière visible. Cette recherche doctorale contribue à la compréhension des propriétés photocatalytiques et plasmoniques, mettant en lumière le potentiel des matériaux nanostructurés pour améliorer la performance et la stabilité catalytiques dans des applications énergétiques et environnementales durables.

**Title :** Photocatalysts for Hydrogen Generation and Wastewater treatment.

**Keywords :** Hydrogen generation; solar fuels; water treatment; metal-based nanoparticles; photocatalysis; cocatalysts; localized surface plasmon resonance.

**Abstract:** Sustainable development is key to addressing energy and environmental challenges. Photocatalysis presents a viable alternative for converting and storing solar energy into fuels such as hydrogen ($H_2$), while also contributing to the reduction of carbon dioxide ($CO_2$) emissions and the degradation of pollutants in air and water. The design of efficient, cost-effective, and stable photocatalysts is essential for advancing solar energy conversion technologies. Titanium dioxide ($TiO_2$) is the most commonly used photocatalyst, known for its low toxicity, low cost, good photocatalytic activity, and chemical and biological stability. However, its use is limited by the rapid and high rate recombination of the electron-hole pair (exciton) and the fact that it can only be excited under UV irradiation due to its large band gap (3.0–3.2 eV). This doctoral thesis focuses on the development of surface-modified photocatalysts with metallic nanoparticles (NPs), which exhibit a synergy between their optical and electronic properties, enhancing the photocatalytic process. Phenomena such as localized surface plasmon resonance (LSPR) in certain transition metals (Au, Pd, Ag) and the formation of the Schottky barrier allow for greater absorption of radiation in the visible spectrum and reduce exciton recombination, thereby increasing photocatalytic activity. In this project, the surface of $TiO_2$ has been modified with plasmonic mono- and bi-metallic NPs, as well as metal oxide NPs (Au, Pd, AuPd, NiFe, NiO), synthesized through chemical and radiolysis methods. These NPs are used as cocatalysts for green hydrogen generation via photocatalysis. We also demonstrated that NPs shape is crucial when using anisotropic gold nanostar-shaped NPs (AuNSs) in contaminated water treatment, effectively reducing the toxic compound 4-nitrothiophenol (4-NTP) to 4-aminothiophenol (4-ATP) under visible light irradiation. This doctoral research contributes to the understanding of photocatalytic and plasmonic properties, highlighting the potential of nanostructured materials to improve catalytic performance and stability for sustainable energy and environmental applications.

# Constancia de aprobación de la tesis

La tesis “**Photocatalysts for Hydrogen Generation and Wastewater Treatment**” presentada para obtener el Grado de Doctora en Nanociencias y Materiales fue elaborada por **Ana Andrea Méndez Medrano** y aprobada el **05 de Diciembre de 2024** por los suscritos, designados por el Colegio de Profesores de la División de Materiales Avanzados del Instituto Potosino de Investigación Científica y Tecnológica, A.C.

**Dra. Gladis Judith Labrada Delgado**
Co-Directora de la tesis

**Dra. Hynd Remita**
Co-Directora de la tesis

**Dr. Héctor Gabriel Silva Pereyra**
Miembro del Comité Tutoral

**Dra. María Alejandra Carreón Álvarez**
Miembro del Comité Tutoral


# Créditos Institucionales

Esta tesis fue elaborada en la División de Materiales Avanzados del Instituto Potosino de Investigación Científica y Tecnológica, A.C., y en el Institut de Chimie Physique de la Université Paris Saclay, bajo la dirección del Dr. José Luis Rodríguez López, la Dra. Gladis Judith Labrada Delgado, y la Dra. Hynd Remita como co-directores de tesis.

Durante la realización del trabajo la autora recibió una beca académica del Consejo Nacional de Ciencia y Tecnología (No. 995288).

La autora recibió una beca en el Programa de apoyo a movilidad para Doble Diploma de nivel doctorado en co-tutela de la embajada de Francia en México, Campus France.

Página en blanco que se va a utilizar para colocar la copia del acta de examen.

# Dedicatorias

Dedico esta tesis con infinito amor y gratitud a mis padres, hermanos, amigos, colegas, profesores y a mis supervisores, que estuvieron apoyándome en concluir este gran objetivo en mi vida. Agradezco su confianza por creer en mí y acompañarme en la culminación de este gran logro en mi vida.

¡Gracias por ser mi inspiración!

# Acknowledgments

I extend my deepest gratitude to my supervisors Dr. José Luis Rodríguez-López and Dr. Gladis Judith Labrada-Delgado from the *Instituto Potosino de Investigación Científica y Tecnológica, A. C. (IPICYT)* and Dr. Hynd Remita of *Institut de Chimie Physique (ICP), CNRS, Université Paris-Saclay*, for giving me the opportunity to be part of this PhD research project in cotutelle. For all your support during my PhD, your knowledge and advices.

Furthermore, I would like to thank my committee members in Mexico, Dr. Gladis Judith Labrada-Delgado, Dr. María Alejandra Carreón-Alvarez, Dr. Héctor Gabriel Silva-Pereyra, and Dr. José Luis Rodríguez-López, as well as, my committee members in France, Dr. Olivier Pluchery, Dr. Loïc Assaud, and Dr. Hynd Remita for their corrections and suggestions throughout my PhD thesis.

I also express my gratitude to the technicians from the *LINAN* at *IPICYT*, Dr. Gladis Judith Labrada Delgado, Dr. Héctor Gabriel Silva Pereyra, Dr. Ignacio Guadalupe Becerril Juárez, M.S. Beatriz Adriana Rivera Escoto, and M.S. Ana Iris Peña Maldonado for their generous assistance and expertise in various characterization techniques.

Additionally, I am thankful to Mireille Benoit of *ICP* for her advices and assistance in the laboratory, Dr. Christophe Colbeau for helpful TRMC discussions, and Dr. Isabelle Lampre for her suggestions and corrections in my PhD research. Special thanks to Dr. Carine Clavaguéra for her contribution with DFT calculations and to Dr. Juan Pedro Palomares Báez of *Universidad Autónoma de Chihuahua* for his contribution with DFTB+ calculations.

I express my appreciation to Dr. Daniel Bahena of the *Advanced Laboratory of Electron Nanoscopy*, *CINVESTAV-IPN*, for the collaboration and his discussions on

HRTEM and HAADF techniques. I am also thankful to Dr. Diana Dragoe from *Institut de Chimie Moléculaire et des Matériaux d'Orsay (ICMMO, Université Paris-Saclay)* for her helpful discussions on XPS data interpretation and to Dr. Vincent Huc from *ICMMO* for the discussions on Suzuki-Miyaura reactions and for the collaboration on plasmonic catalysis and analysis of the products by mass spectrometry.

I would like to thank Dr. Olivier Pluchery and Dr. Claire Abadie for the collaboration with *Institut des Nanosciences de Paris*, *Sorbonne Université,* for allowing me to work in their laboratory and for their guidance during results' discussions.

Finally, I would like to thank *CONAHCYT*-Mexico for the financial support (grant no. 995288) and *CAMPUS FRANC*E for the scholarship provided by the French Embassy in Mexico.

# Index

# Figures

# Tables

# Abbreviations

| | |
|---|---|
| $H_2O$ | Water |
| $H_2$ | Hydrogen |
| $O_2$ | Oxygen |
| $N_2$ | Nitrogen |
| $CO_2$ | Carbon dioxide |
| $TiO_2$-P25 | Commercial titania or titanium dioxide |
| Au | Gold |
| AuSs | Gold seeds |
| AuNSs | Gold nanostars |
| Ag | Silver |
| Pd | Palladium |
| Pt | Platinum |
| Ni | Nickel |
| NiO | Nickel oxide |
| $Ni(OH)_2$ | Nickel hydroxide |
| Fe | Iron |
| Cu | Copper |
| Ti | Titanium |
| $HAuCl_4 \cdot 3H_2O$ | Gold (III) chloride trihydrate |
| $PdCl_2$ | Palladium (II) chloride |
| $Pt(acac)_2$ | Platinum (II) acetylacetonate |
| $Ni(acac)_2$ | Nickel(II) acetylacetonate |
| $Ni(HCO_2)_2 \cdot 2H_2O$ | Nickel (II) formate dihydrate |
| $Fe(acac)_3$ | Iron (III) acetylacetonate |
| $NaBH_4$ | Sodium borohydride |
| $C_2H_5OH$ | Ethanol |
| $CH_3OH$ | Methanol |
| TEOA | Triethanolamine |

| | |
|---|---|
| 4-NTP | 4-Nitrothiophenol |
| 4-NP | 4-Nitrophenol |
| 4-ATP | 4-Aminothiophenol |
| NP | Nanoparticle |
| NPs | Nanoparticles |
| UV | Ultraviolet |
| Vis | Visible |
| $e^-/h^+$ | Electron/hole |
| SC | Semiconductor |
| VB | Valence band |
| CB | Conduction band |
| LSPR | Localized surface plasmon resonance |
| EDS | Energy-dispersive X-ray spectroscopy |
| EELS | Electron energy loss spectroscopy |
| SEM | Scanning electron microscopy |
| TEM | Transmission electron microscopy |
| HRTEM | High-resolution transmission electron microscopy |
| HAADF-STEM | High-angle annular dark-field scanning transmission electron microscopy |
| ICP-OES | Inductively coupled plasma optical spectrometry |
| DRS | Diffuse reflectance spectra |
| XRD | X-ray Diffraction |
| XPS | X-ray photoelectron spectroscopy |
| TRMC | Time resolved microwave conductivity |
| GC | Gas Chromatography |
| MD-MC | Molecular dynamics-Monte Carlo |
| DFT | Density Functional Theory |
| DFTB+ | Density Functional Tight Binding |

# General Abstract

Human society has made remarkable advancements in science, technology and humanities over the past few decades. Unfortunately, these achievements have been accompanied by a surge in ecological and environmental problems and energy crises. To overcome these issues, sustainable development has emerged as a crucial path for modern society, focusing on energy and environmental concerns.

In this context, nanoscience and nanotechnology play a pivotal role. By manipulating materials at the nanoscale, these fields drive significant advancements in energy and environmental applications, aligning closely with the goals of sustainable development. Nanoscience enables the development of more efficient photocatalysts that enhance solar energy capture. Solar energy has gained significant attention as a promising, clean, and abundant energy source. Photocatalysis is inspired by photosynthesis, where nature stores solar energy into chemical bonds. Photocatalysis is a process that uses light to activate catalysts and drive chemical reactions. It has emerged as a promising strategy for harnessing solar light and addressing energy and environmental sustainability challenges.

Hydrogen ($H_2$) is emerging as a promising solar fuel due to its potential as clean energy. There are different methods to produce hydrogen, each with advantages and limitations. Approximately 96% of $H_2$ generation comes from fossil fuels, with 48% generated through natural gas (using the steam reforming method), 30% from oil, and 18% from coal gasification, which results in significant $CO_2$ emissions.[1] Only 4% of $H_2$ is produced through water electrolysis, which is costly and relies on fossil fuel electricity, and a minimal 0.1% comes from other sources.[1] Consequently, $H_2$ production is associated with greenhouse gas emissions, making it less environmentally friendly. Approximately 50 million tons of $H_2$ are generated annually, satisfying just 2% of the global energy demand.[1]

Green hydrogen production by photocatalytic water splitting is a main trend in global scientific research. In this PhD project, titanium dioxide ($TiO_2$) was used as the photocatalyst, a well-known photocatalyst due to its properties such as low toxicity, low cost, good photocatalytic activity, photochemical and biological stability. Nevertheless, its practical applications are limited due to the fast charge carriers' recombination, and it can only be excited under UV irradiation due to its large band gap (3.0-3.2 eV). Different strategies are used to enhance the activity of titania in UV and visible light, such as its doping with atoms such as C[2] or N,[3] its junction with another semiconductor,[4,5] act or surface modification with metal nanoparticles.[6,7,8,9]

Surface modification with metal nanoparticles (NPs) can decrease the charge carriers‘ recombination. It may allow the extension of light absorption into the visible spectrum, leading to the enhancement of photocatalytic activity. This improvement is crucial for applications such as hydrogen generation, water and air treatment, where efficient photocatalysts are needed to degrade pollutants.

Among the metals, platinum (Pt) is the best co-catalyst for photocatalytic $H_2$ generation due to its superior catalytic properties. However, Pt is costly and not abundant, thus replacing it with other metals is important. Bimetallic nanoparticles can induce synergistic effects compared to their monometallic counterparts, improving the photocatalytic activity while using more abundant and less expensive metals.

Additionally, metal nanoparticles such as gold (Au), palladium (Pd), and silver (Ag) present plasmonic effects, enhancing the photocatalytic process through localized surface plasmon resonance (LSPR). This phenomenon is the collective oscillations of conduction-free electrons excited by the incident photons in constructive interference with the electric field of the incident light.[8,10,11,12,13] Incorporating plasmonic nanoparticles will enhance the harvesting of the solar spectrum and increase the photocatalytic activity for $H_2$ generation and water treatment processes

This PhD thesis involves the development and exploration of photocatalysts for green $H_2$ generation and water treatment. These aspects are included in some of the sustainability goals of the United Nations' 2030 Agenda, offering a promising way to solve global energy and environmental problems. The surface of titania has been modified with mono- and bi-metallic nanoparticles for green $H_2$ generation by photocatalysis. The effect of surface modification on the charge carriers' dynamics and hydrogen generation has been studied.

Commercial $TiO_2$-P25 has been modified with AuPd nanoalloys used as cocatalysts for $H_2$ generation. Pd is an efficient co-catalyst with a work function similar to Pt,[14] and 50 times more abundant on Earth and cheaper.[15,16] In the literature, Pd-based bimetallic catalysts are crucial for enhancing the selectivity of hydrogenation reactions using individual Pd atoms on an Au surface.[17,18] Additionally, recent studies mentioned that Pd−Au NPs exhibit a photocatalytic reaction rate for $H_2$ similar to that of Pt NPs.[15,19]

Also, $TiO_2$-P25 has been modified with nickel oxide (NiO) and nickel-iron (NiFe) nanoparticles. Recent studies highlight the potential of Ni and Fe catalysts in photocatalysis. They are inspired by Nature using hydrogenases, which are organometallic enzymes containing Ni and Fe centers that catalyze $H_2$ evolution with performances that rival those of Pt.[20]

Plasmonic catalysis utilizes the unique optical properties of plasmonic nanoparticles, such as Au, Ag, and Pd to enhance catalytic processes. These nanoparticles exhibit LSPR in the visible and near-infrared regions, generating strong electromagnetic fields at their surfaces. This effect boosts catalytic reaction rates by harnessing visible light, thereby improving efficiency and expanding applications in energy conversion, environmental remediation, and chemical synthesis. Researchers can achieve more effective and selective catalysis by leveraging plasmonic effects, potentially advancing sustainable technologies and cleaner industrial processes.

Here, plasmonic catalysis for water treatment has been explored. 4-nitrothiophenol (4-NTP) has been used as a model pollutant. Indeed, high concentrations of 4-NTP can lead to skin irritation, eye damage, respiratory issues, and even death in severe cases. Gold nanostars (AuNSs) were used as photocatalysts to reduce 4-NTP to 4-aminothiophenol (4-ATP), a less toxic organic compound under visible light irradiation.

In **Chapter 1**, we emphasize the crucial role that hydrogen generation and water treatment play in addressing the energy crisis and environmental issues. This chapter introduces the principles of photocatalysis. Titanium dioxide, the most used semiconductor in photocatalysis, chosen as support material is presented with the strategies of its surface modification with metal and metal oxide nanoparticles to enhance its photocatalytic activity. We also introduce the plasmonic properties of metal nanoparticles, such as Au, Ag, and Pd, highlighting their distinctive optical properties afforded by LSPR. This phenomenon generates strong electromagnetic fields that enhances photocatalytic reactions. This section underscores the potential of plasmonic nanoparticles in a variety of applications.

In **Chapter 2**, we describe the synthesis methods and procedures used for synthesizing photocatalysts, including: AuPd/$TiO_2$, NiFe/$TiO_2$, NiO/$TiO_2$, and Au nanostars. Furthermore, we summarize the methodology and principle of the characterization techniques used.

The photocatalysts for hydrogen generation were characterized by advanced techniques such as Transmission Electron Microscopy (TEM), High-Resolution Transmission Electron Microscopy (HRTEM), High-Angle Annular Dark Field Scanning Transmission Electron Microscopy (HAADF-STEM), Energy-Dispersive X-ray Spectroscopy (EDS) or Electron Energy Loss Spectroscopy (EELS), Inductively Coupled Plasma Optical Emission Spectroscopy (ICP-OES), Diffuse Reflectance Spectroscopy (DRS), X-ray Diffraction (XRD), X-ray Photoelectron Spectroscopy (XPS), Time Resolved Microwave Conductivity (TRMC) and Gas Chromatography (GC).

The photocatalysts for water treatment were characterized by advanced techniques such as Scanning Electron Microscopy (SEM), TEM, HRTEM, EDS, UV-vis spectroscopy, Hyperspectral Dark-Field Optical Microscopy, and Atomic Force Microscopy (AFM).

In **Chapter 3**, we present the modification of commercial titania ($TiO_2$-P25) with mono- and bi-metallic nanoparticles (Au, Pd, and AuPd) using a chemical reduction method with sodium borohydride ($NaBH_4$) at room temperature. Surface-modified $TiO_2$ with bimetallic AuPd nanoalloys exhibits high photocatalytic activity for hydrogen generation, this activity is close to that obtained with Pt-modified $TiO_2$. Experimental results are supported by Density Functional Theory (DFT) and Density Functional Tight Binding (DFTB+) calculations, which show that alloying AuPd with low Pd content presents significant synergetic effects for hydrogen generation under UV-visible light. The AuPd/$TiO_2$ photocatalysts are stable under cycling. This work has been published in the journal Solar RRL (https://doi.org/10.1002/solr.202400106), highlighted with the front cover of the issue, as well as by *Centre national de la recherche scientifique* (*CNRS*) (https://www.inc.cnrs.fr/fr/cnrsinfo/des-nanoalliages-dor-et-de-palladium-pour-booster-la-production-dhydrogene).

In **Chapter 4**, $TiO_2$-P25 surface was modified with NiO NPs induced by radiolysis method. All modified samples exhibited superior photocatalytic activity compared to bare $TiO_2$. The results highlight the crucial role of Ni-based NPs modification in enhancing charge carriers' separation, resulting in increased activity under UV-visible light. Additionally, the results revealed that under visible irradiation, NiO NPs inject electrons into the conduction band of $TiO_2$. However, the hydrogen generation with NiO/$TiO_2$ decreases with photocatalytic cycling, probably due to Ni leaching in the aqueous medium, and after the third cycle, a plateau is obtained.

**Chapter 5** deals with the system NiFe/$TiO_2$ for photocatalytic applications. Bimetallic Ni-Fe NPs were synthetized on $TiO_2$-P25 via radiolysis method. Our results show

that the surface-modified $TiO_2$ with bimetallic NiFe NPs exhibits high photocatalytic activity for hydrogen generation. The enhanced photocatalytic activity of NiFe/$TiO_2$ nanoparticles was attributed to the synergistic effect between the NiFe nanoparticles and $TiO_2$, leading to improved charge transfer and separation. However, the hydrogen generation with NiFe/$TiO_2$ decreases with cycling, probably due to Ni leaching in the aqueous medium, and after the third cycle, a plateau is obtained.

**Chapter 6** deals with plasmonic catalysis using gold nanostars (AuNSs). First, we present the synthesis of AuNSs using a seed growth method. The plasmonic properties of these AuNSs were used to reduce the toxic molecule 4-NTP. Plasmon excitation of AuNSs (under visible light irradiation) induces the reduction of 4-NTP to 4-ATP (less toxic). The reduction of 4-NTP was followed by UV-visible spectroscopy. The AuNSs are more effective and stable for 4-NTP reduction than gold nanospheres (AuSs) and can be easily recovered after the photocatalytic test. Hyperspectral dark-field optical microscopy was used to measure the spectrum of individual AuNSs, which exhibit one or two plasmon resonances. The spectra of individual AuNSs were analyzed after adsorption of 4-NTP on their surface and after irradiation. Additionally, atomic force microscopy was used to investigate how the size variation of AuNSs affects the adsorption of 4-NTP and its degradation under visible light excitation. Our findings suggest that plasmonic nanomaterials such as AuNSs have great potential for the degradation of organic pollutants in water, which could lead to new opportunities for environmental remediation.

Finally, **Chapter 7** presents the main conclusions of this work and perspectives for future research. Briefly, we emphasize that (*i*) AuPd nanoalloys with low Pd content are very efficient and stable co-catalysts for the hydrogen evolution reaction. This study shows an example of synergetic effects obtained by alloying two metals. (*ii*) Surface modification with transition metals like Ni-Fe and transition metal oxides (NiO) can improve the photocatalytic activity of $TiO_2$-P25. However, the photocatalyst stability decreases with cycling due to Ni leaching in an aqueous medium. (*iii*) NiFe cocatalysts show good activity for $H_2$ generation, and this activity

is higher that the one with monometallic counterparts. As perspective, alloying Ni and Fe with a noble metal such as Pt or Au (in low content) is expected to enhance the photocatalytic activity and the stability of the photocatalyst. (*iv*) Au nanostars efficiently reduce 4-NTP to 4-ATP (less toxic) under visible light, outperforming Au nanospheres in efficiency and stability.

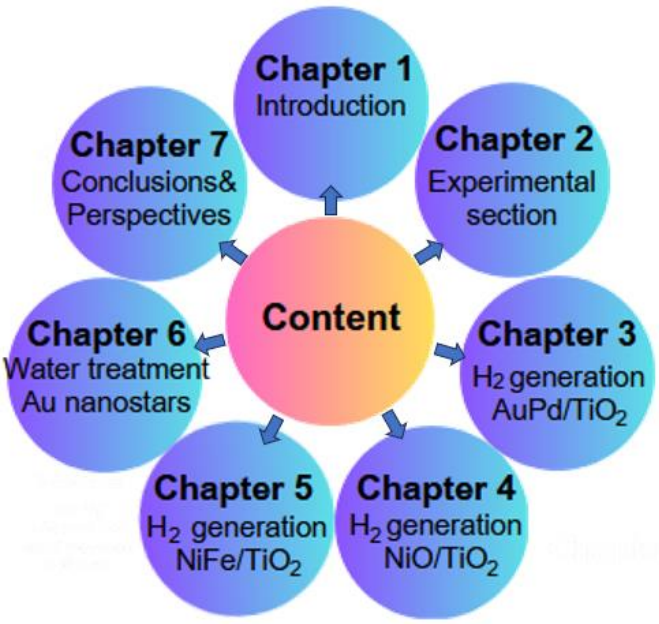


**KEYWORDS:** Hydrogen generation; solar fuels; water treatment; metal-based nanoparticles; nanoalloys; photocatalysis; cocatalysts; localized surface plasmon resonance; synergetic effects.

# Résumé General

## Photocatalyseurs pour la Production d'Hydrogène et le Traitement de l'Eau

La société humaine a réalisé des avancées remarquables dans les domaines de la science, de la technologie et des sciences humaines au cours des dernières décennies. Malheureusement, ces réalisations ont été accompagnées d'une augmentation des problèmes écologiques et environnementaux ainsi que des crises énergétiques. Pour surmonter ces problèmes, le développement durable est devenu un chemin crucial pour la société moderne, en mettant l'accent sur les préoccupations énergétiques et environnementales.

Dans ce contexte, la nanoscience et la nanotechnologie jouent un rôle central. En manipulant les matériaux à l'échelle nanométrique, ces domaines favorisent des avancées significatives dans les applications énergétiques et environnementales, s'alignant étroitement avec les objectifs du développement durable. La nanoscience permet le développement de photocatalyseurs plus efficaces et permet amélioration de la capture de l'énergie solaire. L'énergie solaire a attiré une attention significative en tant que source d'énergie prometteuse, propre et abondante. La photocatalyse s'inspire de la photosynthèse, où la nature stocke l'énergie solaire dans des liaisons chimiques. La photocatalyse est un processus qui utilise la lumière pour activer des catalyseurs et entraîner des réactions chimiques. Elle est apparue comme une stratégie prometteuse pour exploiter la lumière solaire et relever les défis liés à la durabilité énergétique et environnementale.

L'hydrogène ($H_2$) émerge comme un carburant solaire prometteur en raison de son potentiel en tant qu'énergie propre. Il existe différentes méthodes pour produire de l'hydrogène, chacune avec ses propres avantages et limitations. Environ 96 % de la production d'hydrogène provient de processus basés sur les combustibles fossiles; 48 % est généré à partir du gaz naturel (méthode de reformage à la vapeur), 30 % à partir du pétrole, et 18 % à partir de la gazéification du charbon, ce qui entraîne des émissions importantes de $CO_2$. Actuellement, seulement 4 % de l'hydrogène est

produit par électrolyse de l'eau, ce qui est coûteux, s'appuie également sur l'électricité provenant des combustibles fossiles, et un minime 0,1 % provient d'autres sources. Par conséquent, la production d'hydrogène est associée aux émissions de gaz à effet de serre, la rendant moins respectueuse de l'environnement pour le moment. Chaque année, environ 50 millions de tonnes d'hydrogène sont produits, ne répondant qu'à 2 % de la demande énergétique mondiale.

La production d'hydrogène vert par éclatement photocatalytique de l'eau est une tendance majeure dans la recherche scientifique mondiale. Dans ce projet de doctorat, le dioxyde de titane ($TiO_2$) a été utilisé comme photocatalyseur. C'est le photocatalyseur le plus utilisé et étudié en raison de ses propriétés telles que la bonne activité photocatalytique, le faible coût, la faible toxicité ainsi que la stabilité photochimique et biologique. Néanmoins, ses applications pratiques sont limitées en raison de la recombinaison rapide des porteurs de charge, et de plus, il ne peut être excité que sous irradiation UV en raison de la valeur de sa bande interdite (3,0-3,2 eV). Différentes stratégies sont utilisées pour améliorer l'activité du dioxyde de titane sous lumière UV et visible, telles que son dopage avec des atomes comme le C ou le N, son couplage avec un autre semi-conducteur, ou sa modification de surface avec des nanoparticules métalliques.

La modification de surface avec des nanoparticules métalliques peut diminuer la recombinaison des porteurs de charge et permettre l'extension de l'absorption lumineuse dans le spectre visible, ce qui conduit à une amélioration de l'activité photocatalytique. Cette amélioration est cruciale pour des applications telles que la génération d'hydrogène, le traitement de l'eau et de l'air, où des photocatalyseurs efficaces sont nécessaires pour dégrader les polluants.

Parmi les métaux, le platine (Pt) est le meilleur co-catalyseur pour la génération d'hydrogène photocatalytique en raison de ses propriétés catalytiques supérieures. Cependant, le Pt est coûteux et peu abondant, il est donc important de le remplacer par d'autres métaux. Les nanoparticules bimétalliques peuvent induire des effets synergiques par rapport à leurs homologues monométalliques, améliorant l'activité photocatalytique tout en utilisant des métaux plus abondants et moins coûteux.

De plus, les nanoparticules métalliques telles que l'or (Au), le palladium (Pd) et l'argent (Ag) présentent des propriétés plasmoniques, améliorant le processus photocatalytique grâce à la résonance plasmonique de surface localisée (LSPR). Ce phénomène est l'oscillation collective des électrons libres de conduction excités par les photons incidents en interférence constructive avec le champ électrique de la lumière incidente. L'incorporation de nanoparticules plasmoniques permettra de mieux exploiter le spectre solaire et d'augmenter l'activité photocatalytique de la génération d'hydrogène et des processus de traitement de l'eau.

Cette thèse de doctorat concerne le développement et l'exploration de photocatalyseurs pour la génération d'hydrogène vert et le traitement de l'eau. Ces aspects sont inclus dans certains des objectifs de durabilité de l'Agenda 2030 des Nations Unies, offrant une voie prometteuse pour résoudre les problèmes mondiaux d'énergie et d'environnement. La surface du dioxyde de titane a été modifiée avec des nanoparticules mono- et bi-métalliques pour la génération d'hydrogène vert par photocatalyse. L'effet de la modification de surface sur la dynamique des porteurs de charge et la génération d'hydrogène a été étudié.

$TiO_2$-P25 (commercial) a été modifié en surface avec des nanoalliages AuPd. Le Pd est un co-catalyseur efficace avec une fonction de travail similaire à celle du platine (Pt), et 50 fois plus abondant sur terre et moins coûteux. Dans la littérature, les catalyseurs bimétalliques à base de Pd sont cruciaux pour améliorer la sélectivité des réactions d'hydrogénation en utilisant des atomes individuels de Pd sur une surface de Au. De plus, des études récentes ont mentionné que les NPs Pd−Au présentent un taux de réaction photocatalytique pour $H_2$ similaire à celui des NPs de Pt. De plus, $TiO_2$-P25 a été modifié avec des nanoparticules d'oxyde de nickel (NiO) et de nickel-fer (NiFe). Les études récentes soulignent le potentiel des catalyseurs Ni et Fe en photocatalyse, inspirés par la nature utilisant des hydrogénases, qui sont des enzymes organométalliques contenant des centres en Ni et en Fe qui catalysent l'évolution de l'hydrogène avec des performances comparables à celles du Pt.

La catalyse plasmonique utilise les propriétés optiques uniques des nanoparticules plasmoniques, telles que que l'Au, l'Ag et le Pd, pour améliorer les processus catalytiques. Ces nanoparticules présentent une résonance plasmonique de surface

localisée (LSPR) dans les régions visible et proche infrarouge, générant des champs électromagnétiques puissants à leur surface. Cet effet améliore les taux de réaction catalytique en exploitant la lumière visible, améliorant ainsi l'efficacité et étendant les applications dans la conversion d'énergie, la réhabilitation environnementale et la synthèse chimique. En exploitant les effets plasmons, les chercheurs peuvent réaliser une catalyse plus efficace et sélective, potentiellement en faisant progresser les technologies durables et les processus industriels plus propres.

Ici, la catalyse plasmonique pour le traitement de l'eau a été explorée. Le 4-nitrothiophénol (4-NTP) a été utilisé comme polluant modèle. En effet, des concentrations élevées de 4-NTP peuvent entraîner des irritations de la peau, des dommages oculaires, des problèmes respiratoires, et même la mort dans les cas graves. Les nanoétoiles d'or (AuNSs) ont été utilisées comme photocatalyseurs pour réduire le 4-NTP en 4-aminothiophénol (4-ATP), un composé organique moins toxique sous irradiation de lumière visible.

**Chapitre 1**: Nous insistons sur le rôle crucial que joue la génération d'hydrogène et le traitement de l'eau pour faire face à la crise énergétique et aux problèmes environnementaux. De plus, nous expliquons pourquoi le $TiO_2$, le semi-conducteur le plus utilisé en photocatalyse, a été choisi comme matériau de support. Les objectifs de la thèse ont été présentés. Les stratégies de modification de surface du $TiO_2$ avec des nanoparticules métalliques et oxydes métalliques (NPs) pour améliorer son activité photocatalytique sont également exposées.

Nous introduisons les nanoparticules plasmoniques, telles que l'Au, l'Ag et le Pd, en mettant en évidence leurs propriétés optiques dues à la résonance plasmonique de surface localisée (LSPR). Ce phénomène génère de forts champs électromagnétiques qui améliorent les réactions photocatalytiques. Cette section souligne le potentiel des nanoparticules plasmoniques dans une variété d'applications. Nous évoquons les préoccupations concernant le traitement de l'eau et comment la photocatalyse plasmonique, en particulier en utilisant des nanoétoiles d'or, offre une solution prometteuse pour le traitement de l'eau.

**Chapitre 2**: Nous décrivons les méthodes et procédures de synthèse utilisées pour préparer des photocatalyseurs, y compris: $AuPd/TiO_2$, $NiFe/TiO_2$, $NiO/TiO_2$, et des

nanoétoiles d'or. De plus, nous résumerons la méthodologie et le principe des techniques de caractérisation utilisées. Les photocatalyseurs pour la génération d'hydrogène ont été caractérisés par des techniques avancées telles que la Microscopie Électronique en Transmission (TEM), la Microscopie Électronique en Transmission à Haute Résolution (HRTEM), la Microscopie Électronique en Transmission à Champ Annulaire Sombre à Grand Angle (HAADF-STEM), la Spectroscopie de Dispersion d'Énergie par Rayons X (EDS) ou la Spectroscopie de Perte d'Énergie d'Électrons (EELS), la Spectroscopie d'Émission Optique par Plasma Inductivement Couplé (ICP-OES), la Spectroscopie de Réflexion Diffuse (DRS), la Diffraction des Rayons X (XRD), la Spectroscopie de Photoélectrons X (XPS), la Conductivité Micro-ondes Résolue en Temps (TRMC) et la Chromatographie en Phase Gazeuse (GC). Les photocatalyseurs pour le traitement de l'eau ont été caractérisés par différentes techniques telles que la Microscopie Électronique à Balayage (SEM), TEM, HRTEM, EDS, la spectroscopie UV-vis, la Microscopie Optique à Champ Sombre et la Microscopie à Force Atomique (AFM).

**Chapitre 3**: Nous présentons la modification du dioxyde de titane commercial ($TiO_2$-P25) avec des nanoparticules mono- et bi-métalliques (Au, Pd, et AuPd) en utilisant une méthode de réduction chimique avec $NaBH_4$ à température ambiante. Le $TiO_2$ modifié en surface avec des nanoalliages bimetalliques AuPd présente une activité photocatalytique élevée pour la génération d'hydrogène, cette activité étant proche de celle obtenue avec le $TiO_2$ modifié au Pt. Les résultats expérimentaux sont soutenus par des calculs de Théorie de la Fonctionnelle de Densité (DFT) et de Densité Fonctionnelle Tight Binding (DFTB+), qui montrent que l'alliage AuPd avec une faible teneur en Pd présente des effets synergétiques significatifs pour la génération d'hydrogène sous lumière UV-visible. Les photocatalyseurs AuPd/$TiO_2$ sont stables lors des cycles. Ce travail a été publié dans la revue Solar RRL (https://doi.org/10.1002/solr.202400106), avec une mise en avant sur la couverture du numéro, ainsi que par le *Centre national de la recherche scientifique (CNRS)* (https://www.inc.cnrs.fr/fr/cnrsinfo/des-nanoalliages-dor-et-de-palladium-pour-booster-la-production-dhydrogene).

**Chapitre 4**: La surface du $TiO_2$-P25 a été modifiée avec des nanoparticules d'oxyde de nickel (NiO) induites par la méthode de radiolyse. Tous les échantillons modifiés ont montré une activité photocatalytique supérieure par rapport au $TiO_2$. Les résultats soulignent le rôle crucial de la modification des nanoparticules à base de Ni dans l'amélioration de la séparation des porteurs de charge, ce qui entraîne une augmentation de l'activité sous lumière UV. De plus, les résultats ont révélé qu'en irradiation visible, les NPs d'oxyde de nickel injectent des électrons dans la bande de conduction du $TiO_2$. Cependant, la génération d'hydrogène avec $NiO/TiO_2$ diminue avec le cyclage photocatalytique, probablement en raison du leaching (ou dissolution) de Ni dans un milieu aqueux, et après le troisième cycle, un plateau est atteint.

**Chapitre 5**: Nous traitons du système $NiFe/TiO_2$ pour les applications photocatalytiques. Les NPs bimatalliques Ni-Fe ont été synthétisées sur $TiO_2$-P25 via la méthode de radiolyse. Nos résultats montrent que le $TiO_2$ modifié en surface avec des nanoparticules bimétalliques NiFe présente une activité photocatalytique élevée pour la génération d'hydrogène. L'activité photocatalytique améliorée des nanoparticules $NiFe/TiO_2$ est attribuée à l'effet synergique entre les nanoparticules NiFe et le $TiO_2$, conduisant à une amélioration du transfert et de la séparation des charges. Cependant, la génération d'hydrogène avec $NiFe/TiO_2$ diminue avec le cyclage, probablement en raison du lessivage du Ni dans le milieu aqueux, et après le troisième cycle, un plateau est atteint.

**Chapitre 6**: Nous abordons la catalyse plasmonique en utilisant des nanoétoiles d'or (AuNSs). Tout d'abord, nous présentons la synthèse des AuNSs en utilisant une méthode de croissance par graine. Les propriétés plasmoniques de ces AuNSs ont été utilisées pour la réduction d'une molécule toxique le 4-NTP. L'excitation plasmonique des AuNSs (sous irradiation de lumière visible) induit la réduction de 4-NTP en 4-ATP (moins toxique). La réduction de 4-NTP a été suivie par spectroscopie UV-visible. Les AuNSs sont plus efficaces et stables pour la réduction de 4-NTP que les nanosphères (AuSs) et peuvent être facilement récupérées après le test photocatalytique. La microscopie optique à champ sombre a été utilisée pour mesurer le spectre des AuNSs individuels, qui présentent une ou deux résonances

plasmoniques. Les spectres des AuNSs individuels ont été analysés après adsorption de 4-NTP sur leur surface et après irradiation. De plus, la microscopie à force atomique a été utilisée pour étudier comment la variation de taille des AuNSs affecte l'adsorption de 4-NTP et sa dégradation sous excitation de lumière visible. Nos résultats montrent que les nanomatériaux plasmoniques tels que les AuNSs peuvent avoir un grand potentiel pour la dégradation des polluants organiques dans l'eau, ce qui pourrait permettre des applications environnementales.

**Chapitre 7**: Enfin, le Chapitre 7 présente les principales conclusions de ce travail et les perspectives pour les recherches futures. En résumé, nous soulignons que (i) les nanoalliages AuPd avec une faible teneur en Pd sont des co-catalyseurs très efficaces et stables pour la réaction d'évolution de l'hydrogène. Cette étude montre un exemple d'effets synergiques obtenus par l'alliage de deux métaux. (ii) La modification de surface avec des métaux de transition comme Ni et Fe, et des oxydes de métaux de transition (NiO) peut améliorer l'activité photocatalytique du $TiO_2$-P25. Cependant, la stabilité du photocatalyseur diminue avec le cyclage en raison du « leaching » de Ni dans un milieu aqueux. Comme perspective, l'alliage du Ni avec un métal noble tel que le Pt ou l'Au (en faible quantité) devrait améliorer l'activité photocatalytique et la stabilité du photocatalyseur. (iii) Les nanoétoiles d'or réduisent efficacement 4-NTP en 4-ATP (moins toxique) sous lumière visible, surpassant les sphères d'or en termes d'efficacité et de stabilité.

**MOTS-CLÉS:** Génération d'hydrogène ; carburants solaires ; traitement de l'eau ; nanoparticules métalliques ; nanoalliages ; photocatalyse ; cocatalyseurs ; résonance plasmonique de surface localisée ; effets synergétiques.

# Resumen General

## Fotocatalizadores para la Generación de Hidrógeno y el Tratamiento del Agua

La sociedad humana ha realizado avances notables en ciencia, tecnología y humanidades en las últimas décadas. Desafortunadamente, estos logros han estado acompañados por un aumento en problemas ecológicos y ambientales y crisis energéticas. Para superar estas cuestiones, el desarrollo sostenible ha surgido como un camino crucial para la sociedad moderna, centrado en preocupaciones energéticas y ambientales.

En este contexto, la nanociencia y la nanotecnología juegan un papel fundamental. Al manipular materiales a escala nanométrica, estos campos impulsan avances significativos en aplicaciones energéticas y ambientales, alineándose estrechamente con los objetivos del desarrollo sostenible. La nanociencia permite el desarrollo de fotocatalizadores más eficientes que mejoran la captura de energía solar. La energía solar ha ganado una atención significativa como una fuente de energía prometedora, limpia y abundante. La fotocatálisis se inspira en la fotosíntesis, donde la naturaleza almacena energía solar en enlaces químicos. La fotocatálisis es un proceso que utiliza luz para activar catalizadores y llevar a cabo reacciones químicas. Ha emergido como una estrategia prometedora para aprovechar la luz solar y abordar los desafíos de sostenibilidad energética y ambiental.

El hidrógeno ($H_2$) está surgiendo como un combustible solar prometedor debido a su potencial como energía limpia. Existen diferentes métodos para producir hidrógeno, cada uno con ventajas y limitaciones. Aproximadamente el 96% de la generación de $H_2$ proviene de combustibles fósiles, siendo el 48% generado a partir del gas natural (utilizando el método de reformado de vapor), el 30% del petróleo y el 18% de la gasificación de carbón, lo que resulta en emisiones significativas de dióxido de carbono ($CO_2$). Solo el 4% de $H_2$ se produce a través de la electrólisis del agua, que es costosa y depende de electricidad de combustibles fósiles, y un

mínimo del 0.1% proviene de otras fuentes. En consecuencia, la producción de $H_2$ está asociada con emisiones de gases de efecto invernadero, lo que la hace menos ecológico. Aproximadamente, 50 millones de toneladas de $H_2$ se generan anualmente, satisfaciendo solo el 2% de la demanda energética global.

La producción de hidrógeno verde mediante la fotocatálisis de agua es una de las principales tendencias en la investigación científica. En este proyecto de doctorado, se utilizó dióxido de titanio ($TiO_2$) como fotocatalizador, un fotocatalizador bien conocido debido a sus propiedades como baja toxicidad, bajo costo, buena actividad fotocatalítica y estabilidad fotoquímica y biológica. Sin embargo, sus aplicaciones prácticas son limitadas debido a la rápida recombinación de portadores de carga, y solo puede ser excitado bajo irradiación UV debido a su ancho de banda (3.0-3.2 eV). Se utilizan diferentes estrategias para mejorar la actividad de la titania en luz UV y visible, como su dopaje con átomos como C o N, su unión con otro semiconductor, o la modificación superficial con nanopartículas metálicas.

La modificación superficial con nanopartículas metálicas (NPs) puede disminuir la recombinación de los portadores de carga. Esto puede permitir la extensión de la absorción de luz hacia el espectro visible, lo que lleva a un aumento de la actividad fotocatalítica. Esta mejora es crucial para aplicaciones como la generación de hidrógeno, tratamiento de agua y aire, donde se necesitan fotocatalizadores eficientes para degradar contaminantes. Entre los metales, el platino (Pt) es el mejor co-catalizador para la generación fotocatalítica de $H_2$ debido a sus superiores propiedades catalíticas. Sin embargo, el Pt es costoso y no abundante, por lo que es importante reemplazarlo por otros metales. Las nanopartículas bimetálicas pueden inducir efectos sinérgicos en comparación con sus contrapartes monometálicas, mejorando la actividad fotocatalítica mientras se utilizan metales más abundantes y menos costosos.

Además, las nanopartículas metálicas como el oro (Au), el paladio (Pd) y la plata (Ag) presentan efectos plasmónicos, mejorando el proceso fotocatalítico a través de la resonancia plasmónica superficial localizada (LSPR). Este fenómeno se refiere a las oscilaciones colectivas de electrones libres de conducción excitados por los fotones incidentes en interferencia constructiva con el campo eléctrico de la luz

incidente. Incorporar nanopartículas plasmónicas mejorará la captura del espectro solar y aumentará la actividad fotocatalítica para la generación de $H_2$ y procesos de tratamiento de agua.

Esta tesis de doctorado implica el desarrollo y exploración de fotocatalizadores para la generación de $H_2$ verde y el tratamiento de agua. Estos aspectos se incluyen en algunos de los objetivos de sostenibilidad de la Agenda 2030 de las Naciones Unidas, ofreciendo una forma prometedora de resolver problemas globales de energía y medio ambiente. La superficie de titania se ha modificado con nanopartículas mono y bimetálicas para la generación de $H_2$ verde mediante fotocatálisis. Se ha estudiado el efecto de la modificación superficial en la dinámica de los portadores de carga y la generación de hidrógeno.

Se ha modificado el $TiO_2$-P25 comercial con nanoaleaciones de AuPd utilizadas como co-catalizadores para la generación de $H_2$. El Pd es un co-catalizador eficiente con una función de trabajo similar a la del Pt, y 50 veces más abundante en la Tierra y más barato. En la literatura, los catalizadores bimetálicos a base de Pd son cruciales para mejorar la selectividad de las reacciones de hidrogenación utilizando átomos individuales de Pd en la superficie de Au. Además, estudios recientes mencionaron que las NPs de Pd−Au exhiben una tasa de reacción fotocatalítica para $H_2$ similar a la de las NPs de Pt.

También, el $TiO_2$-P25 se ha modificado con nanopartículas de óxido de níquel (NiO) y de níquel-hierro (NiFe). Estudios recientes destacan el potencial de los catalizadores de Ni y Fe en fotocatálisis. Se inspiran en la naturaleza utilizando hidrogenasas, que son enzimas organometálicas que contienen centros de Ni y Fe que catalizan la evolución de $H_2$ con rendimientos que rivalizan con los del Pt.

La catálisis plasmónica utiliza las propiedades ópticas únicas de nanopartículas plasmónicas, como Au, Ag y Pd para mejorar los procesos catalíticos. Estas nanopartículas exhiben LSPR en las regiones visible e infrarroja cercana, generando campos electromagnéticos fuertes en sus superficies. Este efecto aumenta las tasas de reacción catalítica aprovechando la luz visible, mejorando así la eficiencia y ampliando las aplicaciones en conversión de energía, remediación ambiental y síntesis química. Los investigadores pueden lograr una catálisis más

efectiva y selectiva aprovechando los efectos plasmónicos, avanzando potencialmente hacia tecnologías sostenibles y procesos industriales más limpios.

Aquí, se ha explorado la catálisis plasmónica para el tratamiento de agua. Se ha utilizado 4-nitrotiofenol (4-NTP) como contaminante modelo. De hecho, altas concentraciones de 4-NTP pueden provocar irritación de la piel, daño ocular, problemas respiratorios e incluso la muerte en casos severos. Se utilizaron nanostrellas de oro (AuNSs) como fotocatalizadores para reducir 4-NTP a 4-aminotiofenol (4-ATP), un compuesto orgánico menos tóxico bajo irradiación de luz visible.

En el **Capítulo 1**, enfatizamos el papel crucial que juega la generación de hidrógeno y el tratamiento de agua en la resolución de la crisis energética y los problemas ambientales. Este capítulo introduce los principios de la fotocatálisis. Se presenta el dióxido de titanio, el semiconductor más utilizado en fotocatálisis, elegido como material de soporte, junto con las estrategias de modificación de su superficie con nanopartículas metálicas y de óxido metálico para mejorar su actividad fotocatalítica. También introducimos las propiedades plasmónicas de las nanopartículas metálicas, como Au, Ag y Pd, destacando sus propiedades ópticas distintivas proporcionadas por la LSPR. Este fenómeno genera campos electromagnéticos fuertes que mejoran las reacciones fotocatalíticas. Esta sección subraya el potencial de las nanopartículas plasmónicas en una variedad de aplicaciones.

En el **Capítulo 2**, describimos los métodos y procedimientos de síntesis utilizados para sintetizar fotocatalizadores, incluyendo: AuPd/$TiO_2$, NiFe/$TiO_2$, NiO/$TiO_2$ y nanoestrellas de oro (Au). Además, resumimos la metodología y los principios de las técnicas de caracterización utilizadas.

Los fotocatalizadores para la generación de hidrógeno fueron caracterizados mediante técnicas avanzadas como Microscopia Electrónica de Transmisión (TEM), Microscopia Electrónica de Transmisión de Alta Resolución (HRTEM), Microscopia Electrónica de Transmisión de Campo Oscuro de Ángulo Alto (HAADF-STEM), Espectroscopia de Rayos X Dispersiva por Energía (EDS) o Espectroscopia de Pérdida de Energía de Electrones (EELS), Espectroscopia de Emisión Óptica de

Plasma Acoplado Inductivamente (ICP-OES), Espectroscopia de Reflectancia Difusa (DRS), Difracción de Rayos X (XRD), Espectroscopia de Fotoelectrones de Rayos X (XPS), Conductividad de Microondas Resuelta en el Tiempo (TRMC) y Cromatografía de Gases (GC).

Los fotocatalizadores para el tratamiento de agua fueron caracterizados mediante técnicas avanzadas como Microscopia Electrónica de Barrido (SEM), TEM, HRTEM, EDS, espectroscopía UV-vis, Microscopia Óptica de Campo Oscuro Hiperespectral y Microscopia de Fuerza Atómica (AFM).

En el **Capítulo 3**, presentamos la modificación de la titania comercial ($TiO_2$-P25) con nanopartículas mono y bimetálicas (Au, Pd y AuPd) utilizando un método de reducción química con borohidruro de sodio ($NaBH_4$) a temperatura ambiente. La $TiO_2$ modificada en la superficie con nanoaleaciones bimetálicas AuPd exhibe una alta actividad fotocatalítica para la generación de hidrógeno, esta actividad es similar a la obtenida con $TiO_2$ modificado con Pt. Los resultados experimentales están respaldados por cálculos de teoría del funcional de la densidad (DFT) y Tight-Binding basado en la densidad funcional (DFTB+), que muestran que la aleación de AuPd con bajo contenido de Pd presenta efectos sinérgicos significativos para la generación de hidrógeno bajo luz UV-visible. Los fotocatalizadores AuPd/$TiO_2$ son estables bajo ciclos. Este trabajo ha sido publicado en la revista Solar RRL (https://doi.org/10.1002/solr.202400106), destacado en la portada, así como por el *Centre national de la recherche scientifique (CNRS)* (https://www.inc.cnrs.fr/fr/cnrsinfo/des-nanoalliages-dor-et-de-palladium-pour-booster-la-production-dhydrogene).

En el **Capítulo 4**, la superficie de $TiO_2$-P25 fue modificada con NPs de NiO inducidas por el método de radiólisis. Todas las muestras modificadas exhibieron una actividad fotocatalítica superior en comparación con $TiO_2$ sin modificar. Los resultados destacan el papel crucial de la modificación con NPs de Ni en la mejora de la separación de portadores de carga, lo que resulta en una mayor actividad bajo luz UV-visible. Además, los resultados revelaron que bajo irradiación visible, las NPs de NiO inyectan electrones en la banda de conducción de $TiO_2$. Sin embargo, la generación de hidrógeno con NiO/$TiO_2$ disminuye bajo los ciclos fotocatalíticos,

probablemente debido a la lixiviación de Ni en el medio acuoso, y después del tercer ciclo se obtiene un meseta.

El **Capítulo 5** trata sobre el sistema NiFe/$TiO_2$ para aplicaciones fotocatalíticas. Se sintetizaron NPs bimetálicas de Ni-Fe sobre $TiO_2$-P25 mediante el método de radiólisis. Nuestros resultados muestran que la $TiO_2$ modificada en la superficie con NPs bimetálicas de NiFe exhibe una alta actividad fotocatalítica para la generación de hidrógeno. La actividad fotocatalítica mejorada de las nanopartículas NiFe/$TiO_2$ se atribuyó al efecto sinérgico entre las nanopartículas de NiFe y $TiO_2$, lo que lleva a una mejor transferencia y separación de carga. Sin embargo, la generación de hidrógeno con NiFe/TiO2 disminuye bajo los ciclos fotocatalíticos, probablemente debido a la lixiviación de Ni en el medio acuoso, y después del tercer ciclo se obtiene una meseta.

El **Capítulo 6** trata sobre la catálisis plasmónica utilizando nanoestrellas de oro (AuNSs). Primero, presentamos la síntesis de AuNSs utilizando un método de crecimiento por semillas. Las propiedades plasmónicas de estas AuNSs se utilizaron para reducir la molécula tóxica de 4-NTP. La excitación plasmonica de las AuNSs (bajo irradiación de luz visible) induce la reducción de 4-NTP a 4-ATP (menos tóxico). La reducción de 4-NTP fue seguida mediante espectroscopía UV-visible. Las AuNSs son más efectivas y estables para la reducción de 4-NTP que las nanoesferas de oro (AuSs) y se pueden recuperar fácilmente después de la prueba fotocatalítica. Se utilizó la microscopía óptica de campo oscuro hiperespectral para medir el espectro de las AuNSs individuales, que exhiben una o dos resonancias plasmónicas. Los espectros de las AuNSs individuales fueron analizados después de la adsorción de 4-NTP en su superficie y después de la irradiación. Además, se utilizó la microscopía de fuerza atómica para investigar cómo la variación del tamaño de las AuNSs afecta la adsorción de 4-NTP y su degradación bajo excitación de luz visible. Nuestros hallazgos sugieren que los nanomateriales plasmónicos como las AuNSs tienen un gran potencial para la degradación de contaminantes orgánicos en el agua, lo que podría llevar a nuevas oportunidades para la remediación ambiental.

Finalmente, el **Capítulo 7** presenta las conclusiones principales de este trabajo y perspectivas para futuras investigaciones. En resumen, enfatizamos que (i) las nanoaleaciones de AuPd con bajo contenido de Pd son co-catalizadores muy eficientes y estables para la reacción de evolución de hidrógeno. Este estudio muestra un ejemplo de efectos sinérgicos obtenidos mediante la aleación de dos metales. (ii) La modificación de la superficie con metales de transición como Ni-Fe y óxidos de metales de transición (NiO) puede mejorar la actividad fotocatalítica de $TiO_2$-P25. Sin embargo, la estabilidad del fotocatalizador disminuye con el ciclo debido a la lixiviación de Ni en un medio acuoso. (iii) Los co-catalizadores de NiFe muestran buena actividad para la generación de $H_2$, y esta actividad es superior a la de sus contrapartes monometálicas. Como perspectiva, se espera que la aleación de Ni y Fe con un metal noble como Pt o Au (en bajo contenido) mejore la actividad fotocatalítica y la estabilidad del fotocatalizador. (iv) Las nanostrellas de oro reducen eficientemente 4-NTP a 4-ATP (menos tóxico) bajo luz visible, superando a las nanoesferas de oro en eficiencia y estabilidad.

**PALABRAS CLAVE**. Generación de hidrógeno; combustibles solares; tratamiento de agua; nanopartículas basadas en metales; nanoaleaciones; fotocatálisis; resonancia plasmónica superficial localizada; efectos sinérgicos

## General Objectives

The goal of this PhD research work was to develop and study the transition metal-modified photocatalysts and plasmonic catalysts for hydrogen generation and water treatment applications.

## Specific Objetives

The goal of the present work was development of efficient photocatalysts based on metal nanoparticles for hydrogen generation and water treatment. The specific objectives are:

**For hydrogen generation:**

- Synthesis of metal-based nanoparticles (AuPd, NiFe, NiO) on $TiO_2$ surface controlling the size and the composition of the nanoparticles by chemical and radiolytic methods to enhance the UV-visible absorption properties and extend the charge carriers' lifetime.
- Characterization of metal-based nanoparticles by different techniques (TEM, HRTEM, HAADF-STEM, EDS or EELS, ICP-OES, DRS, XRD, and XPS).
- Investigation of charge carriers' dynamics, which is a key factor in photocatalysis by time-resolved microwave conductivity (TRMC).
- Understanding the physical and chemical mechanisms that contribute to enhancement of the photocatalytic activity.
- Study of the stability of the photocatalysts with photocatalytic cycling.

**For water treatment:**

- Synthesis of Au nanostars (AuNSs) by the seed growth method.

- Characterization of AuNSs by advanced materials characterization techniques (SEM, TEM, HRTEM, EDS, and UV-vis spectroscopy).
- Study the plasmonic catalytic properties of AuNSs for degradation of 4-NTP used as a model pollutant and compare this activity with AuSs.
- Measurement of the spectrum of individual nanostars and understand the adsorption of 4-NTP on the gold nanostars' surface and the spectral changes after irradiation using hyperspectral dark-field optical microscopy.
- Investigation of the size effect of AuNSs on adsorption and degradation of 4-NTP using AFM.
- Understanding the physical and chemical mechanisms that contribute to enhancing photocatalytic activity.

## Hypothesis

Development of highly efficient photocatalysts for hydrogen generation and water treatment applications can be achieved by surface modification of photocatalysts with metal-based nanoparticles or plasmonic catalysts of controlled shape, size and composition achieved through chemical and radiolysis methods. The optimization of the synthesis parameters will improve the stability and cost-effectiveness of the photocatalysts. Furthermore, a comprehensive understanding of the fundamental physical and chemical mechanisms will be crucial for enhancing the photocatalytic activity of these systems.

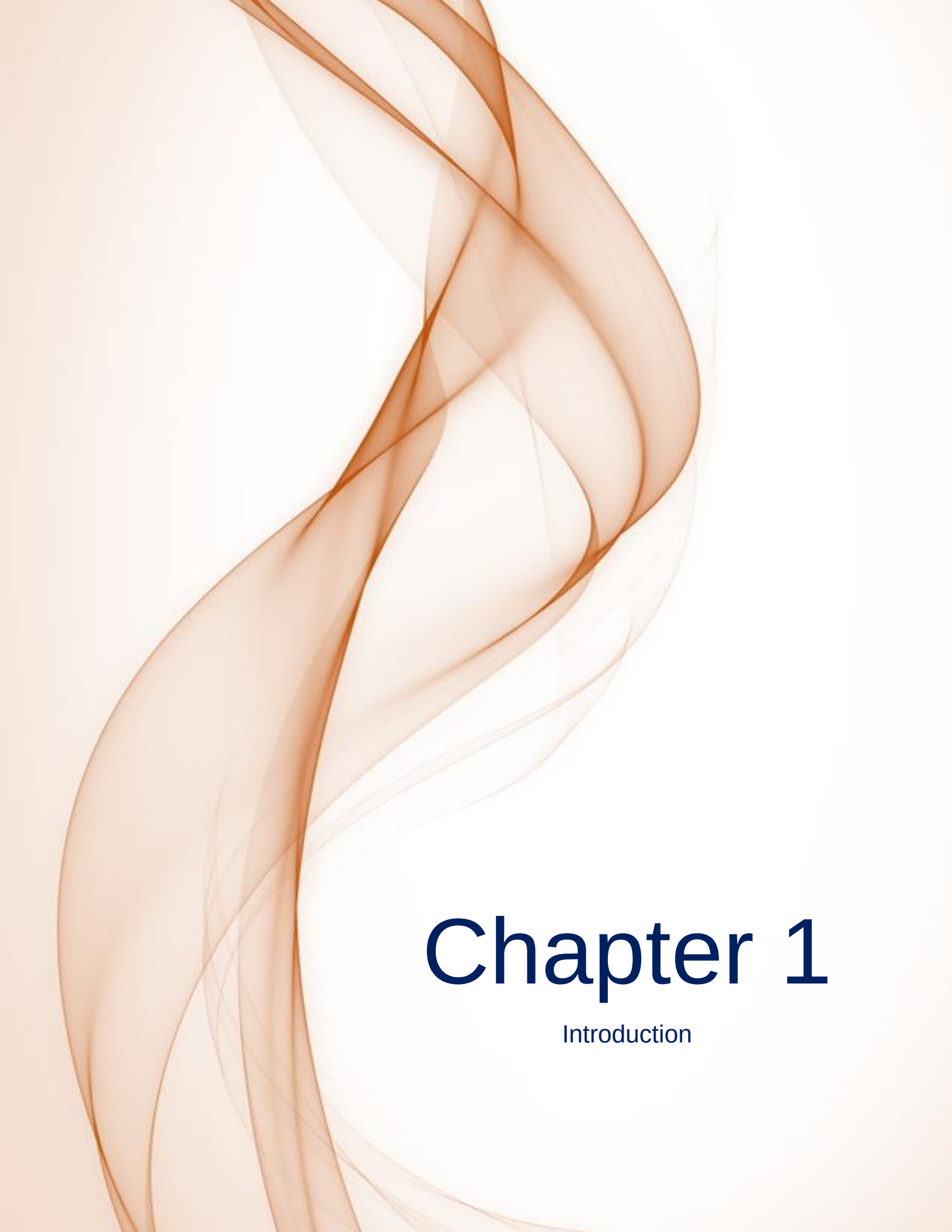

# Chapter 1

Introduction

# Chapter 1. Introduction

## 1.1 Environmental pollution

Global concerns about climate change and the need for sustainable solutions to produce clean energy and address water pollution have become topics of interest to scientists for environmental remediation. The exponential increase in global demand for energy, the growth of the world population, and the still widely use of fossil fuels cause huge $CO_2$ emissions, which are responsible for greenhouse effects and climate change.[21] **Figure 1-1** shows the $CO_2$ emissions from fossil fuels and industry per country in 2023. Achieving net zero emissions is crucial for humanity's survival. The Intergovernmental Panel on Climate Change (IPCC) warns that, without urgent action, global temperatures could surpass 1.5°C (**Figure 1-2**) and potentially exceed 4°C by 2100, rendering the planet increasingly uninhabitable.[22]

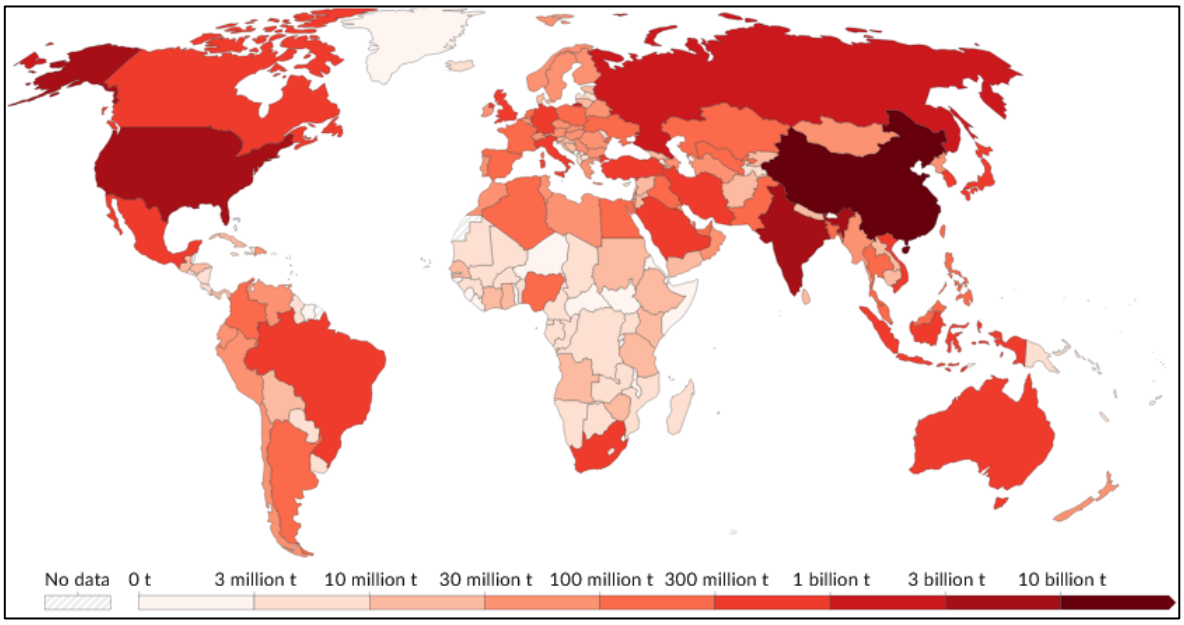


**Figure 1-1.** Annual $CO_2$ emissions from fossil fuels and industry per country 2023.

*Data source:* *Global Carbon Budget (November 2024)*

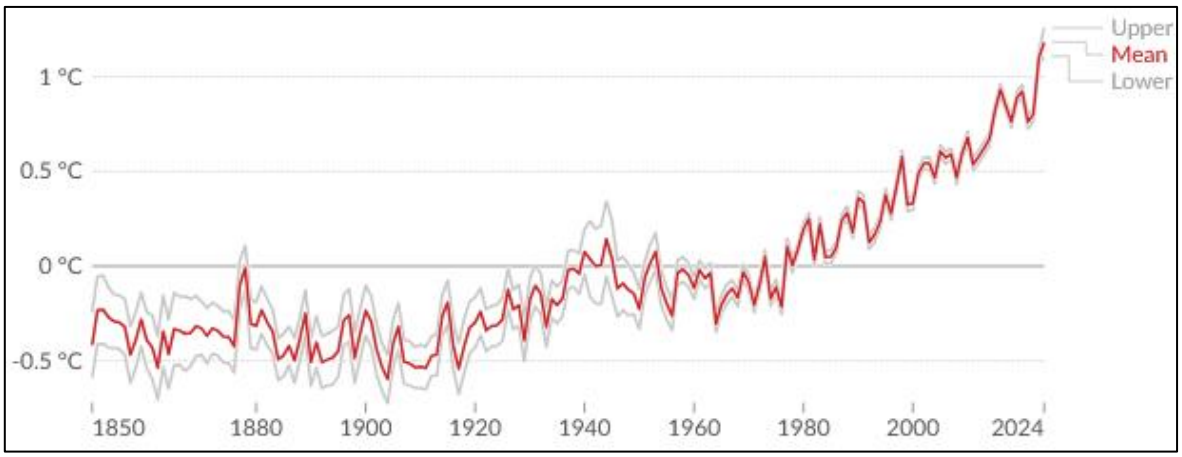


**Figure 1-2.** Global average land-sea temperatures.

*Data source: Met Office Hadley Centre (October 2024).*

Nanoscience explores the manipulation of materials at the nanoscale, where unique physical and chemical properties emerge and differ significantly from those at the bulk level. Nanoparticles (NPs), due to their high surface area-to-volume ratio, exhibit remarkable catalytic properties, making them highly effective in various applications. In catalysis, nanoparticles (such as Pd and Pt NPs) are utilized in catalytic converters for automobiles, where they facilitate the conversion of harmful gases such as carbon monoxide (CO) into less toxic substances. For instance, Au-NPs less than 5 nm are particularly effective for CO oxidation at room temperature, demonstrating superior catalytic activity compared to larger Au particles.[23] The catalytic efficiency of NPs is highly sensitive to their size, with smaller particles often showing enhanced reactivity due to increased surface energy and more active sites. Furthermore, bimetallic catalysts, which combine two different metals, can offer synergistic effects that improve catalytic performance and stability compared to their monometallic counterparts.[7,8,]9 Beyond automotive applications, nanoparticles are also used in industry for the synthesis of many chemicals and in fuel cells, where they enhance the efficiency of electrochemical reactions, and in photocatalysis, where they drive various chemical reactions under light exposure. This versatility underscores the potential of nanoscience and nanoparticles in advancing technology

across multiple fields, including environmental remediation, energy conversion, sensors applications, nanomedicine and photocatalysis.[25,26,27,28,29,30,31]

### 1.1.1 Hydrogen as clean energy

The development of renewable, clean energy sources is crucial for replacing fossil fuels and limiting $CO_2$ emissions. Hydrogen is projected to be not only the cleanest energy, it will also be consolidated as an energy vector that moves us forward in the transition toward a zero carbon footprint, as committed by Hydrogen Europe, among other worldwide initiatives. Since the petroleum crisis in 1973, alternatives have been sought for energy carriers like hydrogen.[32] Hydrogen as fuel produces higher energy power (122 kJ $g^{-1}$) than gasoline (40 kJ $g^{-1}$),[33] and can be obtained from different sources.[34] As mentioned, 96% of $H_2$ generation comes from fossil fuels (which produces a huge amount of $CO_2$) and only 4% from water electrolysis.[1] Recently, hydrogen production by solar water splitting has attracted much interest because it uses light energy and only emits water and oxygen.[35,36] Solar energy is a green, abundant and renewable source due to its natural availability, which offers a promising way to solve environmental and energy issues.[37,38]

### 1.1.2 Water treatment

Water pollution is a significant environmental concern, and finding effective strategies to degrade pollutants in water is a crucial area of research. Pharmaceutical, agricultural, and industrial activities significantly contribute to water pollution, introducing a wide range of contaminants, including organic pollutants, pesticides, and pharmaceuticals into aquatic systems. These pollutants affect aquatic life, ecosystems and human health.[39] One common water pollutant is 4-NTP, which harms aquatic life and human health. Exposure to high concentrations of 4-NTP can lead to skin irritation, eye damage, respiratory issues, and even death in

severe cases. The degradation of such organic pollutants is essential for maintaining water quality and protecting public health.

Photocatalysis has emerged as a promising method for addressing these environmental challenges. By using photocatalysts, pollutants in water can be transformed into less harmful substances when exposed to light. This process is not limited to simple compounds like 4-NTP but extends to more complex organic contaminants, including pharmaceuticals, pesticides, and industrial chemicals.

The combined effects of industrial pollution, climate change, and contamination highlight the urgent need for sustainable and effective environmental solutions. Researchers are actively exploring various solar energy applications, such as hydrogen generation through photocatalytic water splitting and solar photocatalytic water treatment, to address these challenges and advance sustainable energy solutions.

In addition, solar fuels and $CO_2$ reduction are crucial areas of research in addressing global environmental challenges. Solar fuels, generated through processes like photocatalytic water splitting, convert solar energy into storable chemical energy, offering a clean and renewable energy source. Simultaneously, $CO_2$ reduction technologies focus on capturing and converting atmospheric $CO_2$ into useful products, mitigating greenhouse gas effects and contributing to climate change mitigation. Together, these innovations offer a path toward a more sustainable and environmentally friendly future by integrating renewable energy solutions and reducing harmful emissions.

## 1.2 Photocatalysis

Photocatalysis is a process that uses materials (in general semiconductors) capable of harnessing solar energy to drive chemical reactions by generating electrons ($e^-$)

and holes ($h^+$) pairs. These materials act as catalysts under solar light exposure, mimicking natural processes like photosynthesis. Photosynthesis is a natural process used by plants, algae, and some bacteria to convert light energy, usually from the sun, into chemical energy stored in glucose molecules. This process is fundamental to life on Earth, as it provides the primary energy source for nearly all living organisms. In this study, we are inspired by Nature to harvest solar energy with the photocatalysts and store it in chemical bonds. However, most of the inorganic photocatalysts because of their large band gap absorb light in the UV range, which constitutes only 4-5% of the solar spectrum (**Figure 1-3**). The solar spectrum passing through the atmosphere is also composed of 43% of visible and 52% of infrared range of the solar light.[40]

Another limitation in using photocatalysts (apart from their limited absorption) is the high charge carriers‘ recombination rate, which limits the quantum yield of the light energy conversion. The development of materials that efficiently harvest visible light for photocatalysis is essential. Enhancing photocatalyst efficiency by extending charge carriers‘ lifetime, limiting charge carriers‘ recombination and improving surface mobility is also a pivotal point to optimize the process and maximize solar energy utilization.

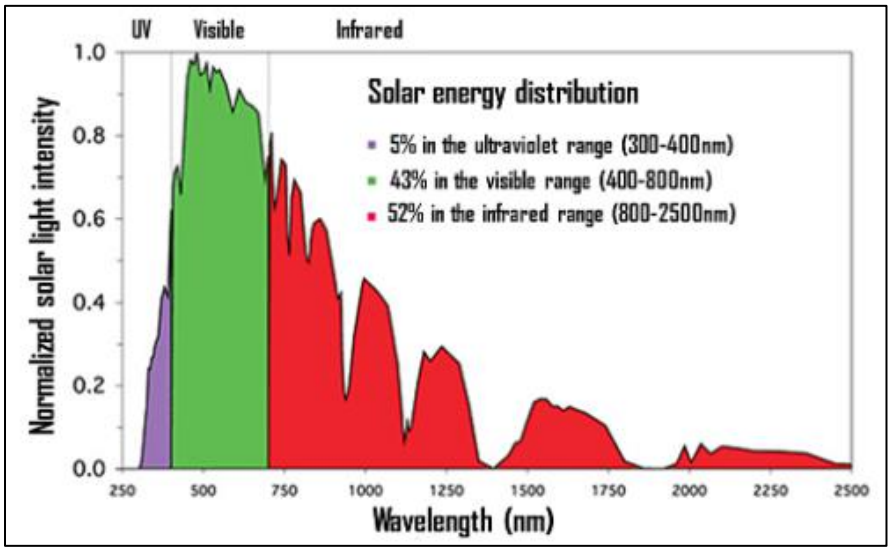


**Figure 1-3.** The spectrum shows the solar radiation received at Earth's surface.[35]

### 1.2.1 Photocatalytic water splitting

Photocatalytic water splitting mimics the natural photosynthesis process in plants by using sunlight to convert water into hydrogen. This method involves harnessing solar energy to generate chemical energy, leading to the production of hydrogen gas ($H_2$) from water. In photocatalytic reactions, electron and hole pairs (also known as *excitons*) are manipulated to facilitate the generation of $H_2$ through redox reactions. Worth to note is that for efficient hydrogen production through photocatalytic water splitting, a semiconductor with a bandgap energy wider than 1.23 eV (redox potential of water) is required.[41,42]

The mechanism of photocatalytic water splitting for $H_2$ production involves several key stages: light harvesting, charge excitation, charge separation and transfer, and surface catalytic reactions (**Figure 1-4**). The process begins when light with sufficient energy higher than or equal to the band gap of the semiconductor is absorbed. It causes pairs of electrons ($e^-$) and holes ($h^+$), i.e., excitons. These charge carriers are then separated, with electrons moving from the valence band (VB) to the conduction band (CB), leaving holes in the VB. A large part of charge carriers recombine or are trapped. When electrons and holes escape recombination and trapping, they can migrate to the surface and participate in redox reactions. Electrons and holes play roles in reduction and oxidation reactions in water or air. Under an inert atmosphere, reduction reactions can occur, such as reduction of $H^+$ leading to the formation of $H_2$ or reduction of $CO_2$. In the presence of oxygen, oxidation reactions can occur, which can be used for the degradation of organic pollutants. These processes take place on the surface of a photocatalyst.

In photocatalytic water splitting, a major challenge is to reduce the recombination of electron-hole pairs, since the short life time of the exciton reduces the efficiency of $H_2$ generation. This recombination issue is particularly problematic in pure water. To address this challenge, sacrificial reagents such as triethanolamine and methanol

are often used to scavenge the holes and, therefore, enhance the charge carriers‘ separation and improve the efficiency of the photocatalytic water splitting process.

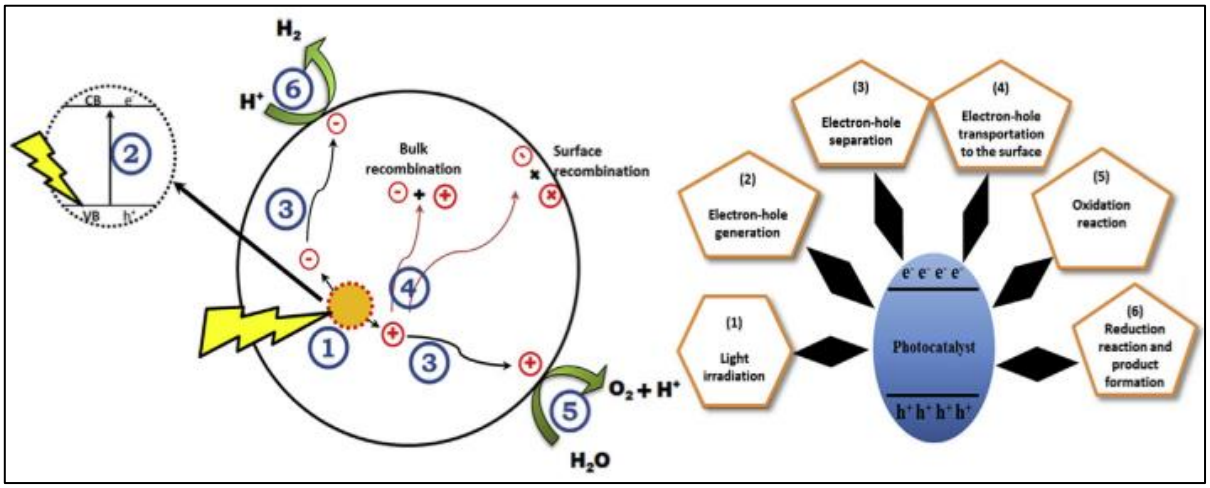


**Figure 1-4.** Diagram of photocatalytic water splitting mechanism for hydrogen generation.[43]

## 1.3 Semiconductors

Semiconducting materials like *n*-type and *p*-type oxides are crucial components in electronic devices such as solar cells, transistors, and sensors. The *n*-type semiconductors present excess electrons, allowing for efficient electricity conduction, while *p*-type semiconductors have positively charged holes that resist electrical current flow. Examples of *n*-type materials include titanium dioxide ($TiO_2$) and zinc oxide (ZnO), while *p*-type materials include nickel oxide (NiO) and copper oxide (CuO).[44]

The energy diagram of a semiconductor is shown in **Figure 1-5**. The charge carriers‘ dynamics occur between the CB and VB. The band gap energy ($E_G$), is the energy difference between CB and VB. The energy vacuum level ($E_{VAC}$) is the energy level of an electron with zero kinetic energy within a ‘‘few nanometers’’ outside the solid surface. The ionization energy (IE) is the difference between $E_{VAC}$ and VB, and

is the minimum energy to remove an electron from the system. In contrast, electron affinity (EA) is the energy gained by an electron from the $E_{VAC}$ to the CB. The work function (WF) is an important parameter for photocatalysis and solar cells due to the band alignments of interfaces such as $TiO_2$/metal and $TiO_2$/*p*-type SC contacts creating Schottky barriers and *p-n* junctions, respectively. The WF is the difference between ($E_{VAC} - E_F$), and means the energy barrier to remove an electron from the Fermi level ($E_F$) to outside the surface ($E_{VAC}$). The WF depends on the position of $E_{VAC}$ and $E_F$, which can be manipulated separately by modifying $TiO_2$ surface.[45]

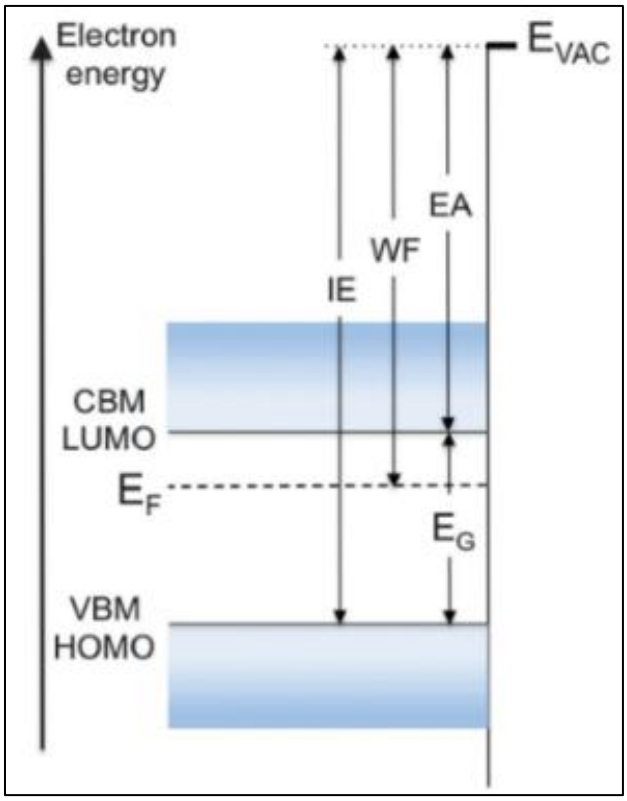


**Figure 1-5.** Energy illustration of a semiconductor with conduction and valence bands aligned to the surface.[45]

**Figure 1-6** illustrates the band positions of various semiconductors in an aqueous electrolyte at pH 1. The CB and VB edges are shown in red and blue, respectively, relative to the vacuum level or normal hydrogen electrode (NHE). Two green dashed lines mark the water reduction and oxidation potentials.[46,47] In this PhD thesis, we

used $TiO_2$ as photocatalytic material because it is cheap and is considered more stable and more efficient than other semiconductors at adequate redox potentials for water splitting.

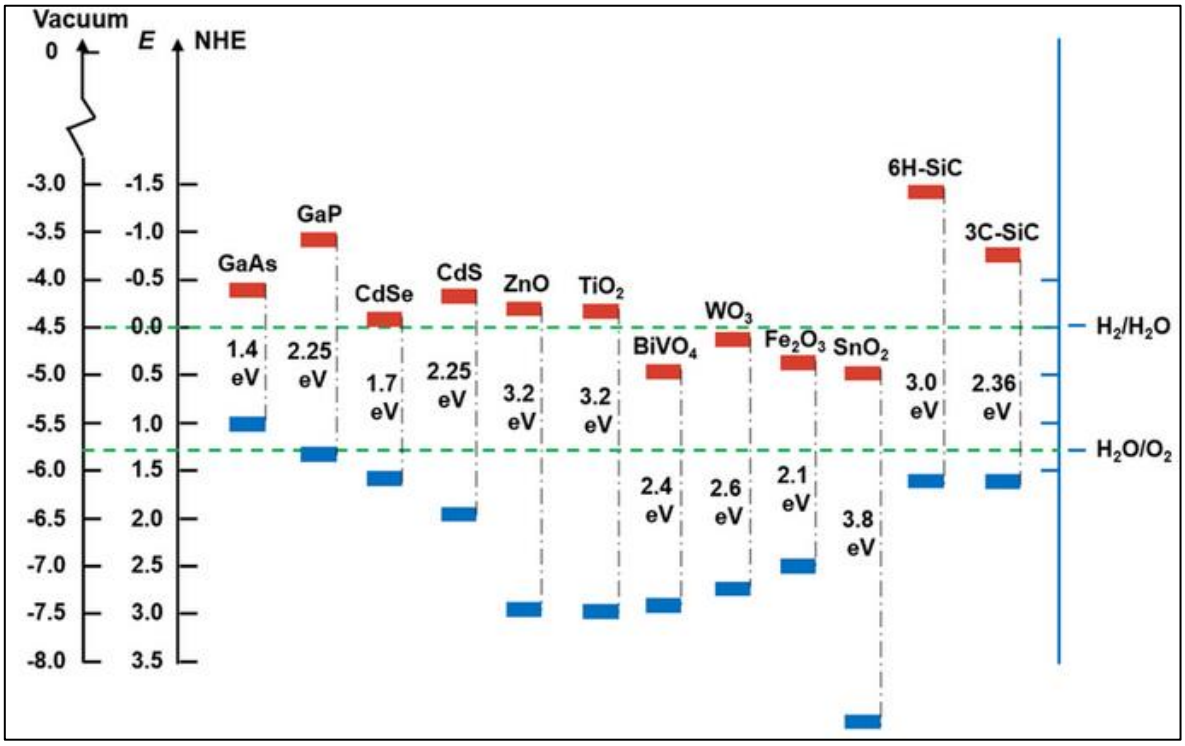


**Figure 1-6.** Band positions of various semiconductors in an aqueous electrolyte at pH 1.[46,47]

### 1.3.1 Titanium dioxide as photocatalytic material

$TiO_2$ is a semiconductor widely used in photocatalysis because of its excellent properties, such as high reactivity, photochemical and biological stability, low toxicity, and low price.[48,49] When $TiO_2$ is excited with photons with higher energy than its band gap (3.2 eV and 3.0 eV for anatase and rutile, respectively).[50] Electrons in the VB migrate to the CB creating holes in the VB, then these charge carriers can achieve chemical reactions (**Figure 1-7**). The limitation of $TiO_2$ application in photocatalysis is mainly due to the fast charge carriers' recombination and its large bandgap, which induces excitation only under UV light irradiation. Furthermore, and

not helping in this process, the UV light window constitutes only 4-5% of the solar light spectrum impinging on the Earth's surface (**Figure 1-3**).[40]

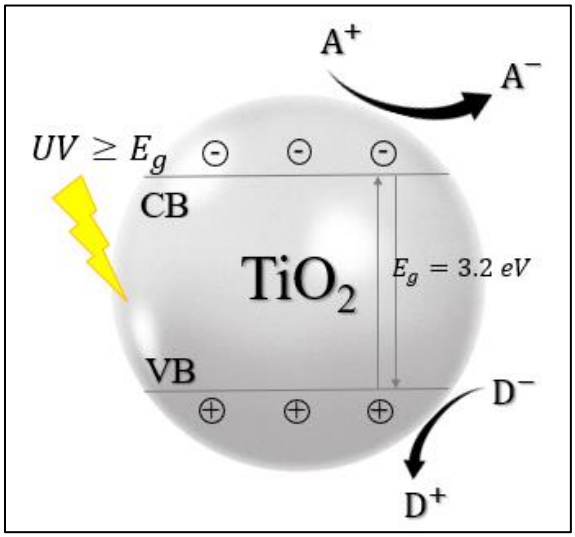


**Figure 1-7.** Titanium dioxide as photocatalytic material excited under UV light.

Anatase titanium dioxide ($TiO_2$) is generally considered more active than rutile phase due to its longer charge carriers' lifetime, a factor that significantly enhances its photocatalytic performance. The charge carriers' dynamics has been demonstrated using TRMC studies.[51] Commercial titania ($TiO_2$-P25) was used for all the experiments consisting of a mixture of anatase–rutile crystalline stable phases. The unit cells of anatase and rutile, $Ti^{4+}$ ions (blue color) and $O^{2-}$ ions (red color), as illustrated in **Figure 1-8**.[52] A synergetic role of anatase-rutile heterojunction due to band alignment increase the number of charge carriers participating in the photoreaction,[50,53,54,55] and longer charge carriers' life time under UV excitation.[56,57,58] However, the direction of charge carriers' transfer in terms of band alignment is still under debate. From the perspective of band alignment, there are five proposed configurations between rutile and anatase (**Figure 1-9**). One view suggests electrons move from anatase to rutile while holes go from rutile to anatase (Type I), and another scenario suggests the opposite (Type II).

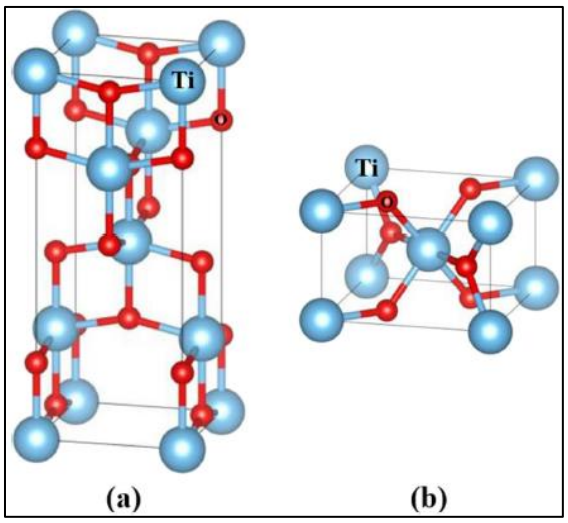


**Figure 1-8.** Unit cells of **(a)** anatase and **(b)** rutile crystalline phases of commercial titania ($TiO_2$-P25).[59]

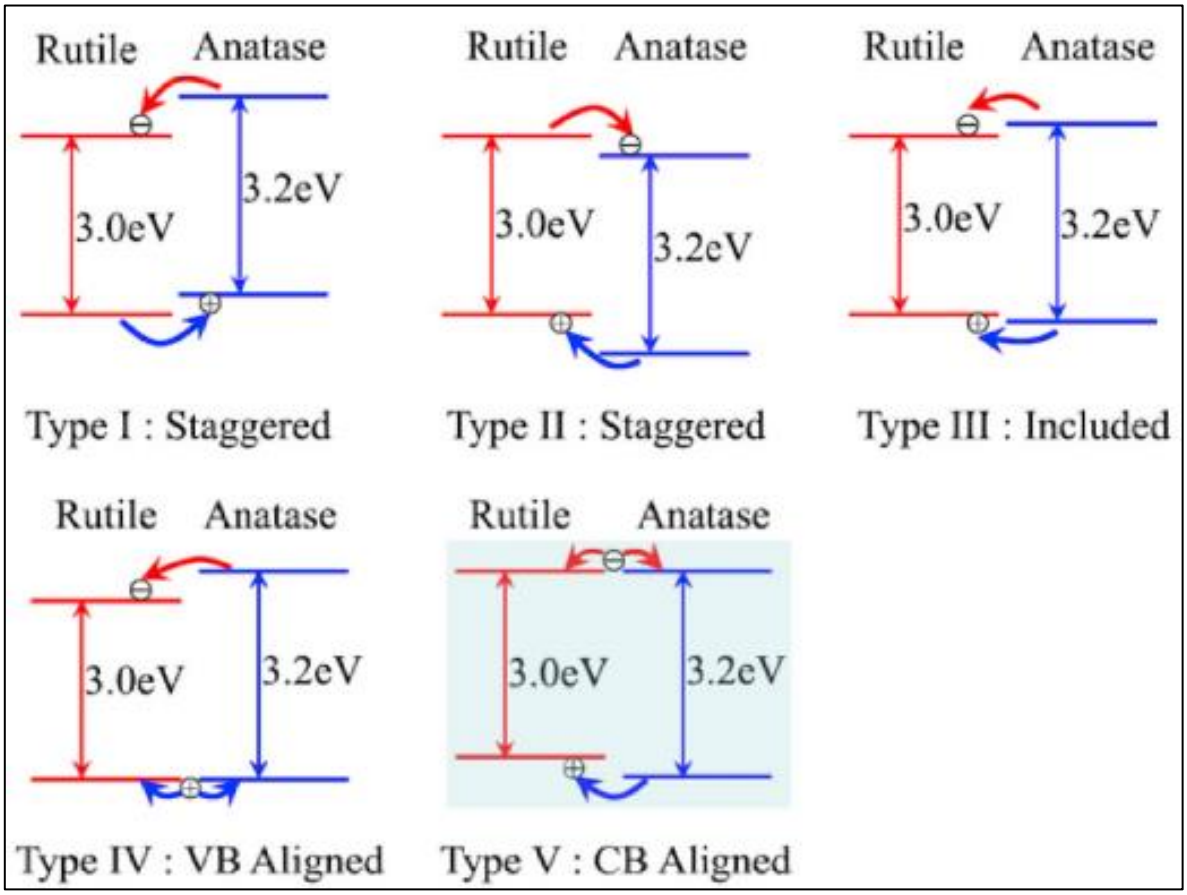


**Figure 1-9.** Illustration of five possible types of band alignments between rutile and anatase $TiO_2$.[52]

## 1.4 Ways to improve the photocatalytic activity under UV-vis light

### 1.4.1 Modified $TiO_2$ surface with metal nanoparticles

As mentioned before, the wide band gap of commercial $TiO_2$-P25 (3.2 eV for anatase and 3.0 eV for rutile phases),[50] and the high rate of charge carriers' recombination limit its activity under visible light, making clear the need of its doping or surface modifications to enhance its performance. To address these limitations and enhance the photocatalytic activity of $TiO_2$, researchers have explored various strategies, including doping with atoms such as C[2] or N,[3] surface modification of $TiO_2$ with plasmonic and transition metals,[51] or heterojunction with transition metal oxides, graphitic carbon nitride or conjugated polymer nanostructures.[4,60,61]

Particularly, surface modification of $TiO_2$ with metal nanoparticles like Pt, Pd, Rh, Au, Ni and Ag) is particularly effective in enhancing the photocatalytic activity under UV-vis light for $H_2$ generation.[15,62,63,64,6,65] By loading these metals onto $TiO_2$ surfaces, the recombination of photo-generated electron-hole pairs can be reduced, leading to improved efficiency. The interaction between the metal nanoparticles and $TiO_2$ creates a Schottky junction (explained below), facilitating the transfer of photo-generated electrons from $TiO_2$ to the metal nanoparticles (**Figure 1-10a**), thus enhancing the separation of electron-hole pairs.[43]

Doping $TiO_2$ with noble metal NPs allows light absorption in the visible region of the spectrum due to the LSPR phenomenon.[6,66,60] Noble metals like Au exhibits strong LSPR (also explained below) in the visible range, allowing efficient transfer of hot photogenerated electrons to the CB of $TiO_2$ under visible light (**Figure 1-10b**), leading to enhanced photocatalytic activity.

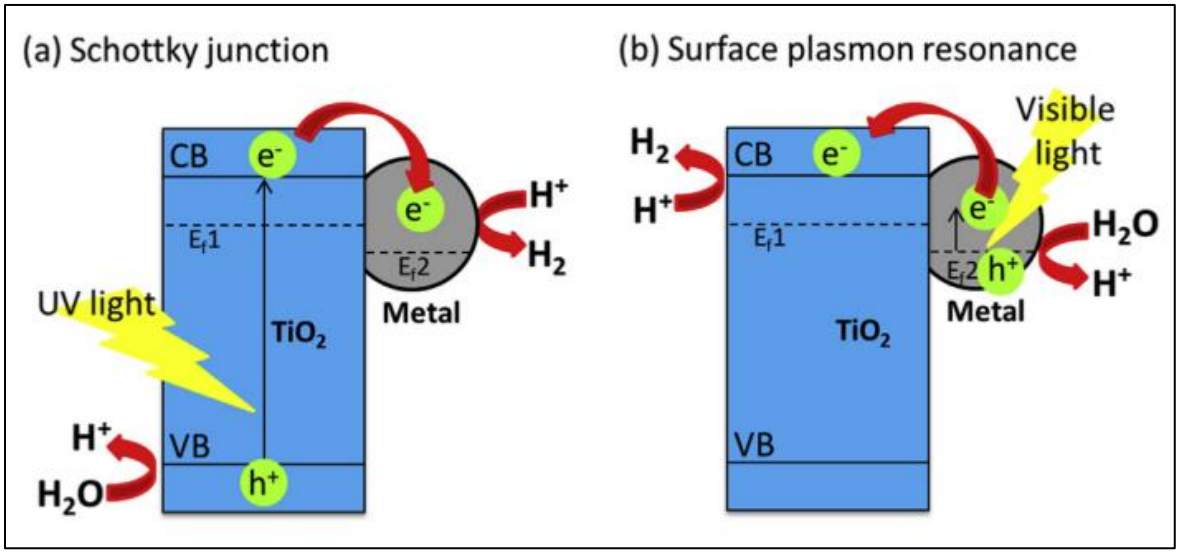


**Figure 1-10. (a)** Illustration of charge transfer in metal/$TiO_2$ under UV light irradiation due to the Schottky junction; **(b)** Schematic diagram illustrating charge transfer in metal/$TiO_2$ under visible light irradiation due to the LSPR.[43]

Among the metals, platinum (Pt) is the best cocatalyst for photocatalytic hydrogen generation.[15,67] However, Pt is costly and scarce, and thus, it is important to replace it with other more abundant metals. Au NPs can also activate $TiO_2$ under visible light due to its LSPR.[6] Surface modification of $TiO_2$ with bimetallic NPs based on Au has been widely applied for photocatalytic hydrogen generation because it is an efficient cocatalyst and is also cheaper and more abundant than Pt. Higher activities for photocatalytic hydrogen generation can be obtained with bimetallic NPs compared with their monometallic counterparts.[8,19,68,14] For instance, bimetallic NPs like AuPd,[19,69] AuPt,[70,71] AuNi,[8] and AuCu,[72,73] have been reported to demonstrate improvements in their electrical, optical, and catalytic properties. These nanoalloys exhibit superior catalytic performance, particularly in selectivity and stability, compared to their individual metal components.

### 1.4.2 The Schottky junction

The photocatalytic activity under UV light is enhanced because metal NPs like Pt, Au, Ag, Ni, and Pd can act as electron traps, inhibiting the charge carriers' recombination.[6,43,74]

The work function of metals plays a crucial role in improving the separation of electron-hole pairs on the semiconductor surface, enhancing the overall efficiency of the photocatalytic process. The work function is the energy required to move an electron from inside the material to the surface. In this case, when the work function of a metal ($\Phi_m$), is larger than the electron affinity of a *n*-type semiconductor ($X_n$), a Schottky barrier or junction forms upon contact between them. This junction creates an electric field that enhances the transfer of electrons from $TiO_2$ to the metal nanoparticles under UV light, leading to the spatial separation of electron-hole pairs (**Figure 1-11**).

The diagram below illustrates the band structure of a Schottky junction formed by an *n*-type SC and a metal. Electrons move from the CB of the SC to that of the metal, moving from higher to lower energy levels due to the Schottky barrier. The barrier potential ($V_D$) represents the difference between the work function of the metal ($\Phi_m$) and the electron affinity of the semiconductor ($X_n$). The height of the barrier determines how easily charge carriers (electrons or holes) can cross the junction.
As these electrons cross the barrier potential ($V_D = \Phi_m - X_n$), they diffuse into the metal, leading to the formation of a depletion region (also called a space-charge region) at the interface, where there is a lack of free charge carriers that extends only into the semiconductor side. This process maintains equilibrium with matching Fermi levels on both sides.

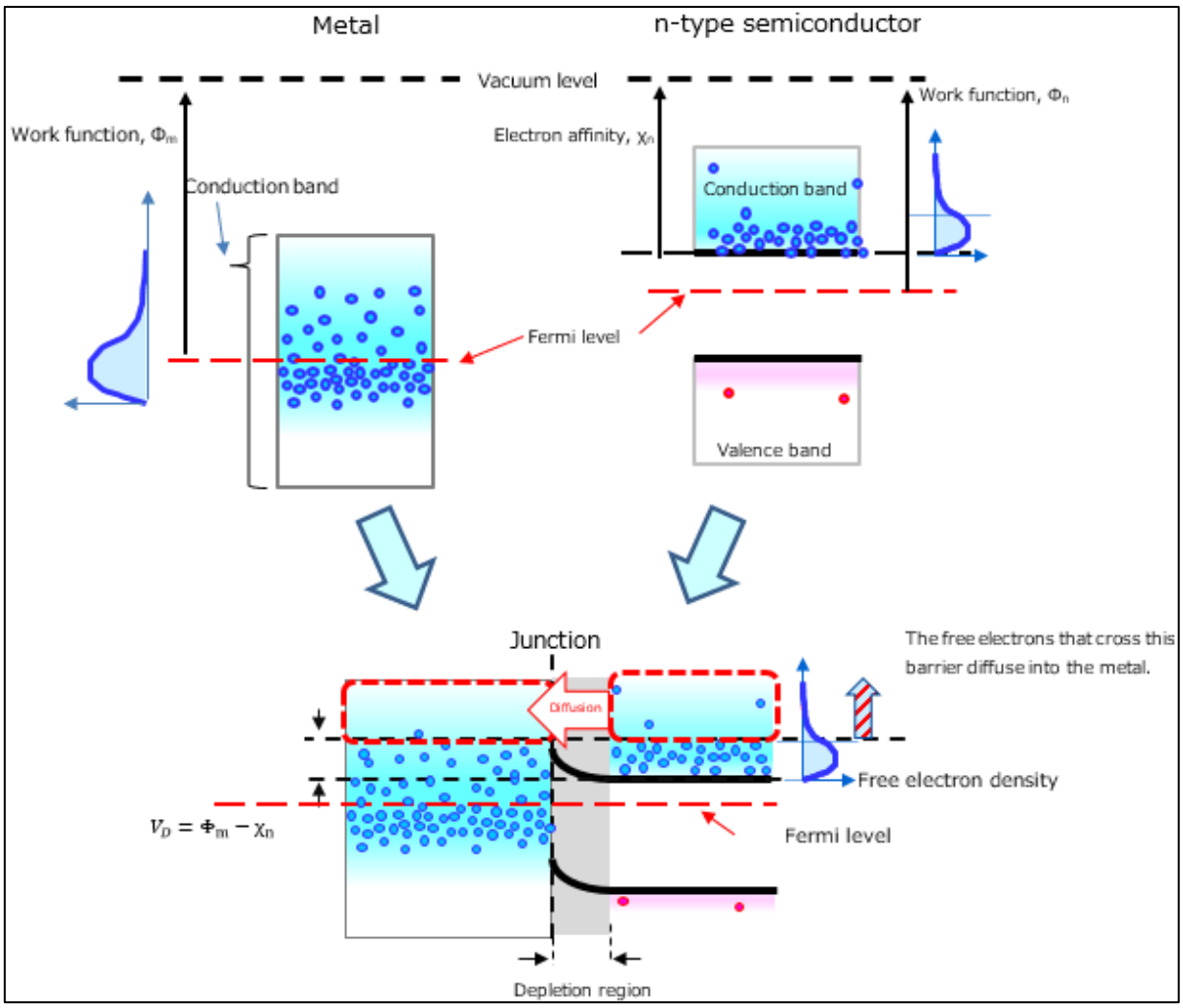


**Figure 1-11.** Schottky junction contact between a metal and an *n*-type semiconductor.
*Data source: Toshiba (2024).*

### 1.4.3 Modified $TiO_2$ surface with other semiconductor

### 1.4.4 *p-n* Heterojunction

A *p-n* heterojunction is formed when two different semiconductor materials with different bandgaps (one wide-bandgap and one narrow-bandgap) are in contact. One side is usually doped p-type (with an excess of holes), and the other is *n*-type (with an excess of electrons).

The *p*-*n* heterojunction alignments are categorized in three types: type I (straddling gap), type II (staggered gap), and type III (broken gap), see **Figure 1-12**. In type I, the VB and CB of the semiconductor A (*p*-type) overlap those of semiconductor B (*n*-type), causing photo-generated electrons and holes to accumulate in semiconductor B, which avoids effective separation. In type III, both the VB and CB of semiconductor A are higher than those of semiconductor B, impeding electron transfer. Type II heterojunctions have the VB and CB of semiconductor A higher than those of semiconductor B, allowing for effective separation where holes move to semiconductor A and electrons move to semiconductor B. This separation enhances the photocatalytic effect. Compared to type I and type III heterojunctions, type II is more effective in promoting the separation of photogenerated electrons and holes.

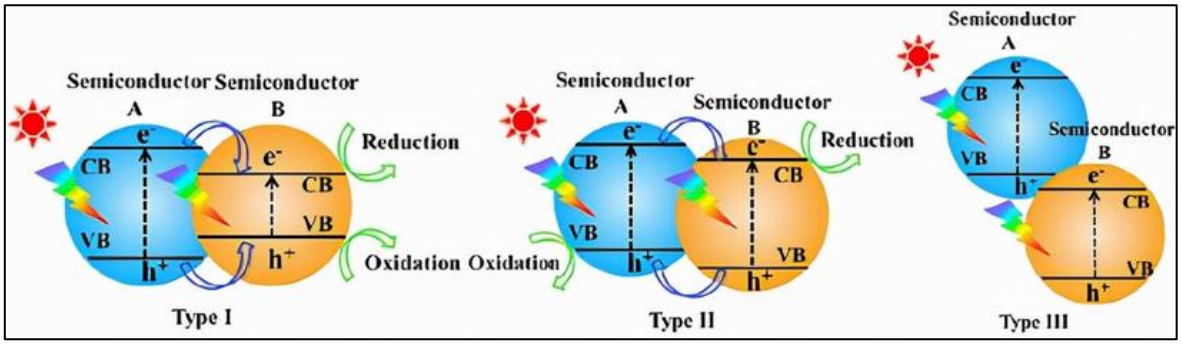


**Figure 1-12.** Different types of heterojunctions Type I (straddling gap), Type II (staggered gap) and Type III (broken gap).[75]

Another way to enhance the photocatalytic activity of $TiO_2$ is by modifying its surface with a *p*-type semiconductor such as NiO, which has a band gap of about 3.5 eV.[76,77,78,79] The combination of *p*-type NiO and *n*-type $TiO_2$ forms a *p*-*n* heterojunction type II. Where electrons from the CB of the NiO flow to the CB of the $TiO_2$, and holes in the VB of $TiO_2$ migrate to the VB of NiO, leading to the formation of a space-charge region at the interface, where there are no free charge carriers, creating an electric field at the interface (**Figure 1-13**). The electric field forms a potential barrier reducing the recombination of charge carriers and facilitates

interfacial charge transfer enhancing the photocatalytic activity of $TiO_2$ under UV-vis light irradiation.[9,76,80,81,82]

Nickel (Ni)-based cocatalysts are ideal candidates in photocatalysis due to their low cost and effectiveness.[83,84] Ni-based nanoparticles such as metallic nickel ($Ni^0$), nickel oxide (NiO)[15,85,86,87] and nickel hydroxide $Ni(OH)_2$ nanoparticles,[88,89] are highly active cocatalysts when integrated with $TiO_2$ semiconductor for photocatalytic $H_2$ production.[90] It has been observed that $Ni^0$-NPs can be present at the interphase between deposited NiO-NPs and $TiO_2$ support and lead to the formation of an Ohmic junction with titania, facilitating the migration of photogenerated electrons to the metal.[8,9] In an Ohmic junction (**Figure 1-14**), there is no significant barrier to the flow of charge carriers, so the current-voltage (I-V) characteristic is linear, following Ohm's law (V=IR).[8,9]

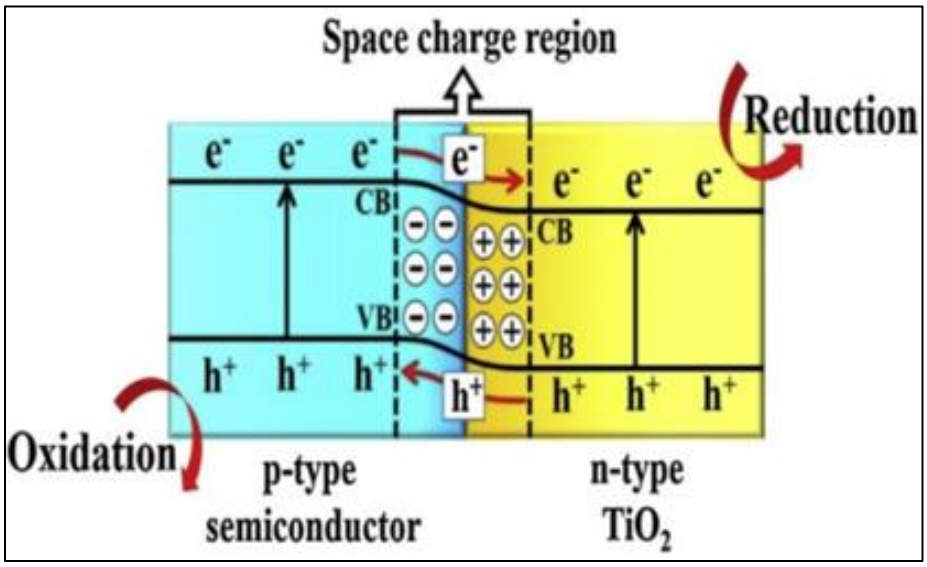


**Figure 1-13.** *p-n* heterojunction formed between two different semiconductors *p*-type and *n*-type.[91]

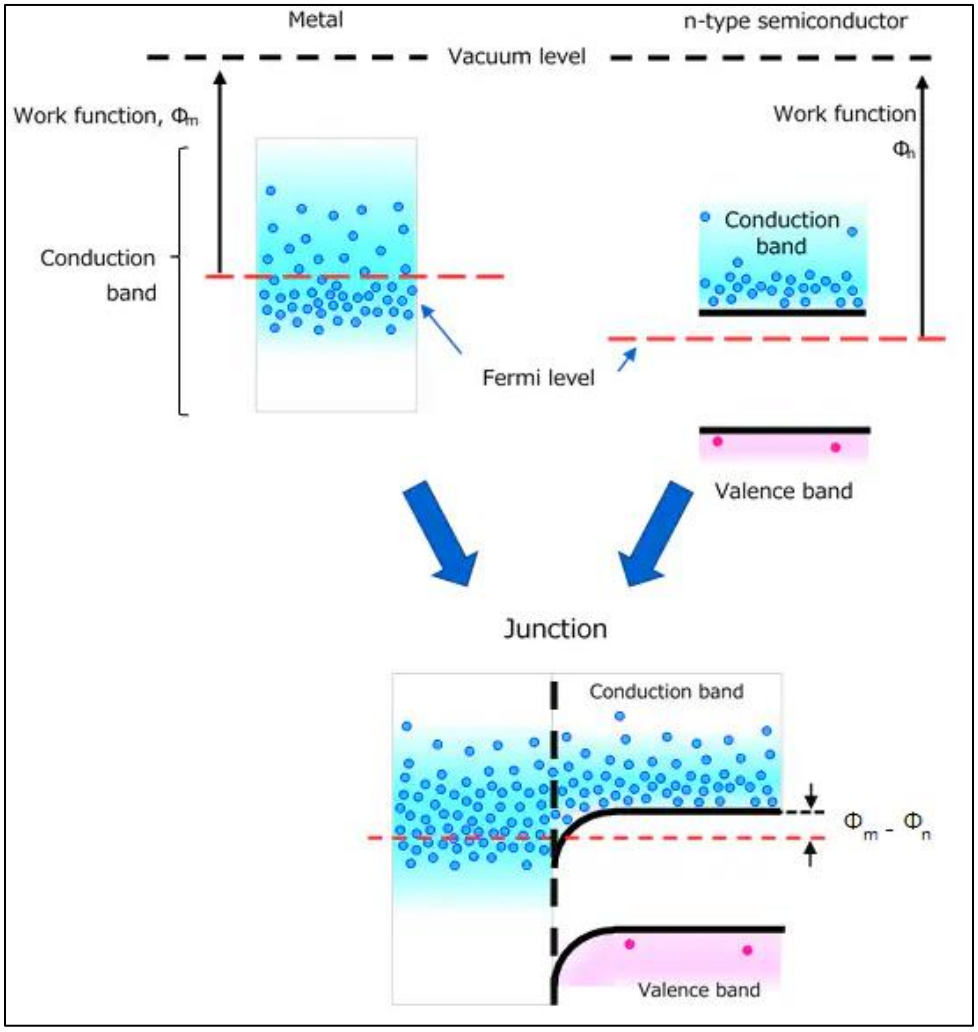


**Figure 1-14.** Ohmic junction formed between metal and *n*-type semiconductor.
*Data source: Toshiba (2024)*.

## 1.5 Plasmonic nanoparticles

Plasmonic nanoparticles are nanoscale particles that exhibit unique optical properties due to their interaction with light. The interaction of noble metal nanoparticles with light is influenced by metal nature, their size, morphology and environment.[15,92,93] These properties arise from the localized surface plasmon resonance (LSPR).

### 1.5.1 Localized Surface Plasmon Resonance (LSPR)

LSPR is the collective oscillation of conduction-free electrons excited by the incident photons in constructive interference with the electric field of the incident light (**Figure 1-15**).[10,11,12,8,13] Plasma is a high-energy state of matter where electrons are detached from atomic nuclei, typically at temperatures similar to those in the sun. At these extreme temperatures, thermal energy overcomes electrostatic forces, causing electrical charges to behave differently from those in normal matter. This rapid movement of charges generates an electromagnetic field.

LSPR can be explained by a confinement of the electromagnetic wave associated with the light inside the NPs. Indeed, when its wavelength is greater than the size of the NPs, the whole NP feels a uniform and oscillating electric field, and consequently, electrons oscillate in phase.

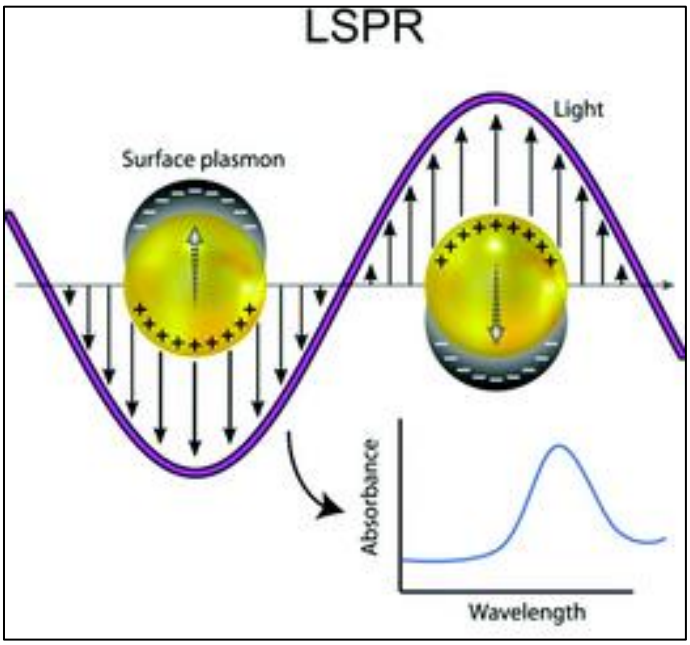


**Figure 1-15.** Illustration of the localized surface plasmon resonance on nanoparticles and their absorbance spectrum.[13]

Nevertheless, this collective oscillation of the electrons is constrained by the reduced dimensions of the nanoparticle in which they are confined. This results in

pronounced absorption (resonance) at wavelengths corresponding to the oscillation of the electrons in the metal. This maximum absorption (plasmon) is around 520 nm (green) for spherical Au NPs of about 10 nm in diameter in aqueous solution see **Figure 1-16**. This absorption leads to the appearance of complementary red colour. For Ag NPs of same size, the plasmon is around 420 nm, resulting in a yellow colour. Furthermore, as the size of Au and Ag nanospheres increases, a red shift in the LSPR is observed see **Figure 1-17**. This shift is due to lower frequencies of electron oscillation, causing electromagnetic delays in larger particles. The LSPR absorption can be tuned by the surrounding dielectric medium, which is influenced by both solvent and substrate effects.[94]

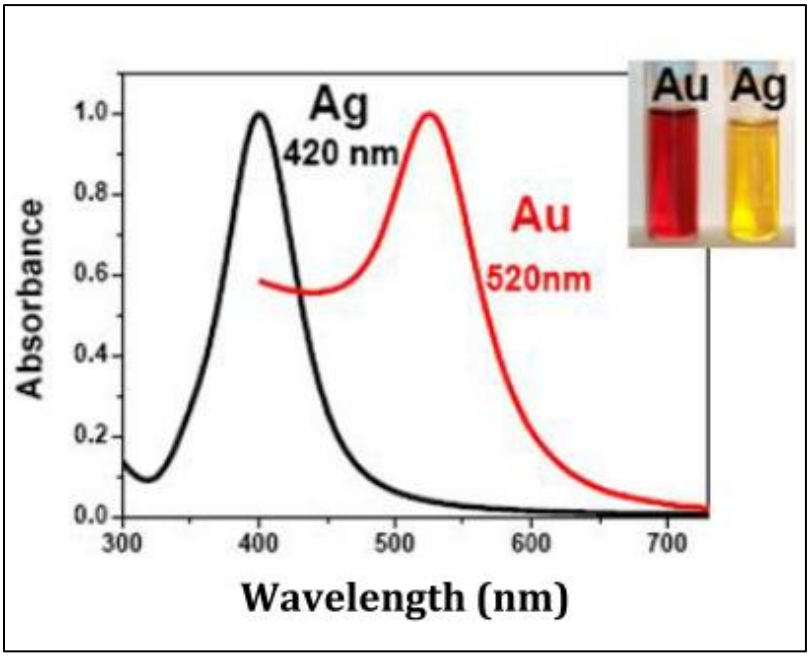


**Figure 1-16.** Plasmonic spectra of spherical Au and Ag spherical nanoparticles in aqueous solutions and their respective vials.[94]

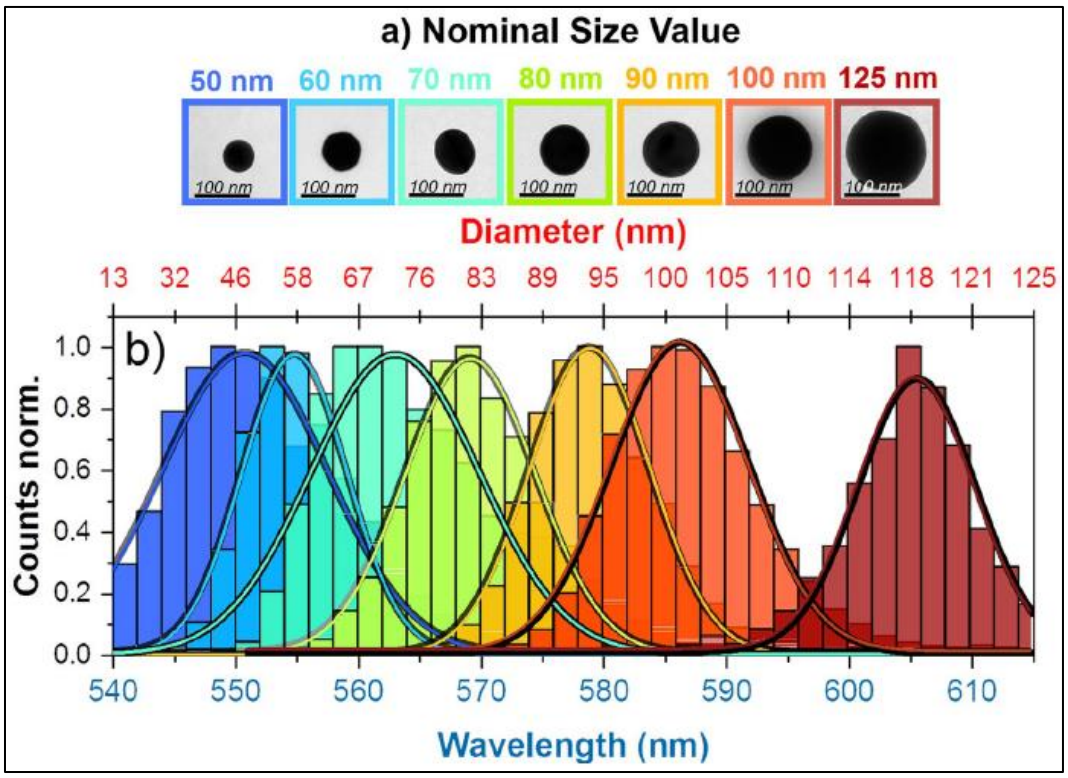


**Figure 1-17. (a)** TEM images of Au nanospheres with different size and their **(b)** histogram distributions of plasmon resonance peaks for the characterized Au nanospheres.[95]

The shape can tune the plasmonic properties. Au nanorods have attracted much attention because of their plasmonic properties (which can be tuned by changing the aspect ratio) and their potential applications in different fields, including sensors, nanomedicine, and photocatalysis.[26,96,97] They exhibit two surface plasmon resonance absorption bands, as shown in **Figure 1-18**. These bands correspond to the oscillation of quasi-free electrons: one band is associated with oscillation along the length of the rod (longitudinal), while the other is perpendicular (transverse). The optical properties of Au nanorods can be tuned by adjusting their aspect ratio. As the rod's length increases, the LSPR frequency decreases.

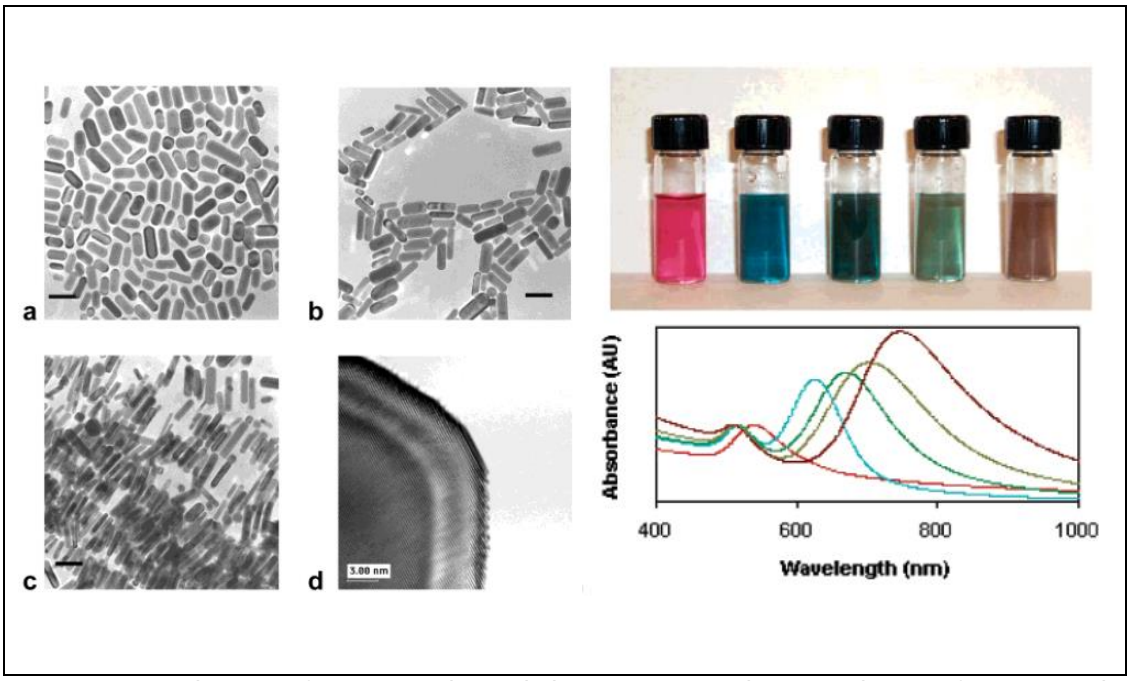


**Figure 1-18.** TEM images of Au nanorods, scale bar = 50 nm, and HRTEM image of Au nanorod. Au nanorods solution, and their corresponding absorption spectrum.[98]

The tunability of plasmonic nanoparticles makes them suitable for a variety of applications, including sensors, nanomedicine and photocatalysis.[25,26,27,28,29,30,31] Surface plasmons play a crucial role in initiating chemical transformations by generating energetic electrons (hot electrons) upon plasmon decay.[99,100,101] The role of "hot" electrons is still a debate in the literature.

For example, in photocatalysis, Au NPs can also activate $TiO_2$ under visible light due to its LSPR.[6] TRMC signals revealed that under visible light, electrons were injected from Au-NPs into the CB of $TiO_2$, attributed to the activation of the LSPR of the Au-NPs see **Figure 1-19**. The action spectra correlated with the absorption spectra, supporting the idea that model pollutants are decomposed by a photocatalytic mechanism.

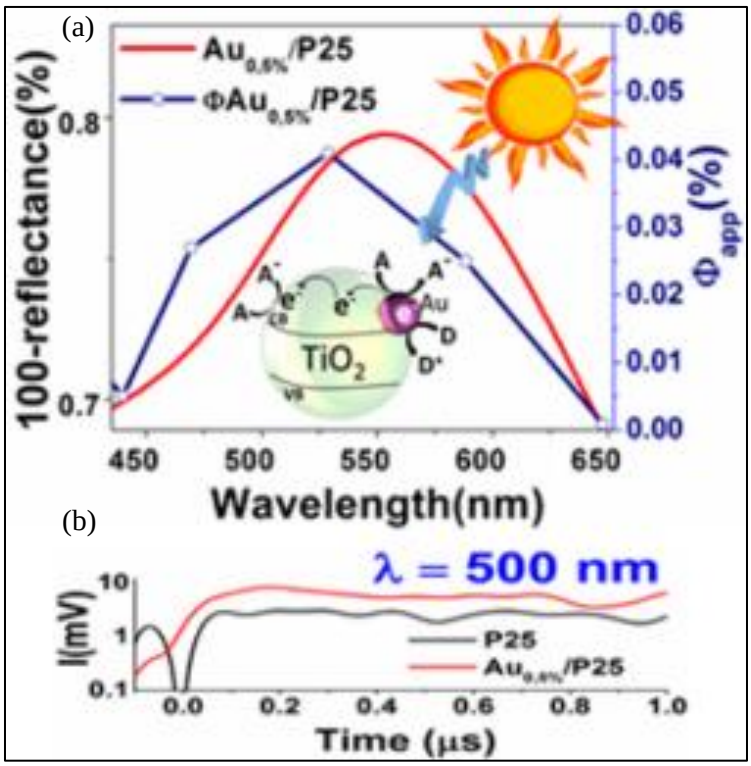


**Figure 1-19. (a)** Comparison between DRS spectra and action spectra of $TiO_2$-P25 and modified $TiO_2$-P25 with 0.5 wt % Au, and their corresponding **(b)** TRMC signals at excitation wavelength of 500 nm (plasmon excitation).[6]

In plasmonic catalysis, *ICP* team demonstrated that spherical Au-NPs facilitated the reduction of 4-NTP to 4-ATP under visible light irradiation.[94] They confirm the formation of 4-ATP on the surface of Au-NPs by UV-visible spectroscopy and Surface-Enhanced Raman Spectroscopy (SERS) but not in the solution. This suggests that the reduction of 4-NTP occurs on the AuNP surface, involving "hot" electrons from plasmon excitation. Additionally, 4-ATP appears to remain tightly bound to the AuNPs. They also found that no degradation was observed for 4-nitrophenol (4-NP) in the presence of the spherical Au-NPs under visible irradiation.[94] This means that the adsorption of the molecules on the NPs is a very important factor for efficient catalysis.

Pd nanostructures are also applied in catalysis for C–C coupling reactions.[102,103]

*ICP* team demonstrates that Pd nanoflowers absorbing in the visible range exhibit high activity in the Suzuki reaction under UV-visible light. The results show much faster kinetics under visible light compared to dark conditions.[102]

Plasmonic nanoparticles are extensively used in sensors due to their sensitivity to changes in the local refractive index, enabling the detection of molecules at low concentrations.[31] For instance, *Pluchery et al.* functionalize spherical AuNPs with thiol molecules.[104] They observed a red shift in the LSPR peak using UV-vis spectroscopy, which was attributed to the adsorption of these molecules on the AuNPs surface.

Ag NPs are also gaining attention as sensitive materials for plasmonic biosensors. *Loiseau et al* mentioned that the combination of Au and Ag NPs enhances plasmonic responses and offers protective properties.[25] In the case of Ag, the number of existing biosensing applications remains still limited compared to AuNPs.

In photothermal therapy, plasmonic nanoparticles convert absorbed light into heat, allowing for the selective destruction of tumor cells with minimal damage to surrounding tissues when localized and irradiated with a laser.[26] *Carreón-Álvarez et al.* demonstrated that AuNSs having maximum absorbance in the infrared region can facilitate photothermal tumor ablation using a laser at 808 nm.[27]

Also, Pd nanostructures possess unique catalytic and optical properties, but their biomedical applications have been limited. Recently, they have shown promise as prodrug activators, photothermal agents, and for anti-cancer and anti-microbial therapies.[105] Pd nanoparticles can catalyze the Suzuki–Miyaura cross-coupling reaction on human thyroglobulin in patient tissue homogenates. This is the first instance of chemoselective native protein modification using transition metal nanoparticles in a near-organ medium.[106] Pd porous nanostructures exhibit excellent cycling sorption properties for hydrogen storage and sensing.[107] These nanomaterials maintain their morphology through various treatments and have potential applications in catalysis, electrocatalysis, sensors, and SERS. Pd

nanostructures are also applied in catalysis and electrocatalysis for alcohol oxidation and hydrogenation reactions.[69,108,109,110,111,112,113]

Despite the potential of plasmonic nanoparticles, challenges such as stability, reproducibility in synthesis, and toxicity must be addressed.

The main objective of this PhD research work was to develop transition metal-modified photocatalysts and plasmonic catalysts for hydrogen generation ($AuPd/TiO_2$, $NiO/TiO_2$, and $NiFe/TiO_2$) and water treatment applications (Au nanostars) by chemical and radiolysis methods. The photocatalysts were characterized using different techniques to understand the physical and chemical mechanisms that contribute to the enhancement of the photocatalytic activity.

# Chapter 2

Experimental Part

# Chapter 2. Experimental part

In this chapter, we will describe the synthesis methods and the procedures used for the preparation of the photocatalysts including: surface modified $TiO_2$ ($AuPd/TiO_2$, $NiFe/TiO_2$, $NiO/TiO_2$) and Au nanostars. Furthermore, we will summarize the characterization techniques and experimental procedures.

## 2.1 Chemical reagents

The chemical reagents employed in the experiments are detailed in the **Table 2-1**. These reagents were analytically pure, commercially available, and utilized without additional purification.

**Table 2-1** Chemical reagents used for the experiments.

| Chemical reagent | Formula | Purity | Company |
|---|---|---|---|
| Commercial Titanium dioxide (Anatase 80%, Rutile 20%) | $TiO_2$-P25 | - | Evonik |
| Gold (III) chloride trihydrate | $HAuCl_4 \cdot 3H_2O$, | 99.9% | Sigma–Aldrich |
| Palladium (II) chloride | $PdCl_2$ | 99% | Sigma–Aldrich |
| Platinum (II) acetylacetonate | $Pt(C_5H_7O_2)_2$ | 97% | Sigma–Aldrich |
| Sodium borohydride | $NaBH_4$ | ≥ 99% | Sigma–Aldrich |
| Triethanolamine | $C_6H_{15}NO_3$ | ≥ 99% | Sigma–Aldrich |
| Nickel (II) acetylacetonate | $Ni(C_5H_7O_2)_2$ | ≥ 99% | Sigma-Aldrich |
| Nickel (II) formate dihydrate | $Ni(HCO_2)_2 \cdot 2H_2O$ | - | Alfa Aesar |
| Iron (III) acetylacetonate | $Fe(C_5H_7O_2)_3$ | ≥ 99% | Sigma-Aldrich |
| Silver nitrate | $AgNO_3$ | 99.9 % | Sigma-Aldrich |
| Sodium citrate tribasic dihydrate | $C_6H_5Na_3O_7 \cdot 2H_2O$ | ≥ 99.0% | Sigma Aldrich |
| Ascorbic acid | $C_6H_8O_6$ | 99.9 % | Sigma Aldrich |
| Hydrochloric acid | HCl | 37% | VMR Chemicals |
| Sodium hydroxide | NaOH | | Sigma Aldrich |
| 4-Nitrothiophenol | $C_6H_5NO_2S$ | 80% | Sigma Aldrich |
| (3-Aminopropyl)triethoxysilane | $H_2N(CH_2)_3Si(OC_2H_5)$ | 99% | Sigma Aldrich |
| Ethanol | $C_2H_5OH$ | 99.94% | VMR Chemicals |
| Methanol | $CH_3OH$ | ≥ 99.9% | Sigma Aldrich |
| 2-Propanol | $(CH_3)_2CHOH$ | | Sigma Aldrich |
| Acetone | $CH_3(CO)CH_3$ | | |
| Nitrous oxide | $N_2O$ | 99.99% | Air Liquide |
| Nitrogen | $N_2$ | 99.99% | Air Liquide |
| Argon | Ar | 99.99% | Air Liquide |
| Ultra-pure water | $H_2O$ | - | Millipore System, 18.2 MΩ |

## 2.2 Synthesis methods

### 2.2.1 Radiolytic reduction

Radiolysis is the interaction of high energy radiation (gamma-rays, X-rays, electron beams, ion beams) with matter. Radiolysis is a powerful method to synthesize metal nanoparticles in solutions, in complex media or on supports using simple physicochemical conditions such as atmospheric pressure, room temperature, and the absence of additional chemical-reducing agents.[114] The interaction of high energy radiation such as γ-rays with polar solvents such as water induces solvent excitation and ionization,[115,116] leading to the formation of various species (Eq.1). In case of water, solvated electrons ($e_s^-$), hydrogen ($H^\bullet$) and hydroxyl ($^\bullet$OH) radicals are induced. At pH 7 the radiolytic yields of the radicals are $G(e_s^-) = 2.7$, $G(H^\bullet) = 0.55$, and $G(^\bullet OH) = 2.8$.[117] Solvated electrons and $H^\bullet$ radicals are strong reducing agents ($E^0(H_2O/e_s^-) = -2.87\ V_{NHE}$, $E^0(H^+/H^\bullet) = -1.88\ V_{NHE}$), which can reduce metal ions or complexes ($M^{n+}$) to their zero valence state ($M^0$).[107] However, $^\bullet$OH radicals present strong oxidizing properties $E^0(^\bullet OH/H_2O) = 2.34\ V_{NHE}$, and thus can cause reverse oxidation of metal atoms and small clusters.[107] To avoid oxidation by $^\bullet$OH radicals and enhance the reduction yield, alcohols like 2-propanol are added to scavenge $^\bullet$OH radicals. The alcohol reacts with $^\bullet$OH, and $H^\bullet$ to form the alcohol radical according to the following reactions (Eq. 2 and 3). Alcohol radicals are almost as powerful reducing agents as $H^\bullet$ atoms $(E^0(CH_3COCH_3)/(CH_3C^\bullet OHCH_3) = -1.8\ V_{NHE}$ at pH 7.[107]

$$H_2O \rightsquigarrow e_s^-,\ H_3O^+, H^\bullet, {}^\bullet OH, H_2, H_2O_2 \quad (1)$$

$$CH_3CHOHCH_3 + OH^\bullet \rightarrow CH_3C^\bullet OHCH_3 + H_2O \quad (2)$$

$$CH_3CHOHCH_3 + H^\bullet \rightarrow CH_3C^\bullet OHCH_3 + H_2 \quad (3)$$

In the case of ethanol solutions, solvated electrons ($e_s^-$) and alcohol radicals ($CH_3C^{\bullet}HOH$) (generated by ethanol irradiation) are strong reducing species, Eq. 4.

$$C_2H_5OH \rightsquigarrow e_s^- + CH_3C^{\bullet}HOH + C_2H_5OH_2^+ \quad (4)$$

Their redox potential determined in water is $E^0(H_2O/e_s^-) = -2.87\ V_{NHE}$ and $E^0(CH_3CHO/(H^+/CH_3C^{\bullet}HOH)) = -1.25\ V_{NHE}$, respectively.[114,118]

This method enables the reduction of metal complexes, which are difficult to reduce by chemical methods at room temperature (such as Ni, Co, Fe or Al).[115,118] The random distribution of reducing agents generated by radiation in the sample, metal atoms form with a uniform distribution throughout the solution. Additionally, the bond strength between two metal atoms is greater than the bond strength between an atom and the solvent or ligand, forming metal clusters through coalescence processes. Nanoparticles of controlled size and shape are obtained.[114,118]

### 2.2.2 Dose rate effect

The dose rate (dose per time) is an important factor in radiolytic synthesis, influencing the reduction rate, nucleation and growth of metal NPs. The amount of radiation (dose) required to reduce metal ions to their zero-valent state depends on the metal precursor, the oxidation degree of the metal and its concentration. Radiation dose is typically measured in Gray, from the International System units (1 Gy = 1 J/kg). **Figure 2-1a** illustrates the nucleation and growth of NPs at high and low dose rate conditions.

At high dose rate, the reduction is very fast, resulting in a higher concentration of seed particles and facilitating nanoparticle formation as separate events. Therefore, nanoparticles of small size are obtained. A low dose rate is advantageous for NPs growth because ion-atom association and reduction on the seeds occur faster than

the production rate of reducing radicals; therefore, larger nanoparticles are in general obtained.

Synthesis of bimetallic nanoparticles is achieved by irradiation of a solution containing ions or complexes of two different metals. The dose rate, which fixes the reduction kinetics, is a very important factor that can determine the structure of the bimetallic NPs as alloys or core-shells. There is a competition between the reduction of the metal ions and the electron transfer from metal ions or atoms of metal M1 to the other ions of metal M2. The synthesis of bimetallic core-shell is in general achieved at low dose rates, where electrons are transferred from the atoms (or partly reduced ions) to the less noble metal ions. This will lead to the formation of core-shell nanoparticles with the more noble metal in the core. At high dose rates, the reduction of metal ions is faster than intermetallic electron transfer, leading to nanoalloys formation where the two metals are quite homogeneously distributed in the NP **Figure 2-1b**.

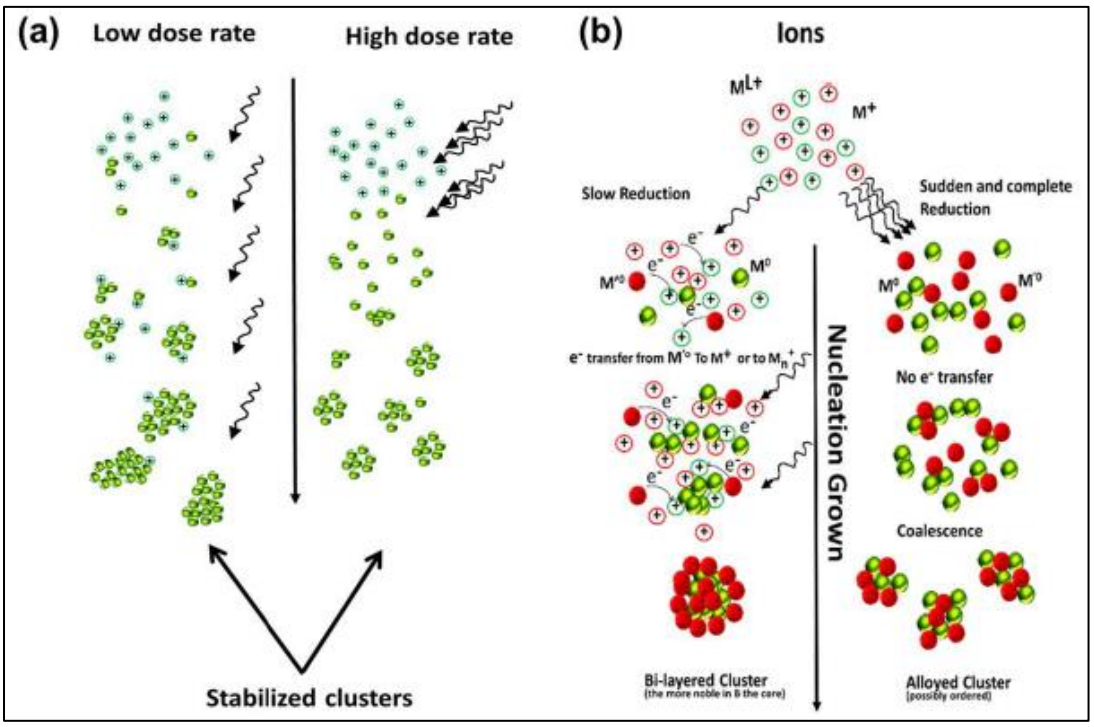


**Figure 2-1. (a)** Illustration depicting nanoparticle nucleation and growth at low and high dose rates, and **(b)** the impact of the dose rate on the competition between intermetallic electron transfer and coalescence processes in the radiolytic reduction of mixed metal ion solutions.[119]

The γ-ray source (**Figure 2-2**) available at the *Institut de Chimie Physique (ICP), Université Paris-Saclay*, is a panoramic cobalt ($^{60}$Co) source with a maximum dose rate of 4 kGy/h (at the beginning of my PhD). This source consists of cylindrical bars stored within a lead container. The source is operated remotely from a control room. During operation, the cobalt bars are elevated vertically from a deep well in the column. Samples are put on the platform, and the distance between the sample and the column determines the dose rate. Once the irradiation is finished, the cobalt bars are returned to the deep, which is filled with deionized water. The radiation chamber has thick walls and features a protective sliding lead door. It can irradiate samples ranging from a few microliters to several liters in volume.

**Figure 2-2.** Gamma source available at the Institut de Chimie Physique, Université Paris Saclay.

### 2.2.3 Chemical reduction

Chemical reduction methods are often used to synthesize metal NPs and can lead to NPs with precise size and shape control. These methods involve reducing metal ions from their salts (or complexes) in solution to form NPs, typically using reducing agents (such as sodium borohydride, ascorbic acid, sodium citrate, etc) and stabilizing agents (ligands, surfactants, polymers, supports). The choice of the

method and conditions significantly influence NP size, shape, and stability, which is crucial for tailoring their optical, electronic, and catalytic properties. In this PhD thesis, Au-based NPs were synthesized using chemical reduction, the most common synthesis method. Review papers focused on the synthesis of AuNPs using chemical reduction methods with $NaBH_4$, ascorbic acid, Turkevich method, seed growth, and others.[120]

The characteristics of AuNPs, such as their formation, size, shape, and function, are significantly influenced by various physical and chemical factors during synthesis. Parameters like reaction temperature, stirring rate, and the ratio of Au to reducing agent play crucial roles in determining the properties of AuNPs.

AuPd nanoalloys were synthesized on $TiO_2$ surface using $NaBH_4$ at room temperature. The synthesis method will be explained in more detail below. $NaBH_4$ is a strong reducing agent, which effectively reduces metal ions from their salts in solution, allowing precise control over nanoparticle size, shape, and composition.

Au nanostars (NSs) were synthesized using a seed-growth method. The synthesis method will be explained in more detail below. In the seed-growth method, Au nanoseeds are first formed by Türkevich (or y-radiolysis) and then induced to grow into Au nanostars. The Turkevich method utilizes sodium citrate as a reducing and stabilizing agent to synthesize AuNPs. Also, in this study, Au seeds were also synthesized by γ-radiolysis. As mentioned, this technique is a powerful method to synthesize metal NPs in solutions on supports using simple physicochemical conditions.

## 2.3 Synthesis of the photocatalysts

### 2.3.1 AuPd/$TiO_2$

The photocatalysts were synthesized by chemical reduction using $NaBH_4$ as reducing agent at room temperature (**Figure 2-3**). Mother solutions of 0.01 M $HAuCl_4$ (30 mL) and 0.01 M $PdCl_2$ (30 mL) were prepared. In a flask, 10 mL of deionized water was added to 250 mg of $TiO_2$ under vigorous stirring for 30 min. Afterwards, an amount of each salt precursor solution was added to the dispersed $TiO_2$ aqueous suspension to prepare photocatalysts with different metal loadings, keeping the vigorous stirring for 1 h. Immediately, a fresh aqueous solution of 2 mL $NaBH_4$ 1 M was prepared in an ice-water bath because $NaBH_4$ reacts violently and quickly with water at room temperature. Freezing water slows the reaction sufficiently enough to allow the reduction of metal ions. Subsequently, 0.5 mL of $NaBH_4$ 1 M were added to the mixture, maintaining vigorous stirring for 2 h. Afterwards, the photocatalysts were washed with deionized water and separated by centrifugation three times at 6500 rpm for 10 min to remove the non-reduced, undesired ions and then dried at 60 °C for 48 h. The supernatants were transparent, indicating that most of the metals were deposited on the titania support. The UV–vis spectra of the supernatants were flat (Figure S3-7, Annex I) compared with the solutions of the salt precursors of $HAuCl_4$ and $PdCl_2$. The $Au^{III}$ and $Pd^{II}$ complexes were reduced by $NaBH_4$ in aqueous solutions at room temperature (Eq. 5 And Eq. 6). The redox potentials are $E_{Au^{3+}/Au^0}$=1.5 V versus the normal hydrogen electrode (NHE), $E_{Pd^{2+}/Pd^0}$=0.83 V versus NHE,[121] and $E^0$=−1.24 V versus NHE.[122,123] The concentration of $NaBH_4$ is a crucial factor in the synthesis; higher concentration induces the reduction of the NPs size.[124]

$$4\mathbf{Au^{III}} + BH_4^- + 8OH^- \rightarrow 4\mathbf{Au^0} + B(OH)_4^- + 4H_2O \quad (5)$$

$$4\mathbf{Pd^{II}} + BH_4^- + 8OH^- \rightarrow 4\mathbf{Pd^0} + B(OH)_4^- + 4H_2O\ (\mathrm{Eq.}\ 3) \quad (6)$$

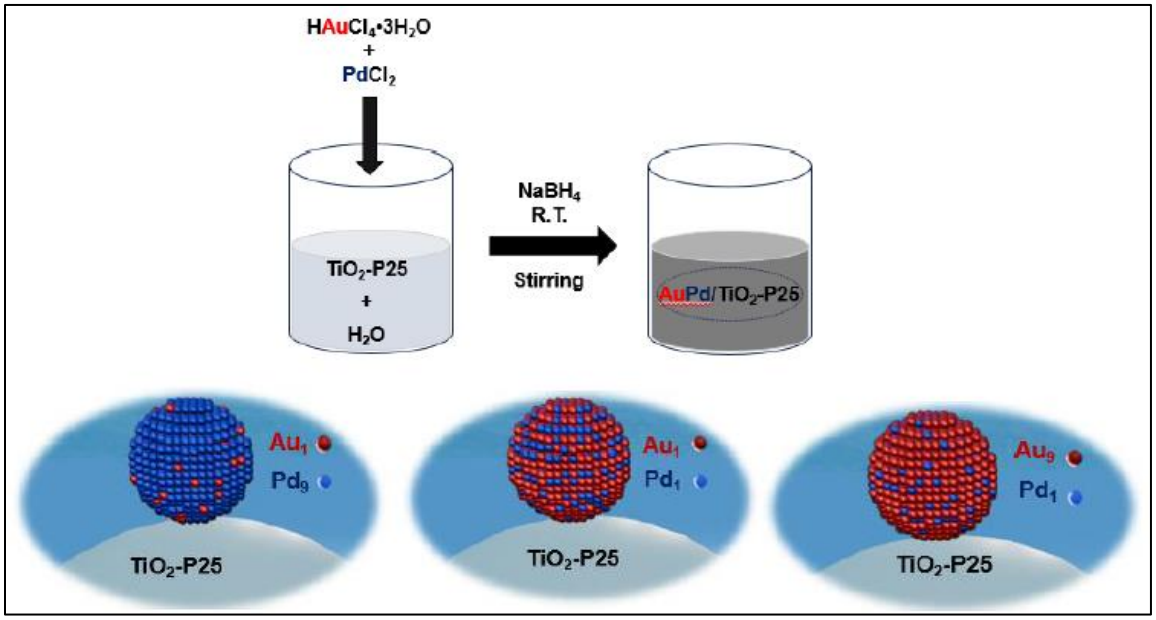


**Figure 2-3.** Photocatalysts synthesis by chemical reduction using $NaBH_4$ as reducing agent at room temperature.[7]

Mono- and bi-metallic ($Au/TiO_2$, $Pd/TiO_2$, and $AuPd/TiO_2$) samples were prepared with 1 wt% metal loading for comparison (**Table 2-2**). The monometallic photocatalysts containing Au and Pd were, respectively, purple and gray, and the color is more intense with the metal loading (**Figure 2-4**). The bimetallic photocatalysts 1 wt% $Au_1Pd_9/TiO_2$ and 1 wt% $Au_1Pd_1/TiO_2$ were gray in color. For 1 wt% $Au_9Pd_1/TiO_2$, the color was gray-purple. Later, the bimetallic photocatalysts with total metal loading of 0.1, 0.2, and 0.5 wt% $AuPd/TiO_2$ were synthesized using the same mass ratios to study the effect of the loading on the photocatalytic activity.

**Table 2-2.** Metal loadings of mono-and bi-metallic photocatalysts.

| **Monometallic photocatalysts** | **Bimetallic photocatalysts** |
|---|---|
| 0.1, 0.5, 0.9 wt% $Au/TiO_2$<br>0.05, 0.1, 0.5, 0.9 wt% $Pd/TiO_2$ | 1 wt% $Au_1Pd_9/TiO_2$<br>1 wt% $Au_1Pd_1/TiO_2$<br>1 wt% $Au_9Pd_1/TiO_2$ |

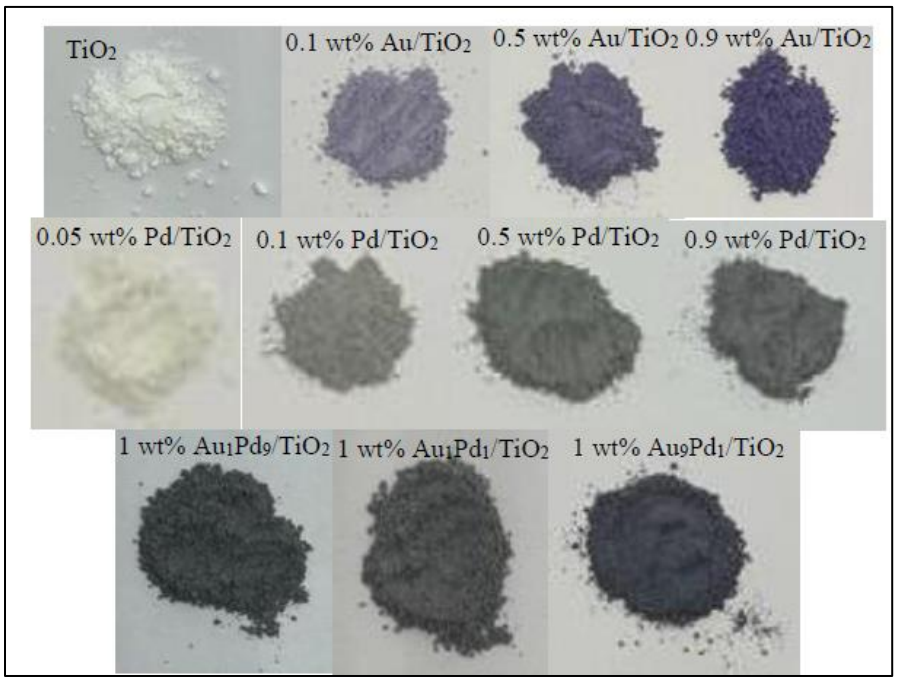


**Figure 2-4.** Mono-and bi-metallic photocatalysts powders and bare $TiO_2$.

Finally, $Pt/TiO_2$ was synthesized (Pt is known as the best cocatalyst for hydrogen generation) to compare the activity of our bimetallic samples $AuPd/TiO_2$ with that of $Pt/TiO_2$. The 1 wt% $Pt/TiO_2$ sample was prepared by the radiolysis method. This method is very powerful to synthesize metal NPs of controlled size and shape in solution and on support.[115,118] Platinum (II) acetylacetonate was used as salt precursor and ethanol as solvent. The solution was stirred 1 h, sonicated for 5 min, degassed with Ar gas (Air Liquide), and then irradiated using a $^{60}Co$ panoramic gamma source. The dose used was 3.2 kGy, which is sufficient for complete reduction of $Pt^{II}$ complexes (at a concentration of $10^{-3}$ M) to their zerovalent state $Pt^0$. After the radiolysis process, the photocatalyst was separated by centrifugation and dried at 60 °C for 24 h to remove any remaining traces of the solvent.

### 2.3.2 NiO/$TiO_2$

The photocatalysts were prepared by the radiolysis method (**Figure 2-5**), using two different metal precursors: nickel (II) acetylacetonate and nickel (II) formate. Titania was surface-modified with different amounts of nickel: the experimental design of metal loadings were 0.1, 0.5, 1.0, 3.5 and 5.0 wt.% Ni/$TiO_2$. The required amounts of the metal precursors were dissolved in ethanol to prepare each photocatalyst. The solutions were first sonicated for 10 minutes, stirred for 30 minutes and degassed with $N_2$ gas. The solutions were then irradiated using a $^{60}Co$ panoramic gamma source. The doses used were sufficient for complete reduction of $Ni^{II}$ complexes to their zerovalent state $Ni^0$ (**Table 2-3**). The solvated electrons ($e_s^-$) and alcohol radicals ($CH_3C^{\bullet}HOH$) reduce the $Ni^{II}$ complexes to their zerovalent state $Ni^0$. After the radiolysis process, the photocatalysts were separated by centrifugation and washed with ethanol three times at 6500 rpm for 10 minutes. Finally, the photocatalysts were dried at 60°C for 24 h to remove any remaining traces of solvent.

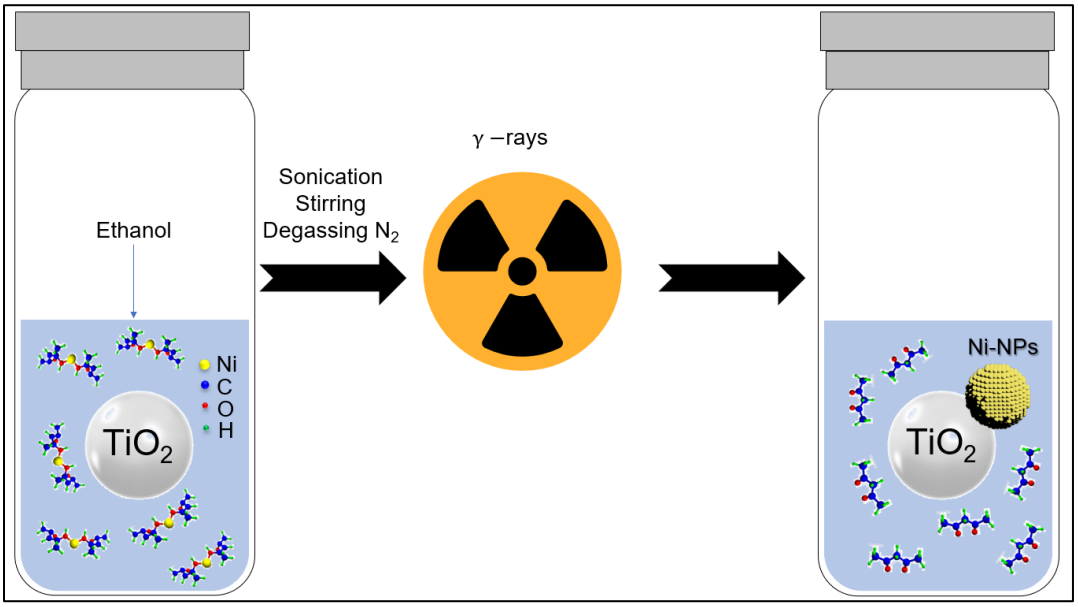


**Figure 2-5.** Synthesis of the photocatalysts Ni-based NPs/$TiO_2$ by radiolysis method.

**Table 2-3.** Doses for the modified samples.

| Sample | Concentration (M) | Dose (kGy) |
|---|---|---|
| 0.1 wt.% Ni/$TiO_2$ | $5.5\times 10^{-5}$ | 0.4 |
| 0.5 wt.% Ni/$TiO_2$ | $2.7\times 10^{-4}$ | 1.8 |
| 1.0 wt.% Ni/$TiO_2$ | $4.5\times 10^{-4}$ | 2.9 |
| 3.5 wt.%. Ni/$TiO_2$ | $1.8\times 10^{-3}$ | 11.6 |
| 5.0 wt.%. Ni/$TiO_2$ | $2.2\times 10^{-3}$ | 14.08 |

### 2.3.3 NiFe/$TiO_2$

The synthesis of the mono- and bi-metallic samples is shown below (**Figure 2-6**). The photocatalysts were prepared with nickel (II) acetylacetonate and iron (III) acetylacetonate salt precursors varying the total metal loading 1 wt%, 2 wt%, 3 wt%, and 5 wt% NiFe/$TiO_2$. The needed amount of metal precursors were dissolved in ethanol for every photocatalyst. The solutions were stirred for 2 h and degassed with Ar for 20 min to eliminate oxygen. Then, the samples were irradiated with a $^{60}Co$ panoramic gamma source. The total dose rates for $10^{-3}$ M of metal concentration required to ensure the complete reduction were 6.4 kGy, 9.6 kGy, and 16 kGy for Ni/$TiO_2$, Fe/$TiO_2$, and NiFe/$TiO_2$, respectively. The solvated electrons ($e_s^-$) and alcohol radicals ($CH_3C^{\bullet}HOH$) reduce $Ni^{II}$ and $Fe^{III}$ to their zerovalent state $Ni^0$. Finally, the photocatalysts were separated by centrifugation three times at 6500 rpm for 10 min and washed thoroughly with ethanol. The supernatants containing only Ni were completely transparent after centrifugation. However, the samples containing Fe supernatants were not wholly transparent; an orange solution was obtained, indicating that $Fe^{3+}$ was not completely reduced. Finally, the samples were dried at 60°C for 24 h. Gray powders were obtained.

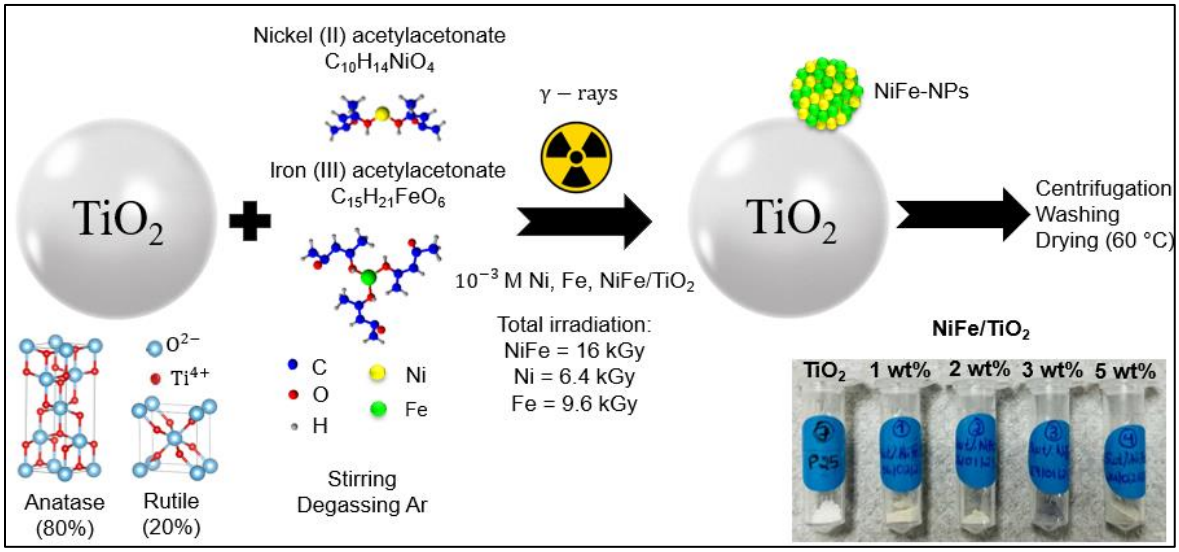


**Figure 2-6.** Synthesis of the photocatalysts by radiolysis method and inset image of $TiO_2$-P25 and the bimetallic samples powders.

### 2.3.4 Au nanostars

The Au nanostars (NSs) were synthesized in two steps by a seed growth-mediated method as illustrated in **Figure 2-7**. Au seeds serve as reduction and nucleation sites, allowing the Au nanostars to grow anisotropically.[125]

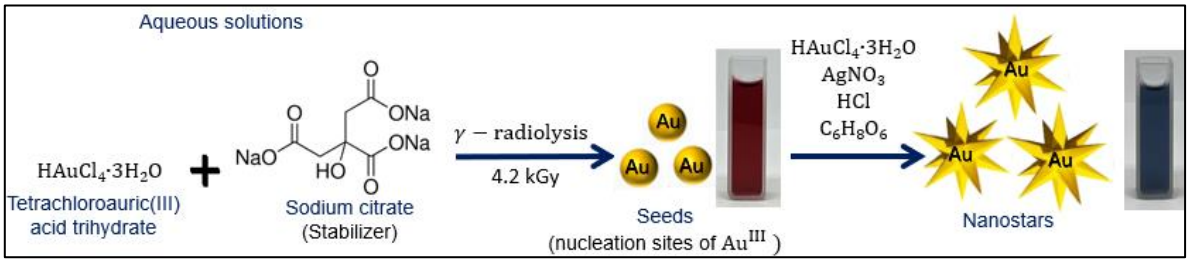


**Figure 2-7.** Au seeds are synthesized by radiolysis technique and Au nanostars are synthesized by seed growth method.

**Au seeds synthesis**. Initially, following Yuang's Protocol,[126] the Turkevich method was used to prepare the Au seeds (AuSs).[127] Au seeds were also synthesized by γ-radiolysis.

An stock aqueous solution of $HAuCl_4$ (30 mL) at 25 mM concentration was prepared and covered with aluminium foil. Subsequently, 100 mg of $C_6H_5Na_3O_7$ used as a stabilizer were dissolved to 10 mL of $H_2O$ in a 30 mL beaker. In another 30 mL beaker, 9.6 mL of $H_2O$ and 0.4 mL of 25 mM $HAuCl_4$ stock solution were stirred for 10 minutes and covered with aluminium foil before the addition of 1.5 mL at 1 % p/v $C_6H_5Na_3O_7$. Afterwards the mixture was sonicated for 10 min, and 76.6 µL of 2-propanol (0.1 M) was added. The solution was degassed with argon few minutes and then immediately irradiated using a $^{60}Co$ panoramic gamma source (dose rate 2 kGy/h) with a total dose of 4.2 kGy. The dose used completely reduced $Au^{III}$ complexes to their zerovalent state $Au^0$. After irradiation, the solution turns from light-yellow to wine-red color with a final concentration of $8.6\times10^{-4}$ M $Au^0$.

**Au nanostars anisotropic growth**. Ascorbic acid ($C_6H_8O_6$) is used to reduce the $Au^{III}$. Notice that $Ag^+$ and $Cl^-$ play an essential role in anisotropic growth and shape control.[128] In a 50 mL beaker, 39.6 mL $H_2O$ and 0.4 mL 25 mM $HAuCl_4$ stock solution were stirred and covered with aluminum foil. Then, various aqueous solutions were prepared in 20 mL beakers, each under stirring and at room temperature. These solutions included: (*i*) 9.17 mL $H_2O$ with 830 µL HCl added, (*ii*) 9.82 mL $H_2O$ with 180 mg $C_6H_8O_6$ added, (*iii*) 9.98 mL $H_2O$ with 20 mg $AgNO_3$ added, and (*iv*) 0.3 mL of the latter solution mixed with 0.7 mL $H_2O$.

To the previously prepared 40 mL solution containing 0.25 mM $HAuCl_4$, 40 µL of 1 M HCl, 400 µL of AuSs solution, 400 µL of 3 mM $AgNO_3$ solution and 200 µL of 0.1 M $C_6H_8O_6$ solution were added simultaneously under vigorous stirring for few seconds; immediately the colour of the mixture with a final concentration of $2.53\times10^{-4}$ M $Au^0$ turned to blue.

## 2.4 Characterization and AnalysisTechniques

The photocatalysts for hydrogen generation were characterized with different techniques such as TEM, HRTEM, HAADF-STEM, EDS, EELS, ICP-OES, DRS, X-

XRD, XPS, and TRMC. The Au nanostars were characterized by UV-visible spectroscopy, SEM, TEM, HRTEM, Hyperspectral dark-field optical microscopy and AFM.

The produced hydrogen was analyzed and quantified by Gas Chromatography (micro-GC). The UV-visible spectroscopy was used to follow the photocatalytic degradation of 4-nitrothiophenol.

The methodology and principle of these techniques will be briefly explained below.

### 2.4.1 Transmission Electron Microscopy (TEM)

TEM FEI TECNAI F30 microscope (**Figure 2-8**) available at *LINAN-IPICYT*. The microscope is equipped with a tungsten field emission gun operated at 300 keV was used to study the morphology, size, and dispersion of the metallic NPs. TEM microscope equipped with an EDS detector to identify the elemental composition of the samples. In the case of $NiO/TiO_2$ photocatalysts, EELS was used to determine the elemental nickel and their oxidation states.

HRTEM and HAADF-STEM were used to analyze the crystalline structure using a modern JEOL 200F (300 kV) model available at the *Advanced Laboratory of Electron Nanoscopy-CINVESTAV-IPN*.

The powder samples for hydrogen generation of $AuPd/TiO_2$ were dissolved in 2-propanol. For the samples of $NiO/TiO_2$ and $NiFe/TiO_2$ were dispersed in ethanol. The solution samples for water treatment (AuNSs and AuSs) were centrifuged and dispersed in water again. All the samples were put under sonication and then few drops of each were deposited on a copper grid.

TEM uses a beam of electrons (300 keV) to pass through a thin sample (thick $<$ 150 nm). Higher voltages result in shorter electron wavelengths and enhanced resolution. The electron gun at the column's top connects to a high-voltage source (300 keV) to set the electron beam's energy. Electromagnetic lenses and apertures

within the microscope column focus and magnify the beam onto the sample and viewing screen or detectors. A vacuum system maintains necessary levels throughout. Most components are computer-controlled, with users adjusting key settings like sample position, magnification, lens current, beam size, and choice of apertures and detectors for data collection. As electrons pass through the specimen, they interact with the atoms, resulting in scattering. The transmitted electrons are then collected to form an image that reveals details of the specimen's crystalline structure.

HRTEM allows atomic resolution micrographs (1.8 Å), provided the material has well-isolated and thin areas or edges (less than 50 nm thick) and is well-oriented in a wide zone axis. Micrographs obtained in this manner serve to confirm the crystalline structure of the sample.

HAADF-STEM is a scanning transmission electron microscopy (STEM) technique that utilizes a high-angle annular dark field detector. It detects electrons scattered at high angles by heavy elements in the specimen, producing contrast sensitive to atomic number variations. HAADF-STEM is ideal for imaging heavy elements in nanoparticles and providing atomic-scale details of their distribution and morphology. These observations were conducted by Dr. Daniel Bahena Uribe at the *Advanced Laboratory of Electron Nanoscopy, CINVESTAV-IPN*.

EDS or EDX is a technique coupled with electron microscopes, including TEM and STEM. When the electron beam interacts with the sample, characteristic X-rays are emitted, which are detected by a special EDS detector. EDS provides elemental composition analysis with spatial resolution down to a few nanometers. It maps elements in materials, identifies phases, and quantifies element concentrations.

EELS is a technique used in TEM and STEM to measure the energy loss of electrons passing through a specimen. It provides information about chemical bonding,

elements' oxidation states, and materials' electronic properties at the atomic scale. This technique identifies light elements that EDS cannot determine.

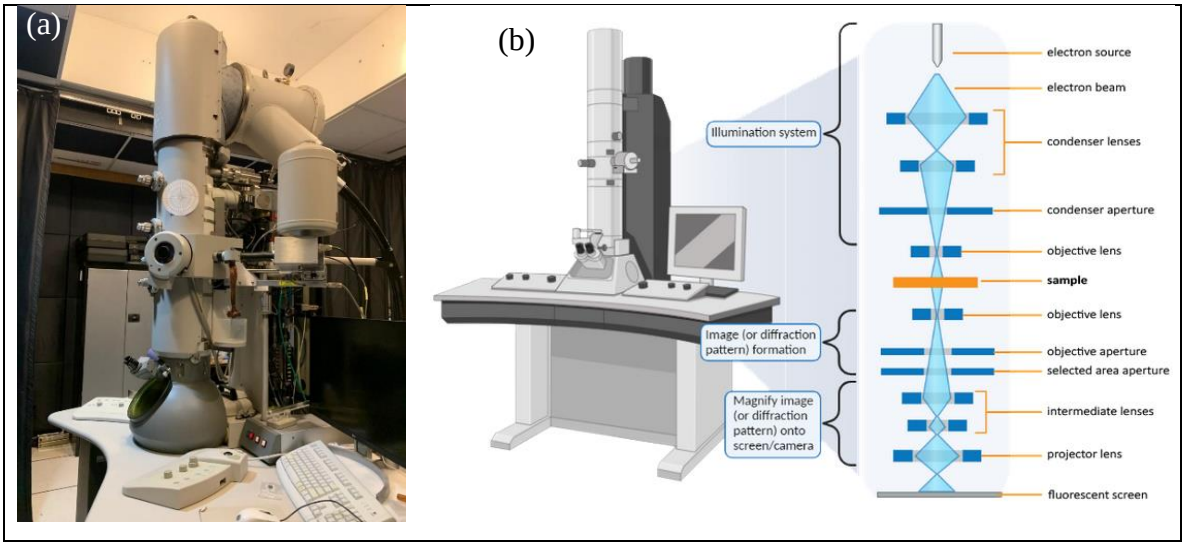


**Figure 2-8. (a)** TEM FEI TECNAI F30 microscope, and **(b)** their diagram.

*Data source figure 2-8b: Nanoscience Instruments (2024).*

### 2.4.2 Inductively Coupled Plasma-Optical Emission Spectrometry

ICP-OES spectrometer using a Varian 720-ES (**Figure 2-9a**) avalaible at *IPICYT*. ICP-OES was utilized for elemental analysis, providing insights into the mass content of the metals on the semiconductor surface ($TiO_2$).

ICP-OES utilizes atoms and ions absorbing energy to move electrons from their ground state to an excited state using high-temperature plasma generated from an inert gas. As these excited atoms return to the ground state, they emit light at specific wavelengths (**Figure 2-9b**). The fundamental principle of ICP-OES involves quantifying the emitted light intensity at each wavelength to determine the metal concentration in the sample. The Beer-Lambert law (Eq. 9) provides a quantitative description of the correlation between light intensity and the concentration of elements in ICP-OES analysis.

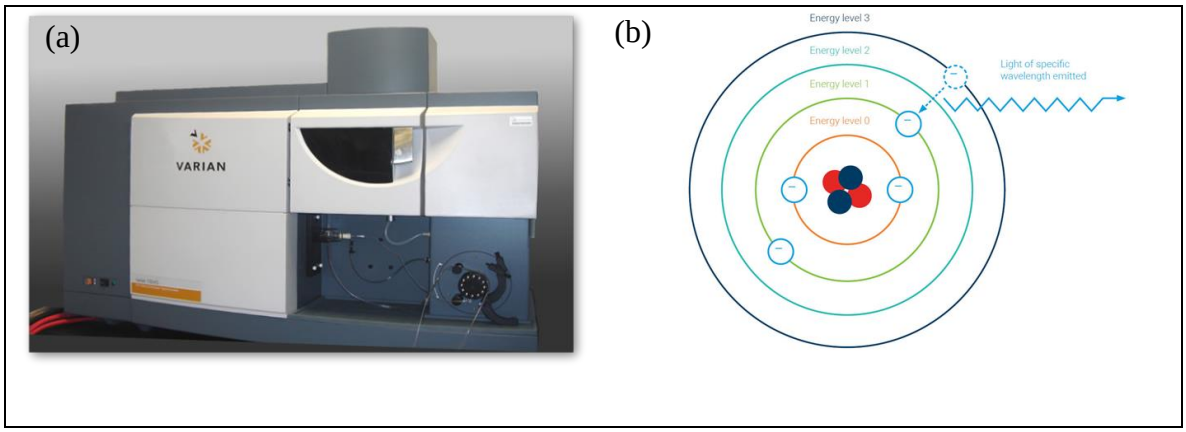


**Figure 2-9. (a)** ICP-OES spectrometer Varian 720-ES, and **(b)** their fundamental principle.
*Data source figure 2-9b: Agilent Technologies (2024).*

### 2.4.3 UV-vis spectroscopy

The optical properties of the aqueous solutions of Au seeds and nanostars and the photocatalytic reactions for water treatment were studied with a single-beam Hewlett-Packard HP 8453 diode array spectrophotometer (**Figure 2-10**) available at *ICP at Université Paris-Saclay*. In general, quartz cells with optical path lengths of 1 cm were used for AuNSs and of 1 mm for AuSs solutions.

UV-vis spectroscopy measures the absorption of photons in the UV and visible regions of the samples. This technique is based on the principle that molecules absorb specific wavelengths of light due to electronic transitions. UV-vis spectroscopy is widely used for quantitative analysis, determining the concentration of substances using Beer-Lambert law (Eq. 7), identifying substances based on their absorption spectra, and studying the electronic structure of molecules. Where $A$ is the absorbance, $\varepsilon$ is the molar absorption coefficient, $c$ is the molar concentration, and $l$ is the path length.

$$A = \varepsilon c l \qquad (7)$$

**Figure 2-10.** Hewlett-Packard HP 8453 diode array spectrophotometer.

The optical properties of the modified-titania were studied with a UV–vis–NIR spectrophotometer Cary 5000 Series from Agilent Technologies (**Figure 2-11**) available at *ICP, Université Paris-Saclay.* The maximum reflectance was set to 100% using $BaSO_4$ as a reference. The spectra for the powder samples were recorded from the 200 to 800 nm region.

When light hits a flat mirror, it reflects at a precise angle following the specular reflection. In contrast, light interacting with powdered or porous materials scatters in various directions due to surface irregularities and particle characteristics. This scattered reflection is termed diffuse reflection. In DRS, a spectrophotometer emits a beam of light (UV, visible, or IR) onto the sample, measuring the intensity of light scattered in all directions across different wavelengths. Light absorption by components in the sample decreases the amount of reflected light detected.

The optical band energies ($E_g$) of the modified samples and bare $TiO_2$ were calculated by the Tauc plot method, considering the indirect transition of anatase phase. By the following (Eq. 8 and 9) reflectance function F(R), where R is the reflectance obtained by DRS, while K and S are the absorptions and scattering coefficients, respectively. F(R) is proportional to the absorption coefficient, where $h$ is the Planck's constant, $\nu$ is the photon's frequency, $E_g$ is the bandgap energy, and $\beta$ is a factor depending on the transition probability and a constant in the optical

frequency range. The *n* factor depends on the nature of the electron transition and is equal to 2 or 1/2 for the direct and indirect transition bandgaps, respectively.

$$\mathrm{F(R)} = \frac{(1-\mathrm{R})^2}{2\mathrm{R}} = \frac{\mathrm{K}}{\mathrm{S}} \qquad (8)$$

$$\mathrm{F(R)}h\nu)^{\mathrm{n}} = \beta\left(h\nu - E_g\right) \qquad (9)$$


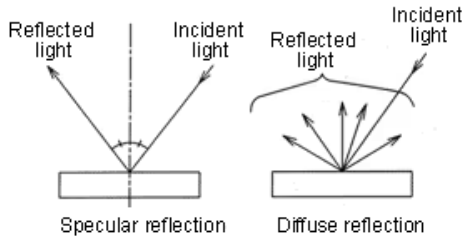


**Figure 2-11. (a)** UV–vis–NIR spectrophotometer (Cary 5000 Series, Agilent Technologies), and **(b)** their principle.

*Data source figure 2-11b: Courtesy of Shimadzu Corporation, Kyoto, Japan (2024).*

### 2.4.4 X-Ray Diffraction (XRD)

XRD investigated the crystal structure of the powder photocatalysts using a SmartLab RIGAKU (**Figure 2-12a**) available at *LINAN-IPICYT*. XRD measurements were performed with Cu Kα radiation, 40 kV, 44 mA, λ = 0.15406 nm over the 2θ range from 20° to 80°, with steps of 0.01° $s^{-1}$.

X-rays are generated when high-voltage electrons accelerate from a cathode towards a metallic target (anode), causing interactions where inner-shell electrons are ejected and higher-level electrons transition to fill these vacancies, emitting characteristic X-ray photons (**Figure 2-12b**). These X-rays are used to bombard crystalline samples to produce their diffraction patterns. In a crystalline sample, atoms are arranged periodically, scattering X-rays in various directions. Most

scattering is destructive, but waves from different atoms occasionally align constructively due to their periodic arrangement, creating diffraction phenomena. This occurs when X-rays diffracted by parallel planes spaced by distance "*d*" satisfy Bragg's law: $n\lambda=2d\sin\theta$. X-ray diffraction identifies the crystalline system and provides three-dimensional details of the crystal structure.

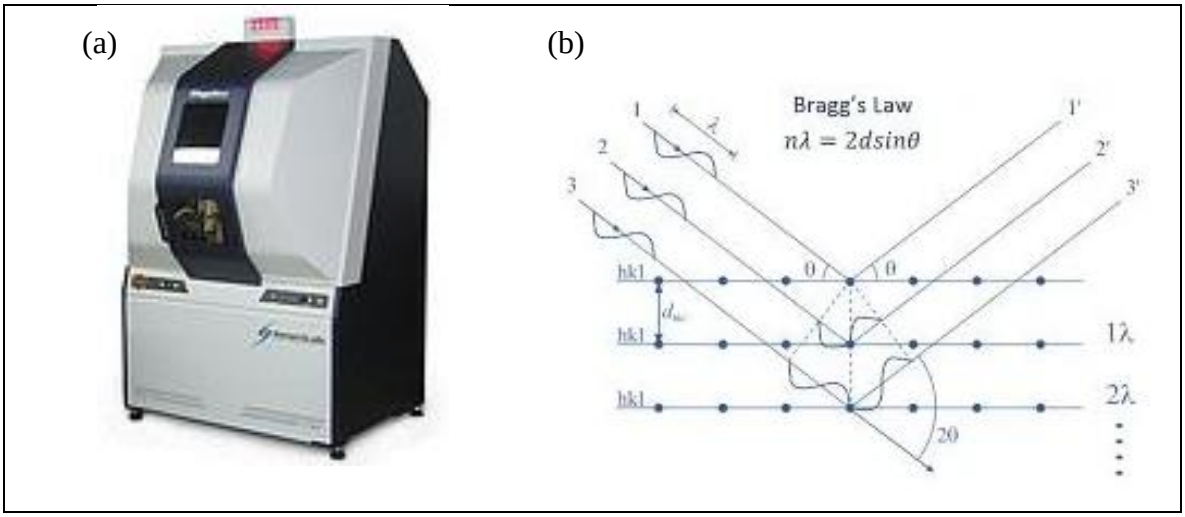


**Figure 2-12. (a)** X-ray diffractometer (SmartLab RIGAKU), and **(b)** their fundamental principle. *Data source: LINAN-IPICYT.*

### 2.4.5 X-ray Photoelectron Spectroscopy (XPS)

XPS analysis was done at *ICMMO-Université of Paris-Saclay*. In collaboration with Diana Dragoe.

XPS technique studies the surface elemental composition and oxidation states. XPS measurements were performed on a K-alpha spectrometer from ThermoFisher. XPS spectrometer is equipped with a monochromated X-ray source (Al $K_\alpha$ = 1486.68 eV) with a spot size of 400 µm, corresponding to an irradiated area of ≈1 $mm^2$. The samples were measured in the powder form. The base pressure was $3 \times 10^{-9}$ mbar. The hemispherical analyzer was operated in constant analyzer energy mode, with pass energy of 200 eV and a step of 1 eV for the acquisition of surveys spectra and pass energy of 50 eV and a step of 0.1 eV for the acquisition of narrow spectra. A

“dualbeam” flood gun was used to neutralize the charge buildup. The binding energies were calibrated against the neutral carbon binding energy set at 284.8 eV. The precision in binding energy is ±0.2 eV. The spectra were recorded and treated by means of *Avantage* software provided by Thermo Fisher. The fitting procedure implied the use of asymmetrical line shapes after the extraction of a Shirley-type background.

X-rays are directed onto a sample, causing electrons to absorb energy and be ejected with specific kinetic energies (**Figure 2-13**). A detector analyzes these energies, creating a plot that shows their distribution. The detector distinguishes electrons of varying energies, enabling the computer to generate spectra. In XPS, atoms within a compound are identified using the Eq. 10.

$$E_B = h\nu - E_K + \Phi_{SP} \qquad (10)$$

The binding energy ($E_B$) is the attraction of an electron to the nucleus, photon energy ($h\nu$) is from the X-ray photons used, and kinetic energy ($E_K$) is the energy of the ejected electrons from the sample. The work function ($\Phi_{SP}$) corrects for the instrument and indicates the minimum energy needed to eject an electron. With known values for work function and photon energy, and by measuring kinetic energy, binding energy can be determined. Electrons farther from the nucleus require less energy to eject, resulting in lower binding energies for higher orbitals. Different electron subshells (*s, p, d,* etc.) also exhibit distinct energies. XPS reveals these electron energies, thereby identifying the composition of a material.

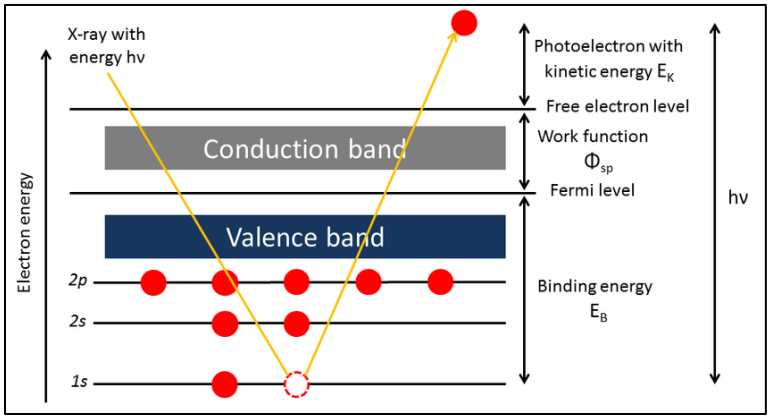


**Figure 2-13.** The physical principle of XPS.[129]

### 2.4.6 Time Resolved Microwave Conductivity (TRMC)

TRMC is a technique that studies the photogenerated charge-carriers' dynamics for the photocatalysts by pulsed light excitation. This technique is a powerful tool to investigate charge carrier lifetime in photocatalysis, where understanding how charge carriers are generated, move, and recombine is essential for improving the efficiency of photocatalytic processes. TRMC is available at *ICP-Université Paris-Saclay*, and the study was conducted in collaboration with Christophe Colbeau-Justin.

The principle of TRMC is the measurement of electrical conductivity of a material over time after optical excitation (UV and visible light).[6,15,68,51,118] The material is illuminated with a pulsed and tunable laser source (from 200 nm to 2000 nm) equipped with an optical parametric oscillator (OPO; EKSPLA, NT342B) was used to excite the samples. The photocatalyst is excited and electrons from the VB flow to the CB, generating electron-hole pairs. After excitation, a microwave field is applied to the sample using a Gunn diode (30 GHz). The microwave field interacts with the free charge carriers (mainly electrons). The sample's conductivity changes due to the movement of charge carriers within the material. The change in conductivity is measured over time as the charge carriers move, recombine, or become trapped.

TRMC technique measures the relative change ($\frac{\Delta P(t)}{p}$) in microwave power reflected from a semiconductor material during its excitation by a laser pulse (**Figure 2-14**). This change ($\Delta\sigma(t)$) could be related to a small perturbation of the sample's conductivity (Eq. 11).

$$\frac{\Delta P(t)}{p} = A\Delta\sigma(t) = Ae\mu_e\Delta n_e(t) \qquad (11)$$

In $TiO_2$-based compounds, electron mobility ($\mu_e$) is much higher than holes. Therefore, $\Delta\sigma(t)$ is mainly due to excess electrons in the CB. $\Delta n_e(t)$ is the excess number of free electrons at time *t*. $A$ (sensitivity factor) is time-independent and relies on the conductivity of the semiconductor and the microwave frequency. The main data provided by the TRMC technique gives the maximum value of the signal ($I_{max}$) corresponds to the number of excess free electrons generated by the laser pulse. The signal decay $I(t)$ (denominated photoconductivity) as a function of time (in *μs* or *ns*) is owing to the decrease of excess electrons after the laser pulse by charge carriers' recombination or trapping.[6,15,68,51,118]

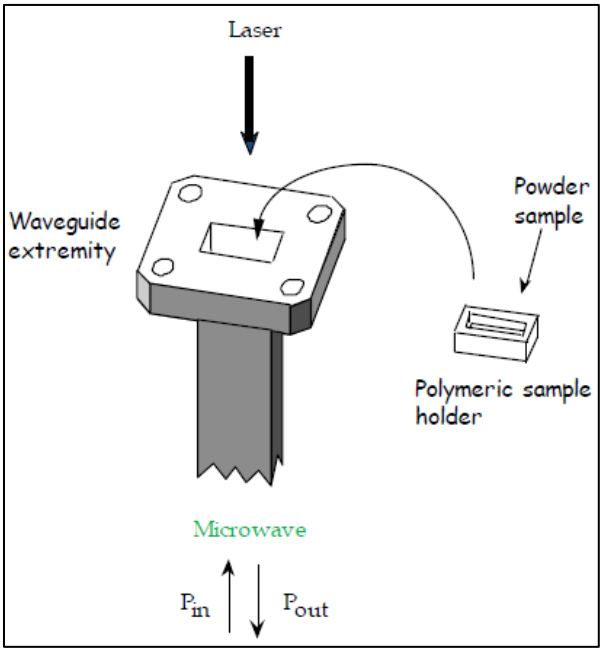


**Figure 2-14.** Time Resolved Microwave Conductivity (OPO; EKSPLA, NT342B).[130]

### 2.4.7 Gas Chromatography (GC)

The photocatalytic hydrogen generation was measured using GC (**Figure 2-15a**) available at *ICP, Université Paris-Saclay*. GC is employed to separate and analyze compounds within mixed gas samples. A standard GC module consists of four main subsystems: injection, separation, detection and data system (**Figure 2-15b**). The sample is introduced into the instrument via its injector. Micro GC Fusion accepts gas-phase samples only at pressures ranging from 0-172 kPa. The carrier gas (mobile phase) injects the sample into the column for analysis. High purity inert gases (99.999%), namely He (C2) and Ar (C1) were used. The inlet pressure of the carrier gas (at the rear of the instrument) must be maintained between 400 and 427 kPa. Micro GC fusion is equipped with internal ventilation via a built-in fan. The air inlet at the front of the equipment must remain clean and unobstructed.

Sample separation upon injection onto the column is achieved through interactions between the sample and the column's coating (stationary phase). The column's coating affects the elution order of compounds: less retentive coatings allow faster

elution of compounds. Elution order primarily hinges on compound boiling point and polarity. Two types of silica capillary columns are utilized (**Figure 2-15c**). Wall Coated Open Tubular (WCOT) columns, which employ a liquid stationary phase based on gas-liquid partitioning (e.g., Dimethylpolysiloxane), and Porous Layer Open Tubular (PLOT) columns, which utilize a solid stationary phase based on gas-solid partitioning for separating compounds by polarity. The capillary column in the Micro GC Fusion is resistively heated to facilitate temperature ramping, which accelerates column temperature increases to reduce analysis time and enhance compound separation efficiency. Following separation in the GC column, the eluted sample enters the detection subsystem, achieving a detection limit of 1 ppm.

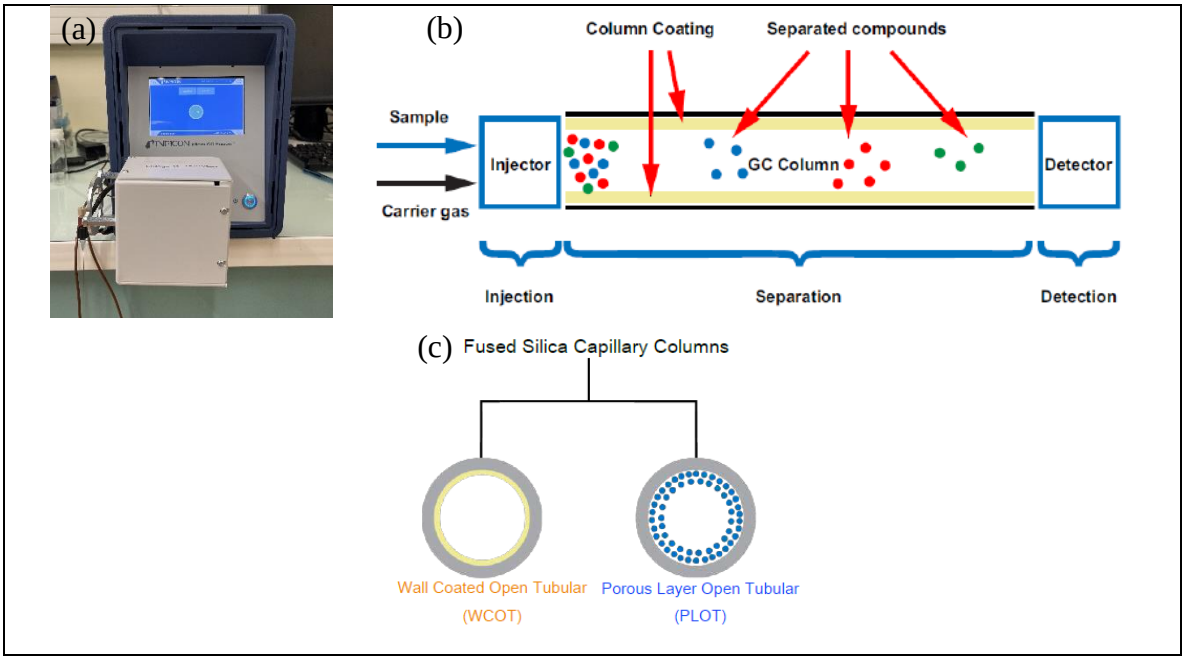


**Figure 2-15. (a)** Micro GC Fusion INFICON, **(b)** GC module consisting of four main subsystems: injection, separation, detection and data system, and **(c)** capillary columns.

*Data source: Operating manual-Micro GC Fusion.*

The photocatalysts for water treatment were characterized by different techniques: SEM, TEM, HRTEM, EDS, UV-vis spectroscopy, Hyperspectral dark-field optical microscopy, and AFM. The methodology and principle of the techniques not yet discussed will be briefly explained below.

### 2.4.8 Scanning Electron Microscopy (SEM)

FEI-FIB Dual Beam Helios Nanolab 600 (**Figure 2-16**) is available at *LINAN-IPICYT*, equipped with an EDS detector. SEM is a non-destructive technique used to analyze the morphology, nanoparticle size, and elemental analysis.

SEM consists of an electron emitter, a column with electromagnetic lenses, and a deflection system. The emitter generates a beam of electrons (incident electrons) accelerated between 200 V and 30 keV, traveling through a vacuum column ($10^{-4}$ Pa). Within the column, electromagnetic lenses and a deflection system manipulate the electron beam to scan the sample surface. When incident electrons interact with the sample generate various signals: secondary electrons, backscattered electrons, X-rays, Auger electrons and cathodoluminescence (UV, visible and IR). These signals are collected by one or more detectors to form images.

Secondary electrons (located at 45° with respect to the plane of the sample): They provide us topographical information due to their low energy (around 3 to 5 eV), they are near to the surface (few nm), allowing them to escape. When a primary beam hits the sample surface causing ionization of the atoms, loosely bound electrons can be emitted and these are called secondary electrons. To explain it with more details, the incident electrons pass near to the nucleus of an atom in the sample, it provides enough energy to a lower energy electron (usually in the K-shell) to jump out of the sample. This causes a slight energy loss and path change in the incident electron and the ionization of the electron in the specimen atom. This ionized electron leaves the atom with a minimal kinetic energy (about 5 eV).
Backscattered electrons (located at 0° with respect to the plane of the sample): They reveal surface composition, creating micrographs with varying brightness based on surface chemical composition. Differences in production rates cause elements with higher atomic numbers to appear brighter. They have suffered one or more dispersion events and escape from the surface with an energy greater than 50 eV. The elastic collision between an electron and the atomic nucleus of the sample

causes the electron to bounce back with a wide-angle directional change (when an electron in the beam collides head-on with the nucleus, being repelled in the opposite direction).

**X-ray Electronic Transitions (located at 45° with respect to the sample plane):** They indicate elemental composition by restoring orbital charge balance after ionization events. Following secondary electron production, a lower energy inner shell electron may be displaced by collision with a primary electron, creating a vacancy. A higher energy outer shell electron can fill this vacancy, emitting energy (often X-rays) to stabilize the atom.

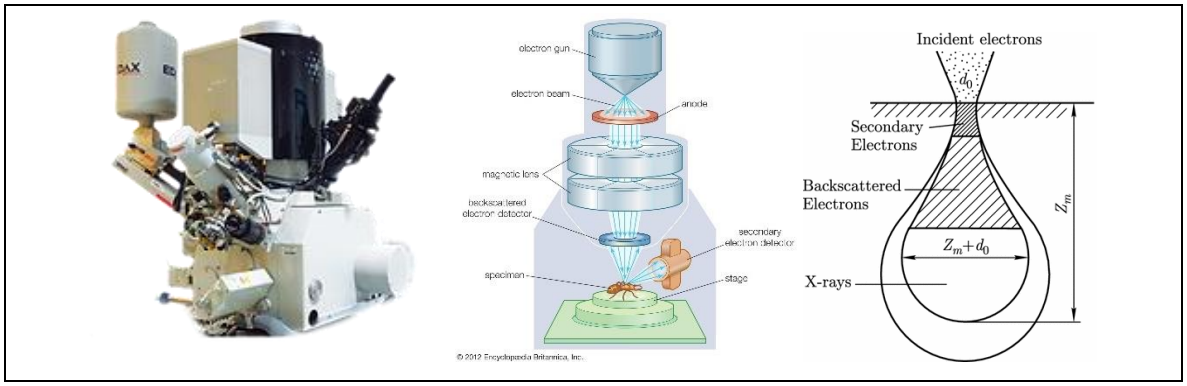


**Figure 2-16.** FEI-FIB Dual Beam Helios Nanolab 600.

*Data source:LINAN-IPICYT.*

### 2.4.9 Hyperspectral Dark-Field Optical Microscopy

Hyperspectral dark-field optical microscopy using a NIKON ECLIPSE LV100ND (**Figure 2-17**) available at the *Sorbonne Université* in collaboration with Olivier Pluchery. Hyperspectral dark-field optical microscopy coupled with a spectrometer was used to analyze the optical scattering of AuNSs and measure their LSPR of individual AuNSs. The reproducibility of the LSPR of AuNSs using a setup described elsewhere.[131] The LSPR bands of identified AuNSs were recorded before and after the adsorption of 4-NTP and then after the photodegradation of 4-NTP. Three

samples were prepared for these experiments using microscope slides (SWIFT, CAT.NO.7101, thickness: 1-1.2 mm) as the substrate (Figure S6-1, Annex IV).

The glass substrates were marked with a slight scratch to be able to precisely localize individual AuNSs. Subsequently, the slides were cleaned by sonication in acetone for 2 minutes and then in ethanol for 2 minutes. The slides were then dried using $N_2$ gas. After the glass substrates underwent silanization with APTES, the silanization introduced amino functional groups, chemically altering the glass surface. This allows specific interactions with the NPs, enabling their adhesion and stability. A solution of 200 µL APTES in 10 mL methanol was prepared, and the microscope slides were immersed in this solution for 1 hour. The APTES solution was removed and replaced with 10 mL of methanol, followed by 3 minutes of sonication. The slides were then placed in a clean beaker containing 10 mL of methanol and put under sonication for 3 minutes; this process was repeated 3 times. Once completed, the slides were dried with $N_2$ gas. Finally, the AuNSs with a concentration of **$1.84\times10^{-4}$ M $Au^0$** were put in contact with the substrate for 1 minute (1 drop), 5 minutes (1 drop), and 15 minutes (2 drops), as shown in Figure S6-1, Annex IV. Then, the slides were rinsed with abundant Milli Q-water and dried using $N_2$ gas before being stored in a box for analysis.

The Nikon Eclipse LV100D microscope is designed with an upright configuration, featuring a light source beneath the stage and an objective lens above it for transmitted light illumination. Dark field imaging is achieved using a specialized condenser with an opaque stop, allowing only scattered or diffracted light from the sample to reach the objective lens. This creates a dark background that highlights these scattered or diffracted light components. Samples for dark field microscopy are typically prepared on transparent substrates such as glass slides, enabling transmitted light to pass through. The samples scatter or diffract light upon illumination. During observation, the sample is placed on the stage and illuminated from below with a focused light beam. The condenser's opaque stop blocks direct light, ensuring a dark background in the resulting image. The objective lens collects

only the scattered or diffracted light, which is then captured by the microscope's camera. The microscope is equipped with a camera for viewing and capturing sample images. These images can be transferred to a computer for further analysis. Dark field microscopy with this instrument provides detailed visualization of fine structures, particles, or features that may not be visible under bright field illumination, offering valuable insights into the sample's scattering or diffraction properties.

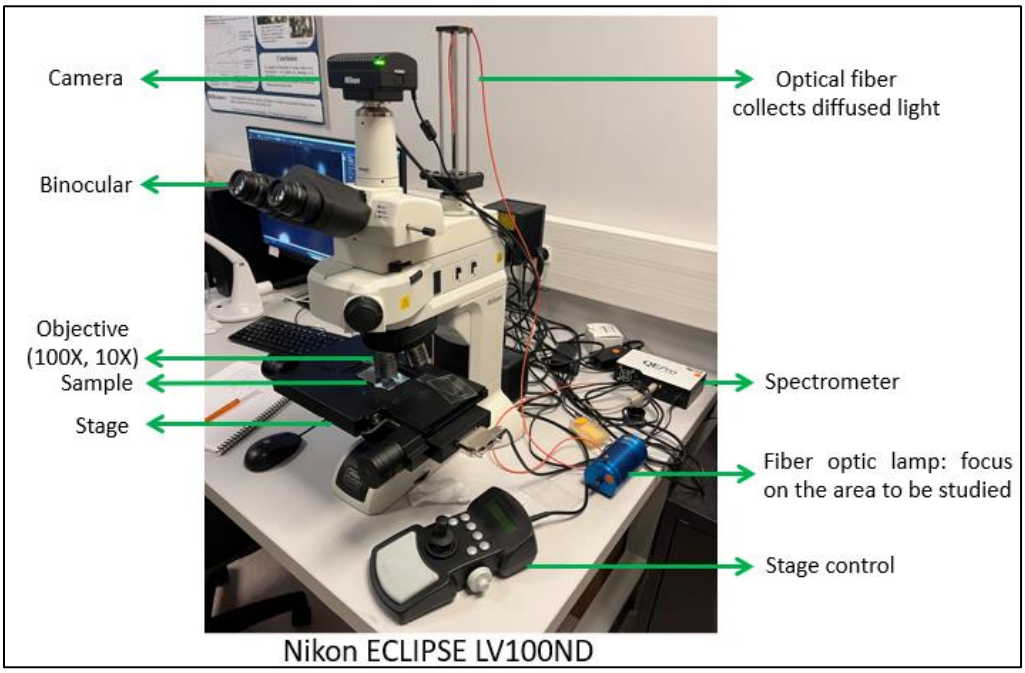


**Figure 2-17.** Dark Field Optical Microscope (Nikon Eclipse LV100D).

### 2.4.10 Atomic Force Microscopy (AFM)

For AFM, we used a Park Systems model NX20 (Figure 2-18), available at Institut des Nanosciences, *Sorbonne Université*, in collaboration with Prof. Olivier Pluchery. AFM was employed to analyze individual AuNSs and measure their size using Gwyddion Software. AFM measurements were operated in tapping mode using a Bruker RTESPA-150 cantilever ($f_0$= 150 kHz, $k$ = 5 N/m) that has a tip radius of 10 nm. The AFM was correlated with dark field optical microscopy images to characterize the same particles using an approach described in detail here.[131]

Tapping mode in AFM is a technique where a cantilever with a sharp tip oscillates at a specific frequency and makes intermittent contact with the sample surface. This oscillation occurs at a higher amplitude than non-contact mode, allowing the tip to tap the surface periodically.[132] In tapping mode, the cantilever intermittently contacts the sample, operating at the transition between repulsive and attractive forces. Tapping mode is particularly useful for imaging soft or delicate samples, as the brief contact minimizes potential damage.


**Figure 2-18.** Atomic Force Microscope (Park SYSTEMS model NX2).

## 2.5 Photocatalytic Tests

### 2.5.1 Photocatalytic Hydrogen Generation Test

The photocatalytic hydrogen generation tests were performed in a closed quartz reactor (**Figure 2-19a**). 20 mg of the photocatalyst were dispersed in 20 mL of aqueous solution containing 25 vol% of the sacrificial electron donor or hole scavenger (triethanolamine (TEOA) or methanol). Before irradiation, the reactor was degassed with inert gas for 20 min under vigorous stirring. Afterward, the samples were irradiated for 5 h using a Peschl photoreactor (**Figure 2-19b-d**) and a Xenon Lamp 300 W LOT-Oriel (250–2000 nm) equipped with a water filter (a large quartz cell) between the lamp and the reactor to screen the infrared light and avoid heating

of the samples (**Figure 2-19e**). An optical filter was used to limit the irradiation to the visible (λ ≥ 420 nm) see **Figure 2-19f**. The hydrogen amount was measured by gas chromatography every hour (Micro GC Fusion, INFICON).

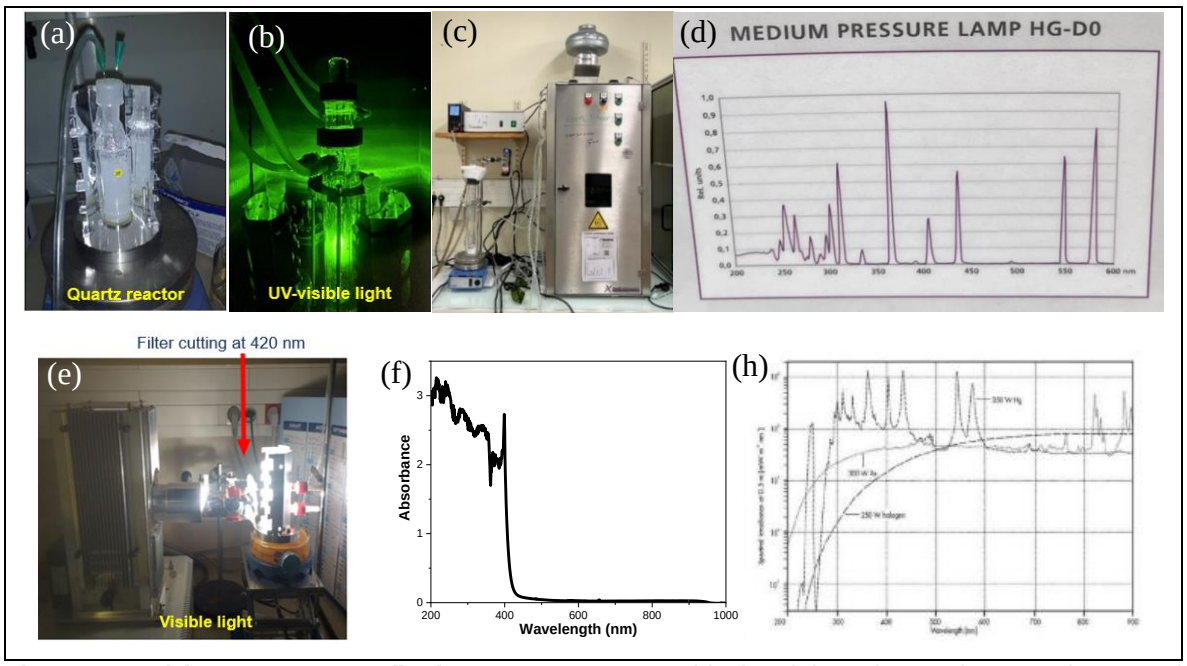


**Figure 2-19. (a)** Quartz reactor, **(b-c)** Mercury Lamp Peschl Ultraviolet Advanced UV-products, and **(d)** their spectrum of the lamp, **(e)** Xenon Lamp 300W LOT-Oriel, **(f)** Filter cutting at 420 nm, and (h) their spectrum of the lamp.

### 2.5.2 Stability with cycling

The photocatalyst stability is an essential parameter that defines the materials' commercial significance. For the photocatalyst stability of AuPd/$TiO_2$, 20 mg of photocatalyst were once again dispersed in 20 mL of 25 vol% of TEOA aqueous solution. The mixture was degassed with Ar for 20 min under vigorous stirring before exposure to irradiation for 5 h in a Peschl photoreactor. The powder was recovered through centrifugation and dried at 60 °C for 24 h. Afterward, the photocatalyst was weighted and dispersed in a 25 vol% TEOA aqueous solution, maintaining a 1 mg $mL^{-1}$ ratio. This process was repeated for four cycles. In the case of the best samples of NiFe/$TiO_2$ and NiO/$TiO_2$ photocatalysts, the recovery of powder after the first cycle

was limited due to the small amount collected. For photocatalyst stability, the reactor was covered with aluminum foil and put under darkness. The next day, the reactor was degassed again and put under irradiation using the same conditions for up to five cycles.

### 2.5.3 Plasmonic catalysis Tests for Water Treatment

The photocatalytic reactions were conducted using a Solar Lamp 300 W LOT-Oriel (**Figure 2-20a-b**), with the distance between the lamp and the reactor set at 16 cm (**Figure 2-20c**). An optical filter ($\lambda > 500$ nm) (**Figure 2-20d**) was used to analyse only the effect of AuNSs and AuSs plasmons for 4-NTP degradation while inhibiting the direct excitation of 4-NTP (absorption bands at 228 nm and 408 nm).

A quartz reactor was used for all the photocatalytic tests equipped with a magnetic stirrer and cap for UV-vis spectroscopy analysis (**Figure 2-20e**). The concentration for AuNSs and AuSs was $1.84\times10^{-4}$ M $Au^0$ and for 4-NTP was $1.64\times10^{-4}$ M within the quartz reactor, and 0.1 M of 2-propanol used as hole scavenger.

A glass container holding 2750 µL of $1.64\times10^{-4}$ M 4-NTP was used for the glass substrate with the AuNSs for hyperspectral dark field optical microscopy analysis (**Figure 2-20f**).

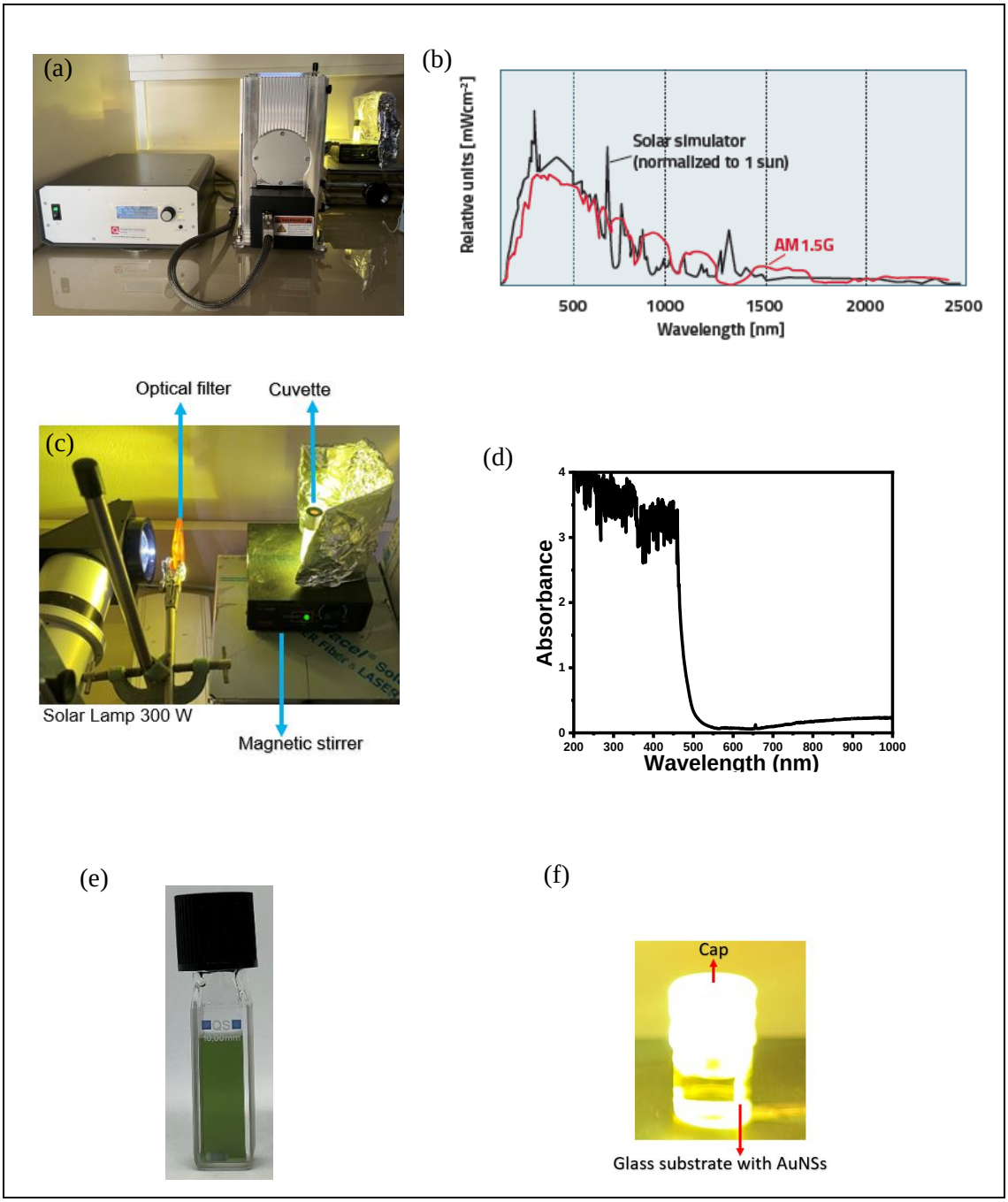


**Figure 2-20. (a)** Solar lamp 300 W LOT-Oriel, **(b)** Solar spectrum, **(c)** photocatalytic test using 16 cm between the lamp and reactor for 4-NTP reduction under visible light, **(d)** optical filter (λ > 500 nm), **(e)** quartz reactor, and **(f)** glass container.

# Chapter 3

Enhanced Photocatalytic Activity of Surface-Modified $TiO_2$ with Bimetallic AuPd Nanoalloys for Hydrogen Generation

# Chapter 3. Enhanced Photocatalytic Activity of Surface-Modified $TiO_2$ with Bimetallic AuPd Nanoalloys for Hydrogen Generation

## 3.1 Introduction

Bimetallic NPs like AuPd,[19,69] AuPt, [70,71] AuNi,[8] and AuCu[72] have been reported to demonstrate improvements in their electrical, optical, and catalytic properties. These nanoalloys exhibit superior catalytic performance, particularly in selectivity and stability, compared to their individual metal components. Therefore, they are highly desirable for a range of applications in catalysis and electrocatalysis. Pd has gained attention due to its efficiency as catalyst in various applications, including catalytic and electrocatalytic processes, hydrogen storage,[107] sensors,[104,31] nanomedicine,[27,105] hydrogenation reactions,[69] C–C coupling reactions,[102,103] mitigating environmental pollution, and automotive emissions regulation. Pd–Au bimetallic NPs exhibit higher selectivity compared to monometallic Pd NPs for hydrogenation reactions.[69,17,18] Porous $Pd_{shell}Au_{core}$ nanostructures are very promising for application in direct ethanol fuel cells as they exhibit good electrocatalytic activity and high stability.[111] Surface modification of $TiO_2$ with bimetallic NPs based on gold has attracted much interest because higher activities for photocatalytic hydrogen generation can be obtained compared with their monometallic counterparts.[8,68,14,19]

Hereby, we report the application of AuPd nanoalloys on $TiO_2$ surface for hydrogen generation by photocatalysis, showing a synergetic effect under UV–vis light for $H_2$ production. The metal loading of both metals was optimized and the role of Au and Pd on the photocatalytic activity was studied using molecular simulations.

## 3.2 Results and Discussions

### 3.2.1 Characterization of the Photocatalysts

The morphology, size, elemental composition, and crystalline structure of 1 wt% AuPd/$TiO_2$ samples with the mass ratios of Au:Pd (9:1. 1:1. 1:9) were analyzed by TEM, HRTEM, and EDX techniques. TEM images in bright field (**Figure 3-1a**, S3-1a, and S3-2a, Annex I) and Z contrast mode (**Figure 3-1b**, S3-1b, and S3-2b, Annex I) show small and spherical AuPd NPs with an average size of 2.5–3 nm (**Figure 3-1e**, S3-1e, and S3-2e, Annex I) well dispersed on $TiO_2$ surface. Table S3-1, Annex I, shows the AuPd NPs average size for 1 wt% AuPd/$TiO_2$ samples with different mass ratios. HRTEM images of 1 wt% AuPd/$TiO_2$ samples show the localization of AuPd NPs on the anatase phase (**Figure 3-1c**, S3-1c, and S3-2c, Annex I). The electronic interaction with AuPd NPs and the anatase phase inhibits the growth and agglomeration of the metal NPs.[6] The interplanar distances were d= 0.35 nm, corresponding to (101) planes of the anatase phase (JCPDS No. 21-1272). The interplanar distances were measured using the Digital Micrograph software deduced by fast Fourier transformation process. The elemental composition was confirmed by EDX analysis showing the presence of Au, Pd, Ti, and Cu from the TEM grid (**Figure 3-1d**, S3-1d, and S3-2d, Annex I). Small signals of Au and Pd were observed for 1 wt% $Au_9Pd_1/TiO_2$ and 1 wt% $Au_1Pd_9/TiO_2$ due to their low content, as shown in **Figure 3-1d** and S3-2d, Annex I, respectively. Moreover, for the sample 1 wt% $Au_1Pd_1/TiO_2$, the EDX signals are almost identical due to the same metal content (Figure S3-1d, Annex I).

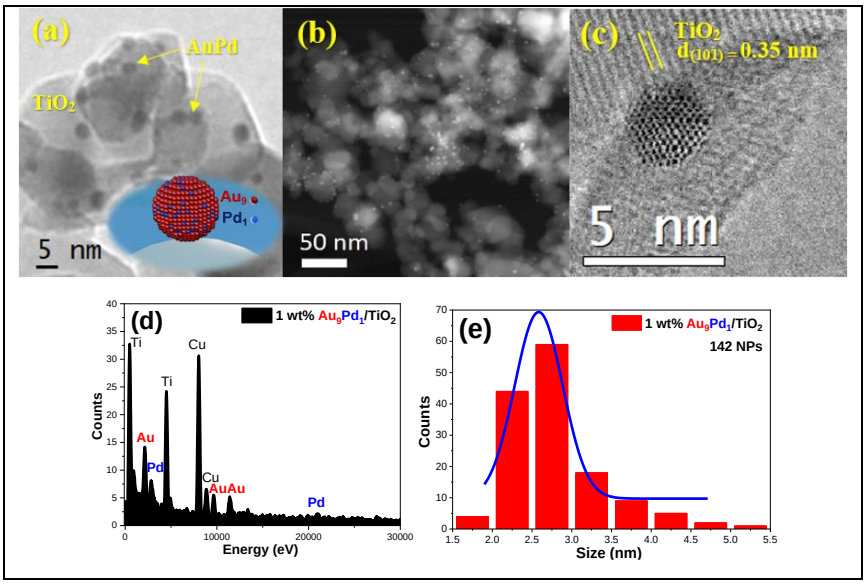


**Figure 3-1.** TEM micrographs of 1 wt% $Au_9Pd_1/TiO_2$ sample in **(a)** bright field and **(b)** Z contrast show spherical AuPd NPs well dispersed on $TiO_2$ surface, **(c)** HRTEM micrograph showing the localization of AuPd NPs on the anatase phase, **(d)** EDS analysis showing the presence of the elements Au, Pd Ti, and Cu (from the TEM grid), and **(e)** histogram of AuPd NPs showing an average size of ~2.6 nm.

In **Figure 3-2**, we present HAADF-STEM micrograph (**Figure 3-2a**) that shows $Au_9Pd_1$ nanoalloys with brighter tiny points corresponding to Au and less bright tiny spots corresponding to Pd (due to the highest atomic number of Au compared with Pd). Additionally, EDX analysis on single NPs for the 1 wt% $Au_9Pd_1/TiO_2$ sample (**Figure 3-2b**) attests the presence of Pd on the surface of the NP, but with homogeneous distribution over all the structure (**Figure 3-2c**). In order to elucidate the chemical ordering of these alloys content, we performed a hybrid MD–MC (molecular dynamics–Monte Carlo, with the reliable Gupta interatomic potential for Au–Pd, see details in Annex I) simulation for each of the ratios, and then we simulated the line scan, shown in **Figure 3-2d** for the alloy content $Au_9Pd_1$: the simulation is in good agreement with the experimental results. Also, the results show that the alloy in all the systems is random, not ordered as in the AuPd bulk alloy previous studies.[133,134] ICP-OES was utilized for elemental analysis, providing insights into the mass content of AuPd nanoalloys on $TiO_2$ surface (see Table S3-2, Annex I).

The bimetallic photocatalysts 1 wt% AuPd/$TiO_2$ and bare $TiO_2$ were characterized by XRD to study the crystallinity of the samples (Figure S3-3, Annex I). The diffracted peaks of the samples coincide with the reference peaks of the anatase and rutile crystalline phases, according to the data JCPDS file nos. 21-1272 and 21-1276, respectively. The junction between anatase and rutile phases in P25 induces longer lifetime of the charge carriers increasing the photocatalytic activity.[53] No diffraction peaks were observed for AuPd NPs due to the low metal loading and the small size of the NPs.[135]

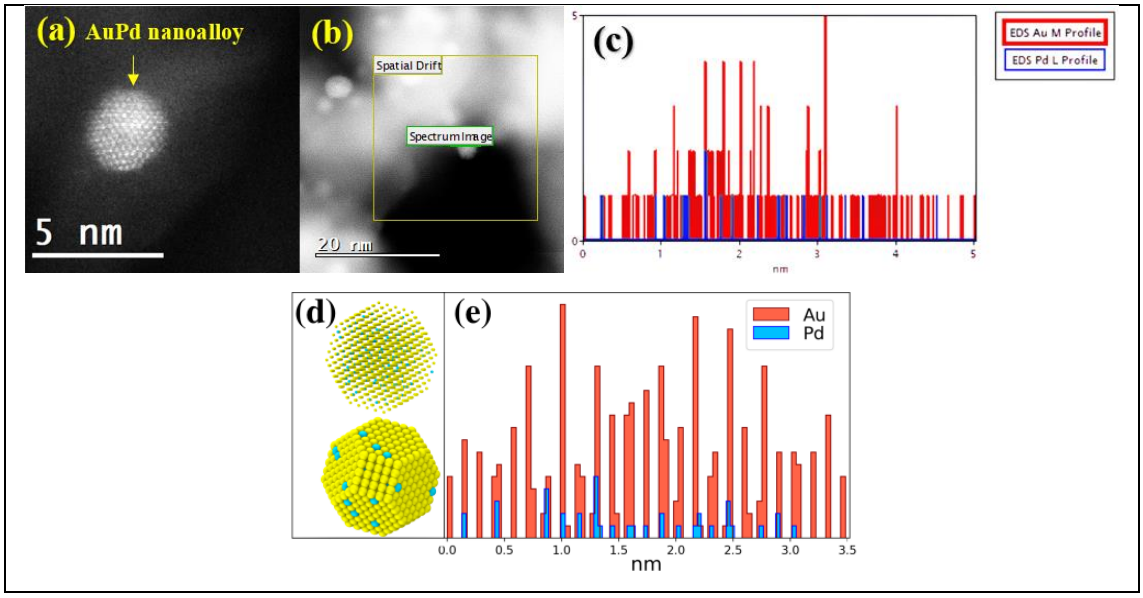


**Figure 3-2.** For the $Au_9Pd_1$ alloy: **(a)** HAADF-STEM micrograph, **(b)** spectrum image, and **(c)** Au–M and Pd–L energy-level profiles. **(d)** Energy optimization structure of $Au_9Pd_1$ NPs by hybrid MD–MC (Gupta) calculation for the identified size and structural shape from the experiment (a 1289 atoms cuboctahedron with 3.5 nm); and **(e)** simulated line scan on this NP and orientation shown, reflecting the chemical ordering.

The UV–vis spectra of the samples showed absorption in the UV region due to $TiO_2$ support (**Figure 3-3a,b,c**). The UV–vis spectra of the monometallic samples Pd/$TiO_2$ show that the surface modification with Pd NPs does not influence the $TiO_2$ bandgap (**Figure 3-3a**). Pd NPs do not introduce energy levels in the bandgap, below the CB and above the VB because of their plasmon in the UV region.[118] Moreover, the monometallic samples of Au/$TiO_2$ show the LSPR of gold with a maximum

absorption peak at 553, 547, and 553 nm for 0.1, 0.5, and 0.9 wt% Au/$TiO_2$ (**Figure 3-3b**). The dielectric constant of the $TiO_2$ support induces a shift of the LSPR of the metal NPs toward larger wavelengths (compared to the NPs in water).[6,136] In the case of the bimetallic sample 1 wt% $Au_9Pd_1/TiO_2$ (**Figure 3-3c**), the LSPR of Au induces an intense and continuous absorption over the entire visible region due to the presence of AuPd nanoalloys rich in gold.[92] However, the sample 1 wt% $Au_1Pd_9/TiO_2$ does not show this characteristic because of the lowest content in gold. Au NPs act as visible absorption centers extending the light absorption of wide bandgap semiconductors to the visible light due to their LSPR. Improving the UV–vis absorption of the photocatalyst is important in photocatalysis to better harvest solar light. The bandgap energies of the bimetallic samples and bare $TiO_2$ were calculated by the Tauc plot method, considering the indirect transition of anatase phase. [50] **Figure 3-3d** shows the Tauc plots for bare $TiO_2$, 1 wt% $Au_1Pd_9/TiO_2$, 1 wt% $Au_1Pd_1/TiO_2$, and 1 wt% $Au_9Pd_1/TiO_2$. The estimated bandgaps were 3.34, 3.33, 3.30, and 3.30 eV, respectively.

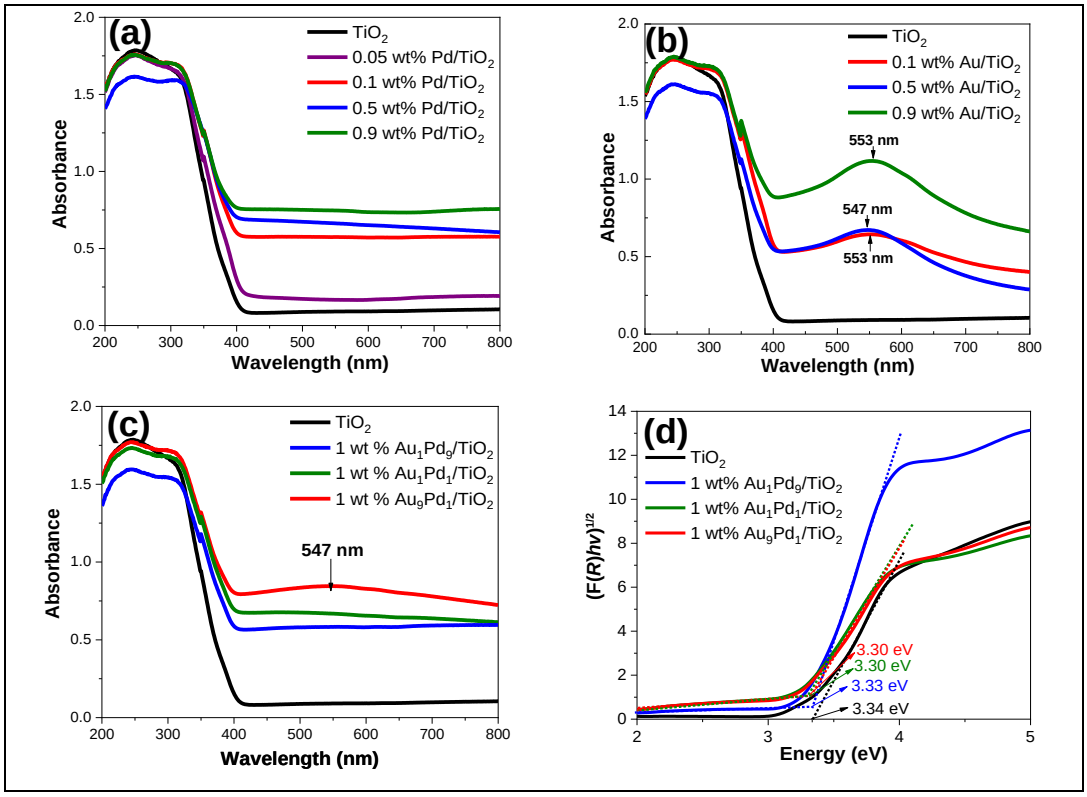


**Figure 3-3.** UV–vis DRS spectra of monometallic samples **(a)** Pd/$TiO_2$ and **(b)** Au/$TiO_2$, and bimetallic samples **(c)** 1 wt% AuPd/$TiO_2$ and **(d)** their corresponding Tauc plot.

TRMC signals of mono- and bi-metallic photocatalysts and bare $TiO_2$ at 360 nm are shown in **Figure 3-4**. TRMC signals show $I_{max}$ values reached for all the samples under UV light excitation, suggesting electron migration from the VB to the CB of $TiO_2$. Then, the $I_{max}$ values decreased, and faster decays were observed for the mono- and bimetallic photocatalysts than bare $TiO_2$. This can be explained by quick trapping by Au, Pd, and AuPd NPs of photogenerated electrons in the CB of $TiO_2$. **Figure 3-4a** shows the signals of $Au/TiO_2$ samples: the decay of the signal increases with the metal loading 0.9 wt% $Au/TiO_2$ > 0.5 wt% $Au/TiO_2$ > 0.1 wt% $Au/TiO_2$. In the case of $Pd/TiO_2$ samples (**Figure 3-4b**), the decay is not correlated with the metal loading and faster decay is obtained with 0.1 wt%. For the bimetallic photocatalysts (**Figure 3-4c**), the decay increases with 1 wt% $Au_1Pd_1/TiO_2$ > 1 wt% $Au_9Pd_1/TiO_2$ > 1 wt% $Au_1Pd_9/TiO_2$. These TRMC results indicate that the AuPd nanoalloys are efficient in electron scavenging reducing the charge-carrier recombination, which is beneficial for the photocatalytic activity.[6,72,51] At 420 nm (Figure S3-4, Annex I), no signal from mono- and bi-metallic samples was higher than the signal obtained by $TiO_2$. At 550 nm (Figure S3-5, Annex I), the gold-based photocatalysts (mono- and bi-metallic samples) show no signal, indicating that at these wavelengths no hot electrons were detected in the CB of titania after Au-LSPR excitation.

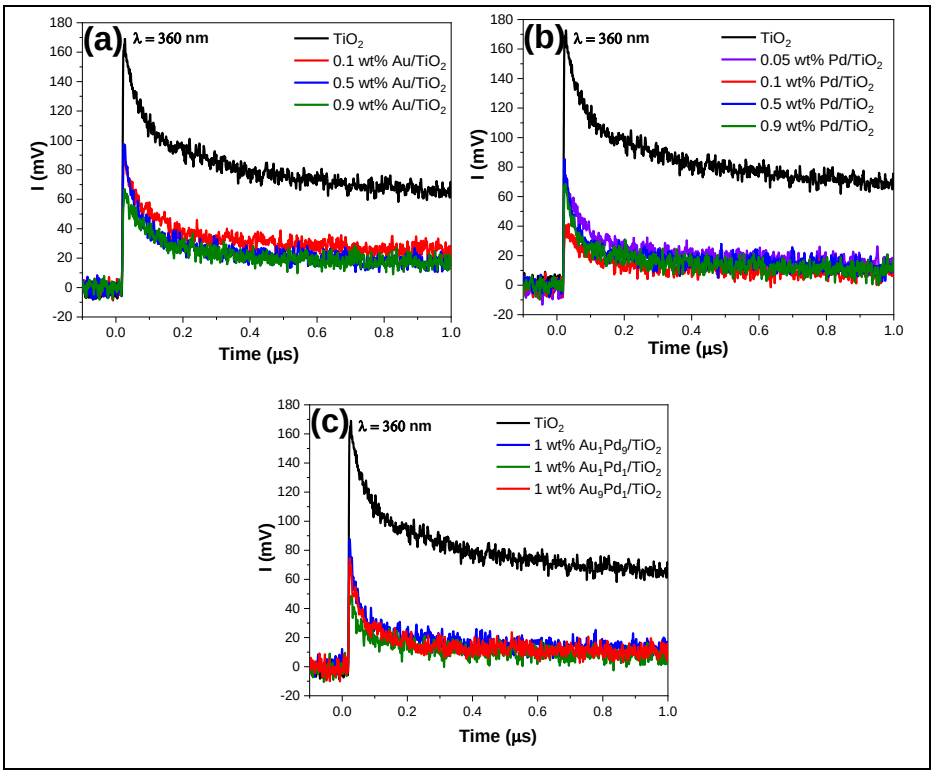


**Figure 3-4.** TRMC signals of monometallic photocatalysts **(a)** Au/$TiO_2$, **(b)** Pd/$TiO_2$, and **(c)** bimetallic photocatalysts 1 wt% AuPd/$TiO_2$ at $\lambda_{exc}$=360 nm with a laser energy of 1.2 mJ.

XPS analysis was performed on the sample surface in order to get information concerning the chemical environment of Au and Pd. The obtained Au 4f and Pd 3d core-level spectra are presented in **Figure 3-5**. Both Au 4f and Pd 3d doublets were fitted using asymmetrical line shapes derived from metallic Au and Pd references. The binding energy scale was calibrated based on Ti $2p_{3/2}$ peak, used as internal reference, considered at 458.7 eV, which places the main O 1s component corresponding to O in $TiO_2$ at 530 eV.[137] As a consequence, the spin–orbit coupling doublet of Au 4f is placed at 83.2 eV (Au $4f_{7/2}$) and 86.8 eV (Au $4f_{5/2}$) and that of Pd 3d at 334.5 eV (Pd $3d_{5/2}$) and 339.8 eV (Pd $3d_{3/2}$). This XPS analysis confirms that AuPd NPs are in metallic states. In both cases, the binding energies of Au 4f and Pd 3d are shifted toward lower values from those given in the literature.[138] For instance, Au $4f_{7/2}$ reported at 84 eV shifted to 83.2 eV and Pd $3d_{5/2}$ from 335 to 334.5 eV. Two points can explain the shift toward lower binding energy values for Au 4f and Pd 3d, *i.e.*, this, first, may be due to the interaction of the support ($TiO_2$) changing its

electronic environment, the electron transfer from the $TiO_2$ to the AuPd NPs,[72,135] and second, may be due to a strong electronic modification and charge transfer between Au and Pd due to its nanoalloy formation.[139,140,141] Bimetallic AuPd nanoalloys have been reported to exhibit negative shifts in both the Au 4f and Pd 3d core levels.[142,143]

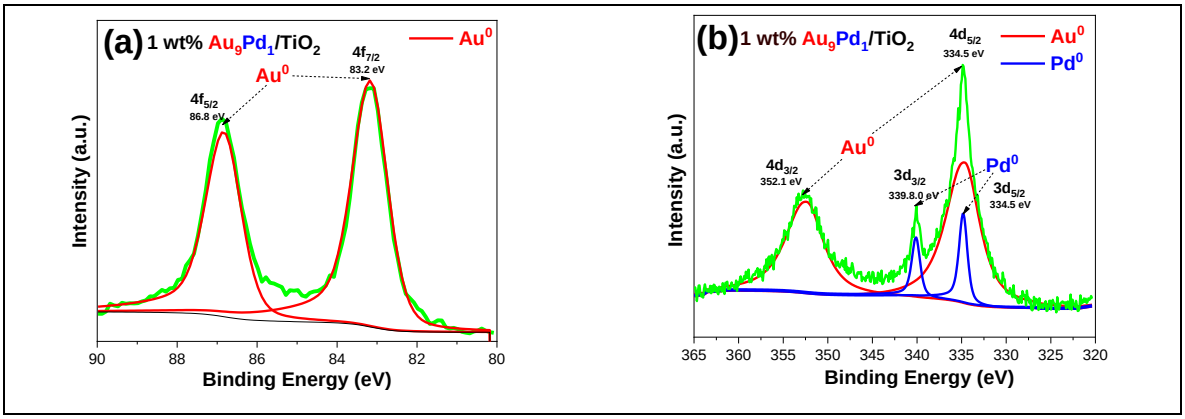


**Figure 3-5.** XPS spectra signals of 1 wt% $Au_9Pd_1/TiO_2$ sample: **(a)** Au 4f core level and **(b)** Au 4d and Pd 3d core levels.

### 3.2.2 Photocatalytic Hydrogen Generation

The photocatalytic hydrogen generation for mono- and bi-metallic samples under UV–vis and visible light is shown in **Figure 3-6a**,**b**, respectively. The monometallic samples present higher hydrogen generation rates than bare $TiO_2$ under UV–vis light (**Figure 3-6a**). The hydrogen generation rate for bare $TiO_2$ was 77.5 μmol $g^{-1}$ $h^{-1}$. The hydrogen generation rates for monometallic samples 0.1, 0.5, and 0.9 wt% Au/$TiO_2$ were 482.6, 534.4, and 788.6 μmol $g^{-1}$ $h^{-1}$, respectively. For 0.05, 0.1, 0.5, and 0.9 wt% Pd/$TiO_2$ metallic samples were 182.9, 1468.2, 1142.0, and 946.4 μmol $g^{-1}$ $h^{-1}$, respectively. The higher hydrogen generation rates of monometallic samples than bare $TiO_2$ are attributed to the work function: metals with higher work functions such as Pd (5.3 eV) and Au (5.1 eV) than the electron affinity of $TiO_2$ (4.0 eV) increase the Schottky barrier effect.[144] The Schottky barrier is formed due to the interface contact between Au and Pd NPs (metallic system) and $TiO_2$ (semiconductor system).[145] The Schottky contact creates an internal electric field

helping the electron–hole transfer and inhibiting the recombination process, which is confirmed by TRMC results (**Figure 3-4a**,**b**). Most importantly, **Figure 3-6a** shows higher hydrogen generation rates for bimetallic samples AuPd/$TiO_2$ compared with their monometallic counterparts. The hydrogen generation rates for 1wt%$Au_1Pd_9/TiO_2$,1 wt%$Au_1Pd_1/TiO_2$, and 1 wt%$Au_9Pd_1/TiO_2$ were 1534.6, 1822.2, and 2325.0 $\mu molg^{-1}h^{-1}$, respectively. The hydrogen generation increases with the Au/Pd ratio (1wt% $Au_9Pd_1/TiO_2$ > 1wt% $Au_1Pd_1/TiO_2$ >1wt% $Au_1Pd_9/TiO_2$). The sample 1wt% $Au_9Pd_1/TiO_2$ shows the highest activity with 2325.0 $\mu molg^{-1}h^{-1}$, which is 30 times higher than bare $TiO_2$ (77.5 $\mu molg^{-1}h^{-1}$). The photocatalytic activity enhancement of the samples can be explained through their morphology, optical properties, crystallinity, and charge-carrier dynamics. TEM images showed smaller AuPd NPs on $TiO_2$ surface for 1 wt% $Au_9Pd_1/TiO_2$ sample (**Figure 3-1e**) than 1 wt% $Au_1Pd_1/TiO_2$ and 1 wt% $Au_1Pd_9/TiO_2$ samples. Smaller NPs have higher work function than larger NPs improving the Schottky barrier effect and therefore reducing the charge-carrier recombination. [6,,144,145] TRMC results confirm that the AuPd nanoalloys are efficient in electron scavenging reducing charge-carrier recombinations and raising the photocatalytic activity under UV light excitation (**Figure 3-4c**). The decay increases when the $TiO_2$ surface is modified with AuPd nanoalloys. The reactive surface sites are well dispersed on the titania surface scavenging electrons in the CB of $TiO_2$ (which reduce $H^+$) inhibiting the charge-carrier recombination, reducing and promoting the recombination of hydrogen atoms, and therefore raising the photocatalytic activity.

The photocatalytic hydrogen generation for mono- and bi-metallic samples under visible light is shown in **Figure 3-6b**. As previously stated, $TiO_2$ is not active under visible light. Pd/$TiO_2$ samples show negligible values for hydrogen generation under visible light. Pd NPs do not modify the spectra of $TiO_2$ in the visible region due to their LSPR in the UV region (**Figure 3-3a**).[102,146] Moreover, Au/$TiO_2$ samples show photocatalytic activity under visible light due to their LSPR (**Figure 3-3b**). The hydrogen rates for 0.1, 0.5, and 0.9 wt% Au/$TiO_2$ samples were 2.4, 2.5, and 5.7 $\mu molg^{-1}h^{-1}$, respectively. Previous studies have shown that hot electrons can be

injected from Au NPs into the CB of $TiO_2$ under visible irradiation. [6,] However, in our case, at 420 nm (Figure S3-4a, Annex I) no signal was higher than the signal obtained with bare $TiO_2$. At 550 nm (Figure S3-5a, Annex I), no detectable TRMC signals were obtained with $Au/TiO_2$ photocatalysts. This can be explained because the electron transfer is quite fast, and even if TRMC technique allows to obtain a signal at nanosecond scale, we cannot define the 10 first nanoseconds during the pulse. The bimetallic samples $AuPd/TiO_2$ show higher hydrogen generation rates than the monometallic counterparts under visible light. The hydrogen generation rates for 1 wt% $Au_1Pd_9/TiO_2$, 1 wt% $Au_1Pd_1/TiO_2$, and 1 wt% $Au_9Pd_1/TiO_2$ were 3.9, 8.5, and 13.0 $\mu molg^{-1}h^{-1}$, respectively. The optical properties were improved with higher Au/Pd ratio (1 wt% $Au_9Pd_1/TiO_2$) showing an intense and continuous absorption over the entire visible region (**Figure 3-3c**). Nevertheless, the same case occurs for bimetallic samples, no signal was higher than the signal obtained with $TiO_2$ at 420 nm (Figure S3-4c, Annex I). At 550 nm (Figure S3-5c, Annex I), no detectable TRMC signals were found. The photocatalytic activity under visible light suggests that hot electrons from Au NPs (in $Au/TiO_2$ and $AuPd/TiO_2$ samples) were injected into the CB of $TiO_2$ due to the activation of Au-LSPR after visible excitation. Finally, decreasing the metal loading is important for large scale hydrogen production due to the high cost of Au and Pd.

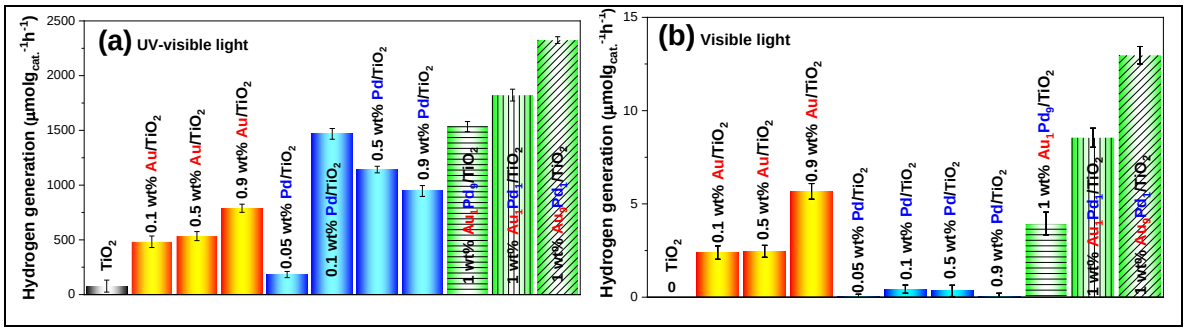


**Figure 3-6. (a,b)** Photocatalytic hydrogen generation for mono- and bi-metallic photocatalysts and bare $TiO_2$ from 25 vol% TEOA aqueous solution under **(a)** UV–vis and **(b)** visible light.

The photocatalysts 0.1, 0.2, and 0.5 wt% $AuPd/TiO_2$ with mass ratios of Au:Pd (1:9, 1:1, 9:1) were tested under UV–vis light (**Figure 3-7**). The samples demonstrate

similar activity as 1 wt% AuPd/$TiO_2$ samples. The hydrogen generation increases with the ratio Au/Pd ($Au_9Pd_1/TiO_2$ > $Au_1Pd_1/TiO_2$ > $Au_1Pd_9/TiO_2$) for all the metal loadings. **Figure 3-8** presents a comparison between our optimal sample 0.5 wt% $Au_9Pd_1/TiO_2$ and 1 wt% Pt/$TiO_2$ (our sample benchmark with high photocatalytic activity; the Pt NPs are about 1 nm size and are well dispersed on $TiO_2$ surface), revealing quite similar (or slightly lower) photocatalytic activities. As we mentioned earlier, Pt is the best cocatalyst for photocatalytic hydrogen generation. Nevertheless, because of its high cost and limited abundance, replacing it with other more abundant metals is important. Table S3-3, Annex I, compares the photocatalytic hydrogen generation under UV–vis light irradiation with data from the literature. The comparison reveals notable differences in the efficiency of different catalysts under distinct conditions. However, compared to other reported studies, our work shows good photocatalytic activity under UV–vis radiation and a slight activity under visible light. Luna et al. obtained synergistic effects with bimetallic Au–Ni and Ni–Pd NPs for hydrogen generation.[8, 15] Also, Su et al. reported strong synergistic effects with 1 wt% $Pd_{shell}Au_{core}/TiO_2$ for photocatalytic hydrogen generation with a specific wavelength at 365 nm (UV LED) using a variety of important feedstock chemicals. Nevertheless, they did not show any activity under visible light.[19]

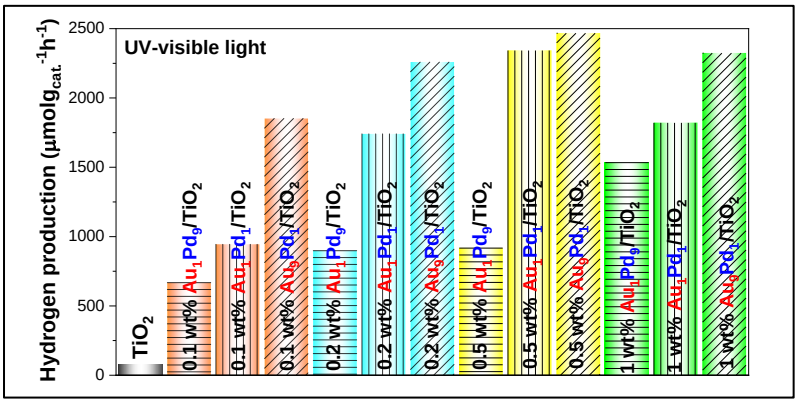


**Figure 3-7.** Photocatalytic hydrogen generation of bimetallic photocatalysts with metal loadings of 0.1, 0.2, 0.5, and 1 wt% AuPd/$TiO_2$ with mass ratios of Au:Pd (1:9, 1:1, 9:1) and bare $TiO_2$ from 25 vol% TEOA aqueous solution under UV–vis light irradiation.

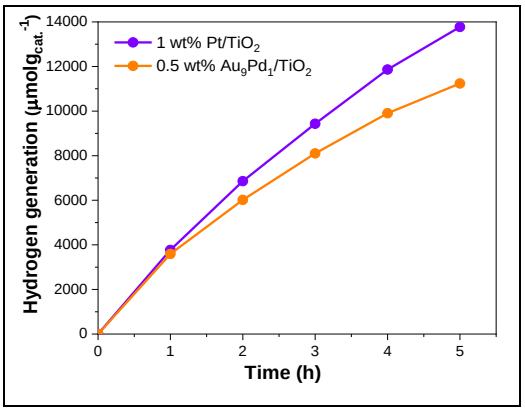


**Figure 3-8.** Comparison of the photocatalytic hydrogen generation of 0.5 wt% $Au_9Pd_1/TiO_2$ with 1 wt% $Pt/TiO_2$ from 25 vol% TEOA aqueous solution under UV–vis light irradiation.

### 3.2.3 DFT Calculations

Density Functional Theory (DFT) and Density Functional Tight Binding (DFTB+) calculations is a collaboration between France and Mexico. Dr. Carine Clavaguéra from *Institut de Chimie Physique* did DFT calculations and Dr. Juan Pedro Palomares Báez from *Universidad Autónoma de Chihuahua* performed DFTB+ calculations. These calculations were used to improve the understanding of the higher hydrogenation rates in the case of bimetallic systems.

DFT is a powerful quantum mechanical method used in computational chemistry and materials science. DFT calculations can predict experimental results with confident results about the electronic structure and bond strengths of atoms, molecules, and solids. DFT is widely used in chemistry, physics, and materials science to study molecular structures, bonding, and reaction mechanisms; electronic properties of materials like band structures; and catalysis, including surface reactions and adsorption.

In this work, the adsorption of two hydrogen atoms on a model of Au NP and $Au_9Pd_1$ NP was investigated at the DFT and DFTB+ quantum levels (see Methods and Annex I for computational details). First, for DFT calculations, the optimized geometries show a different adsorption mode on the metal surface, with each H atom

remaining on one Au for Au NP, and with one H atom on gold and the other H shared between the Pd and the neighboring gold atoms ("Au–H–Pd") for $Au_9Pd_1$ NP (see **Figure 3-9**). This structural change corresponds to different bond lengths, resulting in different electronic effects (Table S3-5, Annex I). The Au–Pd and Au–Au bond lengths around the shared H in the bimetallic cluster are shorter than Au–Au distances in Au NP. In addition, the Au–H and Pd–H distances are longer in $Au_9Pd_1$ NP for the shared H atom, leading to a weaker hydrogen adsorption strength. The analysis of the electron density shows Au–H and Pd–H bonds with a valence electronic population basin of 1.7 electron and 1.6 electron for Au–H and Au–H–Pd, respectively. The strength of the bond was evaluated to be close to a single covalent bond with a Mayer bond order of 0.86 for Au–H in Au NP, and much weaker with a Mayer bond order of 0.37 for Au–H–Pd in $Au_9Pd_1$ NP. This lower hydrogen atom adsorption strength for the bimetallic system may be one explanation for the higher reactivity.

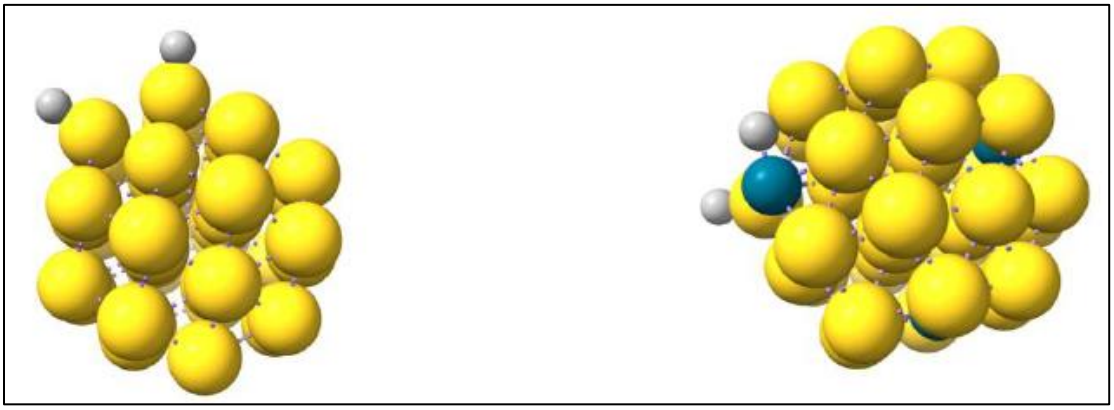

**Figure 3-9.** Optimized geometries of $Au_{38}$-$H_2$ and $Au_{34}Pd_4$-$H_2$ clusters at the DFT/PBE-D3BJ level. Colors: Au in yellow, Pd in turquoise blue, H in grey.

### 3.2.4 DFTB+ Calculations

By DFTB+ using the GFN1-xTB parameterization, we performed molecular dynamics simulations of H atoms with many different arrays (as described in Annex I) over the surface of optimized clusters (N= 38 atoms, with cuboctahedral shape)

for the three $Au_9Pd_1$, $Au_1Pd_1$, and $Au_1Pd_9$ alloys. The systems were brought to a temperature of 298 K and then left at constant temperature during 20 picoseconds, and the main results are hereby briefly presented. The case of $Au_9Pd_1$ was the only system that led to the formation of $H_2$, while for none (among 11 systems built) of the systems in the $Au_1Pd_9$ case did the formation of $H_2$ occur. According to previous DFT results, it seems that when the amount of Pd is higher, the hydrogen atoms are strongly attracted to Pd, and thus their movement is restricted. For the case of $Au_1Pd_1$, the formation of $H_2$ also occurs for one system (among 9 built); however, we notice that the inclusion of H in these 1:1 systems seems to destabilize them (even more than the obtained structures after the energy optimization process) because most of the calculated systems end up suffering a considerable deformation of the NP. More details are given in the Annex I.
https://drive.google.com/drive/folders/1nS_WD9IJdnMFSiFBE7fSi9PQYSoJ5KsA?usp=sharing

### 3.2.5 Proposed Photocatalytic Mechanism

Charge-carrier dynamics, which is a key factor in photocatalysis, was studied by TRMC.[6,9,15,51,68,118] At 360 nm excitation, the mono- and bi-metallic systems and bare $TiO_2$ are activated meaning that electrons migrate to the CB of $TiO_2$, reaching $I_{max}$ values. Moreover, when the surface of $TiO_2$ is modified with mono- and bi-metallic NPs, the $I_{max}$ value decreases compared with bare $TiO_2$ (**Figure 3-4**). This indicates that the metal NPs act as electron traps, inhibiting the charge-carrier recombination. The electron migration from CB of $TiO_2$ to the metal NPs occurs due to the work function and Schottky junction, which creates an internal electric field helping the electron–hole transfer and inhibiting the recombination process.[147,148] **Figure 3-10a** shows a scheme of the photocatalytic mechanism under UV light excitation for bimetallic AuPd/$TiO_2$ sample.

$$TiO_2 \xrightarrow{h\nu > E_g} TiO_2(e^-_{CB} + h^+_{VB}) \quad (3)$$

$$H_2O + e^- \rightarrow H_2 + OH^- \quad (4)$$

$$H^+ + e^- \rightarrow H^\bullet \quad (5)$$

$$H^\bullet + H^\bullet \rightarrow H_2 \quad (6)$$

At 420 nm excitation, hot electrons are injected from AuPd nanoalloys to the CB of $TiO_2$ due to the Au-LSPR excitation.[6] Water molecules or $H^+$ are reduced on the $TiO_2$ surface by the electrons to produce $H_2$ (**Figure 3-10b**), as we mentioned before. Finally, to inhibit the oxidation reaction generated by the photogenerated holes in the VB of $TiO_2$ and AuPd NPs, an electron donor was used (TEOA in our study), which scavenges the holes to generate $H_2$ (Equation 7–10).[149] TEOA can self-sustain the photocatalytic hydrogen generation process, which can be obtained from industrial organic effluents related to dry cleaning, cosmetics, shampoos, detergents, surfactants, textiles, and water repellents.[149]

$$TiO_2(h^+) + OH^- \rightarrow OH^\bullet \quad (7)$$

$$TiO_2(h^+) + H_2O \rightarrow OH^\bullet + H^+ \quad (8)$$

$$TEOA + OH^\bullet \rightarrow HCHO + NH_3 \quad (9)$$

$$HCHO + OH^\bullet \rightarrow H_2 \quad (10)$$

### 2.3.6 Stability with cycling

Finally, the photocatalyst stability was investigated for the 0.5 wt %$Au_9Pd_1/TiO_2$ sample, which demonstrated a stable photocatalytic activity with a slight decrease with cycling (**Figure 3-11**). The dispersion of AuPd nanoalloys, morphology, size, and crystalline structure were analyzed before and after cycling (Figure S3-6, Annex I). TEM images in dark field show the AuPd NPs well dispersed on the $TiO_2$ surface before and after cycling (Figure S3-6a,d). HAADF-STEM micrographs show that the AuPd nanoalloys are quite stable after cycling, showing brighter tiny points corresponding to Au due to its highest atomic number and less brightness tiny spots

corresponding to Pd (Figure S3-6b,e, Annex I). The interplanar distance of 0.23 nm corresponds to (111) plane of Au (Figure S3-6c, Annex I). and the one of 0.2 nm corresponds to the plane (200) of Au (Figure S3-6f, Annex I). The interplanar distances of 0.18 nm (Figure S3-6c,f, Annex I) and 0.16 nm (Figure S3-6c, Annex I) can be assigned to (200) and (211) planes of the anatase phase (JCPDS No. 21-1272), respectively. However, the AuPd NPs size increases from 2.5–2.7 to 3.0–3.2 nm after cycling (Figure S3-6g, Annex I). This metal NPs' sintering probably explains the slight decrease in photocatalytic hydrogen generation due to larger NPs decreasing the work function and diminishing the Schottky barrier effect, increasing charge-carrier recombination. The surface chemical composition and oxidation states of AuPd nanoalloys on the $TiO_2$ surface were analyzed by XPS after cycling. The comparison of the XPS spectra for 0.5 wt% AuPd/$TiO_2$ sample before and after cycling for Au 4f and Pd 3d states is shown in Figure S3-6h,i, Annex I, respectively. After cycling, the XPS spectra are noisy compared to those before cycling. This can be attributed to metal loss after recovering the powder by centrifugation.

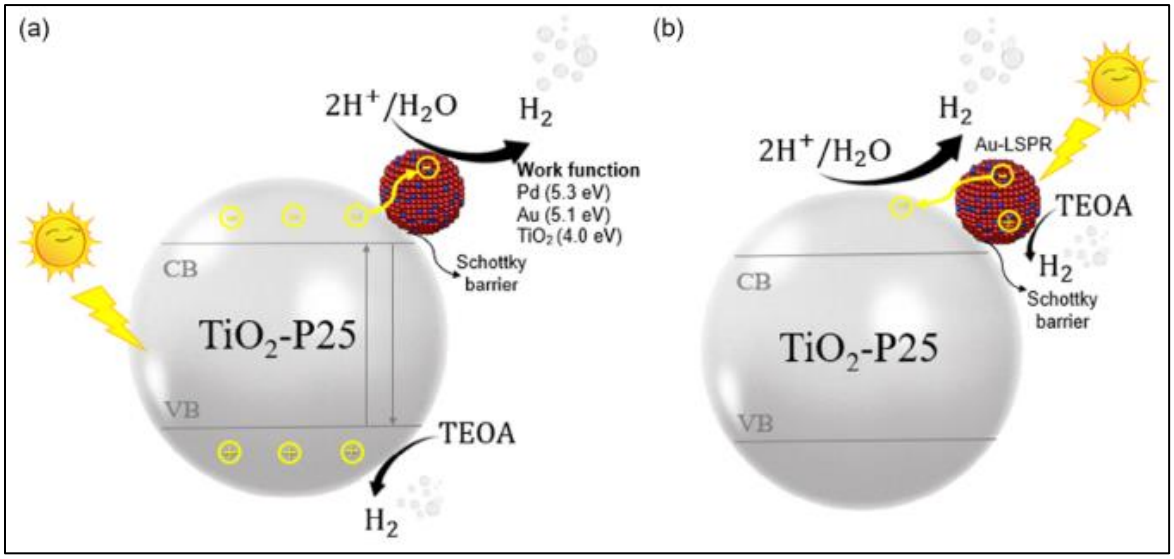


**Figure 3-10.** Proposed photocatalytic mechanism of bimetallic AuPd/$TiO_2$ samples under **(a)** UV and **(b)** visible light irradiation.

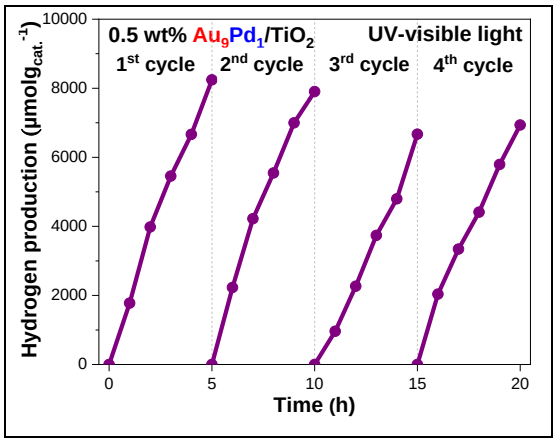


**Figure 3-11.** The photocatalyst stability of 0.5 wt% $Au_9Pd_1/TiO_2$ sample from 25 vol% TEOA aqueous solution under UV–vis light irradiation.

## 3.3 Conclusion

In summary, AuPd nanoalloys homogeneous in size (2.5–3 nm) were deposited on the $TiO_2$ surface by chemical reduction method using $NaBH_4$ at room temperature. The AuPd nanoalloys formation was confirmed by HAADF-STEM and hybrid MD–MC calculations validated this alloy structure. Synergetic effects were obtained with the AuPd nanoalloys: the bimetallic AuPd/$TiO_2$ samples show higher photocatalytic activity for $H_2$ generation under UV–vis light irradiation compared with their monometallic counterparts. The photocatalytic hydrogen generation enhancement of bimetallic samples was explained through their morphology, optical properties, crystallinity, charge carrier dynamics, electronic structure (DFT), and molecular dynamics (DFTB+) calculations. The $Au_9Pd_1/TiO_2$ sample is the most active and it is quite stable with cycling, with a slight decrease in hydrogen generation. TRMC results demonstrated that the surface modification of $TiO_2$ with bimetallic AuPd nanoalloys (electron traps) plays a role in charge carrier separations increasing the activity under UV light irradiation. AuPd nanoalloys can be used as efficient cocatalysts for hydrogen generation with an activity comparable with that of Pt cocatalysts.

# Chapter 4

NiO/$TiO_2$ *p-n* Heterojunction Induced by Radiolysis for Photocatalytic Hydrogen Generation

# Chapter 4. $NiO/TiO_2$ *p-n* Heterojunction Induced by Radiolysis for Photocatalytic Hydrogen Generation

## 4.1 Introduction

The high cost and scarcity of noble metals restrict their practical applications, and therefore, there is a growing need to replace noble metals with abundant and cost-effective alternatives, such as transition metals. Earth-abundant metals such as nickel (Ni)-based cocatalysts are ideal candidates in photocatalysis due to their low cost and effectiveness.[83,84] Ni-based nanoparticles such as metallic nickel ($Ni^0$), nickel oxide (NiO)[15,85,86,87] and nickel hydroxide $Ni(OH)_2$ nanoparticles,[88,89] are highly active cocatalysts when integrated with $TiO_2$ semiconductor for photocatalytic $H_2$ production.[90] It has been observed that $Ni^0$-NPs can be present at the interphase between deposited NiO-NPs and $TiO_2$ support and lead to the formation of an Ohmic junction with titania, facilitating the migration of photogenerated electrons to the metal.[9, 8] NiO is a *p*-type semiconductor with a band gap of about 3.5 eV,[76,77,78,79] thus a *p-n* heterojunction is formed with $TiO_2$ creating an internal electric field that reduces charge carriers' recombination and facilitates interfacial charge transfer.[76,9,80,81,82] This *p-n* heterojunction plays a vital role in enhancing the photocatalytic activity of $TiO_2$ under UV-vis light irradiation.

Thus, innovative materials like $NiO/TiO_2$ composites could play a crucial role in this green energy transition by enhancing the efficiency and feasibility of renewable energy technologies. Recent studies have demonstrated that $NiO/TiO_2$ composites exhibit superior performance in various applications, such as hydrogen production through water splitting, degradation of organic pollutants, and $CO_2$ reduction. Beyond these, $NiO/TiO_2$ composites are increasingly being explored for a vast set of applications in contemporary industries, including energy generation by enhancing the efficiency of photovoltaic cells to improve solar energy conversion rates; in energy storage by developing advanced batteries and supercapacitors with higher capacity, longer lifespan, and faster charge-discharge cycles; as well as in

environmental remediation by efficiently degrading harmful pollutants in air and water, and therefore contributing to cleaner environments. Industries ranging from automotive to consumer electronics are applying these advanced materials to drive innovation and improve product performance. For example, in the transportation sector, the development of NiO/$TiO_2$-based materials can lead to more efficient fuel cells and batteries, directly impacting the efficiency and sustainability of electric and hybrid vehicles. In energy storage, the integration of these materials into batteries and supercapacitors promises significant advancements in storage capacity and energy density, which are crucial for both consumer electronics and grid-scale energy solutions. Also, sensors and electronics technologies will benefit by creating more sensitive and accurate sensors for detecting gases and other environmental challenges.

In this work, the $TiO_2$ (commercial Degussa-P25) surface has been modified with Ni-based NPs induced by radiolytic reduction of two different salt precursors, nickel (II) acetylacetonate and nickel (II) formate. Radiolytic reduction leads to very homogeneous deposition of Ni-based nanoparticles on $TiO_2$, and a better NPs deposition is obtained with nickel (II) acetylacetonate precursor. The choice of the metal salt precursor used for surface modification of $TiO_2$ is essential to design efficient photocatalysts, thus through a comprehensive analysis of the material's structural, optical, and electronic properties, we seek to elucidate the mechanisms underpinning the improved performance of NiO/$TiO_2$ composites. When combined with $TiO_2$, NiO can significantly improve the composite's overall efficiency by enhancing charge separation, reducing recombination rates, and extending light absorption into the visible region. These improvements arise from the synergistic interactions between NiO and $TiO_2$, which facilitate the better use of wider solar spectrum range and improved electron-hole pair dynamics, resulting in a good photocatalytic activity for hydrogen production under UV-visible light.

## 4.2 Results and Discussion

### 4.2.1 Characterization of the Photocatalysts

The morphology, particle size, and dispersion of Ni-based NPs on $TiO_2$ surface were examined by TEM. The Ni-based NPs were difficult to observe by TEM due to the alikeness in the atomic number of Ni and Ti. TEM images show that the reduction of nickel (II) acetylacetonate precursor by radiolysis led to nanoparticles of about 8 nm for 3.5 wt. % $Ni_{acac}$-based NPs/$TiO_2$ sample as illustrated in **Figure 4-1a**. However, with Ni formate as precursor, the Ni-based NPs are not distinguishable by TEM for 3.5 wt.% $Ni_{formate}$-based NPs/$TiO_2$ sample (Figure S4-1a, Annex II), which can be due to the small size of the NPs and the low metal loading. The crystal structure was analyzed by HRTEM for 3.5 wt.% $Ni_{acac}$-based NPs/$TiO_2$ sample (**Figure 4-1b**). The analysis revealed interplanar distances of 0.23 nm and 0.35 nm, corresponding to the lattice planes of NiO (111), and the anatase $TiO_2$ (101), respectively.[9,150] This result confirms the *p-n* heterojunction formation between NiO-NPs and $TiO_2$ support. The NiO-NPs are formed by back oxidation of the $Ni^0$-NPs (induced by radiolysis) when exposed to air during drying. Instead*, the crystalline structure of Ni-based NPs was not detected* for 3.5 wt.% $Ni_{formate}$-based NPs/$TiO_2$ sample due to the small size of Ni-based NPs *(*Figure S4-1b, Annex II)*.* Only an interplanar distance of 0.35 nm, corresponding to the anatase phase of $TiO_2$ (101) was observed.

*EELS was used to* reveal the presence of Ni and its oxidation states. **Figure 4-1c** displays the Ni-$L_2$ and Ni-$L_3$ edges at energy levels of 872 eV and 855 eV, respectively, for the 3.5 wt.% $Ni_{acac}$-based NPs/$TiO_2$ sample. These edges are associated with the $Ni^{2+}$ oxidation state.[151] The appearance of the $L_{2,3}$ ionization edges of nickel is attributed to the transitions of excited inner $p_{1/2}$ ($L_2$ edge) and $p_{3/2}$ ($L_3$ edge) electrons to the empty valence states of *s* and *d* character.[152,153] In the case of the 3.5 wt.% $Ni_{formate}$-based NPs/$TiO_2$ sample (Figure S4-1c, Annex II), no peak corresponding to Ni-$L_2$ and Ni-$L_3$ edges was observed. ICP-OES was used for

elemental analysis, providing insights into the mass content of Ni on $TiO_2$ surface. For 3.5 wt.% $Ni_{acac}$-based NPs/$TiO_2$ and 3.5 wt.% $Ni_{formate}$-based NPs/$TiO_2$ samples, the metal content is 1.30 wt% and 0.13 wt%, respectively. This result confirms that the nickel (II) acetylacetonate precursor is better than nickel (II) formate for Ni-based NPs deposition on the $TiO_2$ surface by radiolysis.

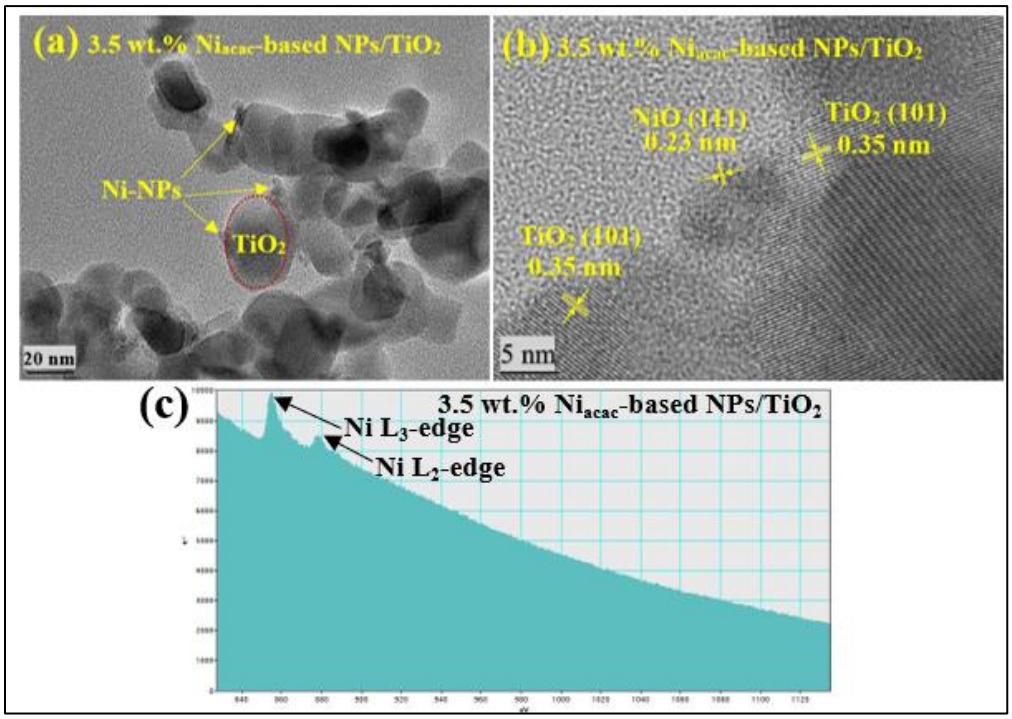


**Figure 4-1. (a)** TEM micrograph, **(b)** HRTEM micrograph, and **(c)** EELS spectrum of 3.5 wt.% $Ni_{acac}$-based NPs/$TiO_2$ modified sample.

The optical properties of the modified photocatalysts and bare $TiO_2$ were investigated by DRS. All samples exhibited strong absorption in the 200-400 nm range, attributed to the $TiO_2$ support (**Figure 4-2a** and S4-2a, Annex II). The modified samples showed a small redshift of the band edge compared to bare $TiO_2$. The absorption in the visible region can be linked to d–d transitions of $Ni^{2+}$, [8,89,154,155,156] $Ni^0$-NPs being sensitive to oxygen.

Band gap energies were calculated using the Tauc plot method for the modified samples and bare $TiO_2$, considering the indirect transition of anatase-phase $TiO_2$.

[50,157] **Figure 4-2b** shows the calculated band gap energies for bare $TiO_2$ (3.26 eV), 0.1 (3.20 eV), 0.5 (3.20 eV), 1.0 (3.18 eV), and 3.5 (3.18 eV) wt.% $Ni_{acac}$-based-NPs/$TiO_2$ samples, respectively. Similarly, Figure S4-2b, Annex II, shows the band gap energies of bare $TiO_2$ (3.26 eV), 0.1 (3.26 eV), 0.5 (3.26 eV), 1.0 (3.26 eV), and 3.5 (3.18 eV) wt.% $Ni_{formate}$-based NPs/$TiO_2$ samples, respectively. There is a slight reduction in the band gap energy for $Ni_{acac}$-modified samples due to the higher content of Ni-based NPs deposited on the $TiO_2$ surface, compared with $Ni_{formate}$-modified samples. It is worth to notice from **Figure 4-2a** that NiO-NPs exhibit absorption in the visible region.[8,155,156]

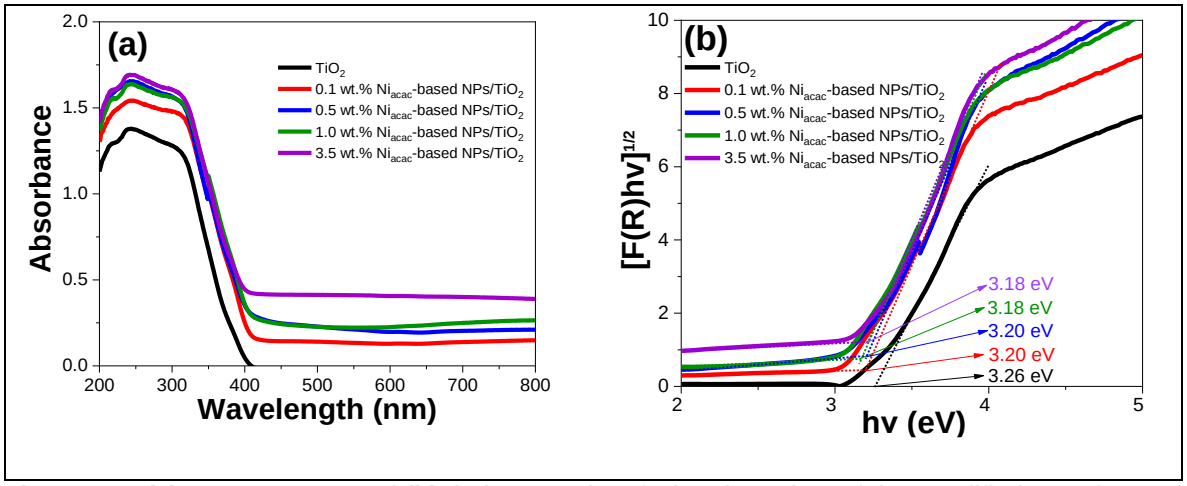


**Figure 4-2. (a)** DRS spectra, and **(b)** their Tauc plot of $Ni_{acac}$-based NPs/$TiO_2$ modified samples and bare $TiO_2$.

XRD analysis was used to study the crystalline structure of the samples (**Figure 4-3** and Figure S4-3, Annex II). The diffracted peaks of the samples coincide with the reference peaks of the anatase and rutile crystalline phases, according to the data JCPDS files No. 21-1272 and No. 21-1276, respectively. No diffracted peaks corresponding to the Ni-based NPs crystalline phases were observed. This observation is consistent with previous studies where researchers also reported the absence of nickel peaks due to the low adsorbed nickel content and very small size of Ni-based NPs.[89,81,154] Moreover, no shifts in diffraction peaks were observed for the Ni-based NPs/$TiO_2$ modified samples. This suggests that the presence of Ni-

based-NPs does not alter the lattice structure of $TiO_2$ and that they are solely absorbed on the $TiO_2$ surface.[154]

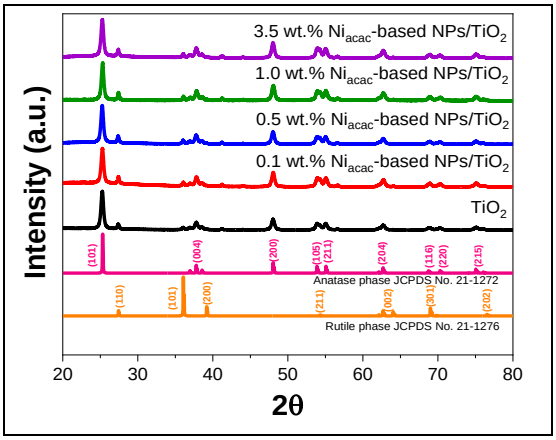


**Figure 4-3.** XRD pattern of $Ni_{acac}$-based NPs/$TiO_2$ modified samples and bare $TiO_2$ with the reference peaks of the anatase and rutile crystalline phases.

The surface chemical composition and oxidation states of Ni-based NPs on the $TiO_2$ surface were analyzed using XPS. The XPS survey for 3.5 wt.% $Ni_{acac}$-based NPs/$TiO_2$ sample shows the peaks corresponding to Ni, Ti, O, and C, indicating the presence of these elements on the modified sample surface, see Figure S4-4a, Annex II. However, in the case of the 3.5 wt.% $Ni_{formate}$-based NPs/$TiO_2$ sample, only peaks for Ti, O, and C were detected (Figure S4-4b, Annex II). The absence of Ni peaks in the latter sample is due to the low content of Ni-based NPs on the $TiO_2$ surface, as determined by ICP-OES. The narrow scan XPS spectra of the 3.5 wt.% $Ni_{acac}$-based NPs/$TiO_2$ sample were analyzed for Ni *2p*, Ti *2p*, O *1s*, and C *1s* (**Figure 4-4a**, **4-4b**, **4-4c**, and **4-4d**), respectively. The Ni*2p* signal was fitted using line shapes derived from $Ni^0$, NiO, and $Ni(OH)_2$ well characterized references. A Shirley-type background was subtracted from all spectra. The Ni*2p* signal shows contributions coming from $Ni^0$ (852.5 eV), NiO (853.8 eV), and $Ni(OH)_2$ (855.9 eV) on the $TiO_2$ surface (**Figure 4-4a)**. The Ni (II) complexes have been reduced by radiolysis, leading to $Ni^0$-NPs on titania. However, these small NPs are sensitive to air and are back oxidized when exposed to air, which explains why the oxidized species are the main components of the Ni 2p core-level spectrum. The $Ni^0$-NPs are

expected to be located at the interphase between NiO-NPs and $TiO_2$, forming an Ohmic junction.[9] In the Ti *2p* core level spectrum (**Figure 4-4b**), two symmetric peaks were observed at 458.7 eV and 464.5 eV, representing Ti $2p_{3/2}$ and Ti $2p_{1/2}$ respectively, which are the spin-orbit coupling components.[89,77] The O *1s* XPS spectrum (**Figure 4-4c**) displayed an asymmetric peak attributed to adsorbed hydroxide species.[77] The O *1s* spectrum showed two peaks at 530.0 eV and 531.2 eV, corresponding to the lattice oxygen of anatase $TiO_2$ and hydroxyl species, respectively.[82,158] The C *1s* spectrum (**Figure 4-4d**) showed the peaks at 284.8 eV, 286.0 eV, and 288.8 eV correspond to C-C, C-O, and C=O, respectively, attributed to carbon pollution.[159]

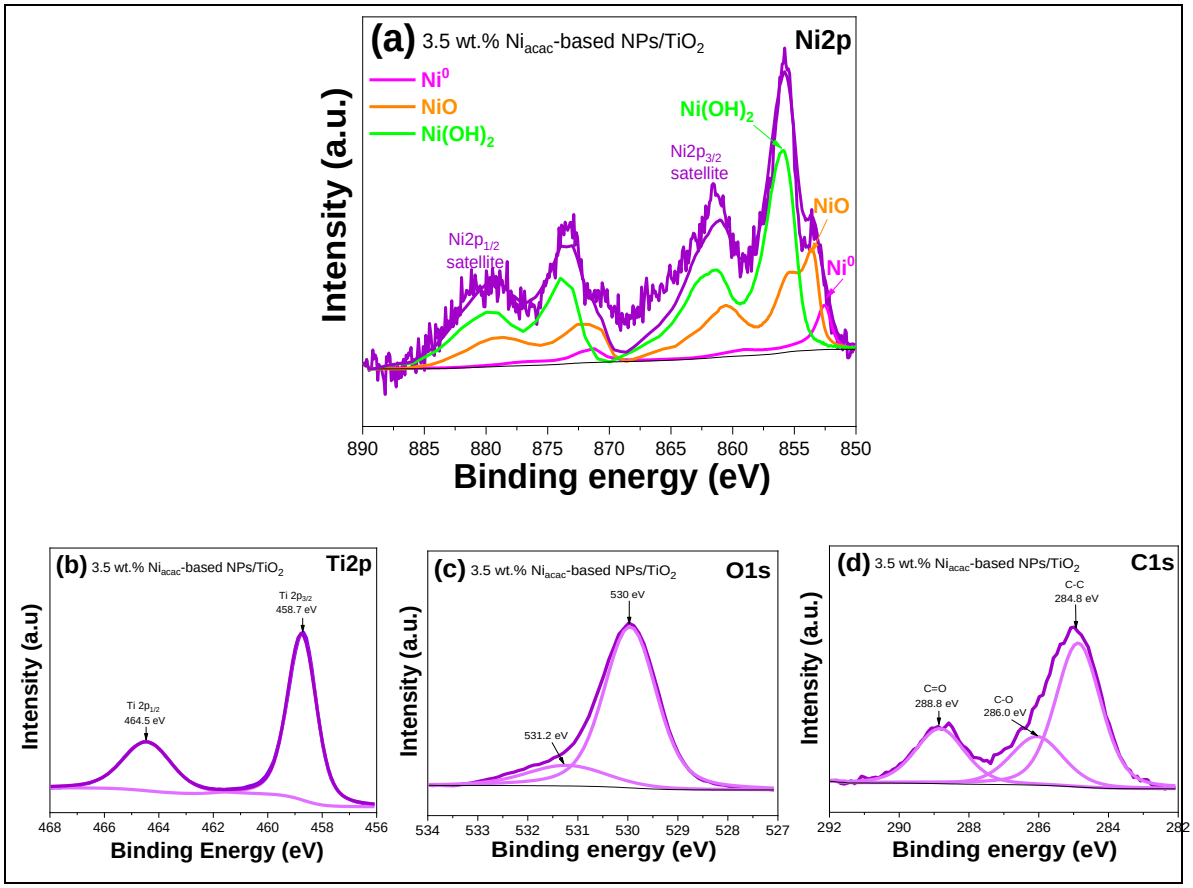


**Figure 4-4.** Narrow scan XPS spectra of **(a)** Ni *2p*, **(b)** Ti *2p*, **(c)** O *1s*, and **(d)** C *1s* of 3.5wt% $Ni_{acac}$-based NPs/$TiO_2$ modified sample.

TRMC signals highlight the significant impact of Ni-based NPs surface modification of $TiO_2$ on the charge carriers' dynamics under UV and visible light excitation (**Figure 4-5** and Figure S4-5, Annex II). Just after the signal pulse, all samples reached $I_{max}$ values, indicating the electron transfer from the VB to the CB of $TiO_2$. Simultaneously, NiO with a bandgap of 3.5 eV is also excited and electron transfer occurs from the VB of NiO to its CB.[9, 8,160] Subsequently, faster decays and reduced $I_{max}$ values were observed for the modified samples compared to bare $TiO_2$ (**Figure 4-5a** and S4-5a, Annex II). The electron transfer from $TiO_2$ to NiO-NPs is not thermodynamically allowed due to their higher position of CB level of NiO compared to the anatase phase $TiO_2$.[15] However, XPS results revealed a trace amount of $Ni^0$ leading to the formation of an Ohmic junction with $TiO_2$. It is anticipated that these $Ni^0$-NPs are located within the interphase between NiO-NPs and $TiO_2$, facilitating the migration of photogenerated electrons to the metal.[9, 8] The TRMC results provide strong evidence that $Ni^0$-NPs effectively scavenge electrons from the CB of $TiO_2$, which is beneficial for the photocatalytic activity. [51,6,72] Simultaneously, the holes that accumulate on the VB of $TiO_2$ will be transferred to the VB of NiO, enabling the effective separation of the charge carriers.[161] For samples modified with nickel (II) acetylacetonate, the decay of signals is faster than nickel (II) formate salt precursor, and this signal decay is faster with increasing the metal loading (**Figure 4-5a**). The 3.5 wt.% $Ni_{acac}$-based NPs/$TiO_2$ sample exhibits the fastest decay rate among the metal loadings (0.1, 0.5, and 1 wt.%). For the samples modified with formate precursor, only small amount of Ni is deposited on $TiO_2$ surface, However, surface modification of titania induces a decay in the TRMC signals (Figure S4-5a, Annex II).

Furthermore, for the surface-modified titania samples, detectable TRMC signals were observed under visible light excitation at 420 nm (**Figure 4-5b** and S4-5b, Annex II). This suggests that NiO-NPs are excited by visible light due to the *d–d* transitions of $Ni^{2+}$.[89,154,155,156] The transfer of photogenerated electrons from the CB of NiO-NPs to the CB of $TiO_2$ is facilitated. For $Ni_{acac}$-modified samples, only 0.1 wt.% shows a detectable signal higher than bare $TiO_2$ (**Figure 4-5b)**. Nevertheless, for

0.5, 1.0, and 3.5 wt.% samples, no detectable TRMC signals were obtained. This can be explained because the electron transfer is quite fast, and even if the TRMC technique does allow us to obtain a signal at the nanosecond scale, we cannot define the 10 first nanoseconds during the pulse. In the case of $Ni_{formate}$-modified samples, all the loadings show higher signals than bare $TiO_2$ (Figure S4-5b, Annex II).

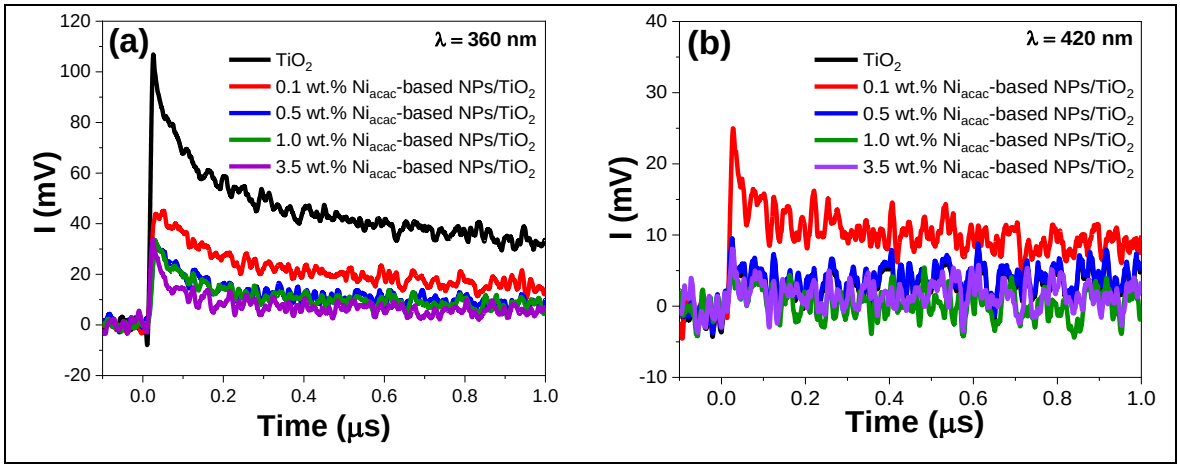


**Figure 4-5.** TRMC signals of $Ni_{acac}$-based NPs/$TiO_2$ modified samples and bare $TiO_2$ at different wavelengths **(a)** $\lambda_{exc}$ = 360 nm, and **(b)** $\lambda_{exc}$ = 420 nm. The laser energy at these wavelengths was 1.1 mJ and 2.3 mJ, respectively.

### 4.2.2 Photocatalytic Hydrogen Generation

The hydrogen generation is significantly enhanced when the $TiO_2$ surface is modified with Ni-based NPs (obtained by radiolysis) under UV-visible light, as shown in **Figure 4-6a**. Ni-based NPs act as active sites that promote hydrogen formation.[9,15,8,90] The *p-n* heterojunction formed between NiO-NPs and $TiO_2$ creates an internal electric field, which reduces charge carriers' recombination and facilitates interfacial charge transfer. The hydrogen generation rate of $TiO_2$ was 23.3 μmol $g_{cat.}^{-1}$ $h^{-1}$. The results demonstrate that $Ni_{acac}$-based NPs/$TiO_2$ samples with theoretical Ni loadings of 0.1, 0.5, 1.0, 3.5, and 5.0 wt.% on $TiO_2$ surface exhibit higher and notable increasingly hydrogen generation rates corresponding to 95.9, 287.8, 563.3, 998.4 and 897.2 $\mu mol g_{cat.}^{-1} h^{-1}$, respectively, as shown in **Figure 4-6b**. Notably, the most active sample was 3.5 wt.% $Ni_{acac}$-based NPs/$TiO_2$ (998.4 $\mu mol g_{cat.}^{-1} h^{-1}$) after 5 hours

of irradiation is 42 times higher than bare $TiO_2$ (23.3 µmol $g_{cat.}^{-1}$ $h^{-1}$). These results suggest that achieving the highest $H_2$ generation rates relies on optimal metal loading. This highlights the significance of carefully controlling the metal loading for optimal performance. However, the hydrogen generation rates with $Ni_{formate}$-based NPs/$TiO_2$ samples were much lower than $Ni_{acac}$-$TiO_2$ because of the very small amount of Ni deposited with Ni formate, see Figure S4-6b, Annex II. Indeed, the deposition of Ni-based NPs on $TiO_2$ is more effective with Ni acetylacetonate as precursor, as proved by ICP-OES results. The 3.5 wt.% $Ni_{acac}$-based NPs/$TiO_2$ and 3.5 wt.% $Ni_{formate}$-based NPs/$TiO_2$ samples were tested under visible light, showing a slight activity with hydrogen generation rates of 1.5 and 0.6 µmol $g_{cat.}^{-1}$ $h^{-1}$, respectively. The sample 0.1 wt.% $Ni_{acac}$-based NPs/$TiO_2$ shows a higher TRMC signal than bare $TiO_2$ (**Figure 4-5b**) under visible excitation, but the hydrogen generation rate (0.4 µmol $g_{cat.}^{-1}$ $h^{-1}$) was lower than 3.5 wt.% $Ni_{acac}$-based NPs/$TiO_2$. This can be due to the larger amount of NiO or NiOH and lower amount of metallic $Ni^0$ NPs, which can play the role of cocatalysts in the formation of H-H bonds leading to $H_2$.

Our results were compared with the literature on Ni-based NPs as cocatalysts on support semiconductors (Table S4-2, Annex II). The comparison reveals notable differences in the efficiency of different catalysts under distinct conditions. The hydrogen generation rate of our best sample 3.5 wt.% $Ni_{acac}$-based NPs/$TiO_2$ is 998.4 µmol$g_{cat.}^{-1}h^{-1}$, ~ 42-fold higher than bare $TiO_2$ NPs, under UV-visible light irradiation. For comparison purposes with other systems reported in the literature, $Ni(OH)_2/TiO_2$ nanotubes demonstrated a rate approximately 12 times higher than $TiO_2$,[89] and Ni/C/$TiO_2$ showed a rate 9 times higher than $TiO_2$.[162] It has been reported that NiO/CdS is active under visible light (Table S4-2, Annex II), CdS being a semiconductor with a small band gap of 2.42 eV.[163,164,165] However, CdS is a toxic compound and tends to corrosion under light irradiation, leading to harmful $Cd^{2+}$. For photocatalytic applications, it is essential to use non-toxic and stable supports.

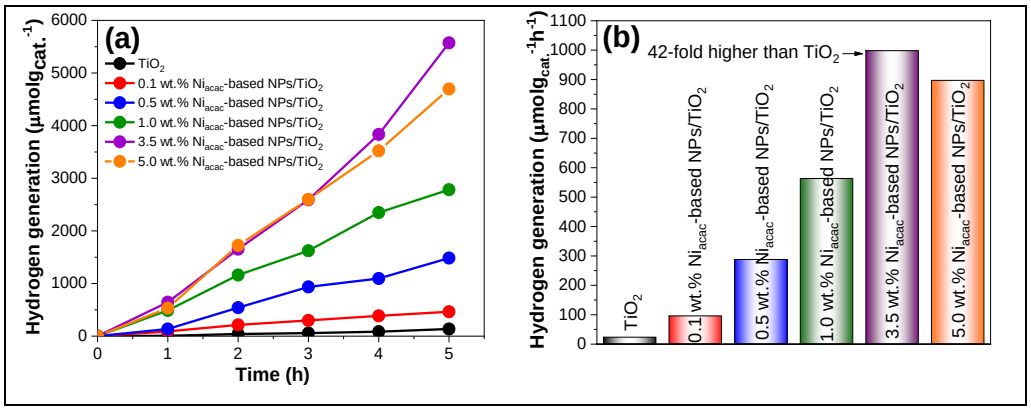


**Figure 4-6. (a)** Photocatalytic hydrogen generation for $Ni_{acac}$-based NPs/$TiO_2$ samples and bare $TiO_2$ under UV-visible light, and **(b)** their hydrogen generation rates ($\mu molg_{cat.}^{-1}h^{-1}$) under UV-visible light irradiation from 25% v/v methanol aqueous solution.

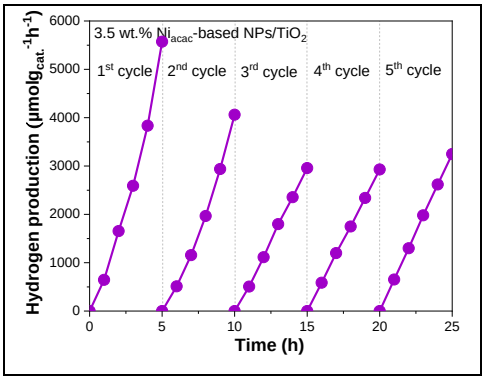


**Figure 4-7.** Photocatalyst stability with cycling for 3.5 wt.% $Ni_{acac}$-based NPs/$TiO_2$ sample under UV-visible light irradiation from 25% v/v methanol aqueous solution.

### 4.2.3 Stability with Cycling

Finally, the photocatalytic stability with cycling of the best sample 3.5 wt.% $Ni_{acac}$-based NPs/$TiO_2$ is studied and presented in **Figure 4-7**. The hydrogen generation decreases after the second cycle. This decrease can be due to leaching of nickel. Indeed, nickel leaching is known in the field of catalysis.[150,166,167] One way to avoid this leaching in catalysis is to alloy Ni with noble metals.[168,169] After the third cycle, a plateau is obtained, evidencing photocatalytic stability, which is crucial for practical applications. The surface chemical composition and oxidation states of Ni-based NPs on the $TiO_2$ surface were analyzed by XPS before and after cycling. The XPS

surveys for 3.5 wt.% $Ni_{acac}$-based NPs/$TiO_2$ sample before and after 5 cycles are shown in Figure S4-7, Annex II. After cycling, the peak corresponding to Ni *2p* at 855.9 eV slightly decreases in intensity, confirming the nickel leaching. The narrow scan XPS spectra comparison of Ni *2p* for the 3.5 wt.% $Ni_{acac}$-based NPs/$TiO_2$ sample before and after cycling is shown **Figure 4-8**. The Ni *2p* signal revealed the presence of NiO (853.8 eV) and $Ni(OH)_2$ (855.9 eV) on the $TiO_2$ surface. $Ni^0$-NPs were not present after cycling.

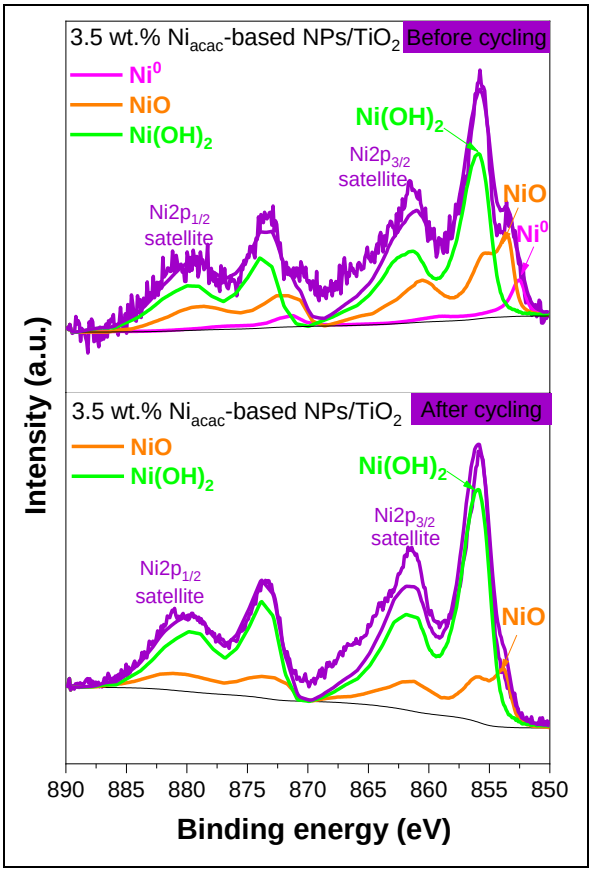


**Figure 4-8.** Narrow scan XPS spectra of Ni2p of 3.5 wt.% $Ni_{acac}$-based NPs/$TiO_2$ sample before and after cycling.

### 4.2.4 Proposed Photocatalytic Mechanism

Hereby, we propose a photocatalytic hydrogen generation mechanism for Ni-based NPs/$TiO_2$ system under UV-visible light irradiation, as shown in **Figure 4-9**. Recent

research papers have investigated the photocatalytic hydrogen generation of the $NiO/TiO_2$ *p-n* heterojunction for $H_2$ production using simulated solar light.[86,87,78,170,171,9] When $NiO/TiO_2$ photocatalysts are exposed to solar light, electron-hole pairs are generated in both semiconductors $TiO_2$ and NiO (**Figure 4-9** and Eq. 5). The relative positions of the CB and VB of the semiconductors are crucial in the photocatalytic process creating an internal electric field that reduces the charge carriers' recombination and facilitates interfacial charge transfer. Photogenerated electrons in the CB of NiO migrate to the CB of $TiO_2$, and photogenerated holes in the VB of $TiO_2$ migrate to the VB of NiO (Eq. 6). This charge transfer decreases the recombination of charge carriers, leading to $H_2$ production. As shown in Eq. 7, reduction of hydrogen ions ($H^+$) forms hydrogen radicals ($H\cdot$) than can recombine to form hydrogen gas ($H_2$) or reduction of water ($H_2O$) see Eq. 8. The photogenerated electrons reaching the $TiO_2$ and NiO-NPs surfaces can reduce $H^+$ to $H_2$.

Additionally, the TRMC results provide strong evidence that $Ni^0$ NPs effectively scavenge electrons from the CB of $TiO_2$ under UV light, which is beneficial for photocatalytic activity.[51,72] As we mentioned before, XPS results revealed a trace amount of $Ni^{0,}$ leading to the formation of an Ohmic junction with $TiO_2$. These $Ni^0$-NPs are located within the interphase between NiO-NPs and $TiO_2$, as schematically shown in **Figure 4-9**, facilitating the migration of photogenerated electrons to the metal.[9,8] The photogenerated electrons reaching the $Ni^0$-NPs surface can also reduce $H^+$ to $H\cdot$ and the Ni-based NPs help the formation of H-H bonds leading to $H_2$ generation.

To prevent the oxidation reaction, methanol ($CH_3OH$) was used as a sacrificial agent, effectively scavenging the holes from the VB of NiO to generate $H_2$.[15,77] Methanol and water molecules react with the holes, producing hydroxyl radicals ($^{\bullet}OH$) see Eq. 9 and Eq.10, which subsequently oxidize $CH_3OH$ molecules into formaldehyde ($CH_2O$), formic acid (HCOOH) and carbon dioxide ($CO_2$) see Eq. 11-14. These

compounds are the primary intermediates in the methanol to $H_2$ reforming. The choice of methanol as a hole scavenger is advantageous due to its high H/C ratio and the absence of C-C links, which reduces the risk of carbon formation and fouling of the photocatalyst.[6,172] Furthermore, TRMC results under visible excitation confirmed detectable signals, indicating that NiO produces photogenerated electrons and holes due to their d-d transitions.[89,154,155,156,8] These photogenerated electrons also migrate from the CB of NiO to the CB of $TiO_2$ when exposed to visible light irradiation.

$$TiO_2 + NiO \xrightarrow{hv>E_g} TiO_2(e^-_{CB} + h^+_{VB}) + NiO\ (e^-_{CB} + h^+_{VB}) \quad (5)$$

$$TiO_2(e^-_{CB} + h^+_{VB}) + NiO\ (e^-_{CB} + h^+_{VB}) \rightarrow TiO_2(e^-_{CB}) + NiO\ (h^+_{VB}) \quad (6)$$

$$2H^+ + 2e^- \rightarrow 2H^{\bullet} \rightarrow H_2 \quad (7)$$

$$2H_2O + 2e^- \rightarrow H_2 + 2OH^- \quad (8)$$

$$H_2O + h^+ \rightarrow {}^{\bullet}OH + H^+ \quad (9)$$

$$CH_3OH + h^+ \rightarrow {}^{\bullet}OH + H^+ \quad (10)$$

$$CH_3OH + {}^{\bullet}OH \rightarrow {}^{\bullet}CH_2OH + H_2O \quad (11)$$

$${}^{\bullet}CH_2OH \rightarrow CH_2OH + H^+ + e^- \quad (12)$$

$$CH_2O + H_2O \rightarrow HCOOH + H_2 \quad (13)$$

$$HCOOH \rightarrow CO_2 + H_2 \quad (14)$$

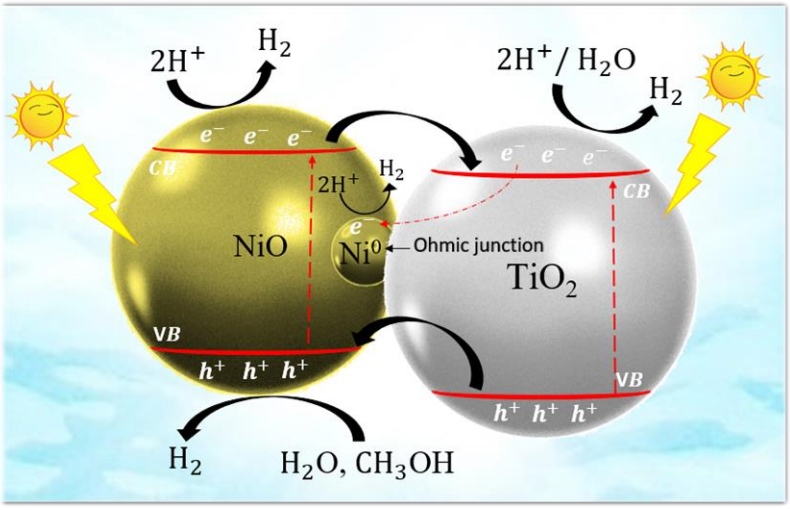


**Figure 4-9.** Photocatalytic mechanism of Ni-based NPs/$TiO_2$ sample under UV-visible light excitation.

## 4.3 Conclusions

Modification of $TiO_2$ surface with Ni-based NPs by radiolysis leads to small Ni-based NPs dispersed on titania. Deposition of Ni-based NPs with Ni acetylacetonate as precursor is more efficient (compared to Ni formate) as confirmed by TEM, HRTEM, EELS, ICP-OES, DRS and XPS techniques. The modified samples exhibited good photocatalytic for hydrogen generation under UV-visible light and also showed a slight activity under visible light. Notably, modification of $TiO_2$ with the precursor nickel (II) acetylacetonate leads to higher hydrogen generation rates than that of nickel (II) formate. The metal loading of Ni for $Ni_{acac}$-modified samples was optimized for the performance of the photocatalytic hydrogen generation. Among the modified samples, the 3.5 wt.% $Ni_{acac}$-based NPs/$TiO_2$ sample demonstrated the most important increase in the photocatalytic activity, with a rate approximately 42-fold higher than bare $TiO_2$. TRMC results provide strong evidence that $Ni^0$-NPs effectively scavenge electrons from the CB of $TiO_2$ under UV light, and Ni oxides NPs inject electrons into the conduction band of $TiO_2$ under visible light.

Additionally, the formation of the *p-n* heterojunction between NiO-NPs and $TiO_2$ played a crucial role in creating an internal electric field that reduced charge carriers' recombination and facilitated interfacial charge transfer. Revealing that modification of $TiO_2$ with Ni-based NPs enhances charge carriers' separation and induces a high photocatalytic activity for $H_2$ generation under UV-visible light. The photocatalytic activity reaches a stable rate after the $2^{nd}$ cycle. These findings advance our understanding of charge carriers' dynamics and offer valuable insights for optimizing photocatalytic systems for sustainable energy applications. Future work will focus on the development of nanoalloys based on Ni (such as NiAu or NiPt), we expect that these co-catalysts will be very active and stable for hydrogen generation. Alloying Ni with Au or Pt will avoid its oxidation and leaching..

# Chapter 5

Surface Modification of $TiO_2$ with Bimetallic NiFe Nanoparticles for Photocatalytic Hydrogen Generation

# Chapter 5. Surface Modification of $TiO_2$ with Bimetallic NiFe Nanoparticles for Photocatalytic Hydrogen Generation

## 5.1 Introduction

In this study, we are inspired by nature to design new co-catalysts that do not require precious metals.[173,174,175] In particular, Nature utilizes hydrogenases, which are organometallic enzymes containing nickel (Ni) and iron (Fe) centers that catalyze hydrogen evolution with performances that rival those of platinum (Pt).[20] Recent studies highlight the potential of NiFe catalysts in photocatalysis. For instance, Tetzlaff et al. synthesized $FexNi_9$-$xS_8$ (x = 3-6) composites inspired by hydrogenases, which demonstrated potential as a photocatalyst for solar-driven hydrogen production.[175] Li et al. demonstrated that NiFe cocatalysts can achieve hydrogen production rates comparable to Pt under optimized conditions.[176] Kim et al. developed $NiFe_2O_4$@$TiO_2$ magnetic nanoparticles (NPs), improving the photocatalytic activity due to the synergistic effects between $NiFe_2O_4$ and $TiO_2$.[177] This combination facilitated efficient charge transfer and reduced electron-hole pair recombination compared to bare $TiO_2$ or $NiFe_2O_4$. Firtina-Ertis et al. explored $NiFe_2O_4$/$TiO_2$-$Ag^+$ photocatalysts and found that those with the smallest crystallite size exhibited the highest $H_2$ production activity.[178] The incorporation of $Ag^+$ nanoparticles altered the bandgap energy and reduced electron-hole recombination, making the photocatalyst more effective under solar light. In this system, ferric ions and silver oxide serve as electron and hole traps, respectively. Domínguez-Arvizu et al. synthesized $NiFe_2O_4$ and $Cu_2O$ to create $NiFe_2O_4$/$Cu_2O$ p-n heterojunctions.[179] These heterojunctions improve charge separation and increase charge carriers' concentration, leading to enhanced hydrogen production during water splitting. The 50/50 mass ratio of $NiFe_2O_4$/$Cu_2O$ proved the most efficient for water-splitting applications. In another study, Gao et al. found that the combination of NiFe-Layered

Double Hydroxide (LDH) nanosheets with small $TiO_2$ nanosheets enhances the photocatalytic hydrogen production by improving the separation of photo-generated electrons and holes compared to bare $TiO_2$.[180] Boppella et al. developed an efficient 2D photocatalyst by combining reduced graphene oxide (rGO), NiFe-LDH, and lanthanum titanate (LTO) nanosheets.[181] This rGO/LTO/NiFe-LDH photocatalyst demonstrated excellent hydrogen evolution, attributed to enhanced charge transfer at the rGO/LTO interface and improved hole trapping by the NiFe-LDH cocatalyst, which increases electron density for hydrogen production. Yue et al. developed sulfurated FeNiS nanoparticles as co-catalysts for CdTe/CdS quantum dots (QDs), highlighting that these nanoparticles offer more bonding sites and active sites for co-catalyze the CdTe/CdS QDs for hydrogen evolution than FeNi LDH nanosheets.[182] The junction between sulfur species and $Cd^{2+}$ in CdTe/CdS QDs facilitated electron transfer between QDs and FeNiS nanoparticles, significantly enhancing photocatalytic hydrogen production. Wang et al. used a novel composite NiFe-Prussian Blue Analog (PBA)-S with ZnCdS, which enhances charge separation, increased active sites, and improved light absorption efficiency, resulting in high photocatalytic activity for hydrogen generation.[183] These advancements highlight the ongoing innovation in photocatalytic materials, aiming to create efficient, non-precious metal-based systems for sustainable hydrogen generation.

In this work, $TiO_2$ (commercial Degussa-P25) surface was modified with NiFe-NPs induced by radiolytic reduction of nickel (II) acetylacetonate and iron (III) acetylacetonate. This method leads to the deposition of small clusters of NiFe-NPs on $TiO_2$. The NiFe-$TiO_2$ modified samples reduce charge carriers‘ recombination, enhancing the photocatalytic hydrogen generation compared with their monometallic counterparts and bare $TiO_2$. The charge carriers’ dynamics was analyzed by Time Resolved Microwave Conductivity (TRMC). These improvements arise from the synergistic interactions between NiFe and $TiO_2$.

## 5.2 Results and Discussion

### 5.2.1 Characterization of the Photocatalysts

TEM was used to analyze the morphology, size, and dispersion of NiFe-NPs on the $TiO_2$ surface. The NiFe-NPs were difficult to observe due to their atomic number being similar to that of Ti. Moreover, NiFe spherical nanoparticles were found over the $TiO_2$ surface, as shown in **Figure 5-1**. The NiFe-NPs are well dispersed and smaller than 2 nm. The elemental composition was studied by EDX analysis (**Figure 5-2a**), and the presence of Ni, Fe, and Ti was confirmed on the Cu grid (**Figure 5-2b**).

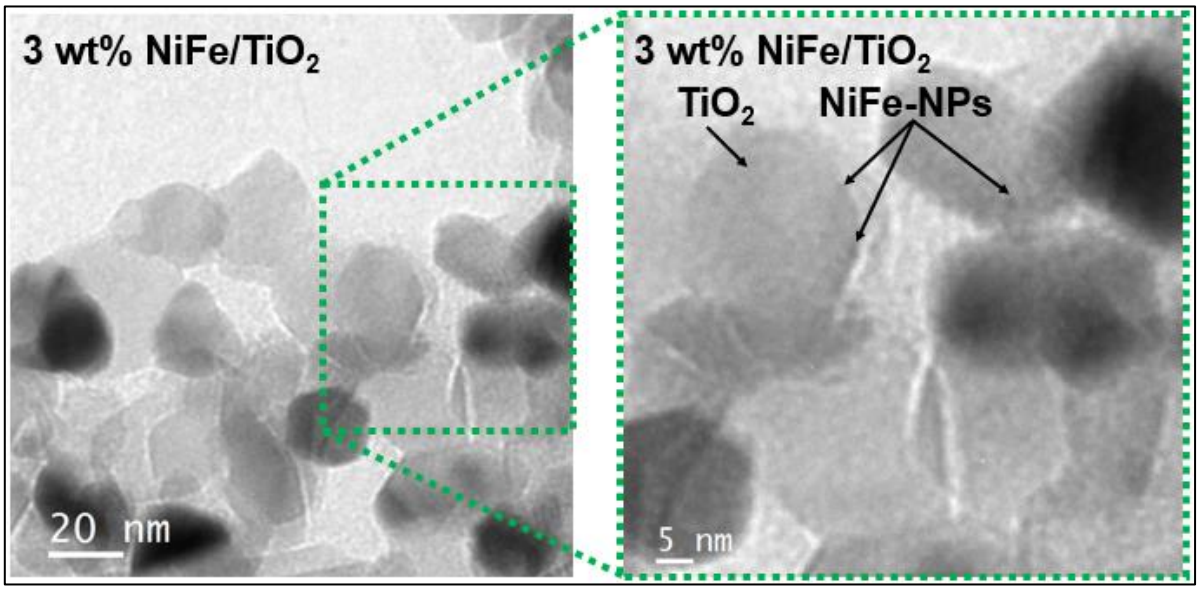


**Figure 5-1.** TEM micrograph in bright field of 3 wt% $NiFe/TiO_2$ sample.

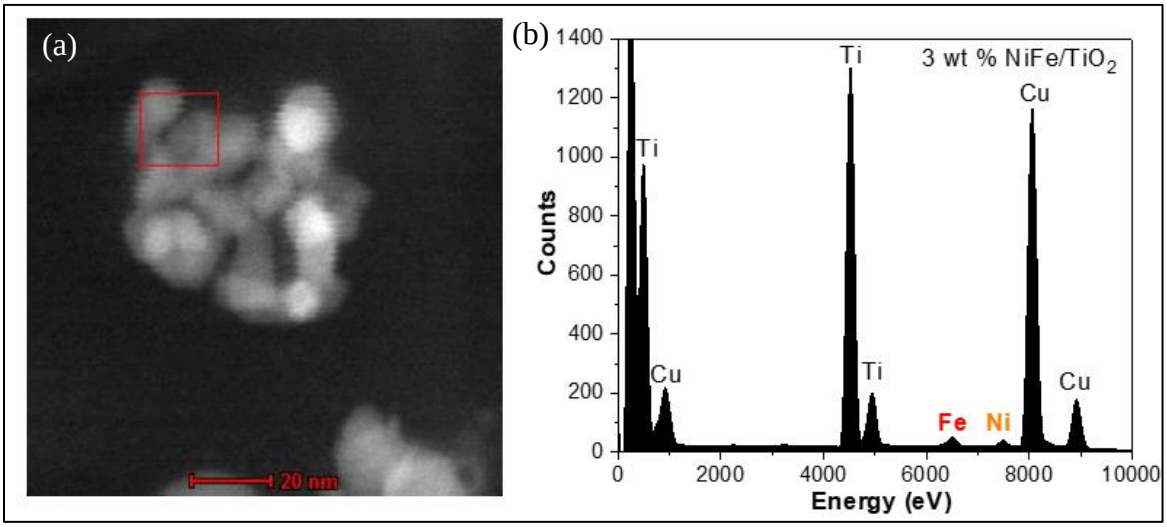


**Figure 5-2. (a)** TEM micrograph in contrast Z-mode of 3 wt% NiFe/$TiO_2$ sample, and **(b)** EDS analysis shows the presence of Ni, Fe and Ti on the Cu grid.

The crystal structure of bare $TiO_2$ and modified samples was investigated by DRX (Figure S5-1, Annex III). However, no diffracted peaks were observed for Ni and Fe crystalline phases. The diffracted peaks of the samples coincide with the reference peaks of the anatase and rutile crystalline phases, according to the data JCPDS files No. 21-1272 and No. 21-1276, respectively. [6,] However, no diffraction peaks were observed for NiFe-NPs due to the low metal loading and the very small size of the metal clusters.

The optical properties of the photocatalysts analyzed by DRS showed absorption bands from 200 nm to 400 nm (UV region) due to $TiO_2$ support, as shown in **Figure 5-3a.** The band gap energies for anatase and rutile phases are 3.2 eV and 3.0 eV.[50] For the modified samples, the band edge shifted towards longer wavelengths compared with bare $TiO_2$. This shift could be attributed to the presence of the transition metal ions, which are known to absorb in the visible region due to d–d transitions.[155]

The band energies of the modified samples and bare $TiO_2$ were calculated by the Tauc method for indirect transition of anatase phase.[157] **Figure 5-3b** shows the Tauc

plots for the modified samples. A shift was observed and the surface-modified titania had less band gap energy than bare $TiO_2$. The estimated band gaps are 3.25 eV, 3.14 eV, 3.14 eV, 3.10 eV, and 3.04 eV for bare $TiO_2$, 1wt% NiFe/$TiO_2$, 2 wt% NiFe/$TiO_2$, 3wt% NiFe/$TiO_2$ and 5wt% NiFe/$TiO_2$, respectively.

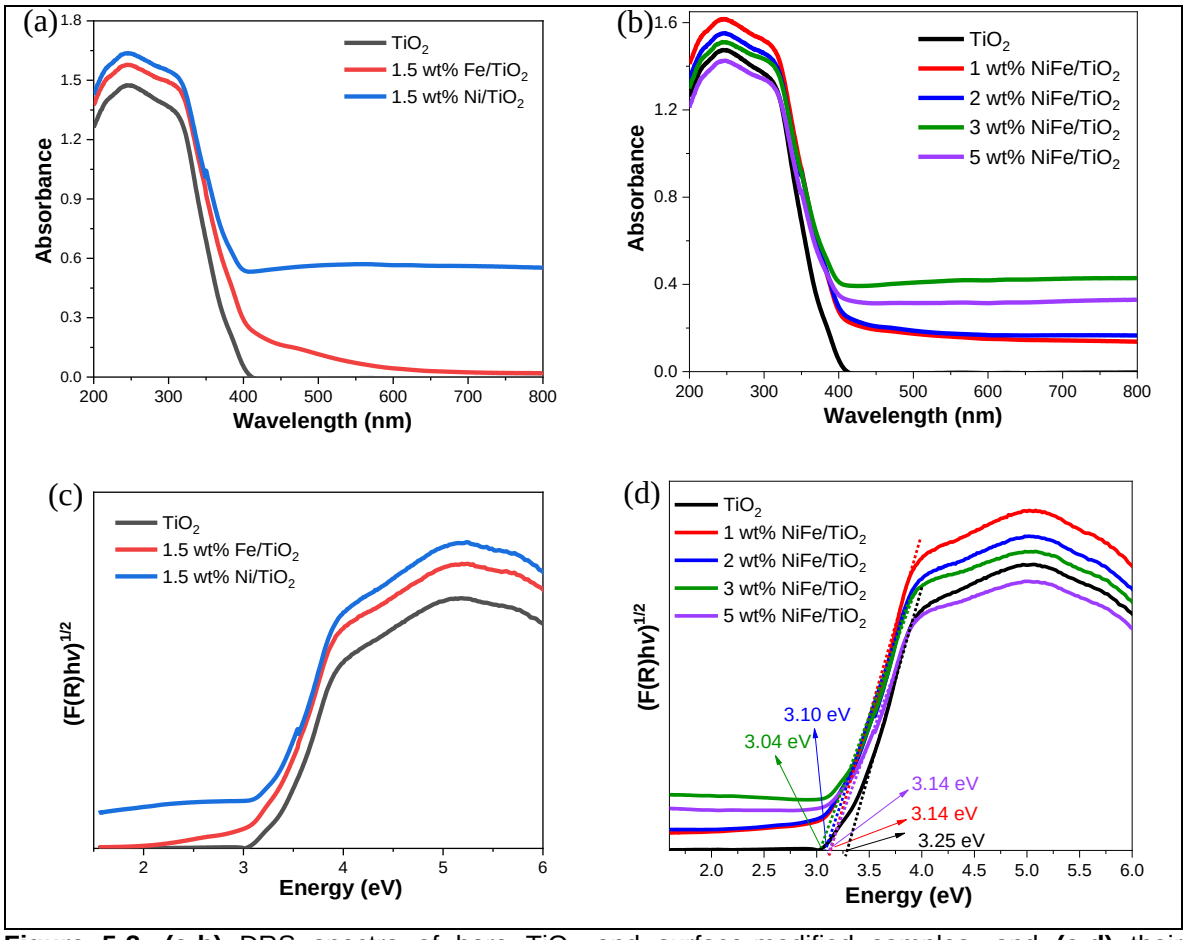


**Figure 5-3. (a-b)** DRS spectra of bare $TiO_2$ and surface-modified samples, and **(c-d)** their corresponding Tauc plot.

TRMC signals of the modified samples and bare $TiO_2$ are shown in **Figure 5-4**. TRMC signals for mono- and bi-metallic samples at 360 nm show $I_{max}$ values reached for all the samples under UV light excitation, suggesting electron migration from the VB to the CB of $TiO_2$. Only for the Fe-monometallic samples, this behaviour is not observed (see **Figure 5-4b**). For the sample Fe-$TiO_2$, electron scavenging by Fe-based nanoparticles might be too fast to be observed at the nanosecond range.

Then, the $I_{max}$ values decreased, and faster decays were observed for the mono- and bi-metallic photocatalysts compared to bare $TiO_2$. This can be explained by quick trapping by Ni and NiFe NPs of photogenerated electrons in the CB of $TiO_2$. The decay of the signal increases for 5 wt% NiFe/$TiO_2$ and 3 wt% NiFe/$TiO_2$ compared with 2 wt% NiFe/$TiO_2$ and 1 wt% NiFe/$TiO_2$ as shown in **Figure 5-4a**. These TRMC results indicate that the NiFe nanoparticles are efficient in electron scavenging, reducing the charge carriers' recombination, which is beneficial for the photocatalytic activity.

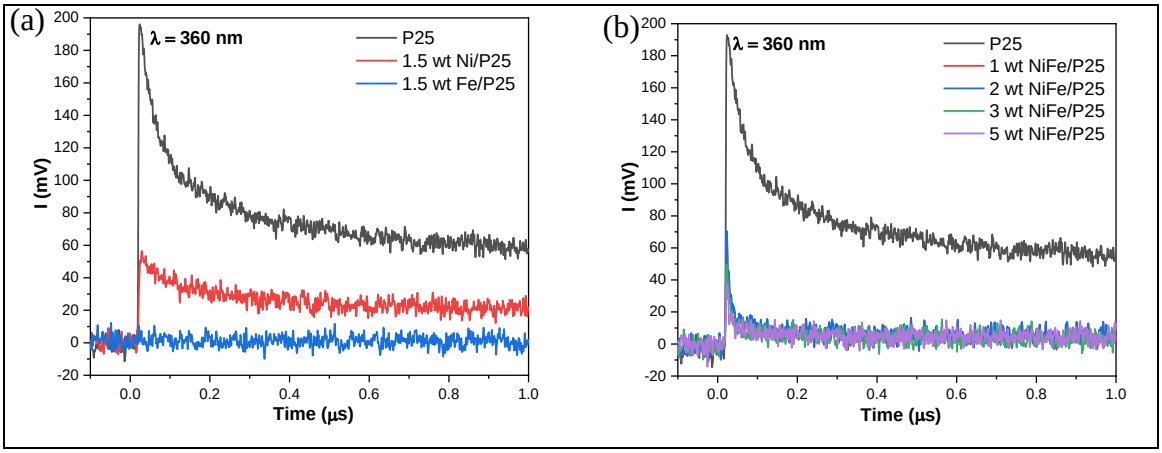


**Figure 5-4. (a-b)** TRMC signals of modified samples and bare $TiO_2$ at $\lambda_{exc.}$ = 360 nm.

### 5.2.2 Photocatalytic Hydrogen Generation

The surface modification of $TiO_2$ with Fe does not increase the photocatalytic activity, contrary to modification with Ni NPs, which leads to a $H_2$ generation rate of 200.3 μmol $g^{-1}$ $h^{-1}$ (**Figure 5-5a**). The photocatalytic hydrogen generation is enhanced when the $TiO_2$ surface is modified with NiFe bimetallic nanoparticles compared with their monometallic counterparts under UV-visible light irradiation (**Figure 5-5b**), and a synergetic effect is obtained. The NiFe/$TiO_2$ modified samples show similar behavior: two slopes are found corresponding to two different rates for hydrogen production before and after 2 h irradiation. In the first 2 h of irradiation, the slopes for 1 wt% NiFe/$TiO_2$, 2 wt% NiFe/$TiO_2$, 3 wt% NiFe/$TiO_2$ and 5 wt% NiFe/$TiO_2$ are 141.3

μmol $g^{-1}$ $h^{-1}$, 161.3 μmol $g^{-1}$ $h^{-1}$, 580.67 μmol $g^{-1}$ $h^{-1}$, and 576.7 μmol $g^{-1}$ $h^{-1}$, respectively. After 2 h of irradiation, an increase in hydrogen generation was observed for NiFe/$TiO_2$ samples. The slopes are 447.5 μmol $g^{-1}$ $h^{-1}$, 1189.2 μmol $g^{-1}$ $h^{-1}$, 1569.4 μmol $g^{-1}$ $h^{-1}$, and 974.8 μmol $g^{-1}$ $h^{-1}$, respectively. The sample with the highest photocatalytic activity for $H_2$ generation was 3 wt% NiFe/$TiO_2$ with an average rate of $H_2$ production of 1173 μmol $g^{-1}$ $h^{-1}$ and for bare $TiO_2$ 35.7 μmol $g^{-1}$ $h^{-1}$, approximately 33-fold higher than bare $TiO_2$ (**Figure 5-5c**). The bimetallic FeNi nanoparticles are very sensitive to oxygen and are probably partly oxidized in the initial phase of the photocatalytic test. Under irradiation in the presence of methanol as hole scavenger, the nanoparticles are probably back-reduced by the electrons in the conduction band of $TiO_2$. This induction time might be due to the partial reduction of Fe and Ni-based nanoparticles leading to reduced NPs, which are more active as cocatalysts that the oxides counterparts. In situ XPS studies will be conducted to understand the photocatalytic mechanism and the role of the oxidation states. Previous studies have also demonstrated that Ni can act as active sites for $H^{\bullet}$ recombination, promoting the formation of H–H bonds.[8,9,15,150]

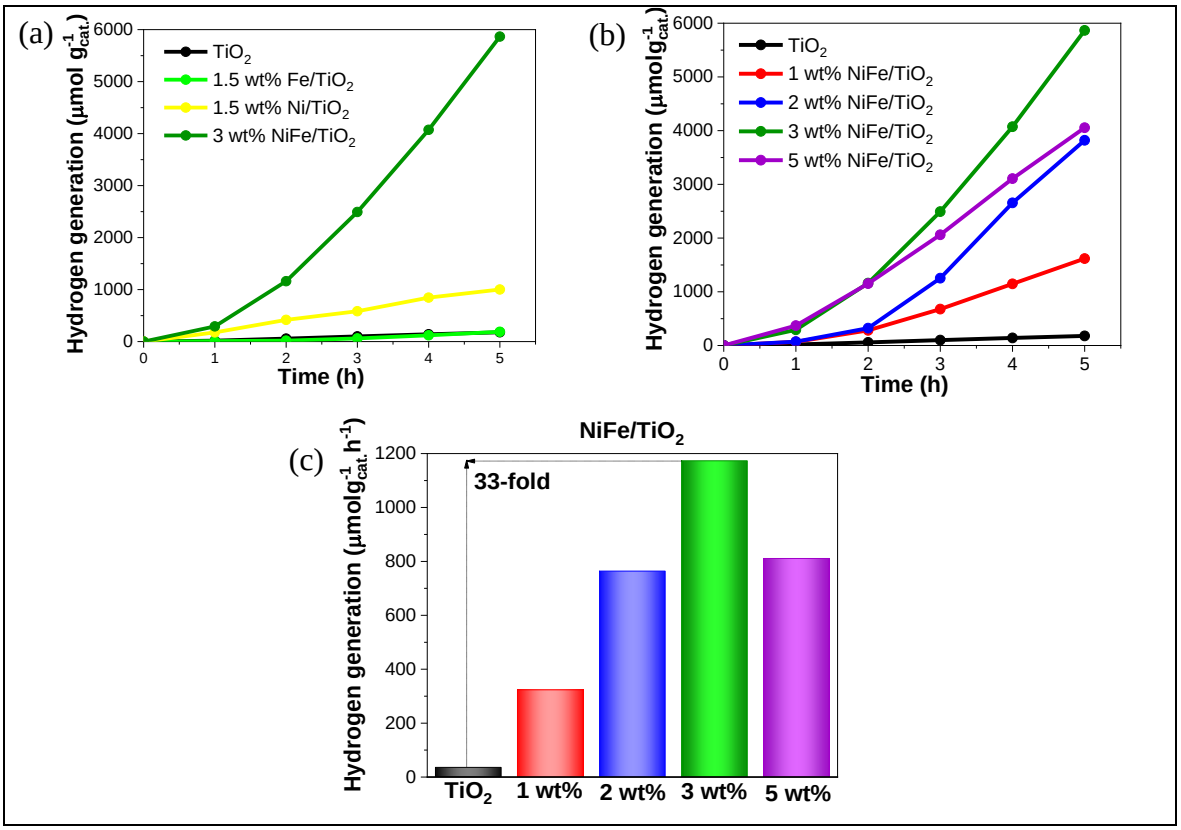


**Figure 5-5.** Photocatalytic hydrogen generation **(a)** monometallic samples, **(b)** bimetallic samples after 5 h of irradiation, and **(c)** photocatalytic hydrogen generation rates (µmol $g^{-1}$ $h^{-1}$) of bimetallic samples and bare $TiO_2$ under UV-visible light irradiation from 25% v/v methanol aqueous solution.

### 5.2.3 Stability with Cycling

The photocatalytic stability was analyzed for the most active sample 3 wt% NiFe/$TiO_2$. A decrease in the photocatalytic activity after the 2nd cycle was observed (**Figure 5-6**). However, in the 3rd, 4th and 5th cycles, the photocatalytic activity showed similar hydrogen generation rate, with a rate of 641 µmol $g^{-1}$ $h^{-1}$ after the 5th cycle. The decrease in the photocatalytic activity is probably due to Ni leaching in aqueous medium. [150] This Ni leaching is known in the field of catalysis and induces a reduction in the catalytic activity of Ni-based catalysts.[150,166,167] One way to avoid this leaching in catalysis is to alloy Ni with a noble metal, such as Pt or Au.

A comparison of our results with published works using Ni and Fe transition metals on different supports was made (Table S5-1, Annex III). Our cocatalysts demonstrate

high photocatalytic activity compared to Fe- and Ni-based cocatalysts reported in literature without noble metals. For example, this activity is 33 times higher than $TiO_2$, compared to NiFe-LDH@ $TiO_2$,[180] and rGO/LTO/NiFe,[181] which are 8 and 9 times greater than $TiO_2$, respectively. Few studies report good photocatalytic activity with modification of CdS (small band gap of 2.42 eV).[50,163,164] However, CdS is a toxic compound and tends to corrosion under light irradiation leading to harmful $Cd^{2+}$. For photocatalytic applications, it is essential to use non-toxic and stable supports.

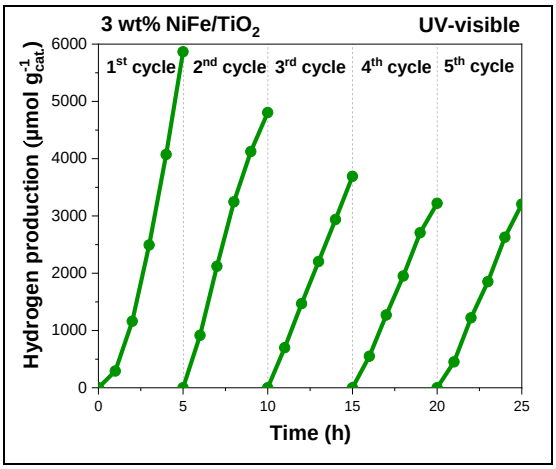


**Figure 5-6.** Photocatalytic hydrogen generation with cycling for 3 wt% NiFe/$TiO_2$ under UV-visible light irradiation from 25% v/v methanol aqueous solution.

## 5.3 Conclusions

Bimetallic 2 nm NiFe-NPs were successfully synthesized by radiolysis on the $TiO_2$ surface. The photocatalysts were characterized by TEM-EDS, DRS, and XRD techniques. Our results demonstrate that the NiFe/$TiO_2$ photocatalysts exhibited higher hydrogen production than their mono-metallic counterparts under UV-visible light, and a synergetic effect is obtained. This activity decreases with cycling for the first two cycles, but stability in the hydrogen generation rate is reached after the third cycle.

Further investigation is needed to determine the oxidation states before and after cycling and to study the charge carriers‘ dynamics in the NiFe/$TiO_2$ photocatalysts.

In situ studies will be conducted to understand the photocatalytic mechanism. The oxidation states of Ni and Fe during the photocatalytic cycle will be analyzed with in-situ XPS.

Finally, Fe and Ni will be associated with a noble metal (such as Au or Pt) to increase the stability of the photocatalyst to oxygen and limit the leaching of Ni with cycling, and trimetallic alloys will be developed (such as NiFeAu, or NiFePt) as cocatalysts for green hydrogen generation.

# Chapter 6

Plasmon Catalysis with Gold Nanostars

# Chapter 6. Plasmon Catalysis with Gold Nanostars

## 6.1 Introduction

Plasmonic nanomaterials have garnered attention for their potential in pollutant degradation using solar light. The surface plasmon resonance, i.e., coherent electron oscillations in metal nanoparticles with the irradiated light, plays a crucial role in initiating chemical transformations by generating energetic electrons upon plasmon decay.[99,100,101] These "hot" electrons interact with molecules on the nanoparticle surface, inducing chemical transformations.[184] Plasmonic $TiO_2$ surface modified with Au NPs was used for water treatment by photocatalysis.[6] TRMC measurements revealed that under visible light, electrons were injected from Au-NPs into the CB of $TiO_2$, attributed to the activation of the LSPR of the Au-NPs. The action spectra correlated with the absorption spectra, supporting the idea that model pollutants are decomposed by a photocatalytic mechanism.

Previous studies by the ICP team reported that spherical Au-NPs facilitated the reduction of 4-NTP to 4-ATP under visible light irradiation.[94] They confirm the formation of 4-ATP on the surface of Au-NPs by UV-visible spectroscopy and SERS but not in the solution. This suggests that the reduction of 4-NTP occurs on the AuNP surface, involving "hot" electrons from plasmon excitation. Additionally, 4-ATP appears to remain tightly bound to the AuNPs. They also found that no degradation was observed for 4-nitrophenol (4-NP) in the presence of the spherical Au-NPs under visible irradiation. This means that the adsorption of the molecules on the NPs is a very important factor for efficient catalysis.

Another study by the *ICP* team demonstrates that Pd nanoflowers absorbing in the visible range exhibit high activity in the Suzuki reaction under UV-visible light. The results show much faster kinetics under visible light compared to dark conditions.[102]

Among the plasmonic nanoparticles, gold nanostars (AuNSs) have emerged as promising candidates due to their unique optical properties given their shape anisotropy,[185] higher specific surface area, and numerous plasmonic hotspots compared to other nanostructures.[186,187] The optical properties of the AuNSs typically exhibit distinctive absorption features due to their morphology. The UV-vis spectra often show multiple peaks, which are indicative of different plasmon resonances resulting from the hybridization of plasmons in the core and tips. [188,189] The long plasmon band usually appears in the near-infrared (NIR) region, while shorter bands may be observed at lower wavelengths. The precise positions and intensities of these peaks can be influenced by factors such as the size and shape of the nanostars. The plasmon band experiences a red shift and an important broadening as the nanostars increase in size.[190] The tunability of these AuNSs increases their versatility for various applications, for example in nanomedicine, catalysis, sensing, and plasmonics.[27,191,192,193,194]

Numerous studies have investigated the catalytic properties of metal NPs and plasmonic materials including AuNSs in reducing 4-NTP.[99,195,196,197,198,199,200] For instance, König et al. utilized AuNSs as catalysts using $NaBH_4$ to generate 4-ATP.[195] They mentioned that 4-NTP molecules interact with metal catalysts through thiol (-SH) groups and whether direct contact with nitro (-$NO_2$) groups is essential for reduction. Electrochemical studies indicate that reduction can occur without direct contact, as electrons can transfer to -$NO_2$ groups through the molecule.[195]

However, Cui et al. reported challenges when attempting the same reaction with $NaBH_4$ and AuNSs, emphasizing the crucial role of the molecular orientation of 4-NTP in influencing catalytic reactions.[196,197] The -$NO_2$ groups were distanced from the catalytic surface in their initial experiment due to strong Au-S binding. In contrast, the -$NO_2$ groups directly interact with the Au surface in the next experiment, facilitating their reduction to amino (-$NH_2$) groups. They mentioned that the direct contact of the -$NO_2$ group to the Au surface is necessary for efficient catalysis.

Besides, Qui et al. demonstrated the reduction of 4-NTP to 4-ATP using a silver plasmonic film, employing SERS without $NaBH_4$.[99]

Other studies have explored the catalytic capabilities of metal films such as Au, Ag, and Cu in facilitating the plasmon-assisted surface-catalyzed dimerization of 4-NTP to form 4,4'-dimercaptoazobenzene (DMAB).[201] Additionally, Hong et al. revealed the enhanced catalytic reduction of 4-NTP to DMAB on silver-coated gold surfaces under surface plasmon excitation.[202] Further investigations have delved into optimizing reaction conditions, such as adjusting light wavelength, to control product formation. Zhou et al. elucidated the influence of light wavelength on the reduction of 4-NTP, impacting the selectivity of reaction products.[203] However, the resulting products from such reactions remain uncertain, with possibilities including 4-ATP or DMAB.[204] As Zhao et al. discussed, theoretical studies have provided insights into plasmon-enhanced heterogeneous catalysis, highlighting the importance of various factors, including pH solution, irradiation, metal substrates, and atmospheric conditions in the reaction mechanism.[205] Furthermore, experimental findings by Sarhan et al. demonstrated the dimerization of 4-NTP to DMAB using gold nanoflowers. Their study revealed significant optical heating of particles. It showed that the reaction is primarily photo-driven, with temperature crucial in influencing the reaction kinetics and product formation.[184] Wang et al. showed the conversion of 4-NTP to DMAB due to the excitation of plasmons on $Au_{core}$-$Ag_{shell}$ bimetallic NPs, highlighting the versatility and potential of plasmonic nanomaterials in catalytic transformations.[206]

In the present work, we report the degradation reaction of 4-NTP by plasmon excitation of AuNSs, used as photocatalysts. In addition to UV-visible absorption spectroscopy, hyperspectral dark-field optical microscopy and atomic force microscopy were employed to investigate the influence of the shape and size of the AuNSs on the reaction.

## 6.2 Results and Discussions

### 6.2.1 Characterization of the Photocatalysts

The absorption spectra of the AuSs exhibit a relatively narrow absorption band with a maximum at 522 nm (**Figure 6-1a** and Figure S6-2a, Annex IV), in agreement with the red wine colour of the solutions (**Figure 2-7**). Such absorption bands are characteristic of LSPR of spherical nanoparticles with diameters between 10 and 50 nm.[207,31]

The absorption spectra of the AuNSs synthesized using radiolysis present a very broad band shifted to the red with a maximum at 670 nm (**Figure 6-1b**), and 687 nm for AuNSs obtained by Yuang's protocol (Figure S6-2b, Annex IV), the colour of the solutions changed to blue (**Figure 2-7**). This shift and broadening can be attributed to morphological variations in the AuNSs.[125]

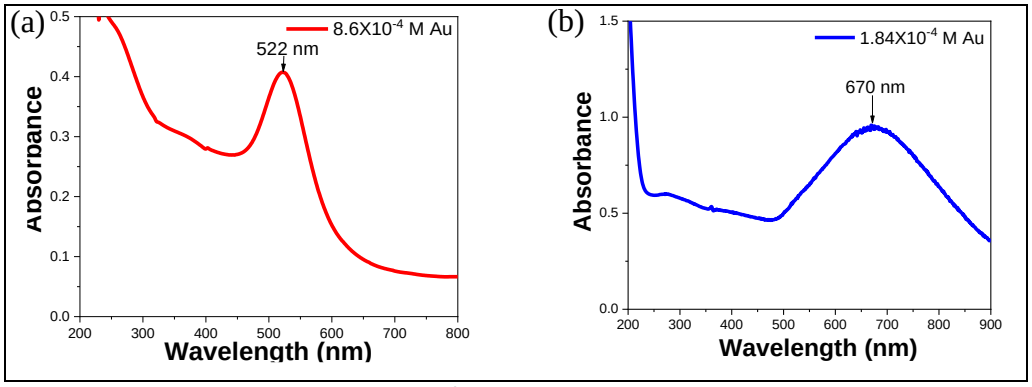


**Figure 6-1.** UV-vis spectra of **(a)** AuSs ($[Au^0]$ = 8.6×10$^{-4}$ M) synthesized by radiolysis method, and **(b)** AuNSs ($[Au^0]$ = 1.84×10$^{-4}$ M) in aqueous solution**.**

TEM micrographs in bright field show Au nanostars with variations in the size from 80 nm to 120 nm (**Figure 6-2a**). Similar sizes are also obtained by AFM analysis of individual AuNSs deposited on glass slides (**Figure 6-15**). **Figure 6-2b** shows an individual Au nanostar with a size of 99 nm. Notably, two prominent peaks towards the core of the Au nanostar were observed, measuring 52 nm and 57 nm, with a

diameter of 8 nm and 12 nm, respectively. From this observation and collective micrographs, we can conclude that the AuNSs present collective peaks that play an essential role in the photocatalytic performance of the system, as will be discussed below. Furthermore, the interplanar distances of 0.235 nm, 0.203 nm and 0.12 nm correspond to the (111), (200) and (311) planes of Au (**Figure 6-2c**). The interplanar distance was measured using the Digital Micrograph software deduced by fast Fourier transformation process.

Elemental mapping of the single nanostar is shown in **Figure 6-2d**, Au in yellow and Ag in blue. Ag seems to be in the whole structure of the Au nanostar. EDS line-scan signals of the single Au nanostar are shown in **Figure 6-2e**, revealing the presence of Au, Ag (coming from the Ag precursor added to help the anisotropic growth), and Cu grid.

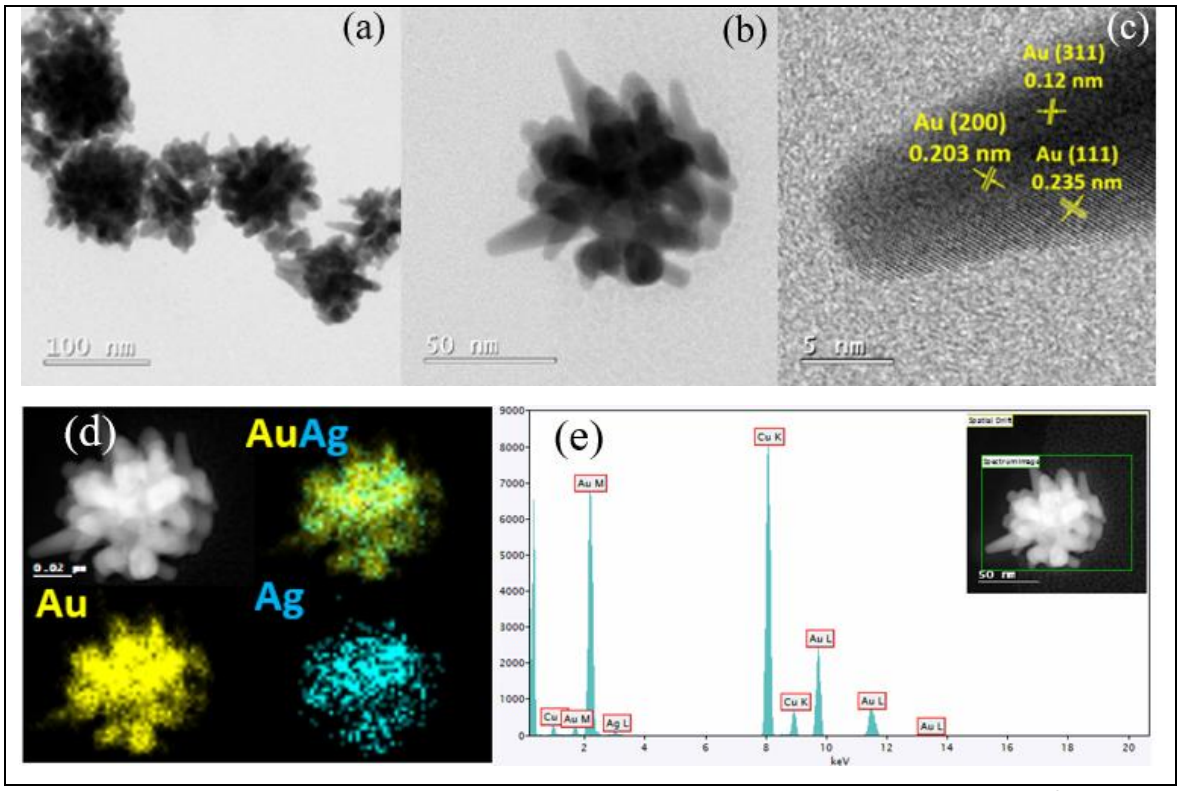


**Figure 6-2. (a)** TEM micrograph of AuNSs with a final concentration of $1.84\times10^{-4}$ M $Au^0$, **(b)** TEM micrograph of a single Au nanostar **(c)** HRTEM micrograph, **(d)** elemental mapping performed to a single Au nanostar (Au in yellow and Ag in blue), and **(e)** their EDS analysis.

### 6.2.2 Catalytic activity of AuNSs for reduction of 4-NTP using $NaBH_4$

For the photocatalytic tests, UV-vis spectroscopy was used to monitor the reaction kinetics of the 4-NTP reduction to 4-ATP.

Initially, aqueous solutions of $6\times10^{-4}$ M of 4-NTP were prepared, and their pH was adjusted from 3.5 to 11 by adding few µL of 0.15 M NaOH solution. The absorption spectrum of 4-NTP exhibits two characteristic absorption bands at 228 and 408 nm in an aqueous alkaline solution, as shown in **Figure 6-3**.

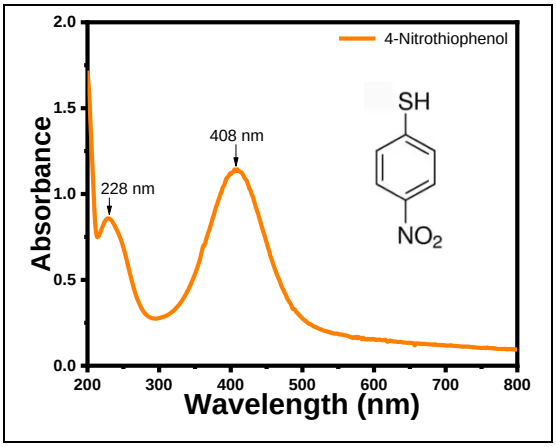


**Figure 6-3.** UV-vis spectrum of 1.64×10-4 M 4-NTP alkaline aqueous solution with characteristic absorption bands at 228 nm and 408 nm. Optical path = 1 cm.

Photocatalytic tests were carried out with the AuNSs synthesized from Au seeds via γ-radiolysis in aqueous alkaline solution. The previously prepared aqueous solutions of AuNSs have an acidic pH. The pH of AuNSs (2.6) was changed to 11 by adding few µL of 0.15 M NaOH solution. 2 mL of AuNSs ($[Au^0]=2.53\times10^{-4}$ M) alkaline aqueous solution were centrifuged and redissolved in 2 mL of Milli-Q water. Immediately, 750 µL of $6\times10^{-4}$ M 4-NTP alkaline aqueous solutions were added to the quartz reactor equipped with a magnetic stirrer and cap. The solution was put under stirring 40 min, and then, the catalytic activity (without irradiation) of the AuNSs was studied for degradation of 4-NTP to 4-ATP using $NaBH_4$ as a reductant. Two concentrations of $NaBH_4$ were used: $5.7\times10^{-2}$ M and $2.5\times10^{-4}$ M. For the highest concentration (**Figure 6-4a**), upon $NaBH_4$ addition, immediate degradation of 4-NTP

occurs, evidenced by the decrease of the characteristic bands at 228 nm and 408 nm. However, simultaneously, the AuNSs-LSPR band width decreases. After 20 minutes of reaction using constant stirring, degradation of 4-NTP continued, and a new peak appeared at 268 nm. However, the AuNSs-LSPR band vanished, indicating that $NaBH_4$ has destroyed the AuNSs. Ultimately, the peaks corresponding to 4-NTP completely disappeared, with the peak at 268 nm reaching its maximum intensity. Due to the destruction of the AuNSs, the $NaBH_4$ concentration was reduced to $2.5\times10^{-4}$ M (**Figure 6-4b**). Upon $NaBH_4$ addition, immediate changes were not apparent. However, after 20 minutes, a decrease in the peak at 408 nm and disappearance of the peak at 228 nm were noted. as well as alterations in the AuNSs-LSPR band. In these conditions, the concentration of $NaBH_4$ is too low for an efficient reduction of 4-NTP, but high enough to destroy the AuNSs. Consequently, employing $NaBH_4$ is not recommended due to the AuNS damage.

We proposed a reaction mechanism (**Figure 6-5)**, where 4-NTP molecules interact with metal catalysts through -SH groups, while $-NO_2$ groups do not directly contact the metal surface. Previous electrochemical studies demonstrated that reduction can occur without direct contact, as electrons can transfer through the molecule to $-NO_2$ groups.[195] Thus, electrons can be transferred either directly or through the thiophenol to the $–NO_2$ groups, suggesting that the reduction on our AuNSs likely occurs via electron transfer through the molecule, regardless of direct contact with the $-NO_2$ groups.

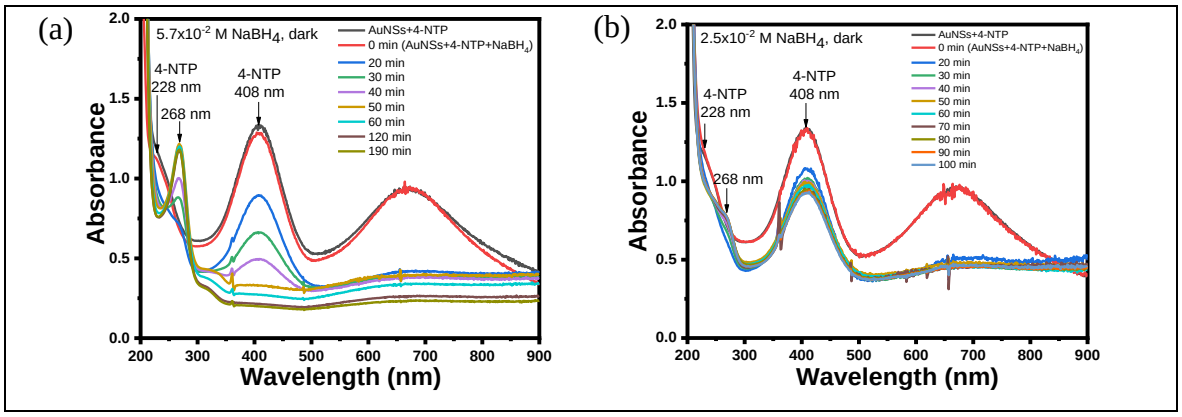


**Figure 6-4.** UV-vis spectra of the reduction of $1.64\times10^{-4}$ M 4-NTP using $NaBH_4$ as reductant under dark and air atmosphere conditions with different concentrations of $NaBH_4$ **(a)** $5.7\times10^{-2}$ M and **(b)** $2.5\times10^{-2}$ M. Optical path: 1 cm.

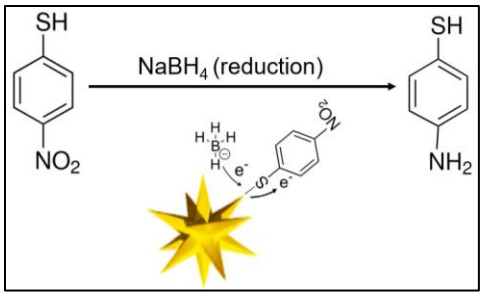


**Figure 6-5.** Reaction mechanism of the reduction of 4-NTP to 4-ATP using $NaBH_4$.

### 6.2.3 Plasmonic reduction of 4-NTP with AuNSs in solution

As mentioned before, the previously prepared aqueous solutions of AuNSs and AuSs had an acidic pH. The pH of AuNSs (2.6) and AuSs (5.6) was changed to 11 by adding few µL of 0.15 M NaOH solution. 2 mL of AuNSs ($[Au^0]=2.53\times10^{-4}$ M) alkaline aqueous solution were centrifuged and redissolved in 2 mL of Milli-Q water. Immediately, 750 µL of $6\times10^{-4}$ M 4-NTP alkaline aqueous solutions were added to the quartz reactor equipped with a magnetic stirrer and cap. In this case, the solution was degassed with $N_2$ for 40 minutes to maintain an inert atmosphere and stirred in darkness (cuvette covered with aluminium foil) to ensure optimal adsorption of 4-NTP.[208] Subsequently, the cuvette was exposed to visible light irradiation (**Figure 2-**

**20c**). To follow the degradation of 4-NTP, UV-visible spectra of the solutions were recorded at different time intervals.

After adding 4-NTP to the AuNSs, the maximum UV-visible absorption of the solution shifted: the LSPR band of AuNSs initially observed at 670 nm is shifted to 684 nm, after 40 minutes under stirring in the dark see **Figure 6-6a**. This shift is due to the adsorption of 4-NTP inducing an increase in the refractive index of the surrounding medium.[104,209] The reduction of 4-NTP by plasmon excitation of AuNSs in alkaline solution under visible light is followed by UV-visible spectroscopy. **Figure 6-6b** shows the evolution of the UV-visible spectrum of the irradiated solution during the 11-hour photocatalytic test. The characteristic absorption bands of 4-NTP at 228 nm and 408 nm regularly decrease in intensity under visible light irradiation, while a new band appears at 268 nm with two isosbestic points at 255 nm and 323 nm. This suggests that 4-NTP degradation involves a unique reaction and it is not accompanied by side products formation. This new band could be attributed to the formation of 4-ATP.[94] The LSPR band of AuNSs at 684 nm throughout the test remains stable, indicating the stability of the AuNSs during the photocatalytic reaction, as confirmed by TEM image, see Figure S6-4, Annex IV. After the photocatalytic reactions, AuNSs were easily recovered after centrifugation of the solution for 10 minutes at 13000 rpm see Figure 6-8b. In the absence of light, no reaction occurs, as shown in **Figure 6-6c**: the absorption bands at 228 nm and 408 nm corresponding to 4-NTP are similar over time. The degradation reaction happens only upon plasmon excitation of the AuNSs, generating hot electrons. As mentioned before, for the proposed reaction mechanism with $NaBH_4$, 4-NTP molecules interact with AuNSs through -SH groups, while $-NO_2$ groups do not directly contact the AuNSs surface. The hot electrons travel through the molecule, reducing the $-NO_2$ to $-NH_2$ groups (**Figure 6-7**). The results confirm that the plasmon effect of AuNSs under visible light contributes to the degradation of 4-NTP and the role of hot electrons in its reduction.

Similar experiments were conducted using AuSs instead of AuNSs at the same concentration in $Au^0$ (Figure S6-5, Annex IV). An initial shift of the LSPR band of AuSs from 522 nm to 530 nm is also observed after adding 4-NTP and its adsorption on the nanoparticles. Upon light irradiation the absorption bands of 4-NTP at 228 nm and 408 nm decrease, but more slowly compared to AuNSs. Also, a decrease in the plasmon band of AuSs at 530 nm is seen, indicating that the AuSs are not stable in contrast to AuNSs. Previous studies reported that spherical Au-NPs facilitated the degradation of 4-NTP under visible light irradiation.[94] However, they also noted changes in the LSPR band of the Au-NPs under $N_2$ atmosphere, attesting the instability and modifications in their morphology. In contrast, our findings demonstrate the unchanged morphology of AuNSs under $N_2$ atmosphere and visible light irradiation. Furthermore, the reaction kinetics was faster for AuNSs (**Figure 6-8**) than AuSs (Figure S6-6, Annex IV) under visible light. Additionally, AuNSs provided better efficiency and stability in reducing 4-NTP under visible light.

The photocatalytic tests of the AuNSs were also performed on one hand with addition of 2-propanol as a hole scavenger. In the case of hole scavenger, 21 µL of 2-propanol were introduced into the solution before degassing with $N_2$ gas. 2-propanol reacts with the holes to be oxidized, leading to the formation of acetone (Eq. 1).[210] On another hand under $N_2O$ as an electron scavenger, the solution was degassed with $N_2O$ for 40 minutes instead of $N_2$. The $N_2O$ can react with the hot electrons, as shown in Eq. 2. $HO^{\bullet}$ radicals are the main oxidizing species.[211]

$$2h^+ + CH_3CH(OH)CH_3 \rightarrow CH_3COCH_3 + 2H^+ \quad (1)$$

$$e^- + N_2O + H_2O \rightarrow HO^{\bullet} + HO^- + N_2 \quad (2)$$

According to **Figure 6-9** and **Figure 6-10**, 4-NTP degradation is faster with 2-propanol than $N_2O$ after 9 hours of irradiation. In both cases, degradation of 4-NTP occurs, but in the presence of 2-propanol, the reaction is faster than under $N_2O$. This enhancement may be attributed to the fact that the hot electrons achieve the reduction reaction over holes in the Au nanostars. However, notice that in the

presence of scavengers, the peak at 268 nm (as shown in **Figure 6-6b** and **Figure 6-4a)** is not so clear, suggesting that other products than 4-ATP are formed.

We also conducted a photocatalytic test for the degradation of 4-nitrophenol (4-NP), but no degradation was observed, as illustrated in Figure S6-7, Annex IV. Additionally, there was no detectable red shift after 40 min of adsorption. This indicates that the 4-NP molecules were not adsorbed on the AuNSs surface. There are two types of molecule-surface interactions: resonant coupling and non-resonant.[212] In resonant coupling, the orbitals of the molecule and surface atoms combine, leading to strong electronic coupling (chemisorption).

In contrast, non-resonant coupling keeps the orbitals with weak electronic coupling (physisorption) with Van der Waals force interactions. The atoms and molecules on the surface are far enough that their orbitals do not interact. As a result, the hot electrons cannot travel through the molecule and reduce the 4-NP. The interaction between plasmonic nanoparticles and molecules is necessary for efficient catalysis.

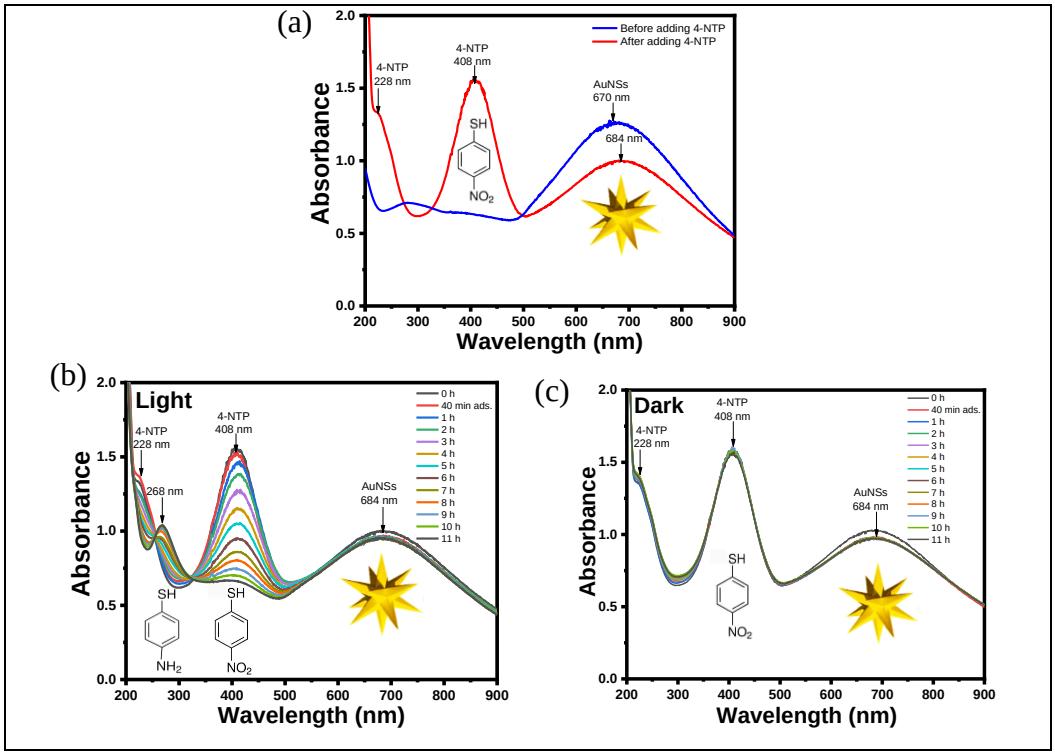


**Figure 6-6.** UV-visible absorption spectra of an alkaline aqueous solution **(a)** before and after adding 4-NTP (1.64×10-4 M) to the AuNSs ([$Au^0$] = 1.84×10-4 M), **(b-c)** under $N_2$ atmosphere, **(b)** visible light (λ>500 nm) irradiation and **(c)** dark. Optical path = 1 cm**.**

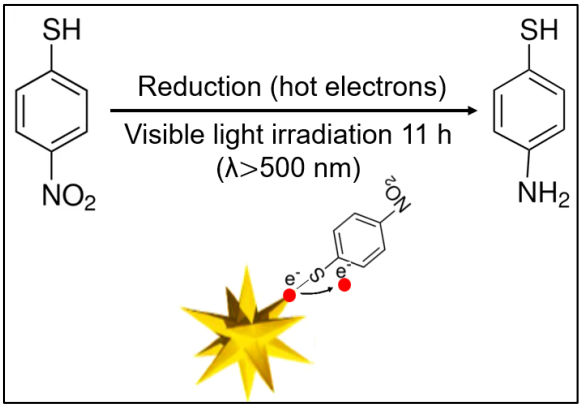


**Figure 6-7.** Reaction mechanism of the reduction of 4-NTP to 4-ATP using AuNSs as catalyst under visible light irradiation.

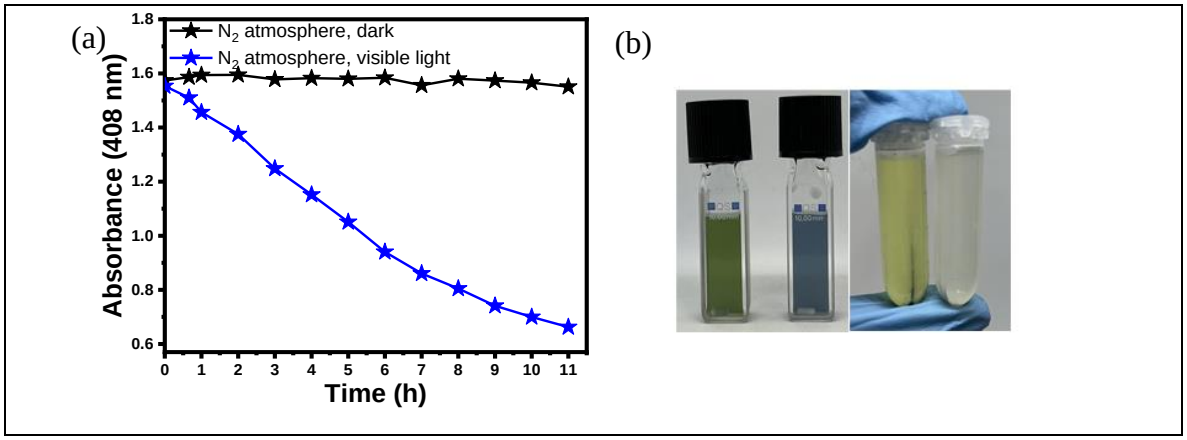


**Figure 6-8. (a)** Temporal evolution of the absorbance at 408 nm of alkaline aqueous solutions containing 4-NTP ($1.64\times10^{-4}$ M) and AuNSs ([$Au^0$] = $1.84\times10^{-4}$ M) under $N_2$ atmosphere and visible light (λ>500 nm) irradiation (blue) compared in the dark (black). **(b)** Photographs of the quartz cuvettes containing the aqueous solution before and after irradiation showing the color change from green to blue and from yellow to colorless after centrifugation and removal of the AuNSs.

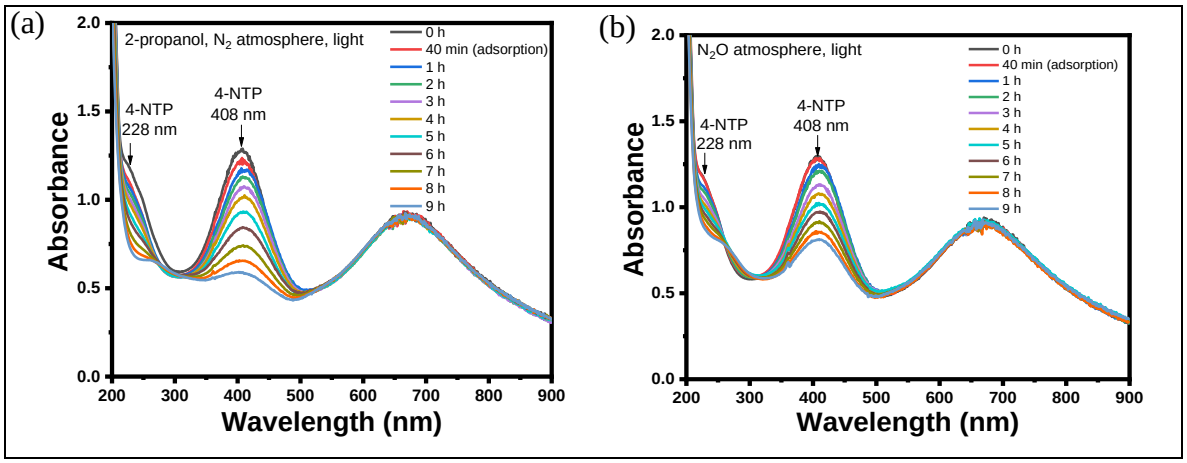


**Figure 6-9.** UV-visible absorption spectra of an alkaline aqueous solution containing 4-NTP ($1.64\times10^{-4}$ M) and AuNSs ([$Au^0$] = $1.84\times10^{-4}$ M) under visible light (λ > 500 nm) **(a)** 0.1 M of 2-propanol as hole scavenger and $N_2$ atmosphere, and **(b)** $N_2O$ atmosphere as electron scavenger. Optical path = 1 cm.

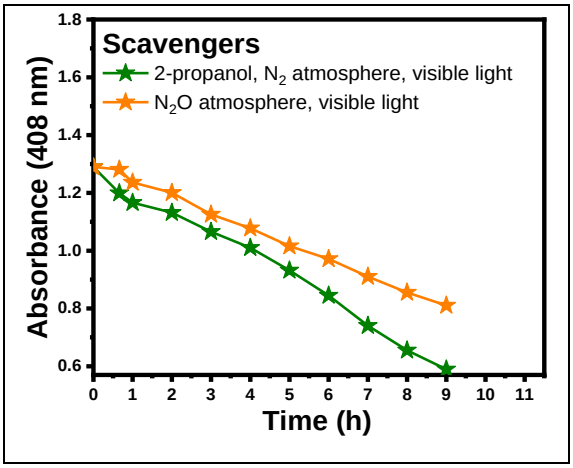


**Figure 6-10.** Temporal evolution of the absorbance at 408 nm of alkaline aqueous solutions containing 4-NTP ($1.64\times10^{-4}$ M) and AuNSs ([$Au^0$] = $1.84\times10^{-4}$ M) under visible light (λ>500 nm) irradiation, green: hole scavenger (2-propanol) under $N_2$ atmosphere, and orange: electron scavenger ($N_2O$)**.**

**AuNSs on glass substrate:** To get a better insight into the interaction of the target molecule (4-NTP) with the Au nanostars and the degradation reaction, a study was carried out on AuNSs deposited on a glass substrate. Figure S6-8, Annex IV, displays dark field images of the glass substrates obtained after different contact times with the AuNSs solution, in which the AuNSs are visible as bright spots due to

their optical scattering. After 1 minute of contact, numerous well dispersed AuNSs were present indicating a good adhesion of the particles on the modified glass surface (Figure S6-8a, Annex IV). After 5 minutes, an increase in the number of AuNSs was observed (Figure S6-8b, Annex IV), while after 15 minutes, the AuNSs started to agglomerate (Figure S6-8c, Annex IV). To enable spectrum analysis of individual AuNSs, the glass substrate in contact for 1 minute, where the AuNSs are well separated, was chosen and 31 AuNSs (bright spots) were selected (**Figure 6-11**).

The visible spectra of the 31 nanostars without 4-NTP labeled from 0 to 31 were recorded in the spectral range 490 – 730 nm corresponding to the LSPR domain, and the reproducibility of the measurements was checked by replicating the spectrum acquisition on the same particles on the first 11 AuNSs (Figure S6-9, Annex IV). The accuracy over the LSPR peak is evaluated at 3 nm. Most of these nanostars displayed a broad LSPR band with a shape suggesting the presence of two bands within our spectral window, while a few exhibited a narrower LSPR band with a more defined maximum, suggesting only one band. Previous papers have already reported single and double bands for AuNSs on glass substrates.[213,214,188,215,216,217] These resonance bands correspond to dipolar and multipolar plasmon modes of the spikes.[193] Deconvolution of the LSPR bands into two components was performed with Gaussian functions using Origin software.

**Figure 6-12** shows the adjustment quality of such deconvolution for four AuNSs. The position and intensity of the two peaks vary from one AuNS to the others. Actually the peak#1 varies from 543 nm to 620 nm and peak#2 from 622 to 700 nm over the 31 AuNSs. These large variations underline the diversity of the AuNSs, as already shown in the TEM images. Moreover, the AuNSs are randomly oriented on the glass substrate. Recent simulation research has explained that the localized surface plasmon resonances of individual nanostars depend on their symmetry and orientation relative to the substrate.[213] These results underline the importance of being able to monitor individual nano-objects.

Then, the spectra of the same 31 nanostars with 4-NTP were recorded. The glass substrate was put in contact for 1 minute in a glass container with the aqueous solution of 4-NTP for 40 minutes under $N_2$ atmosphere without stirring. Subsequently, the slide was rinsed with Milli-Q water and dried with $N_2$ gas for analysis.

For 21 of the AuNSs, a redshift of the LSPR band is observed indicating a change in the refractive index of the surrounding medium,[209] in agreement with the adsorption of 4-NTP, as already observed in solution (**Figure 6-6b**). The shift is negative for the other 10 nanoparticles, probably due to a slight displacement of the nanostar triggered by the adsorption, changing the coupling of the plasmon peaks with the surface. In the following, we concentrate on the AuNSs that exhibit a positive shift.

Besides, other groups have also used AuNSs in different configuration for monitoring molecular adsorption and they found a spectral shift of 7 and 9 nm for Peak#1 and Peak#2 respectively.[189] Moreover, the sensitivity factor of AuNSs was measured to be $m$ = 220. From this value, we could compute using the Van Duyne formula that the expected LSPR shift for a molecule like 4-NTP if it completely cover the AuNSs is +26 nm.[104] Therefore, from these considerations, we will concentrate on the 16 NSs that exhibit a positive spectral shift between 2 and 20 nm.

The spectra of the same 31 nanostars with 4-NTP were recorded after 11 hours of irradiation. The glass substrate was immersed in a glass container containing the 4-NTP solution again for 40 minutes under $N_2$ atmosphere without stirring. The glass container with the plate was put under irradiation with the side where the nanostars were located parallel to the lamp to receive the irradiation directly. Finally, the slide was rinsed with Milli-Q water and dried with $N_2$ gas for analysis.

In comparison with the spectra recorded with 4-NTP before irradiation, most of the LSPR bands exhibit a blue shift. The blue shift after irradiation is attributed to the

change in the refractive index of the surrounding medium: it means that 4-NTP molecules around the AuNSs were degraded. However, for some AuNSs the initial spectra obtained before 4-NTP adsorption were not recovered. This suggests that there are still some organic molecules around the AuNSs, either 4-NTP or reaction products.

**Figure 6-12** presents the LSPR spectra of four AuNPS (bright spots), initially without 4-NTP adsorption and after 4-NTP adsorption before and after irradiation. We observed that the red shift and the subsequent blue shift depend on the AuNSs. AuNS#8 exhibited a considerable red shift after the adsorption of 4-NTP, with a subsequent blue shift upon irradiation due to 4-NTP degradation. In contrast, AuNS#9, displayed negligible red shift and lacked a significant blue shift after irradiation AuNS#7 showed a notable red- shift of peak 2 only after 4-NTP adsorption, but significant blue shift of both peaks after irradiation AuNS#5 exhibited a considerable red shift after 4-NTP adsorption, followed by a blue shift after irradiation due to 4-NTP degradation.

**Figure 6-13** summarizes the plasmon shifts for seven AuNSs, where the positive shift induced by the adsorption of 4-NTP is clearly identified (average value is +8.0 nm and +14.3 nm for peak#1 and peak#2, respectively). The negative shift after irradiation is also clearly visible with values of −17.6 nm and -18.7 nm for peak#1 and peak#2). The complete values of the LSPR peak positions and shifts are given in Figure S6-9, Annex IV. What is striking is that the peaks shift downwards more intensively after irradiation (−17.6 nm), than after 4-NTP adsorption. This indicates that there were some surfactant remaining and preventing the nanoparticles from complete coverage with 4-NTP, and the irradiation induces a photoreaction that completely removed the adsorbed species. To identify the origin of such variations, these AuNSs were observed by AFM (**Figure 6-14**). We found that the bright spots labeled 8 and 9 corresponded to a single AuNS with size of 118 and 88 nm, respectively, whereas the bright spots labeled AuNS 5 and 7 were composed of two AuNSs, with sizes of 100 and 108 nm for the former, and 110 and 125 nm for the

latter. Overall, nanostars 8, 7, and 5 exhibited more significant shifts than nanostar 9, with Peak 2 being more sensitive than Peak 1. The AFM results suggest that AuNSs with larger sizes see **Figure 6-15,** present the larger shift suggesting an enhancement of adsorption and degradation of 4-NTP.

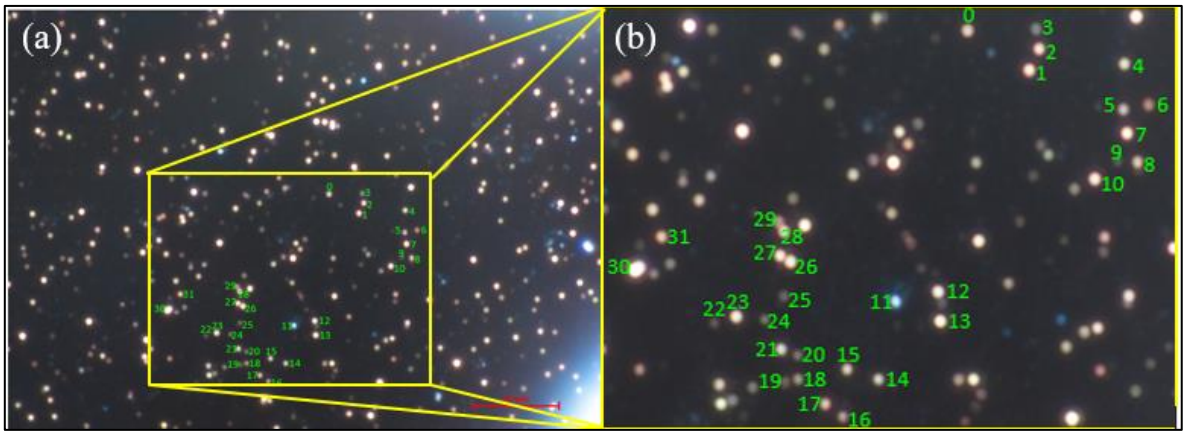


**Figure 6-11.** Dark-field optical microscopy image of AuNSs deposited on the glass substrate **(a)** after 1 minute of contact and **(b)** the zoom image of the nanoparticles selected.

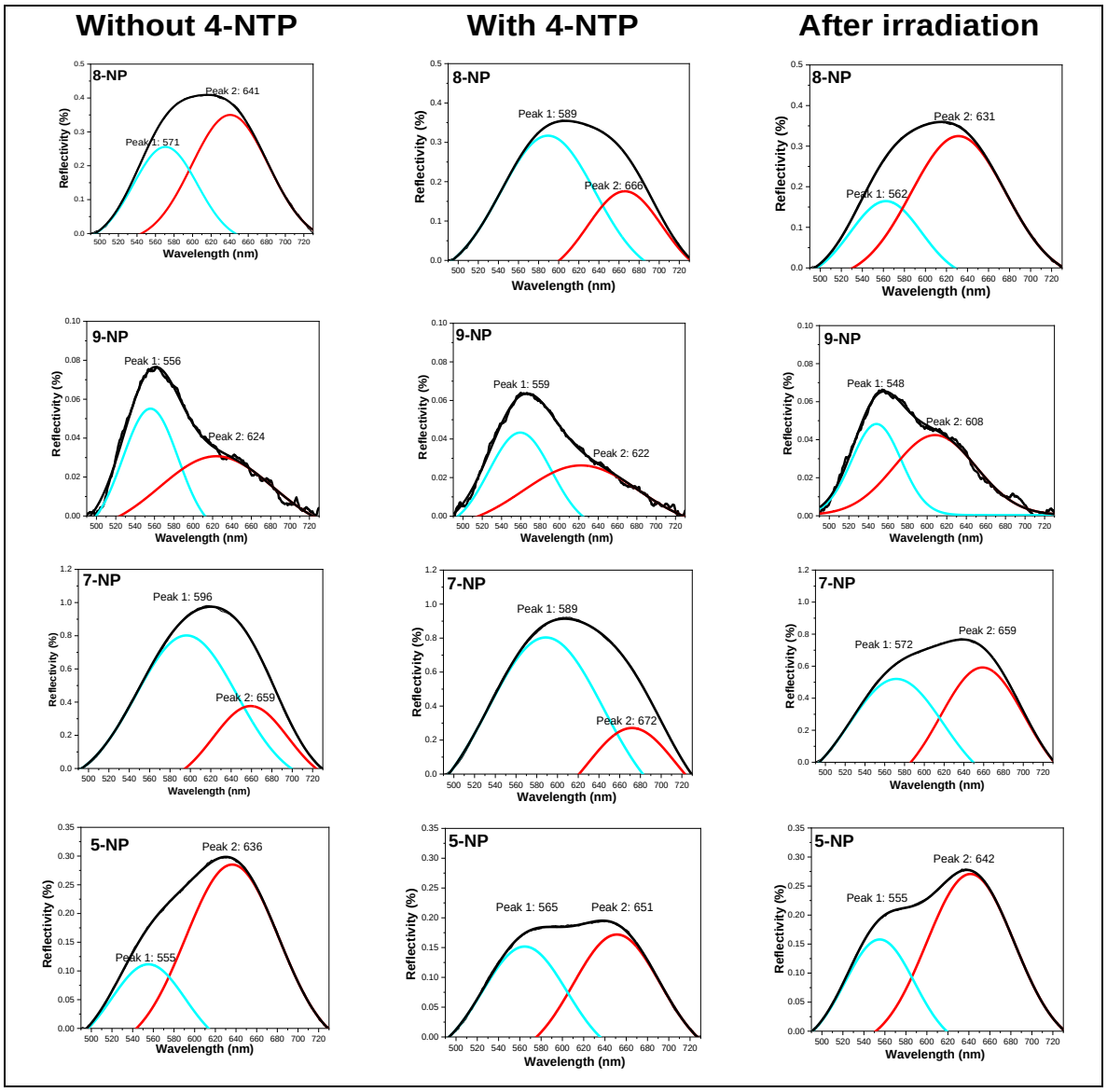


**Figure 6-12.** Scattering spectra of Au nanostars 8, 9, 7 and 5, without 4-NTP, with 4-NTP and after visible light irradiation, with their deconvoluted Peak 1 and Peak 2 using Gaussian function with Origin Software.

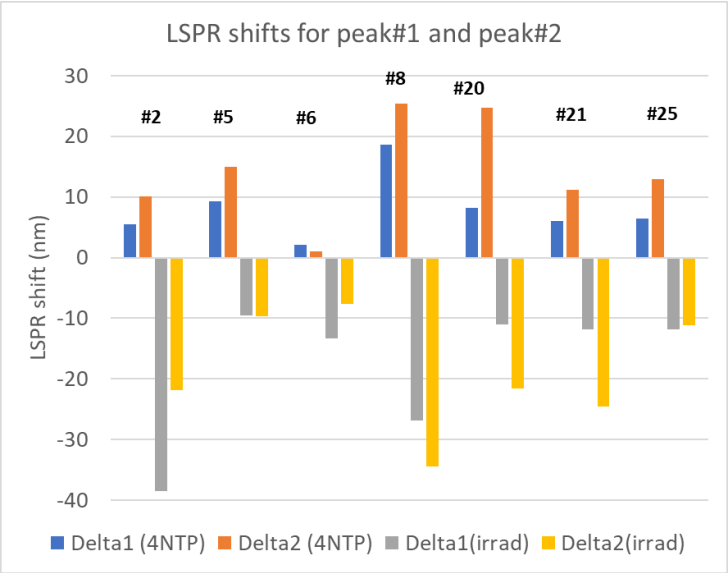


**Figure 6-13.** Plasmonic shift of peak#1 and peak#2 for seven AuNSs, after adsorption of 4-NTP (blue and orange) and after irradiation (grey and yellow).

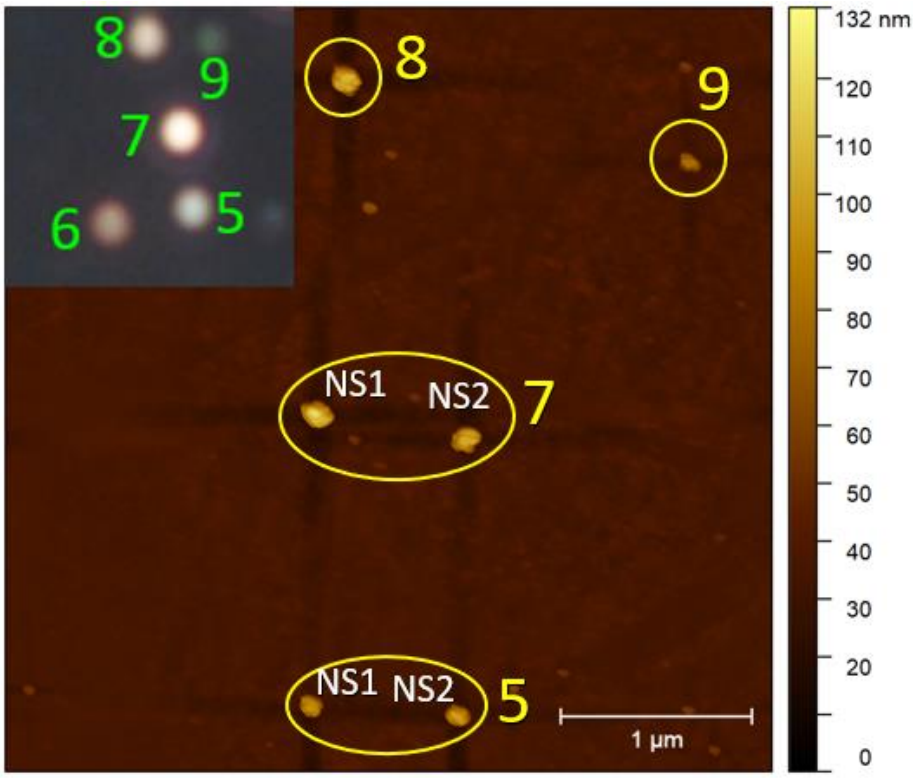


**Figure 6-14.** AFM image (4x4 µm²) of the bright spots in dark field optical microscopy (inset image) labeled AuNS 5, 7, 8, and 9.

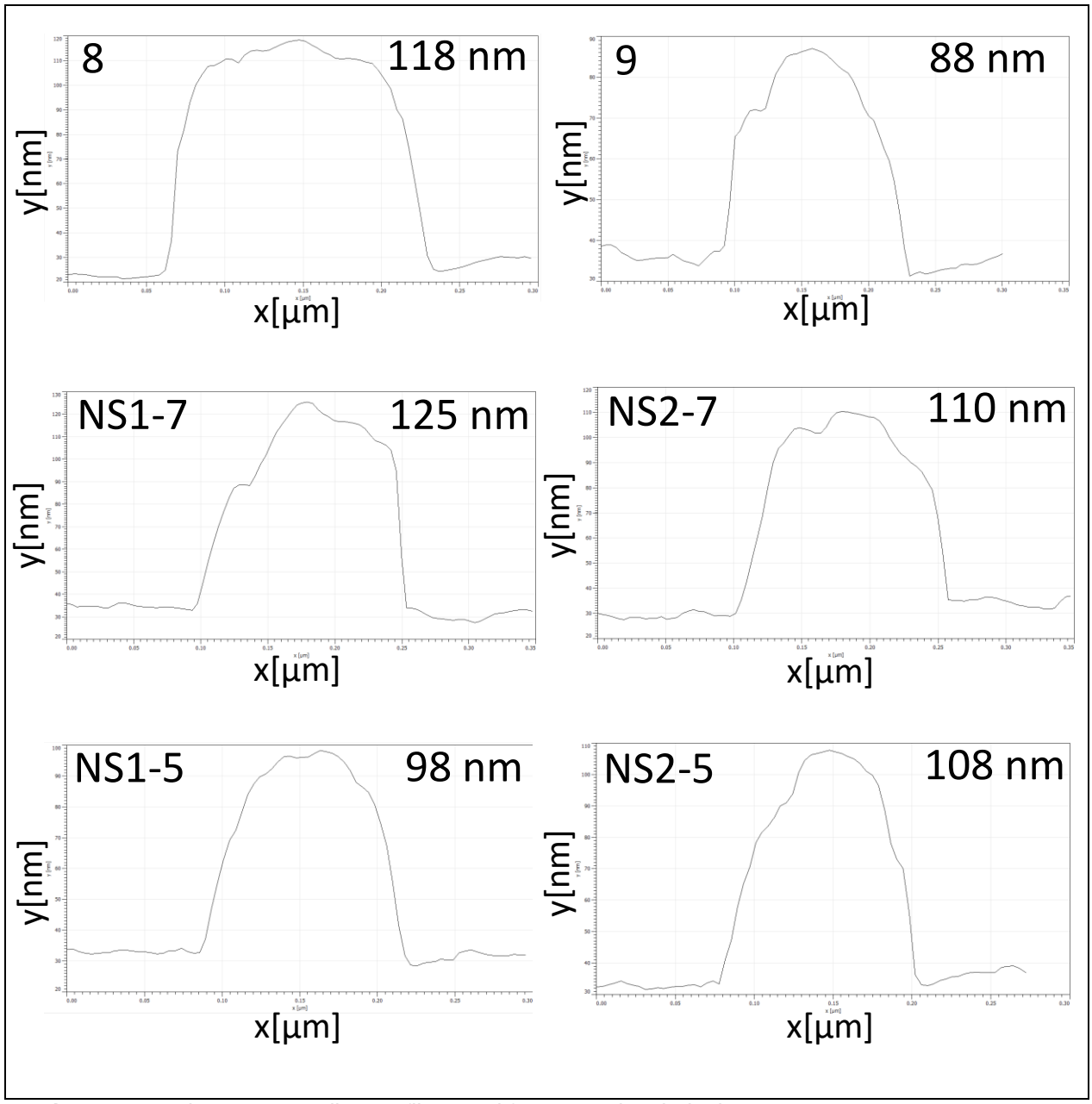


**Figure 6-15.** The corresponding profiles used for measuring their sizes.

## 6.3 Conclusions

In conclusion, the synthesis of AuNSs was achieved using the seed-growth method, resulting in nanostars of different sizes ranging from 80 nm to 120 nm and with a maximum absorbance at 670 nm. The plasmonic properties of these AuNSs were used for the photocatalytic reduction of 4-NTP a toxic molecule into a less toxic one 4-ATP. The reaction kinetics of the reduction of 4-NTP to 4-ATP was analyzed using UV-vis spectroscopy, revealing that the plasmon excitation of AuNSs effectively induced the reduction under visible light irradiation compared to dark conditions. Scavenging experiments show the importance of generated hot electrons under plasmonic excitation. The experiments highlight that the adsorption of the target molecule on the Au nanoparticles is important for plasmonic catalysis. Hot electrons can recombine very fast with holes or react with the surrounding molecules. Indeed, if the target molecule is too far from the plasmonic nanoparticles (more than few nanometers), it cannot be reduced by hot electrons.

Furthermore, AuNSs are more effective for 4-NTP reduction than Au nanospheres (AuSs) because of the presence of hot spots. The AuNSs are stable with cycling and can be easily recovered after the photocatalytic tests.

Dark-field optical microscopy coupled with optical spectroscopy and correlated with AFM analysis suggests that the largest AuNSs (i.e. with long spikes) are the most efficient. These results indicate that AuNSs can be stable and efficient catalysts for the degradation of pollutants under visible light irradiation and other applications in plasmonic catalysis.

# Chapter 7

Conclusions and Perspectives.

# Chapter 7. Conclusions and Perspectives

The research presented in this PhD thesis provides significant insights into the enhancement of photocatalytic activities through surface modification of $TiO_2$ and the use of transition metals NPs including plasmonic NPs for hydrogen generation and water treatment.

After an exhaustive study of the state of the art and set up of the project in **Chapter 1** as an Introduction, and after the description in **Chapter 2**, the synthesis methods used for the systems applied in this thesis. **Chapter 3** starts the exploration of the surface modification of $TiO_2$ with AuPd nanoalloys by chemical reduction method for hydrogen generation. These bimetallic systems improve photocatalytic hydrogen generation under UV-visible light. The observed synergy between Au and Pd in the AuPd/$TiO_2$ composites leads to a notable increase in photocatalytic efficiency compared to their monometallic counterparts. This enhancement is attributed to improved morphology, optical properties, and charge carriers' dynamics. In particular, the $Au_9Pd_1/TiO_2$ sample exhibits excellent stability and performance, highlighting its potential as a highly effective cocatalyst for hydrogen production, comparable to Pt-based catalyst. Experimental results are supported by Density Functional Theory (DFT) and Density Functional Tight Binding (DFTB+) calculations, which show that alloying AuPd with low Pd content presents significant synergetic effects for hydrogen generation under UV-visible light. These theorical calculations are a collaboration between France (ICP) and Mexico.

This work provides insights into the electron transfer of bimetallic nanoparticle-modified $TiO_2$ during the photocatalytic hydrogen evolution reaction. Also, it proposes an effective strategy for the rational design of bimetallic nanoparticle-based cocatalysts. These results are a key first step to reduce the use of expensive and/or scarce metals and the cost of the photocatalyst, and thus promote its practical application in solar energy conversion and solar fuel production.

These results are now published in the journal *Solar RLL*, a work that deserved the main frontal cover of the journal.

**Chapter 4** focuses on the modification of $TiO_2$ with Ni-based NPs by radiolysis method, particularly using nickel (II) acetylacetonate as a precursor. This approach significantly boosts hydrogen generation rates. The formation of a *p-n* heterojunction between NiO-NPs and $TiO_2$ plays a crucial role in enhancing charge carriers' separation and photocatalytic activity under UV-visible light. However, issues with Ni leaching are presented in these systems. Future work will focus on the development of nanoalloys based on Ni (such as NiAu or NiPt), we expect that these co-catalysts will be very active and stable for hydrogen generation. Alloying Ni with Au or Pt will avoid its oxidation and leaching.

In **Chapter 5**, $TiO_2$ was surface-modified with NiFe NPs induced by radiolysis, which is a very effective method to synthesize nanoalloys. These bimetallic photocatalysts based on abundant metals show enhanced hydrogen production compared to their monometallic counterparts, a synergetic effect is obtained. Further investigations into the oxidation states and charge carriers' dynamics is on work. DFT calculation will be performed to understand the role of the cocatalysts and the nanoalloys in hydrogen reduction and formation of H-H bond. Trimetallic cocatalysts will be synthesized by radiolysis (such as NiFeAu, or NiFePt) to enhance the catalytic activity and improve the stability and limit metal leaching.

**Chapter 6 deals with plasmonic catalysis based on Au nanostrars. It** investigates the synthesis of gold nanostars (AuNSs) using a seed-growth method, revealing their effectiveness in plasmonic catalysis for the reduction of 4-NTP to 4-ATP (a less toxic compound) under visible light. The high catalytic activity of AuNSs is attributed to the presence of hot spots in larger nanostars. This study underscores the role of plasmonic excitation in enhancing reaction rates, the importance of hot spots, and the effective adsorption of molecules to the metal surface for effective catalysis.

Overall, these findings collectively advance our understanding of photocatalytic and plasmonic systems, demonstrating the potential of various nanomaterials and modifications to enhance catalytic performance and stability. The continued exploration of alloyed and modified photocatalysts offers promising avenues for sustainable energy applications and efficient pollutants' degradation.

Future research should explore alloyed and composite photocatalysts, focusing on bi- and tri-metallic alloys with transition metals to enhance the stability, activity, and efficiency of the photocatalysts for solar fuel generation. Optimizing synthesis methods, addressing issues like metal leaching, and understanding charge carriers' dynamics are crucial for developing more effective and durable photocatalysts. Further studies on these mechanisms will be essential for advancing photocatalyst knowledge of their performance in sustainable energy and environmental applications. Theoretical investigations and in-situ studies at Synchrotron Soleil will be conducted to understand the photocatalytic mechanisms, which will help in the development of very active and durable photocatalysts. Applications for $CO_2$ reduction with bimetallic NPs will be also studied.

# Annex I. Chapter 3

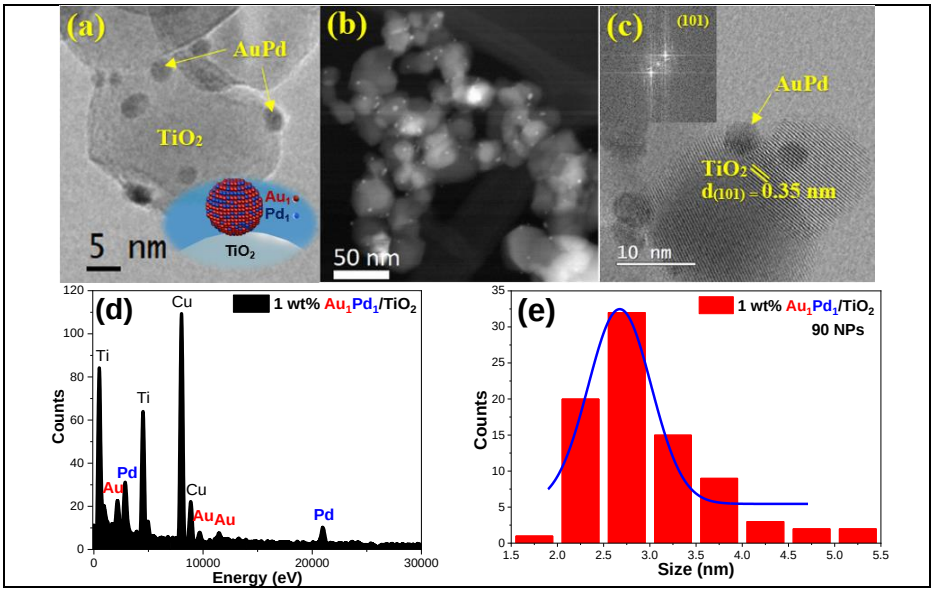


**Figure S3-1.** TEM micrographs of 1 wt% $Au_1Pd_1/TiO_2$ sample in **(a)** bright field and **(b)** *Z* contrast show spherical AuPd-NPs well-dispersed on $TiO_2$ surface, **(c)** HRTEM micrograph showing the localization of AuPd-NPs on the anatase phase, **(d)** EDS analysis showing the presence of the elements Au, Pd, Ti, and Cu (from the TEM grid), and **(e)** histogram of AuPd-NPs shows an average size of ~2.7 nm.

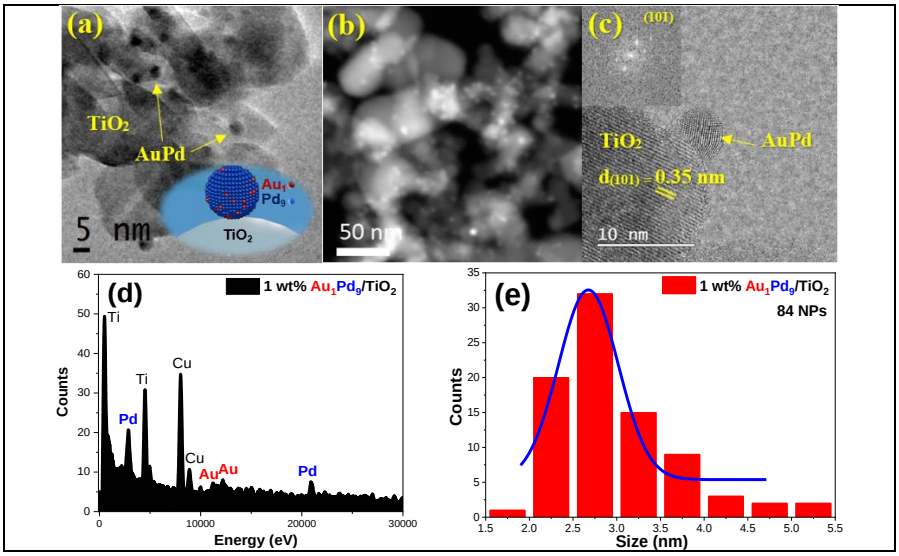


**Figure S3-2.** TEM micrographs of 1 wt% $Au_1Pd_9/TiO_2$ sample in **(a)** bright field and **(b)** *Z* contrast show spherical AuPd-NPs well-dispersed on $TiO_2$ surface, **(c)** HRTEM micrograph shows the localization of AuPd-NPs on the anatase phase, **(d)** EDS analysis showing the presence of the elements Au, Pd, Ti, and Cu (from the TEM grid), and **(e)** histogram of AuPd-NPs showing an average size of ~2.7 nm.

**Table S3-1.** The average size of 1wt% AuPd/$TiO_2$ modified samples.

| Bimetallic samples | AuPd NPs average size | NPs measured |
|---|---|---|
| 1 wt% $Au_1Pd_9/TiO_2$ | 2.7 nm | 84 |
| 1 wt% $Au_1Pd_1/TiO_2$ | 2.7 nm | 90 |
| 1 wt% $Au_9Pd_1/TiO_2$ | 2.6 nm | 142 |
| AuPd-NPs size was measured with Image J software. | | |

**Table S3-2.** ICP-OES results for 1wt% AuPd/$TiO_2$ modified samples.

| Metal | Samples | | |
|---|---|---|---|
| | 1 wt% $Au_1Pd_9/TiO_2$ | 1 wt% $Au_1Pd_1/TiO_2$ | 1 wt% $Au_9Pd_1/TiO_2$ |
| **Au** | 0.14 wt% | 0.41 wt% | 0.81 wt% |
| **Pd** | 1.03 wt% | 0.53 wt% | 0.25 wt% |

Scherrer's equation was used to measured the crystallite size of $TiO_2$ ~20.6 nm from (101) anatase diffracted peak (**Equation S1**). Where $D_{(hkl)}$ is the crystallite size (nm) in the direction vertical to the corresponding lattice plane, λ is the X-ray wavelength equal to 0.154 nm, β is the width of the peak full width at half maximum (FWHM) after correcting for instrumental peak broadening (β expressed in radians), θ is the Bragg angle, and K is the Scherrer constant. K value depends on the crystal shape. In this case, $TiO_2$ crystallite is taken as spherical particles K~1.[218,219]

$$D_{(hkl)} = \frac{K\lambda}{\beta \cos\theta} \qquad \textbf{(Equation S1)}$$

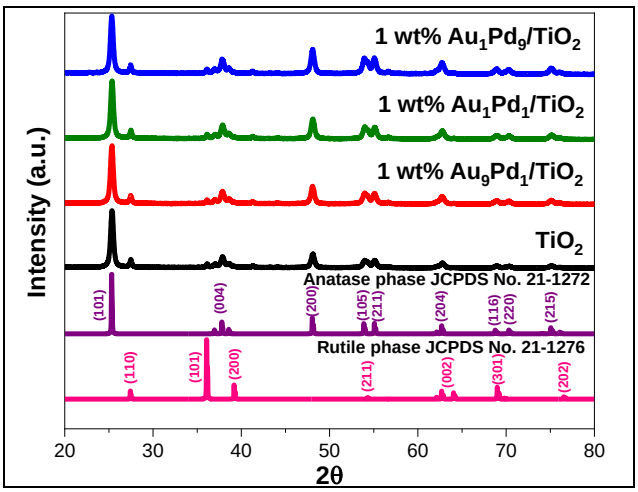


**Figure S3-3.** X-Ray Diffraction (XRD) pattern of 1 wt% AuPd/$TiO_2$ samples and bare $TiO_2$ with the reference peaks of the anatase and rutile crystalline phases.

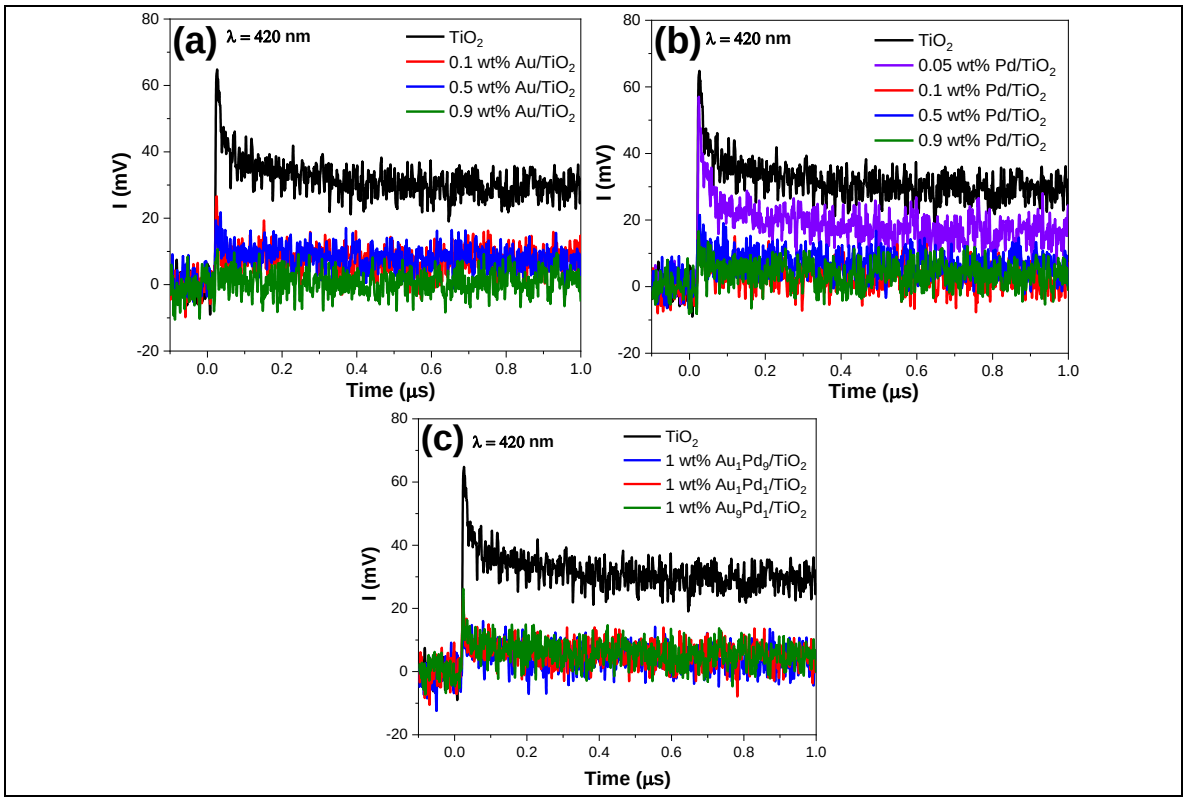


**Figure S3-4.** TRMC signals of monometallic photocatalysts **(a)** Au/$TiO_2$, **(b)** Pd/$TiO_2$ and **(c)** bimetallic photocatalysts 1 wt% AuPd/$TiO_2$ at $\boldsymbol{\lambda_{exc}}$ **=** 420 nm with a laser energy of 9 $mJ$.

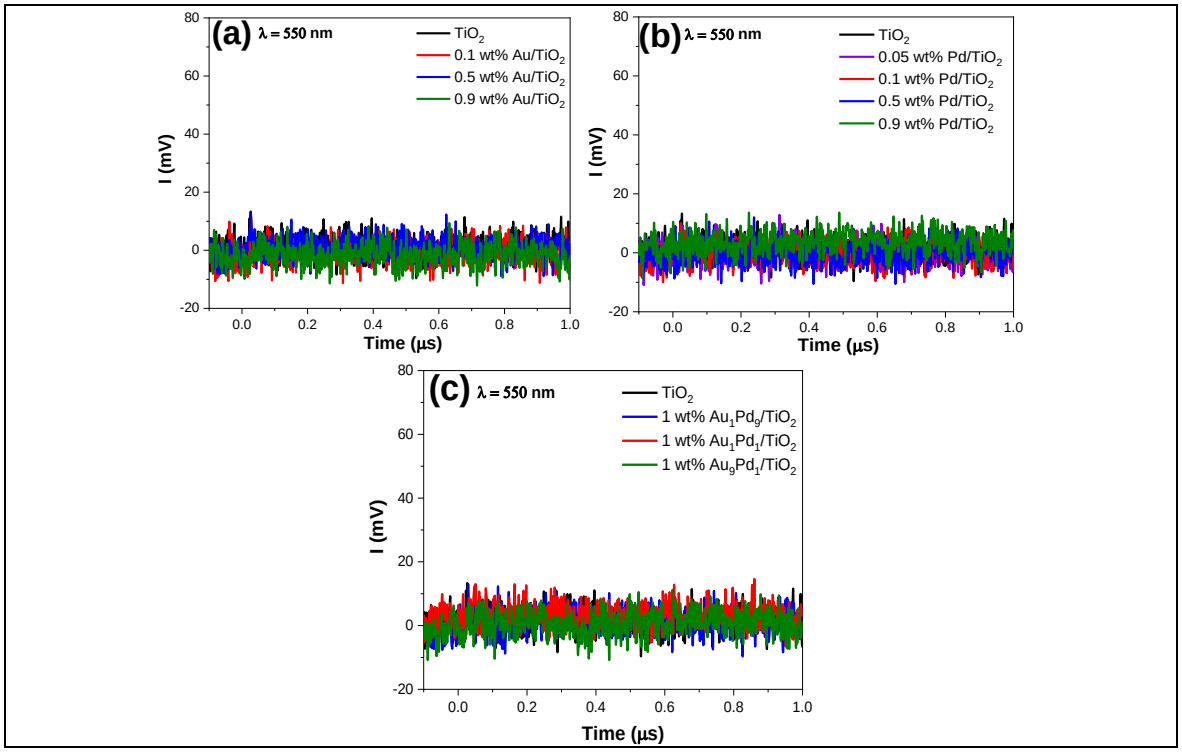


**Figure S3-5.** TRMC signals of monometallic photocatalysts **(a)** Au/$TiO_2$, **(b)** Pd/$TiO_2$ and **(c)** bimetallic photocatalysts 1 wt% AuPd/$TiO_2$ at $\boldsymbol{\lambda_{exc}}$ **=** 550 nm with a laser energy of 7.3 $mJ$.

**Table S3-3.** Comparison of photocatalytic hydrogen generation by metal-modified $TiO_2$ photocatalysts under UV and visible light irradiation.

| Samples | Scavenger | Lamp | Hydrogen generation | Ref. |
|---|---|---|---|---|
| 1 wt% $Au_9Pd_1/TiO_2$ | 25 vol% TEOA | Mercury Lamp | 2325 μmol $g^{-1}$ $h^{-1}$ ~ 30 times higher than $TiO_2$ | Our work |
| 1 wt% $Au_9Pd_1/TiO_2$ | 25 vol% TEOA | 300 W Xe Lamp (λ≥420 nm) | 13.0 μmol $g^{-1}$ $h^{-1}$ | Our work |
| 0.5 wt% $Au_9Pd_1/TiO_2$ | 25% vol% TEOA/ | Mercury Lamp | 2467.9 μmol $g^{-1}$ $h^{-1}$ ~ 32 times higher than $TiO_2$ | Our work |
| 0.5 wt% $PdAu/TiO_2$ | 50% v/v methanol | Solar simulator equipped with a 300W Xe lamp | ~22 μmol $g^{-1}$ $h^{-1}$ | 68 |
| 0.5 wt% $PdAu/TiO_2$ | 50% v/v methanol | 375 nm-LEDs | ~240 μmol $g^{-1}$ $h^{-1}$ | 68 |
| 1wt% $Pd_{shell}Au_{core}/TiO_2$ | 25% v/v glycerol | UV LED (365 nm) | 19.6 mol $kg^{-1}$ $h^{-1}$ | 19 |
| 1-$Ni_1Pd_{10}/TiO_2$ | 50% v/v methanol | Mercury Lamp | ~220 μmol $g^{-1}$ $h^{-1}$ | 15 |
| 0.5 at% Ni:Au 5:1/$TiO_2$ | 50% v/v methanol | Mercury Lamp | ~150 μmol $g^{-1}$ $h^{-1}$ | 8, |
| 0.1 wt%PtNi/PPy | 25% v/v methanol | 300 W xenon lamp | 664 μmol $g^{-1}$ $h^{-1}$ | 150 |
| $CoO_x/TiO_2/Pt$ | 15% v/v methanol | UV- 35 $mWcm^{-2}$ | 275.9 μmol $h^{-1}$ ~ 5 times higher than $TiO_2$ | 220 |
| 1.0 wt% $Pd_{0.7}Ag_{0.3}$/g-$C_3N_4$ | 10 vol% TEOA | 840 $Wm^{-2}$ (300–1100 nm) | 1250 μmol $g^{-1}$ $h^{-1}$ | 221 |

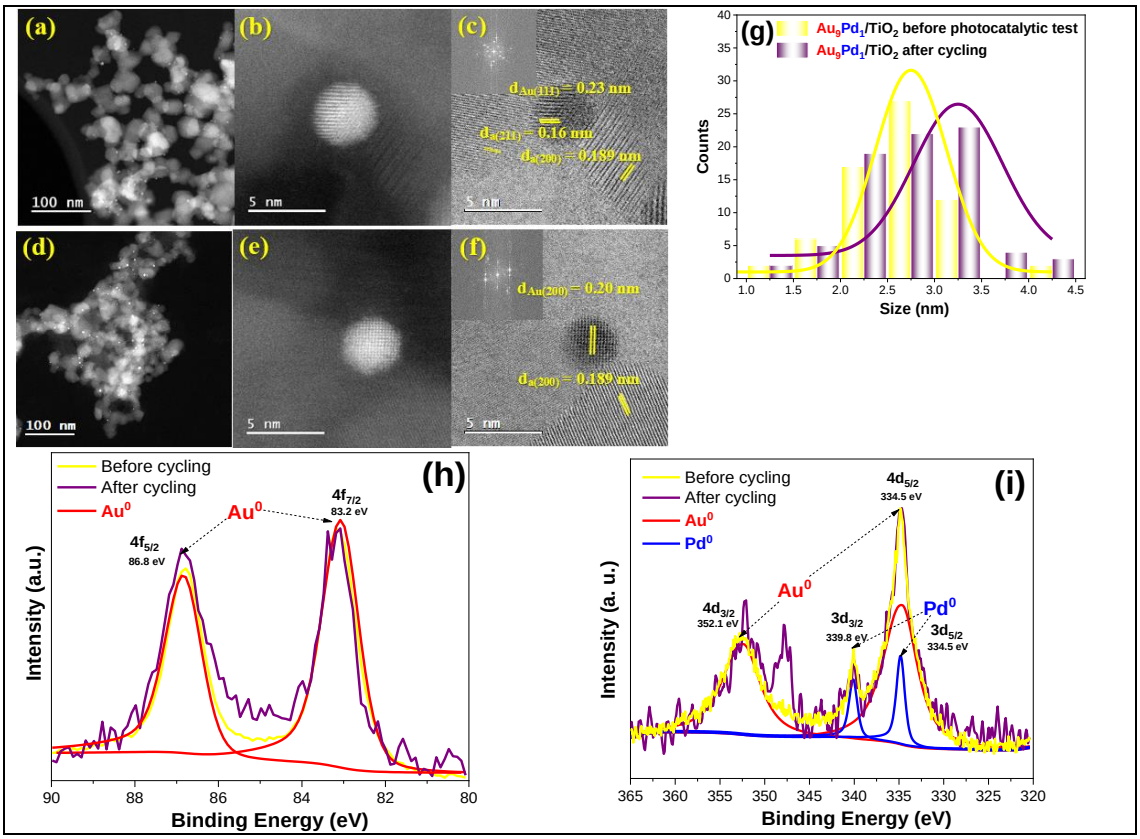


**Figure S3-6.** TEM images in dark field of 0.5 wt% $Au_9Pd_1/TiO_2$ sample **(a)** before and **(d)** after cycling. HAADF-STEM micrographs **(b)** before and **(e)** after cycling. HRTEM micrographs **(c)** before, and **(f)** after cycling. **(g)** The histograms analysis showing AuPd-NPs size increases after cycling. From **(h)** to **(i)** XPS spectra signals of 0.5 wt% $Au_9Pd_1/TiO_2$ sample, **(h)** Au-4f core level and **(i)** Au-4d and Pd-3d core levels. After cycling, the XPS spectra are noisy compared to those before cycling this can be attributed to metal loss after recovering the powder by centrifugation.

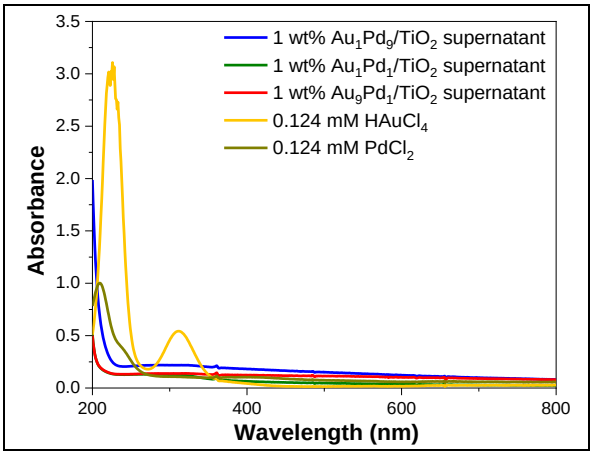


**Figure S3-7.** UV-vis spectra of bimetallic supernatants and salt precursors. Optical path = 1cm.

## DFT calculations and chemical bond analyses

The $Au_{38}$ cluster was considered as a model of small Au-NPs and 4 Au atoms were substituted by 4 Pd atoms at the surface to build the $Au_{34}Pd_4$ cluster. Two hydrogen atoms were added close to the surface on two adjacent atoms, Au-Au or Au-Pd. Several starting points were tested, see **Figure 3-9** for a case for $Au_9Pd_1$. The geometry optimization calculations were carried out at the DFT level using the ORCA 5.0.3 software.[222] The PBE GGA functional was used in association with dispersion corrections in the D3 framework proposed by Grimme with the addition of the Becke–Johnson damping (D3BJ).[223] The SDD pseudopotential (with 19 and 18 valence-electrons treated explicitly for Au and Pd atoms, respectively) and the associated basis set were used for the metal atoms, and the def2-SVP basis set was used for hydrogen atoms. Numerical frequencies were calculated to ensure that the structures corresponded to energy minima. For all the calculations, the 38-atom NP was considered in the singlet spin state. The quantum chemical analyses were performed with the Multiwfn code by analyzing the electron density generated from ORCA.[224] The electron localization function (ELF) was calculated to determine the valence basins.[225]

**Table S3-5.** Structural and electronic properties of $Au_{38}$-$H_2$ and $Au_{34}Pd_4$-$H_2$. "Au only" stands for the Au site with one hydrogen atom. "Au and Pd" refers to the metal atoms around the shared hydrogen.

| | **$Au_{38}$-$H_2$** | **$Au_{34}Pd_4$-$H_2$** |
|---|---|---|
| **Au-H (Å)** | 1.611<br>1.612 | 1.612 (Au only), 1.772 (Au and Pd) |
| **Pd-H (Å)** | - | 1.686 |
| **Au-Au (Å) on average around H atoms** | 2.9-3.0 | 2.9-3.0 (Au only), 2.83-2.87 (Au and Pd) |
| **Au-Pd (Å) on average** | - | 2.803,2.780, 2.803, 2.834 |
| **Au-H Mayer bond order** | 0.86 | 0.88 (Au only), 0.38 (Au and Pd) |
| **Pd-H Mayer bond order** | - | 0.37 |
| **M-H valence ELF basin population (e)** | 1.7 | 1.7 (Au-H), 1.6 (Au-Pd-H) |

## Semiempirical hybrid MD-MC and DFTB+ calculations

### Chemical order

To find the chemical order of the nanoparticles in the three different ratios of Au and Pd, a cuboctahedron of 1286 atoms was used as a model, in which, randomly (complying with the chosen ratio), the type of atomic species was generated (Au or Pd) at each atomic position. As a next step, a hybrid MD-MC (Molecular Dynamics-

Monte Carlo) simulation was carried out for each of the ratios (**Figure S3-8**), considering room temperature.

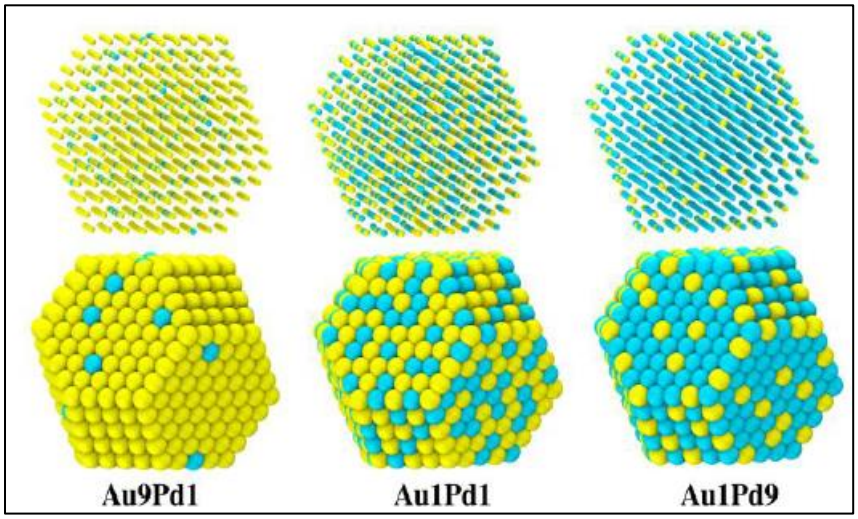


**Figure S3-8.** Resulting alloyed structures for the three ratios used in this study.

4 MC steps were carried out (atomic swaps between Au and Pd) every 100 steps of MD (T = 298 K). This led the system towards the lowest energy configuration (chemical order), preserving the geometry/structure of the nanoparticle. The interaction potential was the Gupta functional form.[226] This interatomic potential has been proven that it is capable of reproducing the chemical order in different types of systems (bulk, nanoparticles, etc.) in a good way. This part of the work was performed using the high performance computing (HPC) LAMMPS software.[227]

## Computational Line scans

Once the chemical order was obtained for each of the ratios studied, another energy optimization process of the atomic positions was carried out to eliminate noise (caused by MD at room temperature). After that, line scans were calculated to see the distribution of both species in the interior of the nanoparticle and compare them with the experimental results. This process was as follows. A random Euler rotation to the three coordinate axes was applied to the nanoparticles. After the application of the three rotations (one on each axis), a histogram of the distribution of both species in the center of the NPs, with radio of 2.5 nm for counting atoms along the X direction, was calculated. This process was performed several times, and selected the histogram that fitted the EDS line scan, which is also in good agreement with the image from the experimental HAADF-STEM. It can be seen that it is very similar to the nanoparticle obtained experimentally, and the evidence of Pd atoms on the surface can also be noted.

## Reactivity of $H_2$ MD-DFTB+ Results

To calculate the reactivity of the nanoparticles, as in DFT calculations, a cuboctahedron with 38 atoms was used as a model. First, the chemical order was optimized in the manner already discussed. **Figure S3-9** shows the structure obtained for the three cases.

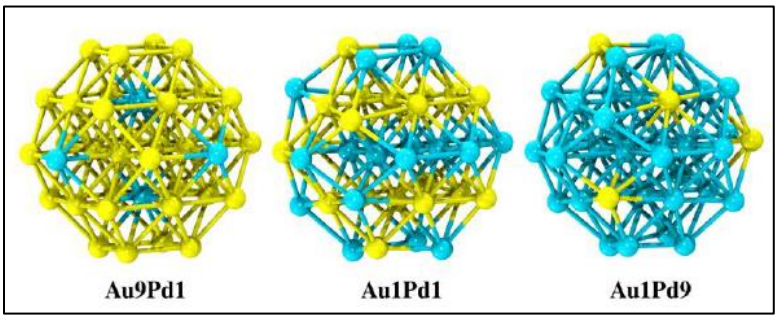


**Figure S3-9.** Energy optimized structures for the three alloy concentrations used in this study, employing a cuboctahedron model with 38 atoms by means of hybrid MD-MC strategy.

As a next step, a pair of hydrogen atoms was added in positions of adjacent atoms in the nanoparticle and the geometries were optimized, in addition to calculating the adsorption energy for each system. In the case of $Au_9Pd_1$, 8 different systems were built, corresponding to different initial positions of the hydrogen add atoms on the surface. For the $Au_1Pd_1$ and $Au_1Pd_9$ cases, 9 and 11 systems were built, respectively. From this point on, all calculations were performed at a higher level of theory using the DFTB+ code,[228] and the GFN1-xTB parameterization.[229]
Starting from the systems optimized in the previous step, molecular dynamics calculations were carried out on them. The systems were brought to a temperature of 298 K and then left at constant temperature along 20 picoseconds. In the case of $Au_9Pd_1$, the only system that led to the formation of $H_2$ was system-1. In the anexed video, it can be observed the simulation in detail about how the formation of $H_2$ occurs.

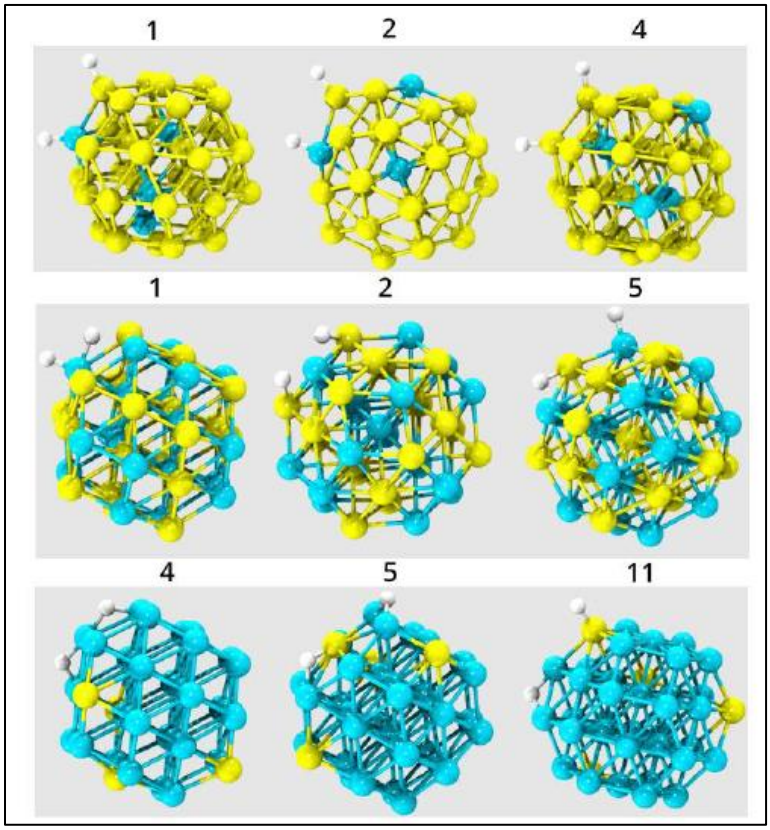


**Figure S3-10.** Some configurations used for the AuPd-$H_2$ system after optimization. The number at the top of each particle is just the label that was given to the system in its respective ratio of Au and Pd.

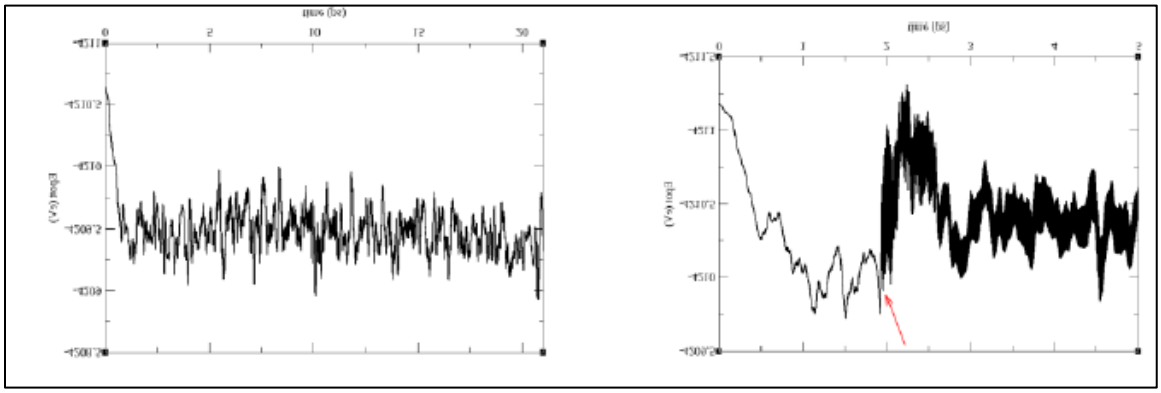

**Figure S3-11.** The left graph shows potential energy vs. time, indicating stability as energy oscillates around a constant value. In contrast, the right graph for system-1 reveals significant changes during the simulation, specifically the formation of $H_2$, marked by the red arrow.

**E-link** for the video showing the formation of $H_2$ on $Au_9Pd_1$ nanoalloys:
https://drive.google.com/drive/folders/1nS_WD9IJdnMFSiFBE7fSi9PQYSoJ5KsA?usp=sharing

# Annex II. Chapter 4

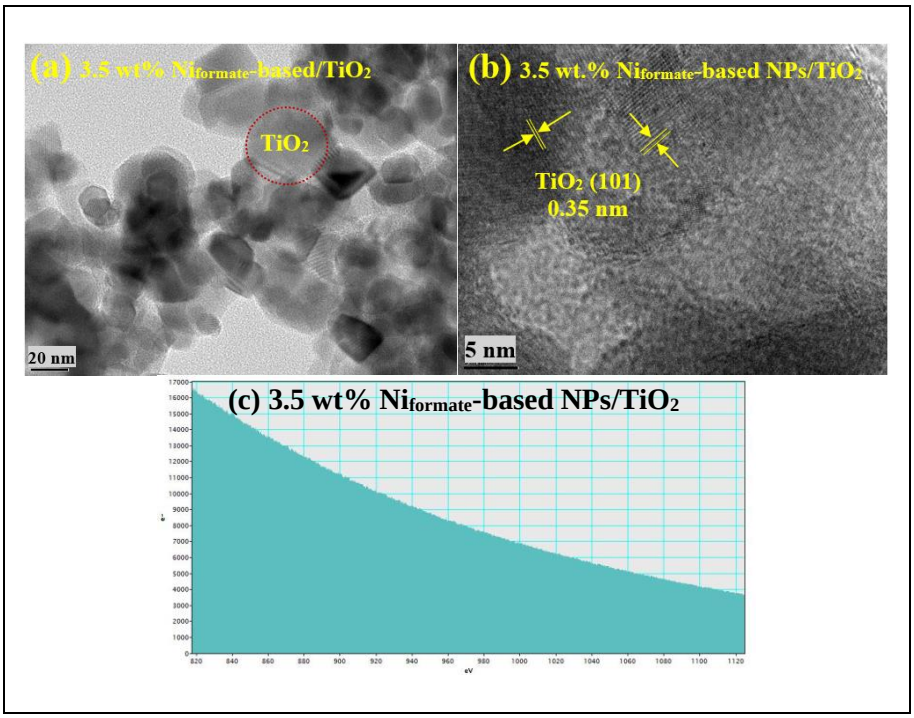


**Figure S4-1. (a)** TEM micrograph, **(b)** HRTEM micrograph and **(c)** EELS spectrum of 3. 5 wt.% $Ni_{formate\text{-}based}$ NPs/$TiO_2$.

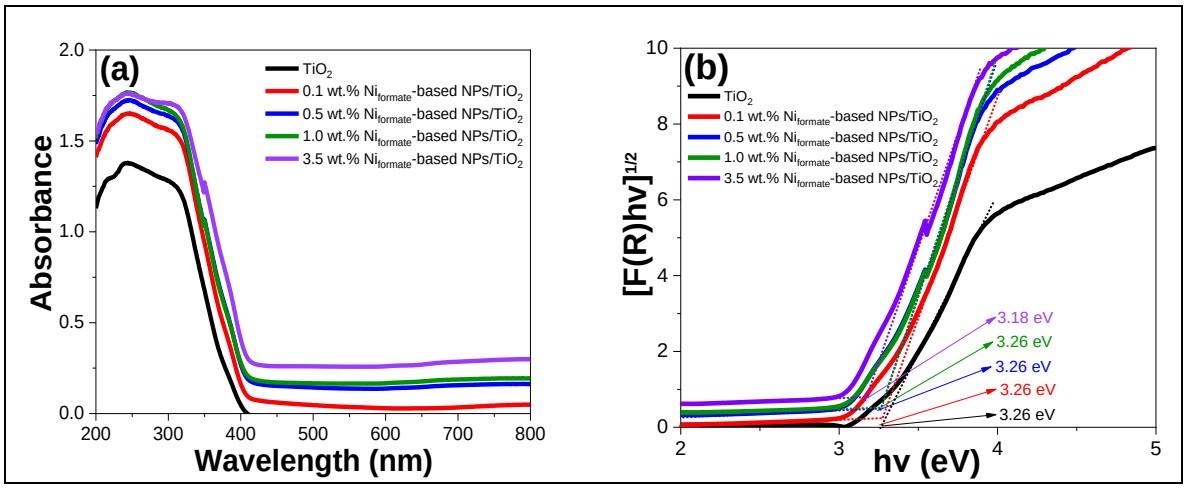


**Figure S4-2. (a)** DRS spectra, and their **(b)** Tauc plot of $Ni_{formate}$-based NPs/$TiO_2$ modified samples and bare $TiO_2$.

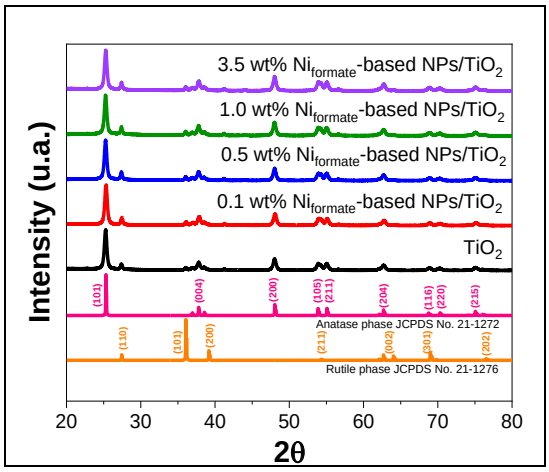


**Figure S4-3.** X-Ray Diffraction (XRD) pattern of Ni$_{formate}$-based NPs/TiO$_2$ modified samples and bare TiO$_2$ with the reference peaks of anatase and rutile crystalline phases.

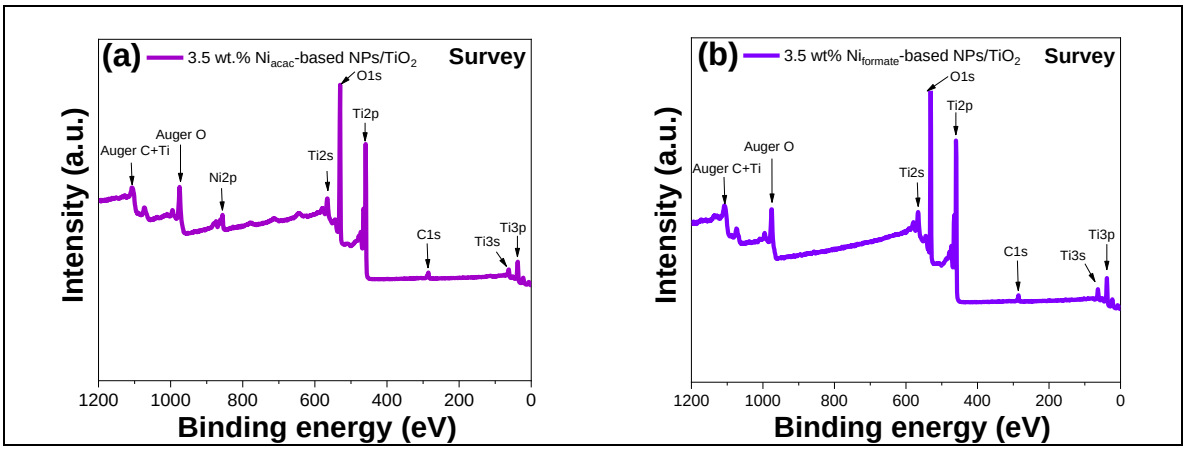


**Figure S4-4.** Survey XPS spectra of **(a)** 3.5wt% Ni$_{acac}$-based NPs/TiO$_2$ and **(b)** 3.5wt% Ni$_{formate}$-based NPs/TiO$_2$ samples.

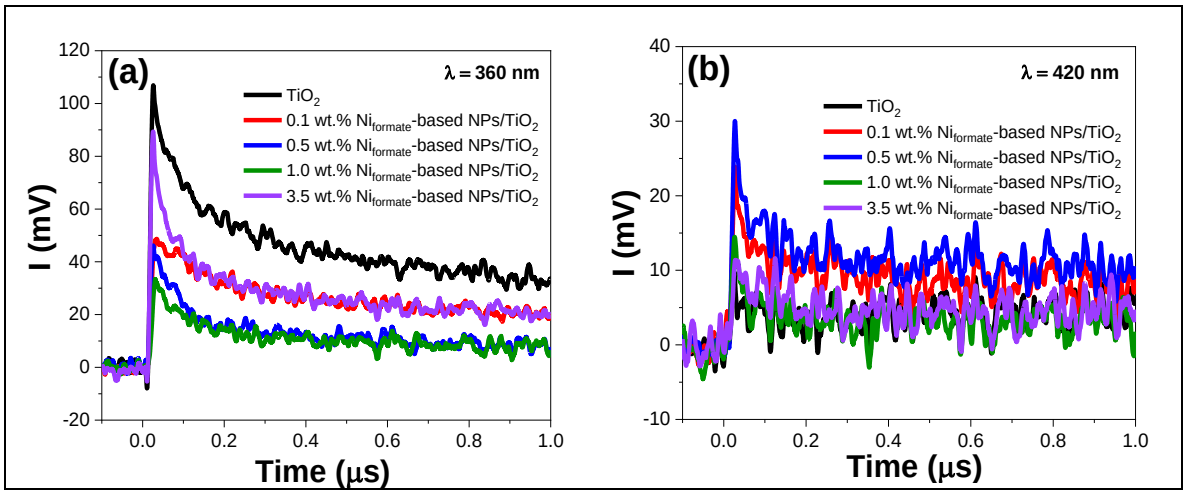


**Figure S4-5.** TRMC signals of Ni$_{formate}$-based NPs/TiO$_2$ modified samples and bare TiO$_2$ at different wavelengths **(a)** $\lambda_{exc}$ = 360 nm, and **(b)** $\lambda_{exc}$ = 420 nm. Laser energy of these wavelengths was 1.1 and 2.3 mJ respectively.

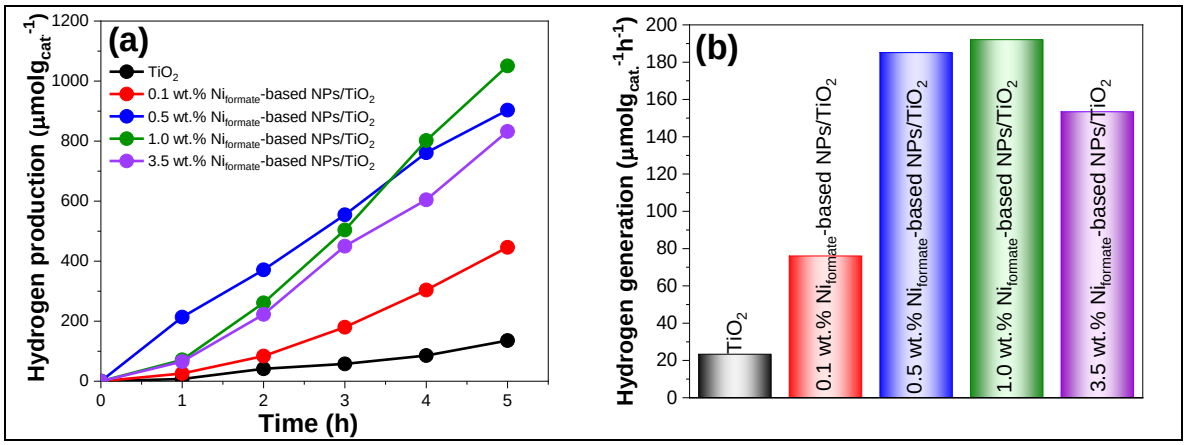


**Figure S4-6. (a)** Photocatalytic hydrogen generation for $Ni_{formate}$-based NPs/$TiO_2$ samples and bare $TiO_2$ under UV-visible light, and **(b)** their hydrogen generation rates (µmol $g_{cat.}^{-1}$ $h^{-1}$) under UV-visible light irradiation from 25% v/v methanol aqueous solution.

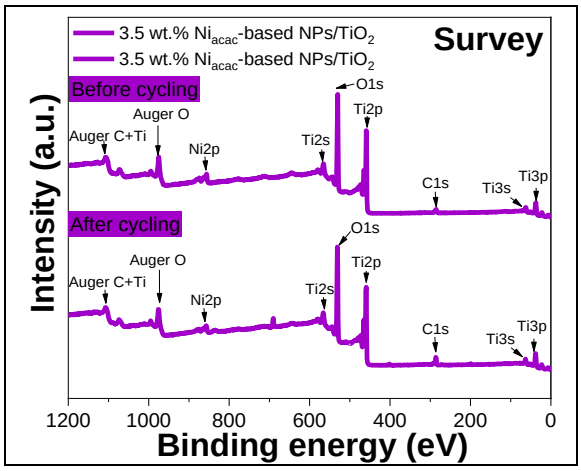


**Figure S4-7.** Survey XPS spectra of 3.5 wt.% $Ni_{acac}$-based NPs/$TiO_2$ sample before and after cycling.

**Table S4-2.** Comparison of hydrogen generation under UV-visible light of the different photocatalysts.

| Samples | Scavenger | Lamp | Hydrogen generation | Ref. |
|---|---|---|---|---|
| 3.5 wt.% Ni-NPs/$TiO_2$ | 25% v/v methanol/water | Hg lamp<br><br>Xenon lamp | 998.4 µmol $g_{cat.}^{-1}$ $h^{-1}$<br>~42-fold higher than $TiO_2$<br>1.5 µmol $g_{cat.}^{-1}$ $h^{-1}$ | Our work |
| Ni/$TiO_2$ | 25% v/v methanol/water | Solarium Philips HB175 lamp Maximum peak at 365 nm | 260.76 µmol $h^{-1}$ | 81 |
| 0.32 mol% Ni/$TiO_2$ | 25% v/v methanol/water | UV-LEDs at 365 nm | 2547 µmol $g_{cat.}^{-1}$ $h^{-1}$<br>~135-fold than $TiO_2$ | 154 |
| NiO/rGO/$TiO_2$ | 80 mL $H_2O$: 20 mL methanol | Solar simulator 300 W equipped with a Xe lamp as source | 240 µmol/h/g | 76 |
| 2.0 wt % $Ni(OH)_2$/$TiO_2$ nanotubes | 5% v/v crude glycerol/water | Solar light | 4719 µmol$g_{cat.}^{-1}h^{-1}$<br>~12-fold higher than $TiO_2$ | 89 |
| Ni/C/$TiO_2$ | 80 mL $H_2O$: 20 mL methanol | 300 W Xe lamp | 1745 µmol$g_{cat.}^{-1}h^{-1}$<br>~9-fold than $TiO_2$ | 162 |
| 1 wt% NiO/$TiO_2$ | methanol/$H_2O$ (1:1 v:v) | 1. 6W Hg vapor light source wavelength range: 320-400 nm | 2693 µmol $g_{cat.}^{-1}$ $h^{-}$ | 77 |
| $NiFe_2O_4$@$TiO_2$ | methanol/water (1:1) | UV-lamp at 365 nm | 18.5 mL of $H_2$-8h | 177 |
| 0.5 wt% Ni/$TiO_2$-P25 | Glycerol (10 vol%) | UV-lamp at 365 nm | 26000 µmol $g_{cat.}^{-1}h^{-1}$<br>>24 h | 155 |
| 1.5 wt% NiO/$TiO_2$ | 200 mL water: 20 mLof methanol | 300 W high-pressure Hg lamp | 162. 6 µmol $h^{-1}$ | 85 |
| NiO/CdS | 100 mL of aqueous solution containing 30 mL methanol | Xe lamp (300 W) filter (λ > 400 nm) | 445.6 µmol $h^{-1}$<br>41 times higher than CdS<br>5 h | 163 |
| 7. wt% NiO/$TiO_2$ | 9 mL water:1 mL glycerol | 300 W Xenon lamp | 8000 µmol $g_{cat.}^{-1}$ $h^{-1}$ | 230 |
| Ni/GO-CdS | Ethanol:water (50/50 vol%) | 4 LED lamps of λ=450 nm (4W each) | 8866 µmol $g_{cat.}^{-1}$ $h^{-1}$ | 164 |
| $Ni(OH)_2$-CdS/g-$C_3N_4$ | 20 mL aqueous sol. containing $Na_2S$ and $Na_2SO_3$ | 300 W Xe-lamp 420 nm cut-off filter | 115.18 µmol $mg_{cat.}^{-1}$ $h^{-1}$ | 165 |

# Annex III. Chapter 5

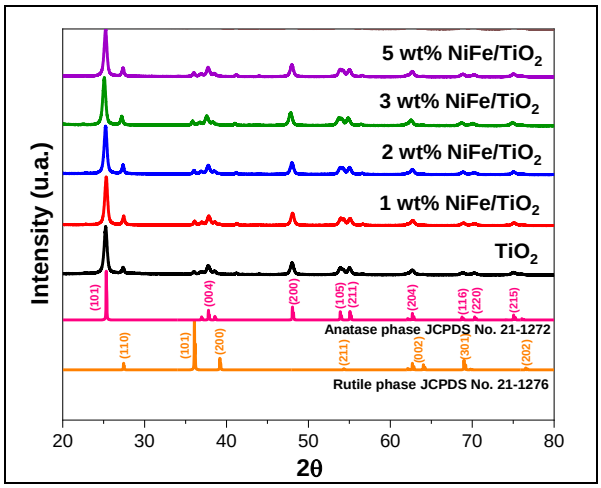


**Figure S5-1.** X-Ray Diffraction (XRD) pattern of bare $TiO_2$ and the modified samples with the reference peaks of anatase and rutile crystalline phases.

**Table S5-1.** Comparison of hydrogen generation rates of the different photocatalysts.

| Samples | Solution ($V_{scavenger}/V_{water}$) | Lamp | Hydrogen generation | Ref. |
|---|---|---|---|---|
| **3 wt% NiFe/$TiO_2$** | **Methanol/water 25% v/v** | **UV-visible 150 W** | **1173 µmol $g^{-1}$ $h^{-1}$** 33 times higher than $TiO_2$ | **This work** |
| NiFe-layered double hydroxide (LDH) @ $TiO_2$ | Methanol/water | Xenon Lamp 300W | 209 mmol $g^{-1}$ 8 times higher than $TiO_2$ | 180 |
| 12 wt% $NiFe_2O_4/TiO_2$-$Ag^+$ | Methanol/water 50:50% v/v | Xenon Light 1000 $Wm^{-2}$ | 137 µmol $g^{-1}$ after 5 h | 178 |
| $NiFe_2O_4/Cu_2O$ 50/50 | Methanol/water 2% v/v | 250 W | 31.37 µmol $g^{-1}$ after 8 h 102.4 µmol $g^{-1}$ after 24 h | 179 |
| 10% NiFe-Prussian blue analogs (PBA)-S/ZnCdS | 10% Lactic acid/water | White LED 5 W | 1003 µmol $g^{-1}$ after 5 h | 183 |
| NiFe NPs-GaN nanowires/Si | Methanol/water | Concentrated light illumination (5 W $cm^{-2}$) | 61.2 mmol $g^{-1}$ $h^{-1}$ | 176 |
| FeNiS-CdTe/CdS | ascorbic acid ($H_2A$) | 300 W Xe lamp fitted with a 420 nm cutoff filter | 26.5 µmol·$h^{-1}$·$mg^{-1}$, | 182 |
| rGO/LTO/NiFe | 10 vol.% triethanolamine (TEOA) | AM 1.5 illumination (100 mW $cm^{-2}$). | 532 µmol $g^{-1}$ $h^{-1}$, which is 9 times higher than that of pure LTO | 181 |

# Annex IV. Chapter 6

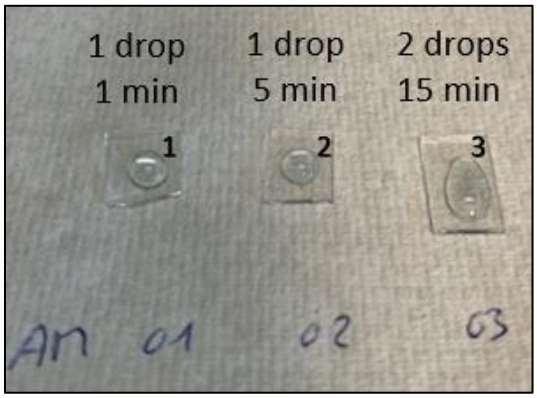


**Figure S6-1.** Microscope slides for dark field optical microscopy.

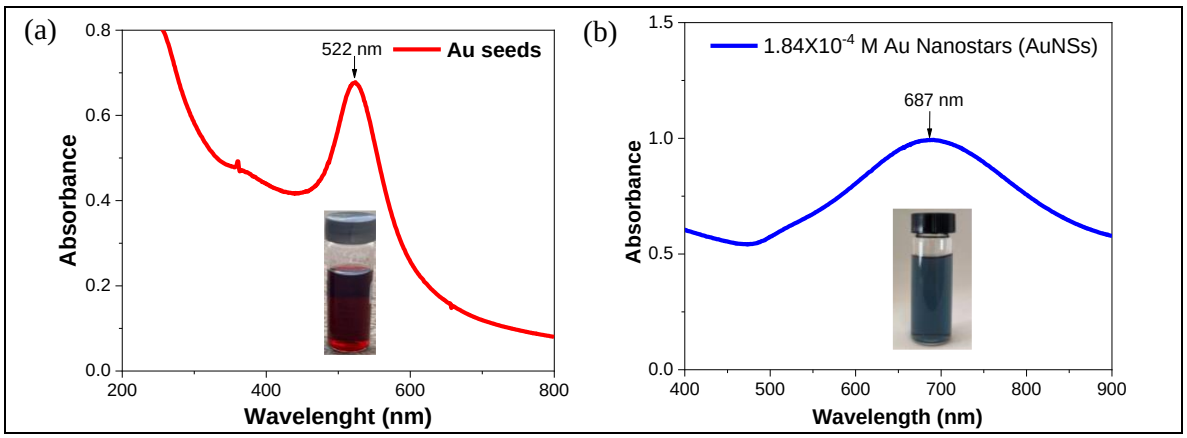


**Figure S6-2.** UV-vis spectra of **(a)** $8.6\times10^{-4}$ M Au, and **(b)** $1.84\times10^{-4}$ M Au in aqueous solution synthetized by Yuang's Protocol.

Electron microscopy allows to analyze the morphology and size of the nanoparticles. Au seeds prepared by chemical reduction showed an average size of approximately 15 nm (Figure S6-3a) and Au nanostars synthesized by chemical method have an average size of approximately 98 nm and feature several tips over their surface, each measuring around 19 nm (Figure S6-3b). The elemental composition was confirmed by EDX analyses. AuSs exhibited signals corresponding to Au and C with 63.8 wt% and 36.2 wt%, respectively (Figure S6-3c). On the other hand, AuNSs displayed signals for Au, Ag (coming from the Ag precursor added to help the anisotropic growth), and C, with 91.99 wt%, 3.26 wt%, and 4.74 wt%, respectively (Figure S6-3d).

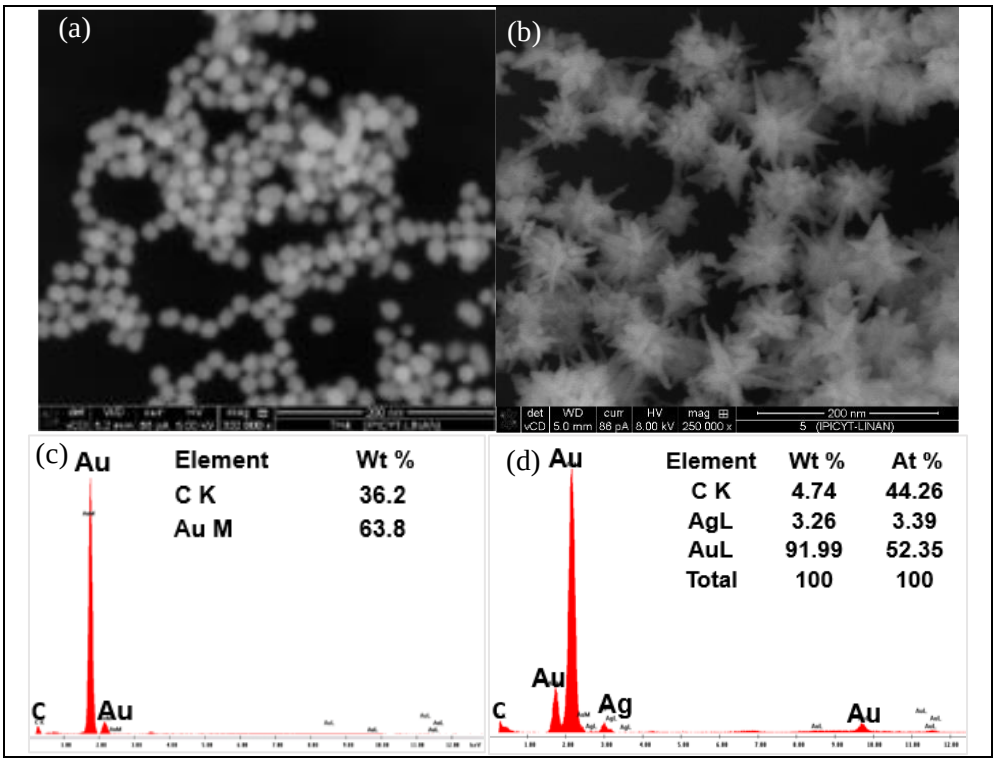


**Figure S6-3.** SEM micrographs of **(a)** 2.2×10-4 M AuSs, and **(b)** 6.33×10-5 M AuNSs, and **(c-d)** their EDS analyses, respectively.

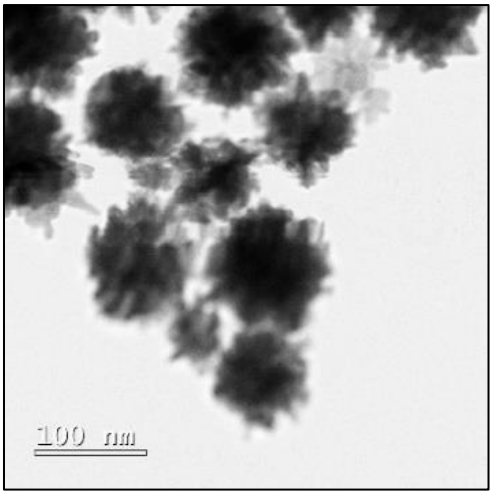


**Figure S6-4.** TEM micrograph of the AuNSs after the photocatalytic test. 11 hours of irradiation (λ > 500 nm) and $N_2$ atmosphere conditions.

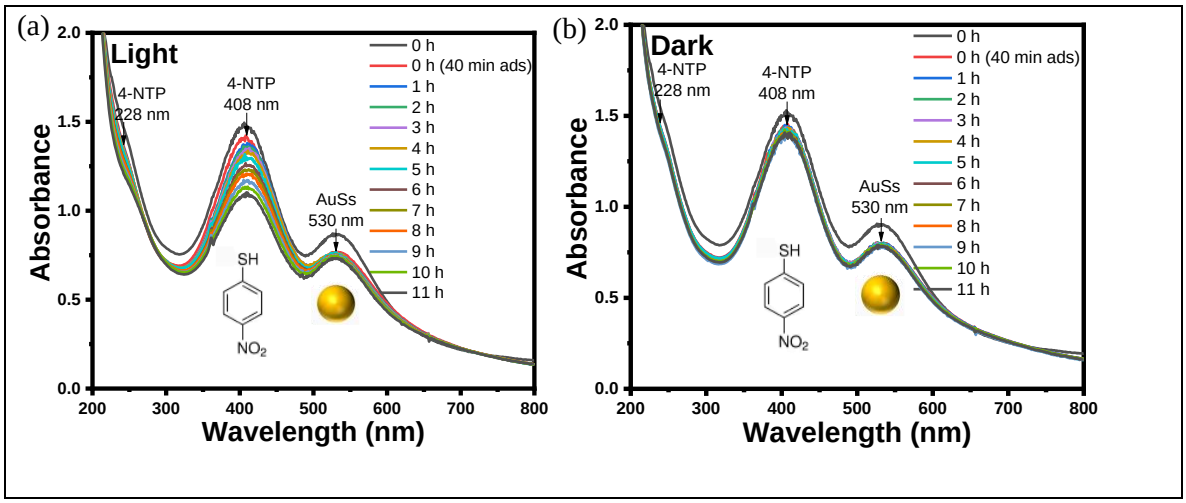


**Figure S6-5. (a)** UV-vis spectrum of the reduction of 1.64×10-4 M 4-NTP by plasmon excitation of 1.84×10-4 M AuSs under visible light (λ > 500 nm) and $N_2$ atmosphere, and **(b)** UV-vis spectrum under dark conditions and $N_2$ atmosphere. Optical path = 1 cm.

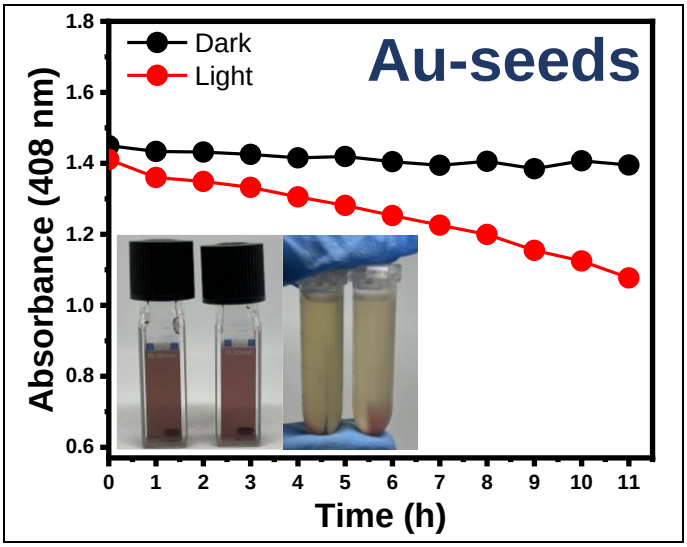


**Figure S6-6.** Comparison of the reaction kinetics for AuSs under visible light and dark conditions.

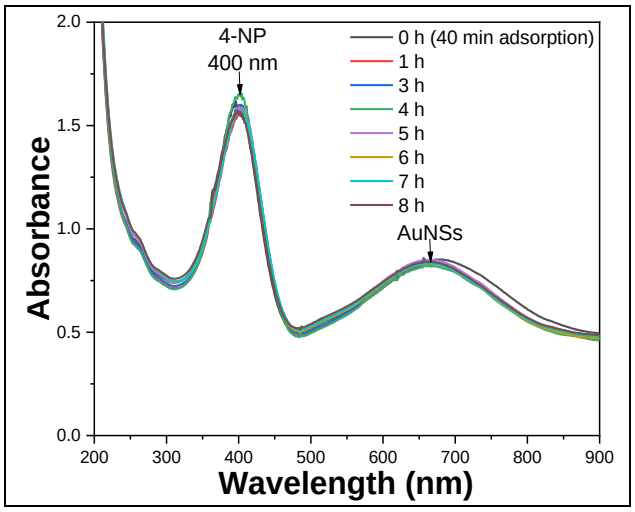


**Figure S6-7.** UV-visible absorption spectrum of an alkaline aqueous solution containing 4-NP ($1.64\times10^{-4}$ M) and AuNSs ([$Au^0$] = $1.84\times10^{-4}$ M) under visible light ($\lambda > 500$ nm) and $N_2$ atmosphere. Optical path = 1 cm.

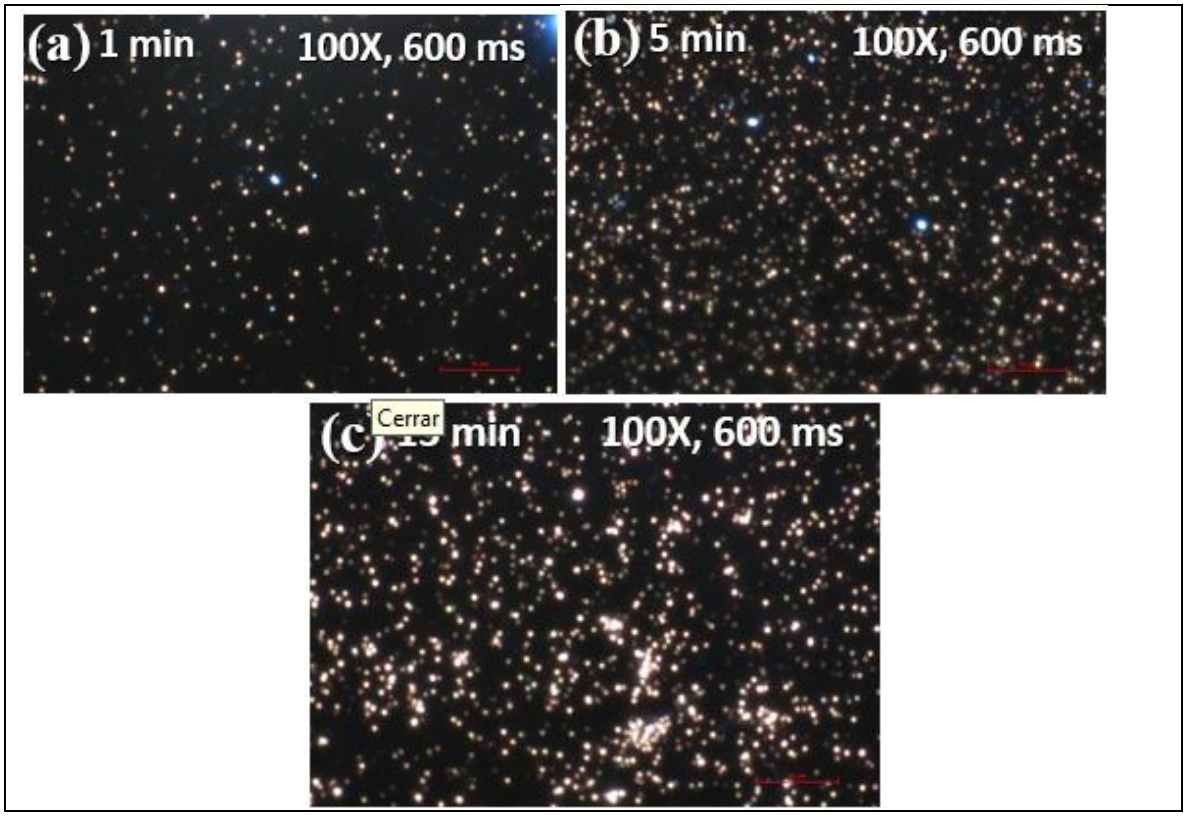


**Figure S6-8.** Dark-field optical microscopy image of AuNSs on the glass substrate for **(a)** 1 min, **(b)** 5 minutes, and **(c)** 15 minutes.

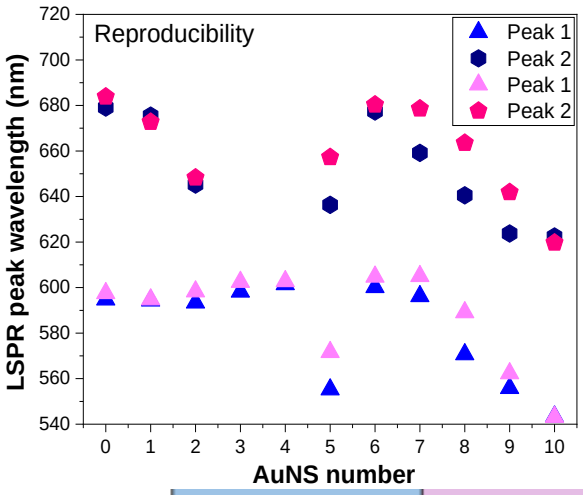


| # Au Nanostar | am | pm |
|---|---|---|
| 0 | Peak 1: 594.72<br>Peak 2: 679.09 | Peak 1: 597.53<br>Peak 2: 683.84 |
| 1 | Peak 1: 594.27<br>Peak 2: 675.53 | Peak 1: 594.75<br>Peak 2: 672.71 |
| 2 | Peak 1: 593.39<br>Peak 1: 645.26 | Peak 2: 598.27<br>Peak 2: 648.26 |
| 3 | Peak 1: 598.2 | Peak 1: 602.47 |
| 4 | Peak 1: 601.45 | Peak 1: 602.75 |
| 5 | Peak 1: 555.22<br>Peak 2: 636.32 | Peak 1: 571.62<br>Peak 2: 657.24 |
| 6 | Peak 1: 600.18<br>Peak 2: 677.35 | Peak 1: 604.76<br>Peak 2: 680.32 |
| 7 | Peak 1: 596.2<br>Peak 2: 659.15 | Peak 1: 605.00<br>Peak 2: 678.60 |
| 8 | Peak 1: 570.65<br>Peak 2: 640.52 | Peak 1: 589.1<br>Peak 2: 663.51 |
| 9 | Peak 1: 555.85<br>Peak 2: 623.77 | Peak 1: 562.29<br>Peak 2: 641.87 |
| 10 | Peak 1: 543.33<br>Peak 2: 622.45 | Peak 1: 543.17<br>Peak 2: 619.7 |

**Figure S6-9.** Reproducibility peaks of the LSPR. (Peak 1 and Peak 2) of individual AuNSs. Blue peaks were measured in the morning, while pink peaks were measured in the afternoon for 11 nanostars.

## References


1. Ahmaruzzaman, M., Mishra, S. R., Gadore, V., Sharma, D. K., Hydrogen Generation by Photolysis of Water Vis-à-Vis Other Conventional and Advanced Non-conventional Methods of Hydrogen Production—A Review. *J. Inorg. Organomet. Polym*. (2024). https://doi.org/10.1007/s10904-024-03272-4
2. Negi C., Kandwal P., Rawat J., Sharma M., Sharma H., Dalapati G., Dwivedi C., Carbon-doped titanium dioxide nanoparticles for visible light driven photocatalytic activity. *Appl. Surf. Sci*. **554**, 149553 (2021). https://doi.org/10.1016/j.apsusc.2021.149553
3. Ansari, S. A., Khan, M. M., Ansari, M. O., Cho, M. H. Nitrogen-doped titanium dioxide (N-doped $TiO_2$) for visible light photocatalysis. *New J. Chem*. **40**, 3000 (2016). https://doi.org/10.1039/C5NJ03478G
4. Yuan, X., Kobylanski, M. P., Cui, Z., Li, J., Beaunier, P., Dragoe, D., Colbeau-Justin, C., Zaleska-Medynska, A., Remita, H. Highly active composite $TiO_2$-polypyrrole nanostructures for water and air depollution under visible light irradiation. *J. Environ. Chem. Eng*. **8**, (2020). DOI: 10.1016/j.jece.2020.104178
5. Sánchez-Rodríguez, D., Méndez Medrano, M. G., Remita, H., Escobar-Barrios, V. Photocatalytic properties of BiOCl-$TiO_2$ composites for phenol photodegradation. J. Environ. Chem. Eng. **6**, 1601 (2018). https://doi.org/10.1016/j.jece.2018.01.061
6. Méndez-Medrano, M. G., Kowalska, E., Lehoux, A., Herissan, A., Ohtani, B., Rau, S., Colbeau-Justin, C., Rodríguez-López, J. L., Remita, H. Surface Modification of $TiO_2$ with Au Nanoclusters for Efficient Water Treatment and Hydrogen Generation under Visible Light. *J. Phys. Chem. C* **120**, 25010 (2016). DOI: 10.1021/acs.jpcc.6b06854
7. Méndez-Medrano, A. A., Bahena-Uribe, D., Dragoe, D., Clavaguéra C., Colbeau-Justin C., Palomares Báez, J. P., Rodríguez-López, J. L., Remita H. Enhanced Photocatalytic Activity of Surface-Modified $TiO_2$ with Bimetallic

AuPd Nanoalloys for Hydrogen Generation. *Solar RRL* **8**, 2400106 (2024). https://doi.org/10.1002/solr.202400106

8. Luna, A. L., Novoseltceva, E., Louarn, E., Beaunier, P., Kowalska, E., Ohtani, B., Valenzuela, M. A., Remita, H., Colbeau-Justin, C. Synergetic effect of Ni and Au nanoparticles synthesized on titania particles for efficient photocatalytic hydrogen production. *Appl. Catal. B* **191**, 18 (2016). DOI: 10.1016/j.apcatb.2016.03.008
9. Wang, C., Dragoe, D., Colbeau-Justin, C., Haghi-Ashtiani, P., Ghazzal, M. N., Remita, H. Highly Dispersed Ni-Pt Bimetallic Cocatalyst: The Synergetic Effect Yields Pt-Like Activity in Photocatalytic Hydrogen Evolution. *ACS Appl. Mater. Interfaces* **15**, 42637 (2023). DOI: 10.1021/acsami.3c08842
10. Kumaravel, V., Mathew, S., Bartlett, J., Pillai, S. C. Photocatalytic hydrogen production using metal doped $TiO_2$: A review of recent advances. *Appl. Catal. B* **244**, 1021 (2019). https://doi.org/10.1016/j.apcatb.2018.11.080
11. Ibrahim, N. S., Leaw, W. L., Mohamad, D., Alias, S. H., Nur, H. A critical review of metal-doped $TiO_2$ and its structure–physical properties–photocatalytic activity relationship in hydrogen production. *Int. J. Hydrog. Energy* **45**, 28553 (2020). https://doi.org/10.1016/j.ijhydene.2020.07.233
12. Ismael, M. A review and recent advances in solar-to-hydrogen energy conversion based on photocatalytic water splitting over doped-$TiO_2$ nanoparticles. *Sol. Energy* **211**, 522 (2020). https://doi.org/10.1016/j.solener.2020.09.073
13. Masson, J. F. Portable and field-deployed surface plasmon resonance and plasmonic sensors. *Analyst* **145**, 3776 (2020). https://doi.org/10.1039/D0AN00316F
14. Gan, X., Lei, D. Plasmonic-metal/2D-semiconductor hybrids for photodetection and photocatalysis in energy-related and environmental processes. *Coord. Chem. Rev*. **469**, 214665 (2022). https://doi.org/10.1016/j.ccr.2022.214665
15. Luna, A. L., Dragoe, D., Wang, K., Beaunier, P., Kowalska, E., Ohtani, B., Bahena Uribe, D., Valenzuela, M. A., Remita, H., Colbeau-Justin, C.

Photocatalytic Hydrogen Evolution Using Ni-Pd/$TiO_2$: Correlation of Light Absorption, Charge-Carrier Dynamics, and Quantum Efficiency. *J. Phys. Chem. C.* **121**, 14302 (2017). DOI: 10.1021/acs.jpcc.7b01167

16. Ksar, F., Ramos, L., Keita, B., Nadjo, L., Beaunier, P., Remita, H. Bimetallic palladium-gold nanostructures: application in ethanol oxidation. *Chem. Mater.* **21**, 3677 (2009). https://doi.org/10.1021/cm901364w
17. Lucci, F. R., Darby, M. T., Mattera, M. F. G., Ivimey, C. J., Therrien, A. J., Michaelides A., Stamatakis, M., Sykes, E. C. H.. Controlling Hydrogen Activation, Spillover, and Desorption with Pd-Au Single-Atom Alloys. *J. Phys. Chem. Lett*. **7**, 480 (2016). https://doi.org/10.1021/acs.jpclett.5b02400
18. Dimitratos, N., Vilé, G., Albonetti, S., Cavani, F., Fiorio, J., López, N., Rossi, L. M., Wojcieszak, R. Strategies to improve hydrogen activation on gold catalysts. *Nat. Rev. Chem.* **8**, 195 (2024). https://doi.org/10.1038/s41570-024-00578-2
19. R. Su, R. Tiruvalam, A. J. Logsdail, Q. He, C. A. Downing, M. T. Jensen, N. Dimitratos, L. Kesavan, P. P. Wells, R.Bechstein, H. H.Jensen, S. Wendt, C. R. A. Catlow, C. J. Kiely, G. J. Hutchings, F. Besenbacher. Designer Titania-Supported Au–Pd Nanoparticles for Efficient Photocatalytic Hydrogen Production. *ACS Nano* **8**, 3490 (2014). https://doi.org/10.1021/nn500963m
20. Brazzolotto, D., Gennari, M., Queyriaux, N., Simmons, T. R., Pécaut, J., Demeshko, S., Meyer, F., Orio, M., Artero, V., Duboc, C. Nickel-centred proton reduction catalysis in a model of [NiFe] hydrogenase. *Nature Chem.* **8**, 1054 (2016). https://doi.org/10.1038/nchem.2575
21. Ahmad, H., Kamarudin, S. K., Minggu, L. J., Kassim, M. Hydrogen from photo-catalytic water splitting process: A review. *Renew. Sustain. Energy Rev*. **43**, 599 (2015). https://doi.org/10.1016/j.rser.2014.10.101
22. Goel, M., Sen, G., Climate Action and Hydrogen Economy. Springer Singapore, 2024.
23. Du, M., Sun, D., Yang, H., Huang, J., Jing, X., Odoom-Wubah, T., Wang, H., Jia, L., Li, Q. Influence of Au particle size on Au/$TiO_2$ catalysts for CO

oxidation. *J. Phys. Chem.* C **118**, 19150 (2014). https://doi.org/10.1021/jp504681f

24. Luna, A. L., Novoseltceva, E., Louarn, E., Beaunier, P., Kowalska, E., Ohtani, B., Valenzuela, M. A., Remita, H., Colbeau-Justin, C. Synergetic effect of Ni and Au nanoparticles synthesized on titania particles for efficient photocatalytic hydrogen production. *Appl. Catal. B* **191**, 18 (2016). DOI: 10.1016/j.apcatb.2016.03.008
25. Loiseau, A., Asila, V., Boitel-Aullen, G., Lam, M., Salmain, M., Boujday, S. Silver-based plasmonic nanoparticles for and their use in biosensing. *Biosensors* **9**, 78 (2019). https://doi.org/10.3390/bios9020078
26. Huang, X., Peng, X., Wang, Y., Wang, Y., Shin, D. M., El-Sayed, M. A., Nie, S. A reexamination of active and passive tumor targeting by using rod-shaped gold nanocrystals and covalently conjugated peptide ligands. *ACS Nano* **4,** 5887 (2010). https://doi.org/10.1021/nn102055s
27. Carreón-Álvarez, C., Sánchez-García, J. L., Sanabria-Ayala, V., Ortiz-Frade, L. A., García-Rodríguez, M. E., Rodríguez-López, J. L., López-Revilla, R. Multibranched gold nanoparticles coated with serum proteins fit for photothermal tumor ablation. *AIP Adv.* **10**, (2020). https://doi.org/10.1063/5.0025368
28. Durán-Álvarez, J. C., Avella, E., Ramírez-Zamora, R. M., Zanella, R. Photocatalytic degradation of ciprofloxacin using mono- (Au, Ag and Cu) and bi- (Au-Ag and Au-Cu) metallic nanoparticles supported on $TiO_2$ under UV-C and simulated sunlight. *Catal. Today* **266**, 175 (2016). https://doi.org/10.1016/j.cattod.2015.07.033
29. Kowalska, E., Janczarek, M., Rosa, L., Juodkazis, S., Ohtani, B. Mono- and bi-metallic plasmonic photocatalysts for degradation of organic compounds under UV and visible light irradiation. *Catal Today* **230**, 131 (2014). https://doi.org/10.1016/j.cattod.2013.11.021
30. Brissaud, C., Besteiro, L. V., Piquemal, J. Y., Comesaña-Hermo, M. Plasmonics: A Versatile Toolbox for Heterogeneous Photocatalysis. *Solar RRL* **7**, 2300195 (2023). https://doi.org/10.1002/solr.202300195

31. Pluchery, O., Lacaze, E., Simion, M., Miu, M., Bragaru, A., Radoi, A. Optical characterization of supported gold nanoparticles for plasmonic biosensors. *CAS*, **1**, 159, (2010). https://doi.org/10.1109/SMICND.2010.5649061.
32. Protti, S., Albini, A., Serpone, N. Photocatalytic generation of solar fuels from the reduction of $H_2O$ and $CO_2$: a look at the patent literature. *Phys. Chem. Chem. Phys*. **16**, 19790 (2014). https://doi.org/10.1039/C4CP02828G
33. Piña-Pérez, Y., Samaniego-Benitez, J. E., Tzompantzi, F., Laurtundo-Rojas, L., Garcia-Garcia, A., Mantilla, A., Romero-Ortiz, G. Photocatalytic hydrogen production using bimetallic and trimetallic hydrotalcite as photocatalysts. *Mater. Lett.* **330**, 133205 (2022). https://doi.org/10.1016/j.matlet.2022.133205
34. Kapdan, I. K., Kargi, F. Bio-hydrogen production from waste materials. *Enzyme Microb. Technol.* **38**, 569 (2006). https://doi.org/10.1016/j.enzmictec.2005.09.015
35. Veziroğlu, T. N., Şahin, S. 21st Century's energy: Hydrogen energy system. *Energy Convers. Manag.* **49**, 1820 (2008). https://doi.org/10.1016/j.enconman.2007.08.015
36. Sharma, S., Ghoshal, S. K. Hydrogen the future transportation fuel: From production to applications. *Renew. Sustain. Energy Rev*. **43**, 1151 (2015). https://doi.org/10.1016/j.rser.2014.11.093
37. Pinaud, B. A., Benck, J. D., Seitz, L. C., Forman, A. J., Chen, Z., Deutsch, T. G., James, B. D., Baum, K. N., Baum, G. N., Ardo, S., Wang, H., Miller, E., Jaramillo, T. F.. Technical and economic feasibility of centralized facilities for solar hydrogen production via photocatalysis and photoelectrochemistry. *Energy Environ. Sci.* **6**, 1983 (2013). https://doi.org/10.1039/C3EE40831K
38. Chen, X., Mao, S. S. Titanium dioxide nanomaterials: Synthesis, properties, modifications and applications. *Chem. Rev*. **107**, 2891 (2007). https://doi.org/10.1021/cr0500535
39. Ladeia Ramos, R., Rezende Moreira, V., Santos Amaral, M. C. Phenolic compounds in water: Review of occurrence, risk, and retention by membrane technology. *J. Environ. Manage*. **351**, 119772 (2024). https://doi.org/10.1016/j.jenvman.2023.119772

40. Boskabadi, M. R., Rogé, V., Bazargan, A., Sargazi, H., Barborini, E. An introduction to photocatalysis. *Photocatalytic Water and Wastewater Treatment. IWA Publishing*, 2022, p. 1-36. doi: 10.2166/9781789061932_0001
41. Kudo, A., Miseki, Y. Heterogeneous photocatalyst materials for water splitting. *Chem. Soc. Rev.* **38**, 253 (2009). doi: 10.1039/B800489G
42. Hennig, H. Semiconductor Photocatalysis: Principles and Applications. *Angew. Chem. Int. Ed.* **54**, 4429 (2015).
43. Fajrina, N., Tahir, M. A critical review in strategies to improve photocatalytic water splitting towards hydrogen production. *Int. J. Hydrogen Energy* **44**, 540 (2019). https://doi.org/10.1016/j.ijhydene.2018.10.200
44. Madkhali, O. A review of novel methods to improve the optical and electrical properties of n-type and p-type sulphides and oxides: leading the frontiers of semiconductor technology. *Phys. Scri*. **99**, 022004 (2024). https://doi.org/10.1088/1402-4896/ad1e44
45. Kahn, A. Fermi level, work function and vacuum level. *Mater. Horiz*. **3**, 7 (2016). https://doi.org/10.1039/c5mh00160a
46. Shi, Y. Growth of 3C-SiC and Graphene for Solar Water-Splitting Application. Linköping University Electronic Press, (2019). https://doi.org/10.3384/diss.diva-159100
47. Grätzel, M. Photoelectrochemical cells. *Nature* **414**, 338 (2001). https://doi.org/10.1038/35104607
48. Yuan, X., Floresyona, D., Aubert, P. H., Bui, T. T., Remita, S., Ghosh, S., Brisset, F., Goubard, F., Remita, H. Photocatalytic degradation of organic pollutant with polypyrrole nanostructures under UV and visible light. *Appl. Catal. B* **242**, 284 (2019). DOI: 10.1016/j.apcatb.2018.10.002
49. Ma, J., Dai, J., Duan, Y., Zhang, J., Qiang, L., Xue, J. Fabrication of PANI-$TiO_2$/rGO hybrid composites for enhanced photocatalysis of pollutant removal and hydrogen production. Renew. Energy **156**, 1008 (2020). https://doi.org/10.1016/j.renene.2020.04.104

50. Zhang, J., Zhou, P., Liu, J., Yu, J. New understanding of the difference of photocatalytic activity among anatase, rutile and brookite $TiO_2$. *Phys. Chem. Chem. Phys.* **16**, 20382 (2014). DOI: 10.1039/c4cp02201g
51. Remita, H., Méndez-Medrano M. G., Colbeau-Justin, C. Effect of Modification of $TiO_2$ with Metal Nanoparticles on its Photocatalytic Properties Studied by Time Resolved Microwave Conductivity, in Visible Light-Active Photocatalysis (Ed: S. Ghosh), Wiley-VCH, Weinheim, Germany, pp. 129–164 (2018).
52. Zhang, D., Dong, S. Challenges in band alignment between semiconducting materials: A case of rutile and anatase $TiO_2$. Prog. Nat. Sci.: Mater. Int. **29**, 277 (2019). https://doi.org/10.1016/j.pnsc.2019.03.012
53. Mi, Y., Weng, Y. Band Alignment and Controllable Electron Migration between Rutile and Anatase $TiO_2$. *Sci. Rep.* **5**, 11482 (2015). https://doi.org/10.1038/srep11482
54. Ohtani, B., Prieto-Mahaney, O. O., Li, D., Abe, R. What is Degussa (Evonic) P25? Crystalline composition analysis, reconstruction from isolated pure particles and photocatalytic activity test. J*. Photochem. Photobiol. A Chem*. **216**, 179 (2010). https://doi.org/10.1016/j.jphotochem.2010.07.024
55. Pfeifer, V., Erhart, P., Li, S., Rachut, K., Morasch, J., Brötz, J., Reckers, P., Mayer, T., Rühle, S., Zaban, A., Mora Seró, I., Bisquert, J., Jaegermann, W., Klein, A. Energy band alignment between anatase and rutile $TiO_2$. *J. Phys. Chem. Lett.* **4**, 4182 (2013). https://doi.org/10.1021/jz402165b
56. Ma, R., Chen, T. Checking the Synergetic Effect between Anatase and Rutile. *J. Phys. Chem. C* **123**, 19479 (2019). https://doi.org/10.1021/acs.jpcc.9b03381
57. Etacheri, V., Seery, M. K., Hinder, S. J., Pillai, S. C. Oxygen Rich Titania: A Dopant Free, High Temperature Stable, and Visible-Light Active Anatase Photocatalyst. *Adv. Funct. Mater*. **21**, 3744 (2011). https://doi.org/10.1002/adfm.201100301
58. Di Paola, A., Cufalo, G., Addamo, M., Bellardita, M., Campostrini, R., Ischia, M., Ceccato, R. & Palmisano, L. Photocatalytic activity of nanocrystalline $TiO_2$ (brookite, rutile and brookite-based) powders prepared by thermohydrolysis of

$TiCl_4$ in aqueous chloride solutions. *Colloids Surf. A: Physicochem. Eng. Asp.* **317**, 366 (2008). https://doi.org/10.1016/j.colsurfa.2007.11.005

59. Jia, J., Yamamoto, H., Okajima, T., Shigesato, Y. On the Crystal Structural Control of Sputtered $TiO_2$ Thin Films. *Nanoscale Res. Lett.* **11**, 324 (2016). https://doi.org/10.1186/s11671-016-1531-5

60. Méndez-Medrano, M. G., Kowalska, E., Lehoux, A., Herissan, A., Ohtani, B., Bahena, D., Briois, V., Colbeau-Justin, C., Rodríguez-López, J. L., Remita, H. Surface Modification of $TiO_2$ with Ag Nanoparticles and CuO Nanoclusters for Application in Photocatalysis. *J. Phys. Chem. C.* **120**, 5143 (2016). DOI: 10.1021/acs.jpcc.5b10703

61. Rafique, M., Hajra, S., Irshad, M., Usman, M., Imran, M., Assiri, M. A., Ashraf, W. M. Hydrogen Production Using $TiO_2$-Based Photocatalysts: A Comprehensive Review. *ACS Omega* **8**, 25640 (2023). DOI: 10.1021/acsomega.3c00963

62. Chung, Y. H., Han, K., Lin, C. Y., O'Neill, D., Mul, G., Mei, B., Yang, C. M. Photocatalytic hydrogen production by photo-reforming of methanol with one-pot synthesized Pt-containing $TiO_2$ photocatalysts. *Catal. Today* **356**, 95 (2020). DOI: 10.1016/j.cattod.2019.07.042

63. Chen, Y., Soler, L., Armengol-Profitós, M., Xie, C., Crespo, D., Llorca, J. Enhanced photoproduction of hydrogen on $Pd/TiO_2$ prepared by mechanochemistry. *Appl. Catal. B* **309**, 121275 (2022). DOI: 10.1016/j.apcatb.2022.121275

64. Fang, S., Liu, Y., Sun, Z., Lang, J., Bao, C., Hu, Y. H. Photocatalytic hydrogen production over Rh-loaded $TiO_2$: What is the origin of hydrogen and how to achieve hydrogen production from water?. *Appl. Catal. B* **278**, 119316 (2020). DOI: 10.1016/j.apcatb.2020.119316

65. Gogoi, D., Namdeo, A., Golder, A. K., Peela, N. R. Ag-doped $TiO_2$ photocatalysts with effective charge transfer for highly efficient hydrogen production through water splitting. *Int. J. Hydrog. Energy* **45**, 2729 (2020). DOI: 10.1016/j.ijhydene.2019.11.127

66. Grabowska, E., Zaleska, A., Sorgues, S., Kunst, M., Etcheberry, A., Colbeau-Justin, C., Remita, H. Modification of titanium(IV) dioxide with small silver nanoparticles: Application in photocatalysis. *J. Phys. Chem. C* **117**, 1955 (2013). https://doi.org/10.1021/jp3112183

67. Luo, M., Lu, P., Yao, W., Huang, C., Xu, Q., Wu, Q., Kuwahara, Y., Yamashita, H. Shape and Composition Effects on Photocatalytic Hydrogen Production for Pt-Pd Alloy Cocatalysts. *ACS Appl. Mater. Interfaces* **8**, 20667 (2016). https://doi.org/10.1021/acsami.6b04388

68. Luna, A. L., Matter, F., Schreck, M., Wohlwend, J., Tervoort, E., Colbeau-Justin, C., Niederberger, M. Monolithic metal-containing $TiO_2$ aerogels assembled from crystalline pre-formed nanoparticles as efficient photocatalysts for $H_2$ generation. *Appl. Catal. B* **267**, 118660 (2020). DOI: 10.1016/j.apcatb.2020.118660

69. Redjala, T., Remita, H., Apostolescu, G., Mostafavi, M., Thomazeau, C., Uzio, D. Bimetallic Au-Pd and Ag-Pd clusters synthesised by γ or electron beam radiolysis and study of the reactivity/structure relationships in the selective hydrogenation of buta-1,3-diene. *Oil Gas Sci. Technol*. **61**, 789 (2006). https://doi.org/10.2516/ogst:2006019

70. Wang, F., Jiang, Y., Lawes, D. J., Ball, G. E., Zhou, C., Liu, Z., Amal, R. Analysis of the Promoted Activity and Molecular Mechanism of Hydrogen Production over Fine Au-Pt Alloyed $TiO_2$ Photocatalysts. *ACS Catal*. **5**, 3924 (2015). https://doi.org/10.1021/acscatal.5b00623

71. Mirdamadi-Esfahani, M., Mostafavi, M., Keita, B. Nadjo L., Kooyman P., Remita, H. Bimetallic Au-Pt nanoparticles synthesized by radiolysis: Application in electro-catalysis. *Gold Bull* **43**, 49 (2010). https://doi.org/10.1007/BF03214966

72. Hai, Z., El Kolli, N., Uribe, D. B., Beaunier, P., José-Yacaman, M., Vigneron, J., Etcheberry, A., Sorgues, S., Colbeau-Justin, C., Chen, J., Remita, H. Modification of $TiO_2$ by bimetallic Au-Cu nanoparticles for wastewater treatment. *J. Mater. Chem. A* **1**, 10829 (2013). DOI: 10.1039/c3ta11684

73. Hai, Z., El Kolli, N., Chen, J., Remita, H. Radiolytic synthesis of Au-Cu bimetallic nanoparticles supported on $TiO_2$: Application in photocatalysis. *New J. Chem.* **38**, 5279 (2014). https://doi.org/10.1039/C4NJ00883A

74. Méndez-Medrano, M. G., Kowalska, E., Ohtani, B., Bahena Uribe, D., Colbeau-Justin, C., Rau, S., Rodríguez-López, J. L., Remita, H. Heterojunction of CuO nanoclusters with $TiO_2$ for photo-oxidation of organic compounds and for hydrogen production. *J. Chem. Phys.* **153**, 034705 (2020). https://doi.org/10.1063/5.0015277

75. Xiao, Y., Guo, X., Yang, N., Zhang, F. Heterostructured MOFs photocatalysts for water splitting to produce hydrogen. *J. Energy Chem*. **58**, 508 (2021). https://doi.org/10.1016/j.jechem.2020.10.008

76. Yu, X., Zhang, J., Zhao, Z., Guo, W., Qiu, J., Mou, X., Li, A., Claverie, J. P., Liu, H. NiO-$TiO_2$ p-n heterostructured nanocables bridged by zero-bandgap rGO for highly efficient photocatalytic water splitting. *Nano Energy* **16**, 207 (2015). DOI: 10.1016/j.nanoen.2015.06.028

77. Uddin, M. T., Nicolas, Y., Olivier, C., Jaegermann, W., Rockstroh, N., Junge, H., Toupance, T. Band alignment investigations of heterostructure NiO/$TiO_2$ nanomaterials used as efficient heterojunction earth-abundant metal oxide photocatalysts for hydrogen production. *Phys. Chem. Chem. Phys.* **19**, 19279 (2017). DOI: 10.1039/c7cp01300k

78. Liu, J., Li, Y., Ke, J., Wang, S., Wang, L., Xiao, H. Black NiO-$TiO_2$ nanorods for solar photocatalysis: Recognition of electronic structure and reaction mechanism. *Appl. Catal. B* **224**, 705 (2018). DOI: 10.1016/j.apcatb.2017.11.028

79. D'Amario, L., Föhlinger, J., Boschloo, G., Hammarström, L. Unveiling hole trapping and surface dynamics of NiO nanoparticles. *Chem. Sci.* **9**, 223 (2018). DOI: 10.1039/c7sc03442c

80. Ibupoto, Z. H., Abbasi, M. A., Liu, X., Alsalhi, M. S., Willander, M. The synthesis of NiO/$TiO_2$ heterostructures and their valence band offset determination. *J. Nanomater.* (2014). DOI: 10.1155/2014/928658

81. Melián, E. P., Suárez, M. N., Jardiel, T., Rodríguez, J. M. D., Caballero, A. C., Araña, J., Calatayud, D. G., Díaz, O. G. Influence of nickel in the hydrogen production activity of $TiO_2$. *Appl. Catal. B* **152**, 192 (2014). DOI: 10.1016/j.apcatb.2014.01.039

82. Yu, C., Li, M., Yang, D., Pan, K., Yang, F., Xu, Y., Yuan, L., Qu, Y., Zhou, W. NiO nanoparticles dotted $TiO_2$ nanosheets assembled nanotubes P-N heterojunctions for efficient interface charge separation and photocatalytic hydrogen evolution. *Appl. Surf. Sci*. **568**, 150981 (2021). DOI: 10.1016/j.apsusc.2021.150981

83. Xu, Y., Xu, R. Nickel-based cocatalysts for photocatalytic hydrogen production. *Appl. Surf. Sci*. **351**, 779 (2015). DOI: 10.1016/j.apsusc.2015.05.171

84. Wang, Z., Fan, J., Cheng, B., Yu, J., Xu, J. Nickel-based cocatalysts for photocatalysis: Hydrogen evolution, overall water splitting and $CO_2$ reduction. *Mater. Today Phys.* **15**, 100279 (2020). DOI: 10.1016/j.mtphys.2020.100279

85. Sreethawong, T., Suzuki, Y., Yoshikawa, S. Photocatalytic evolution of hydrogen over mesoporous $TiO_2$ supported NiO photocatalyst prepared by single-step sol-gel process with surfactant template. *Int. J. Hydrog. Energy* **30**, 1053 (2005). DOI: 10.1016/j.ijhydene.2004.09.007

86. Zheng, D., Zhao, H., Wang, S., Hu, J., Chen, Z. NiO-$TiO_2$ p-n heterojunction for solar hydrogen generation. *Catalysts* **11**, 1427 (2021). DOI: 10.3390/catal11121427

87. Rawool, S. A., Pai, M. R., Banerjee, A. M., Arya, A., Ningthoujam, R. S., Tewari, R., Rao, R., Chalke, B., Ayyub, P., Tripathi, A. K., Bharadwaj, S. R. *pn* Heterojunctions in NiO:$TiO_2$ composites with type-II band alignment assisting sunlight driven photocatalytic $H_2$ generation. *Appl. Catal. B* **221**, 443 (2018). DOI: 10.1016/j.apcatb.2017.09.004

88. Yu, J., Hai, Y., Cheng, B. Enhanced photocatalytic $H_2$-production activity of $TiO_2$ by $Ni(OH)_2$ cluster modification. *J. Phys. Chem. C* **115**, 4953 (2011). DOI: 10.1021/jp111562d

89. Lakshmana Reddy, N., Cheralathan, K. K., Durga Kumari, V., Neppolian, B., Muthukonda Venkatakrishnan, S. Photocatalytic Reforming of Biomass Derived Crude Glycerol in Water: A Sustainable Approach for Improved Hydrogen Generation Using $Ni(OH)_2$ Decorated $TiO_2$ Nanotubes under Solar Light Irradiation. *ACS Sustain. Chem. Eng.* **6**, 3754 (2018). DOI: 10.1021/acssuschemeng.7b04118

90. Xie, L., Hao, J. G., Chen, H. Q., Li, Z. X., Ge, S. Y., Mi, Y., Yang, K., Lu, K. Q. Recent advances of nickel hydroxide-based cocatalysts in heterogeneous photocatalysis. *Catal. Commun*. **162**, 106371 (2022). DOI: 10.1016/j.catcom.2021.106371

91. Low, J., Cheng, B., Yu, J. Surface modification and enhanced photocatalytic $CO_2$ reduction performance of $TiO_2$: a review. *Appl. Surf. Sci.* **392,** 658 (2017). https://doi.org/10.1016/j.apsusc.2016.09.093

92. Verma, P., Kuwahara, Y., Mori, K., Yamashita, H. Pd/Ag and Pd/Au bimetallic nanocatalysts on mesoporous silica for plasmon-mediated enhanced catalytic activity under visible light irradiation. *J Mater. Chem. A* **4**, 10142 (2016). https://doi.org/10.1039/C6TA01664B

93. Zielińska-Jurek, A. Progress, Challenge, and Perspective of Bimetallic $TiO_2$-Based Photocatalysts. *J. Nanomater.* **2014**, 208920 (2014). https://doi.org/10.1155/2014/208920

94. Iyad Sarhid, Catalysis assisted by plasmon. Catalysis. Université Paris Saclay (COmUE), 2019. English. ⟨NNT: 2019SACLS227⟩.

95. Calvo, R., Thon, A., Saad, A., Salvador-Matar, A., Manso-Silván, M., Ahumada, Ó., Pini, V. Size characterization of plasmonic nanoparticles with dark-field single particle spectrophotometry. *Sci. Rep.* **12**, 17231 (2022). https://doi.org/10.1038/s41598-022-21649-8

96. Pellas, V., Hu, D., Mazouzi, Y., Mimoun, Y., Blanchard, J., Guibert, C., Salmain, M., Boujday, S. Gold Nanorods for LSPR Biosensing: Synthesis, Coating by Silica, and Bioanalytical Applications. *Biosensors* **10,** 146 (2020). https://doi.org/10.3390/bios10100146

97. Hu, L., Li, Y., Peng, X., Zheng, W., Xu, W., Zhu, J., Lee, L. Y. S., Chu, P. K., Wong, K. Y. $TiO_2$ film supported by vertically aligned gold nanorod superlattice array for enhanced photocatalytic hydrogen evolution. *J. Chem. Eng.* **417**, 127900 (2021). https://doi.org/10.1016/j.cej.2020.127900
98. Kim, F., Song, J. H., Yang, P. Photochemical synthesis of gold nanorods. *J. Am .Chem. Soc.* **124,** 14316 (2002). https://doi.org/10.1021/ja028110o
99. Qiu, L., Pang, G. A., Zheng, G., Bauer, D., Wieland, K., Haisch, C. Kinetic and Mechanistic Investigation of the Photocatalyzed Surface Reduction of 4-Nitrothiophenol Observed on a Silver Plasmonic Film via Surface-Enhanced Raman Scattering. *ACS Appl. Mater. Interfaces* **12,** 21133 (2020). https://doi.org/10.1021/acsami.0c05977
100. Lin, T. W., Tasi, T. T., Chang, P. L., Cheng, H. Y. Reversible Association of Nitro Compounds with p-Nitrothiophenol Modified on Ag Nanoparticles/Graphene Oxide Nanocomposites through Plasmon Mediated Photochemical Reaction. *ACS Appl. Mater. Interfaces* **8**, 8315 (2016). https://doi.org/10.1021/acsami.6b01522
101. Cortés, E., Xie, W., Cambiasso, J., Jermyn, A. S., Sundararaman, R., Narang, P., Schlücker, S., Maier, S. A. Plasmonic hot electron transport drives nano-localized chemistry. *Nat. Commun.* **8**, 14880 (2017). https://doi.org/10.1038/ncomms14880
102. Sarhid, I., Abdellah, I., Martini, C., Huc, V., Dragoe, D., Beaunier, P., Lampre, I., Remita, H. Plasmonic catalysis for the Suzuki–Miyaura cross-coupling reaction using palladium nanoflowers. *New J. Chem.* **43**, 4349 (2019). DOI: 10.1039/C8NJ06370B
103. Astruc D. Palladium Nanoparticles as Efficient Green Homogeneous and Heterogeneous Carbon−Carbon Coupling Precatalysts: A Unifying View. *Inorg. Chem.* **46**, 1884 (2007). https://doi.org/10.1021/ic062183h
104. Dileseigres, A. S., Prado, Y., Pluchery, O. How to Use Localized Surface Plasmon for Monitoring the Adsorption of Thiol Molecules on Gold Nanoparticles?. *Nanomaterials* **12,** 292 (2022). https://doi.org/10.3390/nano12020292

105. Dumas, A., Couvreur, P. Palladium: a future key player in the nanomedical field?. *Chem. Sci.* **6**, 2153 (2015). DOI: 10.1039/C5SC00070J

106. Peramo, A., Dumas, A., Remita, H., Benoît, M., Yen-Nicolay, S., Corre, R., Louzada, R. A., Dupuy, C., Pecnard, S., Lambert, B., Young, J., Desmaële, D., Couvreur, P. Selective modification of a native protein in a patient tissue homogenate using palladium nanoparticles. *Chem. Commun.* **55**, 15121–15124 (2019). https://doi.org/10.1039/C9CC07803G

107. Ksar, F., Sharma, G. K., Audonnet, F., Beaunier, P., Remita, H. Palladium urchin-like nanostructures and their $H_2$ sorption properties. *Nanotechnology*, **22**, 30, (2011). https://doi.org/10.1088/0957-4484/22/30/305609.

108. Karimi, B., Abedi, S., Clark, J. H., Budarin, V. Highly Efficient Aerobic Oxidation of Alcohols Using a Recoverable Catalyst: The Role of Mesoporous Channels of SBA-15 in Stabilizing Palladium Nanoparticles. *Angew. Chem. Int. Ed.* **45**, 4776 (2006). DOI: 10.1002/anie.200504359

109. Min, S. K., Kim, N., Cheon, M. P., Jae, S. L., Kyung, Y. K., Park, J. Park. Palladium Nanoparticles Entrapped in Aluminum Hydroxide: Dual Catalyst for Alkene Hydrogenation and Aerobic Alcohol Oxidation. *Org. Lett*. **7**, 1077 (2005). https://doi.org/10.1021/ol047381w

110. Ksar, F., Surendran, G., Ramos, L., Keita, B., Nadjo, L., Prouzet, E., Beaunier, P., Hagège, A., Audonnet, F., Remita, H. Palladium Nanowires Synthesized in Hexagonal Mesophases: Application in Ethanol Electrooxidation. *Chem. Mater.* **21**, 1612 (2009). https://doi.org/10.1021/cm803492j

111. Surendran, G., Ksar, F., Ramos, L., Keita, B., Nadjo, L., Prouzet, E., Beaunier, P., Dieudonné, P., Audonnet, F., Remita. Palladium Nanoballs Synthesized in Hexagonal Mesophases. *J. Phys. Chem. C* **112**, 10740 (2008). https://doi.org/10.1021/jp801703z

112. Ghosh, S., Bera, S., Karmakar, N., Basu, R. N. Enhanced Electrocatalytic Activity of Branched Pd Nanostructures Decorated Conducting Polymer Nanofibers for Alkaline Fuel Cells. *Mater. Today: Proc*. **5**, 9733 (2018). https://doi.org/10.1016/j.matpr.2017.10.160

113. Ghosh, S., Teillout, A. L., Floresyona, D., De Oliveira, P., Hagège, A., Remita, H. Conducting polymer-supported palladium nanoplates for applications in direct alcohol oxidation. *Int. J. Hydrogen Energy* **40**, 4951 (2015). https://doi.org/10.1016/j.ijhydene.2015.01.101
114. Remita, H., Lampre, I. Synthesis of Metallic Nanostructures Using Ionizing Radiation and Their Applications. *Materials* **17**, 364 (2024). DOI: 10.3390/ma17020364
115. Ray, P., Clément, M., Martini, C., Abdellah, I., Beaunier, P., Rodriguez-Lopez, J. L., Huc, V., Remita, H., Lampre, I. Stabilisation of small mono- and bimetallic gold-silver nanoparticles using calix[8]arene derivatives. *New J. Chem.* **42**, 14128 (2018). DOI: 10.1039/c8nj02451k
116. Myron, J. J. J., Freeman, G. R. The radiolysis of ethanol liquid phase. *Can. J. Chem.* **43**, (1965). DOI: 10.1139/v65-05
117. Gachard, E., Remita, H., Khatouri, J., Keita, B., Nadjo, L., Belloni, J. Radiation-induced and chemical formation of gold clusters. *New J. Chem.* **22**, 1257 (1998). https://doi.org/10.1039/A804445G
118. Tahiri Alaoui, O., Herissan, A., Le Quoc, C., Zekri, M. E. M., Sorgues, S., Remita, H., Colbeau-Justin, C. Elaboration, charge-carrier lifetimes and activity of Pd-$TiO_2$ photocatalysts obtained by gamma radiolysis. *J. Photochem. Photobiol. A: Chem.* **242**, 34 (2012). https://doi.org/10.1016/j.jphotochem.2012.05.030
119. Belloni, J. Nucleation, growth and properties of nanoclusters studied by radiation chemistry: Application to catalysis. *Catal. Today* **113**, 141. (2006). https://doi.org/10.1016/j.cattod.2005.11.082
120. Daruich De Souza, C., Ribeiro Nogueira, B., Rostelato, M. E. C. M. Review of the methodologies used in the synthesis gold nanoparticles by chemical reduction. *J. Alloys Compd.* **798**, 714 (2019). https://doi.org/10.1016/j.jallcom.2019.05.153
121. Sahoo, M., Mansingh, S., Subudhi, S., Mohapatra, P., Parida, K. A plasmonic AuPd bimetallic nanoalloy decorated over a GO/LDH hybrid nanocomposite: Via a green synthesis route for robust Suzuki coupling reactions: A paradigm

shift towards a sustainable future. *Catal. Sci. Technol.* **9**, 4678 (2019). DOI: 10.1039/C9CY01085H

122. Susana, C. R., Jorge, P. J., Pablo, H., Luis, M. L. M., Paul, M. Colloidal gold-catalyzed reduction of ferrocyanate (III) by borohydride ions: A model system for redox catalysis. *Langmuir* **26**, 1271 (2010). https://doi.org/10.1021/la902442p
123. Pasqualeti, A. M., Olu, P. Y., Chatenet, M., Lima, F. H. B. Borohydride electrooxidation on carbon-supported noble metal nanoparticles: Insights into hydrogen and hydroxyborane formation. *ACS Catal.* **5**, 2778 (2015). https://doi.org/10.1021/acscatal.5b00107
124. Liu, Q. M., Zhou, D. B., Yamamoto, Y., Ichino, R., Okido, M. Preparation of Cu nanoparticles with $NaBH_4$ by aqueous reduction method. *Transactions of Nonferrous Metals Society of China (English Edition)* **22**, 117 (2012). https://doi.org/10.1016/S1003-6326(11)61149-7
125. Ortiz-Castillo, J. E., Gallo-Villanueva, R. C., Madou, M. J., Perez-Gonzalez, V. H. Anisotropic gold nanoparticles: A survey of recent synthetic methodologies. *Coord. Chem. Rev.* **425**, 213489 (2020). https://doi.org/10.1016/j.ccr.2020.213489
126. Yuan, H., Khoury, C. G., Hwang, H., Wilson, C. M., Grant, G. A., Vo-Dinh, T. Gold nanostars: Surfactant-free synthesis, 3D modelling, and two-photon photoluminescence imaging. *Nanotechnology* **23**, 7 (2012). https://doi.org/10.1088/0957-4484/23/7/075102
127. Kimling, J., Maier, M., Okenve, B., Kotaidis, V., Ballot, H., Plech, A. Turkevich method for gold nanoparticle synthesis revisited. *J. Phys. Chem. B* **110**, 15700 (2006). https://doi.org/10.1021/jp061667w
128. Ma, T., Yang, W., Liu, S., Zhang, H., Liang, F. A Comparison Reduction of 4-Nitrophenol by Gold Nanospheres and Gold Nanostars. *Catalysts* **7**, 38 (2017). https://doi.org/10.3390/catal7020038
129. Vandenbroucke, A. M. Abatement of volatile organic compounds by combined use of non-thermal plasma and heterogeneous catalysis. (2017).

130. Colbeau-Justin, C., Kunst, M., Huguenin, D. Structural influence on charge-carrier lifetimes in $TiO_2$ powders studied by microwave absorption. *J. Mater. Sci.* **38**, 2429 (2003). https://doi.org/10.1023/A:1023905102094
131. Abadie, C., Liu, M., Prado, Y., Pluchery, O. Hyperspectral dark-field optical microscopy correlated to atomic force microscopy for the analysis of single plasmonic nanoparticles: tutorial. *J. Opt. Soc. Am. B* **41,** 1678 (2024). https://doi.org/10.1364/JOSAB.523547
132. Xia, F., Rangelow, I. W., Youcef-Toumi, K. Active Probe Atomic Force Microscopy. Springer Nature Switzerland AG, 2024. https://doi.org/10.1007/978-3-031-44233-9
133. Berthier, F., Legrand, B. Analysis of Au–Pd driving forces via the effective site energy model: LRO, antisites and enthalpy of permutation. J. Condens. Matter Phys. 2020, 32, 354001. 10.1088/1361-648X/ab87ce
134. Berthier, F., Creuze, J., Gabard, T., Legrand, B., Marinica, M. C., Mottet, C.. Order-disorder or phase-separation transition: Analysis of the Au-Pd system by the effective site energy model. *Phys. Rev. B* **32**, 014108 (2019). https://doi.org/10.1103/PhysRevB.99.014108
135. Chang, J. B., Liu, C. H., Liu, J., Zhou, Y. Y., Gao, X. , Wang, S. D. Green-chemistry Compatible Approach to $TiO_2$-supported PdAu Bimetallic Nanoparticles for Solvent-free 1-Phenylethanol Oxidation under Mild Conditions. *Nanomicro. Lett.* **7**, 307 (2015). https://doi.org/10.1007/s40820-015-0044-6
136. Nishimura, S., Abrams, N., Lewis, B. A., Halaoui, L. I., Mallouk, T. E., Benkstein, K. D., Van de Lagemaat, J., Frank, A. J. Standing wave enhancement of red absorbance and photocurrent in dye-sensitized titanium dioxide photoelectrodes coupled to photonic crystals. .*J. Am. Chem. Soc.* **125**, 6306 (2003). https://doi.org/10.1021/ja034650p
137. Biesinger, M. C., Payne, B. P., Grosvenor, A. P., Lau, L. W. M., Gerson, A. R., Smart, R. S. C. Resolving surface chemical states in XPS analysis of first row transition metals, oxides and hydroxides: Cr, Mn, Fe, Co and Ni. *Appl. Surf. Sci.* **257**, 2717 (2011). https://doi.org/10.1016/j.apsusc.2010.10.051

138. Moulder, J. F., Stickle, W. F., Sobol, P. E. ', Bomben, K. D. & Chastain, J. Handbook of X-Ray Photoelectron Spectroscopy, Perkin-Elmer, Minnesota, USA, 1992.
139. Wang, F., Zhang, H., Zhang, Z., Ma, Q., Kong, C., Min, S. Carbonized wood membrane decorated with AuPd alloy nanoparticles as an efficient self-supported electrode for electrocatalytic $CO_2$ reduction. *J. Colloid. Interface Sci.* **607**, 312 (2022). https://doi.org/10.1016/j.jcis.2021.08.156
140. Liu, B., Li, K., Luo, Y., Gao, L., Duan, G. Sulfur spillover driven by charge transfer between AuPd alloys and $SnO_2$ allows high selectivity for dimethyl disulfide gas sensing. *J. Chem. Eng.* **420**, 129881. (2021). https://doi.org/10.1016/j.cej.2021.129881
141. Xu, J., White, T., Li, P., He, C., Yu, J., Yuan, W., Han, Y. F. Biphasic Pd-Au alloy catalyst for low-temperature CO oxidation. *J. Am. Chem. Soc.* **132**, 10398 (2010). https://doi.org/10.1021/ja102617r
142. Casey, É., Holmes, J. D., Collins, G. PdAu Nanosheets for Visible-Light-Driven Suzuki Cross-Coupling Reactions. *ACS Appl. Nano Mater.* **5**, 16196 (2022). https://doi.org/10.1021/acsanm.2c03216
143. Zhu, X., Guo, Q., Sun, Y., Chen, S., Wang, J. Q., Wu, M., Fu, W., Tang, Y., Duan, X., Chen, D., Wan, Y. Optimising surface d charge of AuPd nanoalloy catalysts for enhanced catalytic activity. *Nat. Commun.* **10**, 1428 (2019). https://doi.org/10.1038/s41467-019-09421-5
144. Zhang, Y., Pluchery, O., Caillard, L., Lamic-Humblot, A. F., Casale, S., Chabal, Y. J., Salmeron, M. Sensing the charge state of single gold nanoparticles via work function measurements. *Nano Lett.* **15**, 51 (2015).https://doi.org/10.1021/nl503782s
145. Lechaptois, L., Prado, Y., Pluchery, O. KPFM visualisation of the Schottky barrier at the interface between gold nanoparticles and silicon. *Nanoscale* **15**, 7510 (2023). https://doi.org/10.1039/D3NR00178D
146. de Marchi, S., Núñez-Sánchez, S., Bodelón, G., Pérez-Juste, J., Pastoriza-Santos, I. Pd nanoparticles as a plasmonic material: Synthesis, optical

properties and applications. *Nanoscale* **12**, 23424 (2020). https://doi.org/10.1039/D0NR06270G

147. Le, H. J., van Dao, D. & Yu, Y. T. Superfast and efficient hydrogen gas sensor using PdAualloy@ZnO core–shell nanoparticles. *J. Mater. Chem. A* **8**, 12968 (2020). https://doi.org/10.1039/D0TA03552A
148. Tyagi, M.S. (1984). Physics of Schottky Barrier Junctions. In: Sharma, B.L. (eds) Metal-Semiconductor Schottky Barrier Junctions and Their Applications. Springer, Boston, MA. https://doi.org/10.1007/978-1-4684-4655-5_1
149. Chowdhury, P., Gomaa, H., Ray, A. K. Sacrificial hydrogen generation from aqueous triethanolamine with Eosin Y-sensitized Pt/$TiO_2$ photocatalyst in UV, visible and solar light irradiation. *Chemosphere* **121**, 54 (2015). https://doi.org/10.1016/j.chemosphere.2014.10.076
150. Yuan, X., Dragoe, D., Beaunier, P., Uribe, D. B., Ramos, L., Méndez-Medrano, M. G., Remita, H. Polypyrrole nanostructures modified with mono- And bimetallic nanoparticles for photocatalytic $H_2$ generation. *J. Mater. Chem. A* **8**, 268 (2020). DOI: 10.1039/c9ta11088g
151. Langenberg, E., Rebled, J., Estraḋ, S., Daumont, C. J. M., Ventura, J., Coy, L. E., Polo, M. C., García-Cuenca, M. V., Ferrater, C., Noheda, B., Peiró, F., Varela, M., Fontcuberta, J. Long-range order of $Ni^{2+}$ and $Mn^{4+}$ and ferromagnetism in multiferroic $(Bi_{0.9}La_{0.1})_2NiMnO_6$ thin films. *J. Appl. Phys*. **108**, 123907 (2010). DOI: 10.1063/1.3524278
152. Potapov, P. L., Kulkova, S. E., Schryvers, D., Verbeeck, J. Structural and chemical effects on EELS $L_{3,2}$ ionization edges in Ni-based intermetallic compounds. *Phys. Rev. B* **64**, 184110 (2001). DOI: 10.1103/PhysRevB.64.184110
153. De Groot, F. M. F., Hu, Z. W., Lopez, M. F., Kaindl, G., Guillot, F., Tronc, M. Differences between $L_3$ and $L_2$ x-ray absorption spectra of transition metal compounds. *J. Chem. Phys*. **101**, 6570 (1994). DOI: 10.1063/1.468351
154. Wang, W., Liu, S., Nie, L., Cheng, B., Yu, J. Enhanced photocatalytic $H_2$-production activity of $TiO_2$ using $Ni(NO_3)_2$ as an additive. *Phys. Chem. Chem. Phys.* **15**, 12033 (2013). DOI: 10.1039/c2cp43628k

155. Chen, W. T., Chan, A., Sun-Waterhouse, D., Llorca, J., Idriss, H., Waterhouse, G. I. N. Performance comparison of Ni/$TiO_2$ and Au/$TiO_2$ photocatalysts for $H_2$ production in different alcohol-water mixtures. *J. Catal*. **367**, 27 (2018). DOI: 10.1016/j.jcat.2018.08.015
156. Chen, J., Wang, M., Hu, J., Han, J., Yu, H., Guo, R. $TiO_2$ nanosheet/NiO nanorod/poly(dopamine) ternary hybrids towards efficient visible light photocatalysis. *Colloids Surf. A: Physicochem. Eng. Asp.* **637**, 128197 (2022). DOI: 10.1016/j.colsurfa.2021.128197
157. Makuła, P., Pacia, M., Macyk, W. How To Correctly Determine the Band Gap Energy of Modified Semiconductor Photocatalysts Based on UV-Vis Spectra. *J. Phys. Chem. Lett.* **9**, 6814 (2018). DOI: 10.1021/acs.jpclett.8b02892
158. Zhao, H., Li, C. F., Liu, L. Y., Palma, B., Hu, Z. Y., Renneckar, S., Larter, S., Li, Y., Kibria, M. G., Hu, J., Su, B. L. n-p Heterojunction of $TiO_2$-NiO core-shell structure for efficient hydrogen generation and lignin photoreforming. *J. Colloid Interface Sci*. **585**, 694 (2021). DOI: 10.1016/j.jcis.2020.10.049
159. Lai, B., Mei, F., Gu, Y. Bifunctional Solid Catalyst for Organic Reactions in Water: Simultaneous Anchoring of Acetylacetone Ligands and Amphiphilic Ionic Liquid “Tags” by Using a Dihydropyran Linker. *Chem. Asian J.* **13**, 2529 (2018). DOI: 10.1002/asia.201800567
160. Kim, S. I., Thiyagarajan, P., Jang, J. H. Great improvement in pseudocapacitor properties of nickel hydroxide via simple gold deposition. *Nanoscale* **6**, 11646 (2014). DOI: 10.1039/c4nr02204a
161. Chen, J., Wang, M., Han, J., Guo, R. $TiO_2$ nanosheet/NiO nanorod hierarchical nanostructures: p–n heterojunctions towards efficient photocatalysis. *J. Colloid Interface Sci.* **562**, 313 (2020). DOI: 10.1016/j.jcis.2019.12.031
162. Zhao, X., Xie, W., Shao, X., Wang, Z., Yang, B., Yang, C., Wang, J., Su, X. An effective Ni/C co-catalyst for promoting photocatalytic hydrogen evolution over $TiO_2$ nanospheres. *Mater. Sci. Semicond. Process.* **148**, 106775 (2022). DOI: 10.1016/j.mssp.2022.106775
163. Chen, X., Chen, W., Lin, P., Yang, Y., Gao, H., Yuan, J., Shangguan, W. In situ photodeposition of nickel oxides on CdS for highly efficient hydrogen

production via visible-light-driven photocatalysis. *Catal. Commun*. **36**, 104 (2013). DOI: 10.1016/j.catcom.2013.03.016

164. Quiroz-Cardoso, O., Oros-Ruiz, S., Solís-Gómez, A., López, R., Gómez, R. Enhanced photocatalytic hydrogen production by CdS nanofibers modified with graphene oxide and nickel nanoparticles under visible light. *Fuel* **237**, 227 (2019). DOI: 10.1016/j.fuel.2018.10.013
165. Yan, Z., Sun, Z., Liu, X., Jia, H., Du, P. Cadmium sulfide/graphitic carbon nitride heterostructure nanowire loading with a nickel hydroxide cocatalyst for highly efficient photocatalytic hydrogen production in water under visible light. *Nanoscale* **8**, 4748 (2016). DOI: 10.1039/c6nr00160b
166. Rosen, B.M., Quasdorf, K. W., Wilson, D. A., Zhang, N., Resmerita, A. M., Garg, N. K., Percec, V. Nickel-catalyzed cross-couplings involving carbon-oxygen bonds. *Chem. Rev.* **111**, 1346 (2011). DOI: 10.1021/cr100259t
167. Dong, Y., Jv, J. J., Li, Y., Li, W. H., Chen, Y. Q., Sun, Q., Ma, J. P., Dong, Y. Bin. Nickel-metalated porous organic polymer for Suzuki-Miyaura cross-coupling reaction. *RSC Adv.* **9**, 20266 (2019). DOI: 10.1039/c9ra03679b
168. Kaniukov, E. Y., Shumskaya, A. E., Kutuzau, M. D., Bundyukova, V. D., Yakimchuk, D. V., Borgekov, D. B., Ibragimova, M. A., Korolkov, I. V., Giniyatova, S. G., Kozlovskiy, A. L., Zdorovets, M. V. Degradation mechanism and way of surface protection of nickel nanostructures. *Mater. Chem. Phys*. **223**, 88 (2019). DOI: 10.1016/j.matchemphys.2018.09.010
169. De, S., Zhang, J., Luque, R., Yan, N. Ni-based bimetallic heterogeneous catalysts for energy and environmental applications. *Energy Environ. Sci.* **9**, 3314 (2016). DOI: 10.1039/c6ee02002j
170. Sun, B., Zhou, G., Gao, T., Zhang, H., Yu, H. NiO nanosheet/$TiO_2$ nanorod-constructed *p-n* heterostructures for improved photocatalytic activity. *Appl. Surf. Sci*. **364**, 322 (2016). DOI: 10.1016/j.apsusc.2015.12.158
171. Mannaa, M. A., Qasim, K. F., Alshorifi, F. T., El-Bahy, S. M., Salama, R. S. Role of NiO Nanoparticles in Enhancing Structure Properties of $TiO_2$ and Its Applications in Photodegradation and Hydrogen Evolution. *ACS Omega* **6**, 30386 (2021). DOI: 10.1021/acsomega.1c03693

172. Ortega Méndez, J. A., López, C. R., Pulido Melián, E., González Díaz, O., Doña Rodríguez, J. M., Fernández Hevia, D., Macías, M. Production of hydrogen by water photo-splitting over commercial and synthesised Au/$TiO_2$ catalysts. *Appl. Catal. B* **147**, 439 (2014). DOI: 10.1016/j.apcatb.2013.09.029
173. Leone, L., Sgueglia, G., La Gatta, S., Chino, M., Nastri, F., Lombardi, A. Enzymatic and Bioinspired Systems for Hydrogen Production. *Int. J. Mol. Sci.* **24**, 8605 (2023).https://doi.org/10.3390/ijms24108605
174. Fukuzumi, S., Lee, Y. M., Nam, W. Thermal and photocatalytic production of hydrogen with earth-abundant metal complexes. *Coord. Chem. Rev.* **355**, 54 (2018). https://doi.org/10.1016/j.ccr.2017.07.014
175. Tetzlaff, D., Simon, C., Achilleos, D. S., Smialkowski, M., Junge Puring, K., Bloesser, A., Piontek, S., Kasap, H., Siegmund, D., Reisner, E., Marschall, R., Apfel, U. P. $Fe_xNi_{9-x}S_8$ (x = 3-6) as potential photocatalysts for solar-driven hydrogen production?. *Faraday Discuss* **215**, 216 (2019). https://doi.org/10.1039/C8FD00173A
176. Li, J., Sheng, B., Chen, Y., Yang, J., Ma, T., You, C., Li, Y., Yu, T., Song, J., Pan, H., Wang, X. ,Zhou, B. Nickel-Iron Bimetal as a Cost-Effective Cocatalyst for Light-Driven Hydrogen Release from Methanol and Water. *ACS Catal*. **13**, 10153 (2023), https://doi.org/10.1021/acscatal.3c02024.
177. Kim, H. S., Kim, D., Kwak, B. S., Han, G. B., Um, M. H., Kang, M. Synthesis of magnetically separable core@shell structured $NiFe_2O_4$@$TiO_2$ nanomaterial and its use for photocatalytic hydrogen production by methanol/water splitting. *J. Chem. Eng.* **243**, 272 (2014). DOI: 10.1016/j.cej.2013.12.046
178. Firtina-Ertis, I., Kerkez-Kuyumcu, Ö. Synthesis of $NiFe_2O_4$/$TiO_2$-$Ag^+$ S-scheme photocatalysts by a novel complex-assisted vapor thermal method for photocatalytic hydrogen production. *J. Photochem. Photobiol. A Chem*. **432**, 114106 (2022). https://doi.org/10.1016/j.jphotochem.2022.114106
179. Domínguez-Arvizu, J. L., Jiménez-Miramontes, J. A., Hernández-Majalca, B. C., Valenzuela-Castro, G. E., Gaxiola-Cebreros, F. A., Salinas-Gutiérrez, J. M., Collins-Martínez, V., López-Ortiz, A. Study of $NiFe_2O_4$/$Cu_2O$ p-n heterojunctions for hydrogen production by photocatalytic water splitting with

visible light. *J. Mater. Res. Technol*. **21**, 4184 (2022). https://doi.org/10.1016/j.jmrt.2022.11.026

180. Gao, C., Li, Y., Zhang, Z., Li, W., Zhong, J., Zhang, H., Zhang, Y., Deng, L., Sun, Z., Chen, G., Zhang, H., Wang, L., Zhuang, C., Han, X. Improving photocatalytic hydrogen production via ultrafine-grained precipitates formed nearby surface defects of NiFe-LDH nanosheets. *J. Chem. Eng.* **446**, 137301 (2022). https://doi.org/10.1016/j.cej.2022.137301
181. Boppella, R., Choi, C. H., Moon, J., Ha Kim, D. Spatial charge separation on strongly coupled 2D-hybrid of rGO/La2Ti2O7/NiFe-LDH heterostructures for highly efficient noble metal free photocatalytic hydrogen generation. *Appl Catal. B* **239**, 178 (2018), https://doi.org/10.1016/j.apcatb.2018.07.063.
182. Yue, D., Qian, X., Kan, M., Ren, M., Zhu, Y., Jiang, L., Zhao, Y. Sulfurated [NiFe]-based layered double hydroxides nanoparticles as efficient co-catalysts for photocatalytic hydrogen evolution using CdTe/CdS quantum dots. *Appl Catal B* **209**, 155 (2017), https://doi.org/10.1016/j.apcatb.2017.02.075
183. Wang, K., Li, S., Wang, G., Li, Y., Li, Y., Jin, Z. Fabrication of NiFe-PBA-S/ZnCdS form S-scheme for improved photocatalytic hydrogen evolution. *Int. J. Energy Res*. **46**, 19508 (2022), https://doi.org/10.1002/er.8522
184. Sarhan, R. M., Koopman, W., Schuetz, R., Schmid, T., Liebig, F., Koetz, J., Bargheer, M. The importance of plasmonic heating for the plasmon-driven photodimerization of 4-nitrothiophenol. *Sci. Rep.*, **9**, 3060, (2019). https://doi.org/10.1038/s41598-019-38627-2.
185. Lu, Z., Dong, J., Han, Q., Gao, W., Wang, Y., Liu, J., Wang, Z., Sun, Z., Wang, B., Qi, J. Au@Ag nanorod horizontal arrays: Self-assembly preparation and in situ monitoring SERS of plasmonic catalytic reaction. *J. Alloys Compd.,* **834**, 155139, (2020). doi.org/10.1016/j.jallcom.2020.155139.
186. Ngo, N. M., Tran, H. V., Lee, T. R. Plasmonic Nanostars: Systematic Review of their Synthesis and Applications. *ACS Appl, Nano Mater.,* **5**, 14051, (2022). https://doi.org/10.1021/acsanm.2c02533

187. Meng, X., Baride, A., Jiang, C. Ligand Controlled Morphology Evolution of Active Intermediates for the Syntheses of Gold Nanostars. *Langmuir,* **32**, 6674, (2016). https://doi.org/10.1021/acs.langmuir.6b01592.
188. Hao, F., Nehl, C. L., Hafner, J. H., Nordlander, P. Plasmon Resonances of a Gold Nanostar. *Nano Lett.*, **7**, 729, (2007). https://doi.org/10.1021/nl062969c
189. Dondapati, S. K., Sau, T. K., Hrelescu, C., Klar, T. A., Stefani, F. D., Feldmann, J. Label-free biosensing based on single gold nanostars as plasmonic transducers. *ACS Nano* **4**, 6318 (2010). https://doi.org/10.1021/nn100760f
190. Khoury, C. G., Vo-Dinh, T. Gold Nanostars For Surface-Enhanced Raman Scattering: Synthesis, Characterization and Optimization. *J. Phys. Chem. C* **112**, 18849 (2008). https://doi.org/10.1021/jp8054747
191. Yang, R., Gao, Y., Ouyang, Z., Shi, X., Shen, M. Gold nanostar-based complexes applied for cancer theranostics. *VIEW*, **3**, 20200171, (2022), https://doi.org/10.1002/VIW.20200171.
192. Fabris, L. Gold Nanostars in Biology and Medicine: Understanding Physicochemical Properties to Broaden Applicability. *J. Phys. Chem. C* **124**, 26540 (2020). https://dx.doi.org/10.1021/acs.jpcc.0c08460
193. Tsoulos, T. V., Han, L., Weir, J., Xin, H. L., Fabris, L. A closer look at the physical and optical properties of gold nanostars: An experimental and computational study. *Nanoscale* **9**, 3766 (2017). https://doi.org/10.1039/c6nr09091e.
194. Wang, Y., Polavarapu, L., Liz-Marzán, L. M. Reduced graphene oxide-supported gold nanostars for improved SERS sensing and drug delivery. *ACS Appl. Mater. Interfaces* **6**, 21798 (2014). https://doi.org/10.1021/am501382y
195. König, M., Radojcic, A., Schlücker, S., Xie, W. Label-free SERS monitoring of hydride reduction catalyzed by Au nanostars. *J. Raman Spectrosc.* **47**, 1024 (2016). https://doi.org/10.1002/jrs.4971.
196. Cui, Q., Xia, B., Mitzscherling, S., Masic, A., Li, L., Bargheer, M., Möhwald, H. Preparation of gold nanostars and their study in selective catalytic reactions. *Colloids Surf. A: Physicochem. Eng. Asp.* **465**, 20 (2015). https://doi.org/10.1016/j.colsurfa.2014.10.028.

197. Cui, Q., Yashchenok, A., Li, L., Möhwald, H., Bargheer, M. Mechanistic study on reduction reaction of nitro compounds catalyzed by gold nanoparticles using in situ SERS monitoring. *Colloids Surf. A: Physicochem. Eng. Asp.* **470**, 108 (2015). https://doi.org/10.1016/j.colsurfa.2015.01.075.

198. Yang, J., Wang, X. Y., Zhou, L., Lu, F., Cai, N., Li, J. M. Highly sensitive SERS monitoring of catalytic reaction by bifunctional Ag-Pd triangular nanoplates. *J. Saudi Chem. Soc.* **23**, 887 (2019). https://doi.org/10.1016/j.jscs.2019.01.007.

199. Dai, Q., Li, L., Wang, C., Lv, C., Su, Z., Chai, F., Fabrication of a Flowerlike Ag Microsphere Film with Applications in Catalysis and as a SERS Substrate. *Eur. J. Inorg. Chem.* **2018**, 2835 (2018). https://doi.org/10.1002/ejic.201800119.

200. Zhang, K., Li, G., Hu, Y. In-situ loading of well-dispersive silver nanoparticles on nanocrystalline magnesium oxide for real-time monitoring of catalytic reactions by surface 2 enhancement Raman spectroscopy, *Nanoscale* **7**, 16952 (2015), https://doi.org/10.1039/C5NR05718C.

201. Dong, B., Fang, Y., Chen, X., Xu, H., Sun, M. Substrate-, wavelength-, and time-dependent plasmon-assisted surface catalysis reaction of 4-nitrobenzenethiol dimerizing to *p,p'*- Dimercaptoazobenzene on Au, Ag, and Cu films. *Langmuir* **27**, 10677 (2011). https://doi.org/10.1021/la2018538.

202. Hong, M., Yokota, Y., Wong, R. A., Hayazawa, N., Kazuma, E., Kim, Y. Underpotential Deposition of Silver on Gold for Surface Catalysis of Plasmon-Enhanced Reduction of 4-Nitrothiophenol. *J. Phys. Chem. C* **125**, 16569 (2021). https://doi.org/10.1021/acs.jpcc.1c05887.

203. Zhou, B., Ou, W., Shen, J., Zhao, C., Zhong, J., Du, P., Bian, H., Li, P., Yang, L., Lu, J., Li, Y. Y. Controlling Plasmon-Aided Reduction of *p*-Nitrothiophenol by Tuning the Illumination Wavelength. *ACS Catal.* **11,** 14898 (2021). https://doi.org/10.1021/acscatal.1c04091

204. Kim, K., Choi, J. Y., Shin, K. S. Surface-Enhanced Raman Scattering of 4-Nitrobenzenethiol and 4-Aminobenzenethiol on Silver in Icy Environments at Liquid Nitrogen Temperature. *J. Phys. Chem. C* **118**, 11397 (2014). https://doi.org/10.1021/jp5015115

205. Zhao, L. Bin, Zhang, M., Huang, Y. F., Williams, C. T., Wu, D. Y., Ren, B., Tian, Z. Q. Theoretical Study of Plasmon-EnhancedSurface Catalytic Coupling Reactions of Aromatic Amines and Nitro Compounds. *J. Phys. Chem. Lett.* **5**, 1259 (2014). https://doi.org/10.1021/jz5003346
206. Wang, Y., Li, Y., Zhang, Z., Xie, W. Enhanced Plasmonic Hot Electron Transfer on Aucore-Agshell Nanoparticles under Visible-Light Irradiation. *ChemCatChem*, **15**, 22, (2023). https://doi.org/10.1002/cctc.202300919.
207. Pluchery, O., Prado, Y., Watkins, W. A complete explanation of the plasmonic colours of gold nanoparticles and of the bichromatic effect. *J. Mater. Chem. C.* **11**, 15824 (2023). https://doi.org/10.1039/D3TC02669H.
208. Sarhid, I., Lampre, I., Dragoe, D., Beaunier, P., Palpant, B., Remita, H. Hexacyano Ferrate (III) Reduction by Electron Transfer Induced by Plasmonic Catalysis on Gold Nanoparticles. *Materials* **12**, 3012 (2019). https://doi.org/10.3390/ma12183012.
209. Chen, H., Ming, T., Zhao, L., Wang, F., Sun, L. D., Wang, J., Yan, C. H. Plasmon-molecule interactions. *Nano Today* **5**, 494 (2010). https://doi.org/10.1016/j.nantod.2010.08.009.
210. Fuku, K., Hashimoto, K., Kominami, H. Photocatalytic reductive dechlorination of chlorobenzene to benzene in 2-propanol suspension of metal-loaded titanium(iv) oxide nanocrystals in the presence of dissolved sodium hydrox ide. *Chem. Commun.* **46**, 5118 (2010). https://doi.org/10.1039/C0CC00589D.
211. Cui, Z. *Radiation Induced Synthesis of Conducting Polymers and their Metal Nanocomposites. Material chemistry*. Université Paris Saclay (COmUE), 2017 https://theses.hal.science/tel-01595963
212. Pierre Bléteau, P. Thesis: *Électrochimie induite par les plasmons et plasmonique organique.* Université Paris Cité (2024).
213. Charchi, N., Li, Y., Huber, M., Kwizera, E. A., Huang, X., Argyropoulos, C., Hoang, T. Small mode volume plasmonic film -coupled nanostar resonators. *Nanoscale Adv.* **2**, 2397 (2020). https: //doi.org/10.1039/D0NA00262C

214. Hrelescu, C., Sau, T. K., Rogach, A. L., Jäckel, F., Feldmann, J. Single gold nanostars enhance Raman scattering. *Appl. Phys. Lett.* **94**, 153113 (2009). https://doi.org/10.1063/1.3119642

215. Nehl, C. L., Liao, H., Hafner, J. H. Optical properties of star-shaped gold nanoparticles. *Nano Lett.* **6**, 683 (2006). https://doi.org/10.1021/nl052409y.

216. Shao, L., Susha, A. S., Cheung, L. S., Sau, T. K., Rogach, A. L., Wang, J. Plasmonic Properties of Single Multispiked Gold Nanostars: Correlating Modeling with Experiments. *Langmuir* **28**, 8979 (2012). https://doi.org/10.1021/la2048097

217. Tran, V., Thiel, C., Svejda, J. T., Jalali, M., Walkenfort, B., Erni, D., Schlücker, S. Probing the SERS brightness of individual Au nanoparticles, hollow Au/Ag nanoshells, Au nanostars and Au core/Au satellite particles: Single-particle experiments and computer simulations. *Nanoscale* **10**, 21721 (2018). https://doi.org/10.1039/C8NR06028B.

218. Uvarov, V., Popov, I. Metrological characterization of X-ray diffraction methods at different acquisition geometries for determination of crystallite size in nano-scale materials. *Mater. Charact*. **85**, 111 (2013). https://doi.org/10.1016/j.matchar.2013.09.002

219. Uvarov, V., Popov, I. Metrological characterization of X-ray diffraction methods for determination of crystallite size in nano-scale materials. *Mater. Charact*. **58**, 883 (2007). https://doi.org/10.1016/j.matchar.2006.09.002

220. Zhang, J., Yu, Z., Gao, Z., Ge, H., Zhao, S., Chen, C., Chen, S., Tong, X., Wang, M., Zheng, Z., Qin, Y. Porous TiO2 Nanotubes with Spatially Separated Platinum and CoOx Cocatalysts Produced by Atomic Layer Deposition for Photocatalytic Hydrogen Production. *Angew. Chem*. **129**, 834 (2017). https://doi.org/10.1002/anie.201611137

221. Majeed, I., Manzoor, U., Kanodarwala, F. K., Nadeem, M. A., Nadeem, M. A., Hussain, E., Ali, H., Badshah, A., Stride, J. A. Pd–Ag decorated g-C3N4 as an efficient photocatalyst for hydrogen production from water under direct solar light irradiation. *Catal. Sci. Technol*. **8**, 1183 (2018). https://doi.org/10.1039/C7CY02219K

222. Neese, F., Wiley Interdiscip. *Rev. Comput. Mol. Sci*. **2**, 73 (2012). https://doi.org/10.1002/wcms.81

223. Grimme, S., Ehrlich, S., Goerigk, L. Effect of the damping function in dispersion corrected density functional theory. *J. Comput. Chem.* **32**, 1456 (2011). https://doi.org/10.1002/jcc.21759

224. Lu, T., Chen, F. Multiwfn: A multifunctional wavefunction analyzer. *J. Comput. Chem*. **33**, 580 (2012). https://doi.org/10.1002/jcc.22885

225. Becke, A. D., Edgecombe, K. E. Edgecombe. A simple measure of electron localization in atomic and molecular systems. *J. Chem. Phys*. **92**, 5397 (1990). https://doi.org/10.1063/1.458517

226. Pittaway, F., Paz-Borbón, L. O., Johnston, R. L., Arslan, H., Ferrando, R., Mottet, C., Barcaro, G., Fortunelli, A. Theo-retical Studies of Palladium−Gold Nanoclusters: Pd−Au Clusters with up to 50 Atoms. *J. Phys. Chem. C* **113**, 9141 (2009). https://doi.org/10.1021/jp9006075

227. Thompson, A. P., Aktulga, H. M., Berger, R., Bolintineanu, D. S., Brown, W. M., Crozier, P. S., in 't Veld, P. J., Kohlmeyer, A., Moore, S. G., Nguyen, T. D., Shan, R., Stevens, M. J., Tranchida, J., Trott, C., Plimpton, S. J. LAMMPS - a flexible simulation tool for particle-based materials modeling at the atomic, meso, and continuum scales. *Comput. Phys. Commun*. **271**,108171 (2022). https://doi.org/10.1016/j.cpc.2021.108171

228. Hourahine, B., Aradi, B., Blum, V., Bonafé, F., Buccheri, A., Camacho, C., Cevallos, C., Deshaye, M. Y., Dumitric, T., Dominguez, A., Ehlert, S., Elstner, M., Van Der Heide, T., Hermann, J., Irle, S., Kranz, J. J., Köhler, C., Kowalczyk, T., Kubař, T., Lee, I. S., Lutsker, V., Maurer, R. J., Min, S. K., Mitchell, I., Negre, C., Niehaus, T. A., Niklasson, A. M. N., Page, A. J., Pecchia, A., Penazzi, G., Persson, M. P., Å&tild;ezáč, J., Sánchez, C. G., Sternberg, M., Stöhr, M., Stucken-berg, F., Tkatchenko, A., Yu, V. W. Z. & Frauenheim, T. DFTB+, a software package for efficient approximate density functional theory based atomistic simulations. *J. Chem. Phys*. **152**, 124101 (2020). https://doi.org/10.1063/1.5143190

229. Grimme, S., Bannwarth, C., Shushkov, P.. A Robust and Accurate Tight-Binding Quantum Chemical Method for Structures, Vibrational Frequencies, and Noncovalent Interactions of Large Molecular Systems Parametrized for All spd-Block Elements (*Z* = 1–86). *J. Chem. Theory Comput.* **13**, 1989 (2017). https://doi.org/10.1021/acs.jctc.7b00118

230. Eisapour, M., Zhao, H., Zhao, J., Roostaei, T., Li, Z., Omidkar, A., Hu, J., Chen, Z. p-n heterojunction of nickel oxide on titanium dioxide nanosheets for hydrogen and value-added chemicals coproduction from glycerol photoreforming. *J. Colloid. Interface Sci*. **647**, 255 (2023). DOI: 10.1016/j.jcis.2023.05.138

# Scientific Contributions (2021-2024)

## Publications

Ana Andrea Méndez-Medrano, Daniel Bahena-Uribe, Diana Dragoe, Carine Clavaguéra, Christophe Colbeau-Justin, Juan Pedro Palomares Báez, José Luis Rodríguez-López*, Hynd Remita*. **Enhanced Photocatalytic Activity of Surface-Modified $TiO_2$ with Bimetallic AuPd Nanoalloys for Hydrogen Generation**. *Solar RRL.* ***8***, 2400106 (2024)**.** https://doi.org/10.1002/solr.202400106.

Article in process:
Ana Andrea Méndez-Medrano, Xiaojiao Yuan, Diana Dragoe, Christophe Colbeau-Justin, José Luis Rodríguez-López,* and Hynd Remita*. **NiO/$TiO_2$ *p-n* Heterojunction Induced by Radiolysis for Photocatalytic Hydrogen Generation,** *to be submitted.*

Article in process:
Ana Andrea Méndez-Medrano, Diana Dragoe, Christophe Colbeau-Justin, José Luis Rodríguez-López,* and Hynd Remita*. **Surface Modification of $TiO_2$ with bimetallic NiFe nanoparticles Reduction of 4-Nitrothiophenol by Plasmon Excitation of Gold Nanostars under Visible Light,** *to be submitted.*

Article in process:
Ana Andrea Méndez-Medrano, Isabelle Lampre, Olivier Pluchery, Claire Abadie, Daniel Bahena-Uribe, José Luis Rodríguez-López,* and Hynd Remita*. **Plasmonic Catalysis with Gold Nanostars,** *to be submitted.*

## Conferences

### Oral presentations

### International

1.- ***XXXI International Materials Research Congress (IMRC), Cancún, Mexico. August 13-18, 2023***. Photocatalytic Hydrogen Generation by $TiO_2$ Modified with AuPd Nanoalloys. Ana Andrea Méndez-Medrano, Daniel Bahena-Uribe, José Luis Rodríguez-López, Hynd Remita.

2.- ***XXXI International Materials Research Congress (IMRC), Cancún, Mexico. August 13-18, 2023***. Surface Modification of Titania with NiFe Nanoparticles for Photocatalytic Hydrogen Generation. Ana Andrea Méndez-Medrano, José Luis Rodríguez-López, Hynd Remita.

3.- ***3rd MOMENTOM International Congress, Gif-sur-Yvette, France. March 8-10, 2023***. Enhancement of Photocatalytic Hydrogen Generation on $TiO_2$ by AuPd Nanoalloys. Ana Andrea Méndez-Medrano, José Luis Rodríguez-López, Hynd Remita.

4.- ***XXX International Materials Research Congress, Cancún, Mexico. Aug 14-19, 2022***. Surface Modification of $TiO_2$ with bimetallic AuPd nanoparticles for Photocatalytic Hydrogen Generation, Ana Andrea Méndez-Medrano, José Luis Rodríguez-López, Hynd Remita.

### National

5.- ***Congreso Estatal de Ciencia e Ingeniería de Materiales (CECIM), San Luis Potosí, Mexico. April 24-26, 2024***. Enhanced Photocatalytic Activity of Surface-

Modified $TiO_2$ with Bimetallic AuPd Nanoalloys for Hydrogen Generation. Ana Andrea Méndez-Medrano, Daniel Bahena-Uribe, Diana Dragoe, Carine Clavaguéra, Christophe Colbeau-Justin, Juan Pedro Palomares Báez, José Luis Rodríguez-López, Hynd Remita.

6.-***GDR Solar Fuels, Fréjus, France. Nov 14-16, 2022***. Surface Modification of $TiO_2$ with Bimetallic AuPd Nanoparticles for Photocatalytic Hydrogen Generation. Ana Andrea Méndez-Medrano, José Luis Rodríguez-López, Hynd Remita.

**Poster presentations**

**International**

1.- ***12th European Conference on Solar Chemistry and Photocatalysis: Energy and Environmental Applications, June 07-21, 2024, Belfast, Northern Ireland, United Kingdom***. Enhanced Photocatalytic Activity of Surface-Modified $TiO_2$ with Bimetallic AuPd Nanoalloys for Hydrogen Generation. Ana Andrea Méndez-Medrano, Daniel Bahena-Uribe, Diana Dragoe, Carine Clavaguéra, Christophe Colbeau-Justin, Juan Pedro Palomares Báez, José Luis Rodríguez-López, Hynd Remita.

2.- ***Plasmonics School 2023-Paris Saclay. Oct 23-27, 2023***. Photocatalytic Hydrogen Generation by $TiO_2$ Modified with AuPd Nanoalloys. Ana Andrea Méndez-Medrano, Daniel Bahena-Uribe, José Luis Rodríguez-López, Hynd Remita.

3.- ***3rd MOMENTOM International Congress, Gif-sur-Yvette, France. Mar 8-10, 2023***. Enhancement of Photocatalytic Hydrogen Generation on $TiO_2$ by AuPd Nanoalloys. Ana Andrea Méndez-Medrano, José Luis Rodríguez-López, Hynd Remita.

4.- ***Nanoalloys International Research Network, Paris, France. Dec 7-9, 2022***. Photocatalytic Hydrogen Generation by $TiO_2$ Modified with AuPd Nanoalloys. Ana Andrea Méndez-Medrano, José Luis Rodríguez-López, Hynd Remita.

5.- ***1st SENERGYLAB, Workshop on Recent Advances in Sensors and Energy Driven Applications, Cergy, France. Dec 2, 2022***. Enhanced Photocatalytic Activity of Surface-Modified $TiO_2$ with Bimetallic AuPd Nanoalloys for Hydrogen Generation. Ana Andrea Méndez-Medrano, José Luis Rodríguez-López, Hynd Remita.

6.- ***GOLD 2022 Conference, Quebec, Canada. Jul 17-20, 2022***. Surface Modification of $TiO_2$ with bimetallic AuPd Nanoparticles for Photocatalytic Hydrogen Generation. Ana Andrea Méndez-Medrano, José Luis Rodríguez-López, Hynd Remita.

**National**

7.- ***State Congress of Science and Engineering, San Luis Potosí, Mexico. May 2-4, 2023***. Nickel Oxide/Titania *p-n* Heterojunction Induced by Radiolysis for Photocatalytic Hydrogen Generation. Ana Andrea Méndez-Medrano, Xiaojiao Yuan, José Luis Rodríguez-López, Hynd Remita.

8.- ***Graduate Students Congress in Materials Science, San Luis Potosí, Mexico. Apr 27-29, 2022***. Surface Modification of $TiO_2$ with bimetallic AuPd Nanoparticles for Photocatalytic Hydrogen Generation. Ana Andrea Méndez-Medrano, José Luis Rodríguez-López, Hynd Remita.

## Trainings

- Seminars at IPICYT (online) and ICP.
- French courses at Cité Internationale Universitaire Paris (2h by week).
- On November 10th 2021, I attended the Journée thématique Processus photo-induits et plasmon de surface, Université de Nantes, Laboratoire CEISAM.
- On December 10th, 2021, the Université Paris-Saclay launched the *Institute forSustainable Energy*. We presented a poster of the research group.
- MOlecules and Materials for the ENergy of TOMorrow (MOMENTOM), November 2nd-December 17th 2021, online.
- Intégrité scientifique dans les métiers de la recherche, Completed on August 31th 2022, Université de Bordeaux (https://www.fun-mooc.fr/en/)
- XXIV Science week, June 20th, 2022, San Luis Potosí, Mexico.
- Writing and publishing research papers, October 26th, 2022, Université Paris-Saclay.
- Improving Grant Writing Skills in English, September 30th-December 19th, 2022, Academic Writing Center.
- Writing Skills in Science 1, January 9th-February 6th, 2023, Academic Writing Center.
- Why and how to develop your postdoc project, February 20th 2023.
- Introduction to Open Science, June 27th 2023, online.
- Presentation of My experience at Université Paris-Saclay, Institut de Chimie Physique, June 28th 2023, IPICYT, San Luis Potosí, Mexico
- “Science from the Laboratory”, July 6th and July 13th 2023, IPICYT, San Luis Potosí, Mexico.
- VSS, violences sexistes et sexuelles, RPS, risques psychosociaux, travail, discriminations, October 1st 2023, Université Paris Saclay, online.
- Paris-Saclay Plasmonics School, October 23rd-27th, 2023.

Solar RRL
www.solar-rrl.com

# Enhanced Photocatalytic Activity of Surface-Modified $TiO_2$ with Bimetallic AuPd Nanoalloys for Hydrogen Generation

*Ana Andrea Méndez-Medrano, Daniel Bahena-Uribe, Diana Dragoe, Carine Clavaguéra, Christophe Colbeau-Justin, Juan Pedro Palomares Báez, José Luis Rodríguez-López,* and Hynd Remita**

**Herein, commercial titania ($TiO_2$-P25) is modified with mono- and bi-metallic (Au, Pd, and AuPd) nanoparticles synthesized by chemical reduction method using $NaBH_4$ as a strong reducing agent at room temperature. Bimetallic AuPd nanoalloys homogeneous in size and well dispersed on the $TiO_2$ surface are obtained. The charge-carrier dynamics, which is a key factor in photocatalysis, is studied by time-resolved microwave conductivity. The results reveal that surface modification plays a crucial role in charge-carrier separation, increasing the activity under UV–vis light irradiation. The bimetallic AuPd nanoalloys formation is confirmed by high-angle annular dark field scanning transmission electron microscopy and corroborated by semiempirical molecular dynamics simulations (Gupta-LAMMPS). The surface-modified $TiO_2$ with bimetallic AuPd nanoalloys exhibits higher photocatalytic activity compared to $TiO_2$ modified with their monometallic counterparts. The experimental results are also supported by density functional theory and density functional tight binding calculations, which show that alloying AuPd with low Pd content presents significant synergetic effects for hydrogen generation under UV–vis light from aqueous triethanolamine solutions. Additionally, the AuPd/$TiO_2$ photocatalysts are stable with cycling.**

## 1. Introduction

Humanity is facing major crises such as air pollution and climate change. The exponential increase in global demand in energy, along with the growth of the world population, as well the still widely use of fossil fuels causes huge $CO_2$ emissions, responsible for greenhouse effects and climate change.[1] To mitigate these challenges, the development of renewable, clean energy sources is crucial for replacing fossil fuels and limiting $CO_2$ emissions, and hydrogen is projected to be not only the cleanest energy, it will also be consolidated as energy vector that moves us forward in the transition toward a zero carbon footprint, as committed by Hydrogen Europe, among other worldwide initiatives.

Since the petroleum crisis in 1973, alternatives have been sought for energy carriers like hydrogen.[2] Hydrogen as fuel produces higher energy power (122 kJ $g^{-1}$) than gasoline (40 kJ $g^{-1}$),[3] and can be obtained from different sources.[4] Currently, 95% of hydrogen production comes from fossil fuels and only 5% from water electrolysis.[5] Recently, hydrogen production by solar water splitting has attracted much interest because it uses light energy and only emits water and oxygen.[6,7] Solar energy is a green, abundant and renewable source due to its natural availability, which offers a promising way to solve environmental and energy issues.[8,9] Hydrogen generation by photocatalytic water splitting requires a semiconductor with a bandgap energy wider than 1.23 eV (redox potential of water).[10,11] Titania ($TiO_2$) is a semiconductor widely used in photocatalysis because of its excellent properties such as high reactivity, photochemical and biological stability, low toxicity, and low price.[12,13] The l imitation of $TiO_2$ application in photocatalysis is mainly due to the fast charge-carrier recombination and its large bandgap (3.1–3.2 eV for anatase and rutile phases, respectively), which induces excitation only under UV light irradiation. However,

A. A. Méndez-Medrano, C. Clavaguéra, C. Colbeau-Justin, H. Remita
Institut de Chimie Physique
UMR 8000 CNRS
Université Paris-Saclay
91405 Orsay, France
E-mail: hynd.remita@universite-paris-saclay.fr

A. A. Méndez-Medrano, J. L. Rodríguez-López
Advanced Materials Department
Instituto Potosino de Investigación Científica y Tecnológica, A.C.
San Luis Potosí, SLP 78216, México
E-mail: jlrdz@ipicyt.edu.mx

The ORCID identification number(s) for the author(s) of this article can be found under https://doi.org/10.1002/solr.202400106.

DOI: 10.1002/solr.202400106

D. Bahena-Uribe
Laboratorio Avanzado de Nanoscopia Electrónica
Centro de Investigación y de Estudios Avanzados del I.P.N.
CINVESTAV
Mexico, D.F. 07360, Mexico

D. Dragoe
Institut de Chimie Moléculaire et des Matériaux d'Orsay
UMR 8182 CNRS
Université Paris-Saclay
91405 Orsay, France

J. P. Palomares Báez
Facultad de Ciencias Químicas
Universidad Autónoma de Chihuahua
Campus II, Chihuahua, Chihuahua 31125, México

 

UV light constitutes only 4% of the solar light impinging on the Earth's surface.[14]

In this work, we used commercial titania ($TiO_2$-P25) as photocatalytic material because it is considered more stable and more efficient than other semiconductors at the adequate redox potentials for water splitting. $TiO_2$-P25 consists of a mixture of anatase–rutile crystalline phases and exhibits better photocatalytic activity than other types of $TiO_2$ due to the anatase–rutile heterojunction,[15,16] which is responsible of longer charge-carrier lifetime (compared to pure anatase phase) under UV excitation.[17–19] However, modification of titania for its activation under visible light is essential to better harvest solar light. Doping $TiO_2$ with plasmonic metal nanoparticles (NPs) allows light absorption in the visible region of the spectrum due to the localized surface plasmon resonance (LSPR) phenomenon.[14,20,21] In addition, the photocatalytic activity under UV light is enhanced because the metal NPs can act as electron traps inhibiting the charge-carrier recombination.[14,22] The LSPR is the collective oscillation of conduction-free electrons excited by the incident photons in constructive interference with the electric field of the incident light.[23–26] The LSPR depends strongly on the metal nature, size, and morphology of the NPs.[27–29] Among the noble metals, platinum (Pt) is the best cocatalyst for photocatalytic hydrogen generation.[29,30] However, Pt is costly and scarce, and thus, it is important to replace it with other more abundant metals, such as gold (Au), which has been widely applied for photocatalytic hydrogen generation because it is an efficient cocatalyst, and it is also cheaper and more abundant than Pt. Au NPs can also activate $TiO_2$ under visible light due to its LSPR.[14]

Bimetallic NPs like AuPd,[31,32] AuPt,[33,34] AuNi,[26] and AuCu[35,36] have been reported to demonstrate improvements in their electrical, optical, and catalytic properties. These nanoalloys exhibit superior catalytic performance, particularly in selectivity and stability, compared to their individual metal components. Therefore, they are highly desirable for a range of applications in catalysis and electrocatalysis.[37]

Pd has gained attention due to its efficiency as catalyst in various applications, including catalytic and electrocatalytic processes, hydrogen storage, sensors, nanomedicine, hydrogenation reactions, C–C coupling reactions, mitigating environmental pollution, and automotive emissions regulation.[32,38–47] Pd–Au bimetallic NPs exhibit higher selectivity compared to monometallic Pd NPs for hydrogenation reactions[32,48,49] Porous $Pd_{shell}-Au_{core}$ nanostructures are very promising for application in direct ethanol fuel cells as they exhibit a very good electrocatalytic activity and a high stability.[40] Surface modification of $TiO_2$ with bimetallic NPs based on gold has attracted much interest because higher activities for photocatalytic hydrogen generation can be obtained compared with their monometallic counterparts.[26,31,50,51]

Hereby, we report the application of AuPd nanoalloys on $TiO_2$ surface for hydrogen generation by photocatalysis, showing a synergetic effect under UV–vis light for $H_2$ production. The metal loading of both metals was optimized and the role of Au and Pd on the photocatalytic activity was studied using molecular simulations.

## 2. Results and Discussion

### 2.1. Alloying, Chemical Order, and Electronic Structure Characterization

The morphology, size, elemental composition, and crystalline structure of 1 wt% $AuPd/TiO_2$ samples with the mass ratios of Au:Pd (9:1. 1:1. 1:9) were analyzed by transmission electron microscopy (TEM), high-resolution TEM (HRTEM), and energy dispersive X-rays analysis (EDX) techniques. TEM images in bright field (**Figure 1**a, S1a, and S2a, Supporting Information) and $Z$ contrast mode (Figure 1b, S1b, and S2b, Supporting Information) show small and spherical AuPd NPs with an average size of ≈2.5–3 nm (Figure 1e, S1e, and S2e, Supporting Information) well dispersed on $TiO_2$ surface. Table S1, Supporting Information shows the AuPd NPs average size for 1 wt% $AuPd/TiO_2$ samples with different mass ratios. HRTEM images of 1 wt% $AuPd/TiO_2$ samples show the localization of AuPd NPs on the anatase phase (Figure 1c, S1c, and S2c, Supporting Information). The electronic interaction with AuPd NPs and the anatase phase inhibits the growth and agglomeration of the metal NPs.[14] The interplanar distances were $d = 0.35$ nm, corresponding to (101) planes of the anatase phase (JCPDS No. 21-1272). The interplanar distances were measured using the Digital Micrograph software deduced by fast Fourier transformation process. The elemental composition was confirmed by EDX analysis showing the presence of Au, Pd, Ti, and Cu from the TEM grid (Figure 1d, S1d, and S2d, Supporting Information). Small signals of Au and Pd were observed for 1 wt% $Au_9Pd_1/TiO_2$ and 1 wt% $Au_1Pd_9/TiO_2$ due to their low content, as shown in Figure 1d and S2d, Supporting Information, respectively. Moreover, for the sample 1 wt% $Au_1Pd_1/TiO_2$, the EDX signals are almost identical due to the same metal content (Figure S1d, Supporting Information).

In **Figure 2**, we present high-angle annular dark field scanning transmission electron microscopy (HAADF-STEM) micrograph (Figure 2a) that shows $Au_9Pd_1$ nanoalloys with brighter tiny points corresponding to Au and less bright tiny spots corresponding to Pd (due to the highest atomic number of Au compared with Pd). Additionally, EDX analysis on single NPs for the 1 wt% $Au_9Pd_1/TiO_2$ sample (Figure 2b) attests the presence of Pd on the surface of the NP, but with homogeneous distribution over all the structure (Figure 2c). In order to elucidate the chemical ordering of these alloys content, we performed a hybrid MD–MC (molecular dynamics–Monte Carlo, with the reliable Gupta interatomic potential for Au–Pd, see details in Supporting Information) simulation for each of the ratios, and then we simulated the line scan, shown in Figure 2d for the alloy content $Au_9Pd_1$: the simulation is in good agreement with the experimental results. Also, the results show that the alloy in all the systems is random, not ordered as in the AuPd bulk alloy previous studies.[52,53]

Inductively coupled plasma-optical emission spectrometry was utilized for elemental analysis, providing insights into the mass content of AuPd nanoalloys on $TiO_2$ surface (see Table S2, Supporting Information).

The bimetallic photocatalysts 1 wt% $AuPd/TiO_2$ and bare $TiO_2$ were characterized by X-ray diffraction (XRD) to study the

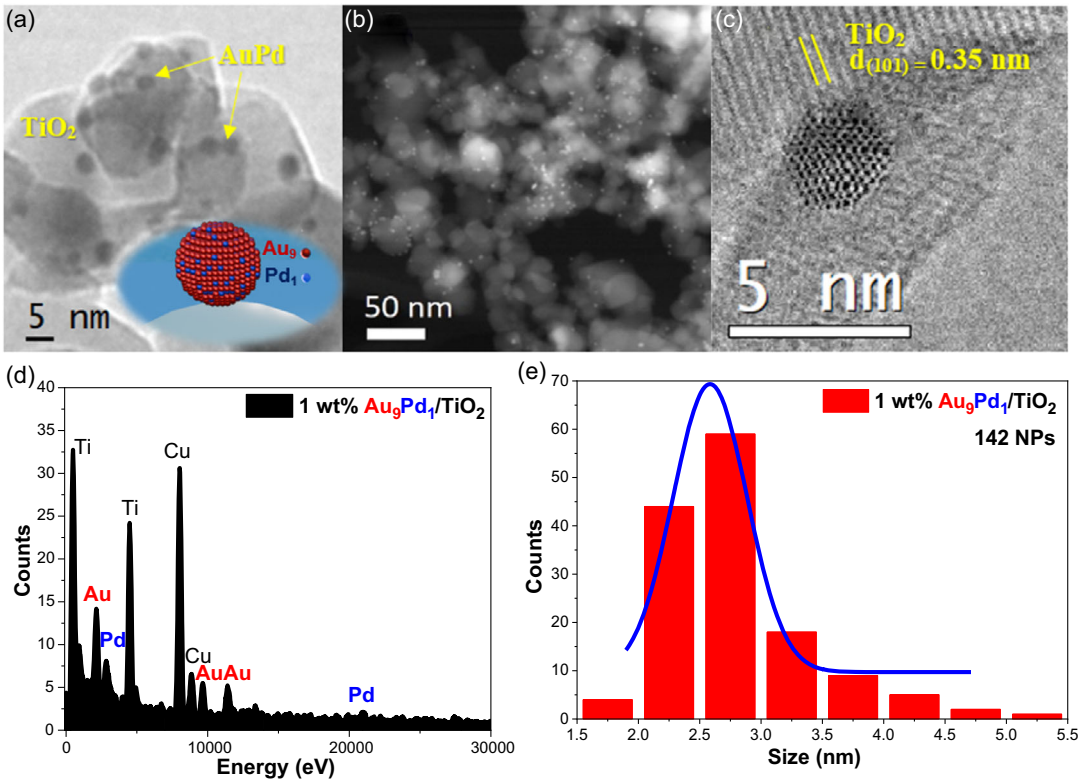


**Figure 1.** TEM micrographs of 1 wt% $Au_9Pd_1/TiO_2$ sample in a) bright field and b) *Z* contrast show spherical AuPd NPs well dispersed on $TiO_2$ surface, c) HRTEM micrograph showing the localization of AuPd NPs on the anatase phase, d) EDS analysis showing the presence of the elements Au, Pd Ti, and Cu (from the TEM grid), and e) histogram of AuPd NPs showing an average size of ~2.6 nm.

crystallinity of the samples (Figure S3, Supporting Information). The diffracted peaks of the samples coincide with the reference peaks of the anatase and rutile crystalline phases, according to the data JCPDS file nos. 21-1272 and 21-1276, respectively. The junction between anatase and rutile phases in P25 induces longer lifetime of the charge carriers increasing the photocatalytic activity.[54] No diffraction peaks were observed for AuPd NPs due to the low metal loading and the small size of the NPs.[55]

The UV–vis spectra of the samples showed absorption in the UV region due to $TiO_2$ support (**Figure 3**a–c). The UV–vis spectra of the monometallic samples $Pd/TiO_2$ show that the surface modification with Pd NPs does not influence the $TiO_2$ bandgap (Figure 3a). Pd NPs do not introduce energy levels in the bandgap, below the conduction band (CB) and above the valence band (VB) because of their plasmon in the UV region.[56] Moreover, the monometallic samples of $Au/TiO_2$ show the LSPR of gold with a maximum absorption peak at 553, 547, and 553 nm for 0.1, 0.5, and 0.9 wt% $Au/TiO_2$ (Figure 3b). The dielectric constant of the $TiO_2$ support induces a shift of the LSPR of the metal NPs toward larger wavelengths (compared to the NPs in water).[14,57] In the case of the bimetallic sample 1 wt% $Au_9Pd_1/TiO_2$ (Figure 3c), the LSPR of Au induces an intense and continuous absorption over the entire visible region due to the presence of AuPd nanoalloys rich in gold.[27] However, the sample 1 wt% $Au_1Pd_9/TiO_2$ does not show this characteristic because of the lowest content in gold. Au NPs act as visible absorption centers extending the light absorption of wide bandgap semiconductors to the visible light due to their LSPR. Improving the UV–vis absorption of the photocatalyst is important in photocatalysis to better harvest solar light.

The bandgap energies of the bimetallic samples and bare $TiO_2$ were calculated by the Tauc plot method, considering the indirect transition of anatase phase.[16] Figure 3d shows the Tauc plots for bare $TiO_2$, 1 wt% $Au_1Pd_9/TiO_2$, 1 wt% $Au_1Pd_1/TiO_2$, and 1 wt% $Au_9Pd_1/TiO_2$. The estimated bandgaps were 3.34, 3.33, 3.30, and 3.30 eV, respectively. The optical band energy ($E_g$) can be determined by the following Equation (1) and (2) for reflectance function $F(R)$, where $R$ is the reflectance obtained by diffuse reflectance spectroscopy (DRS), while $K$ and $S$ are the absorptions and scattering coefficients, respectively. $F(R)$ is proportional to the absorption coefficient, where $h$ is the Planck's constant, $\nu$ is the photon's frequency, $E_g$ is the bandgap energy, and $\beta$ is a factor depending on the transition probability and a constant in the optical frequency range. The $n$ factor depends on the nature of the electron transition and is equal to 2 or 1/2 for the direct and indirect transition bandgaps, respectively.

$$F(R) = \frac{(1-R)^2}{2R} = \frac{K}{S} \quad (1)$$

$$(F(R)h\nu)^n = \beta(h\nu - E_g) \quad (2)$$

Time-resolved microwave conductivity (TRMC) signals of mono- and bi-metallic photocatalysts and bare $TiO_2$ at 360 nm

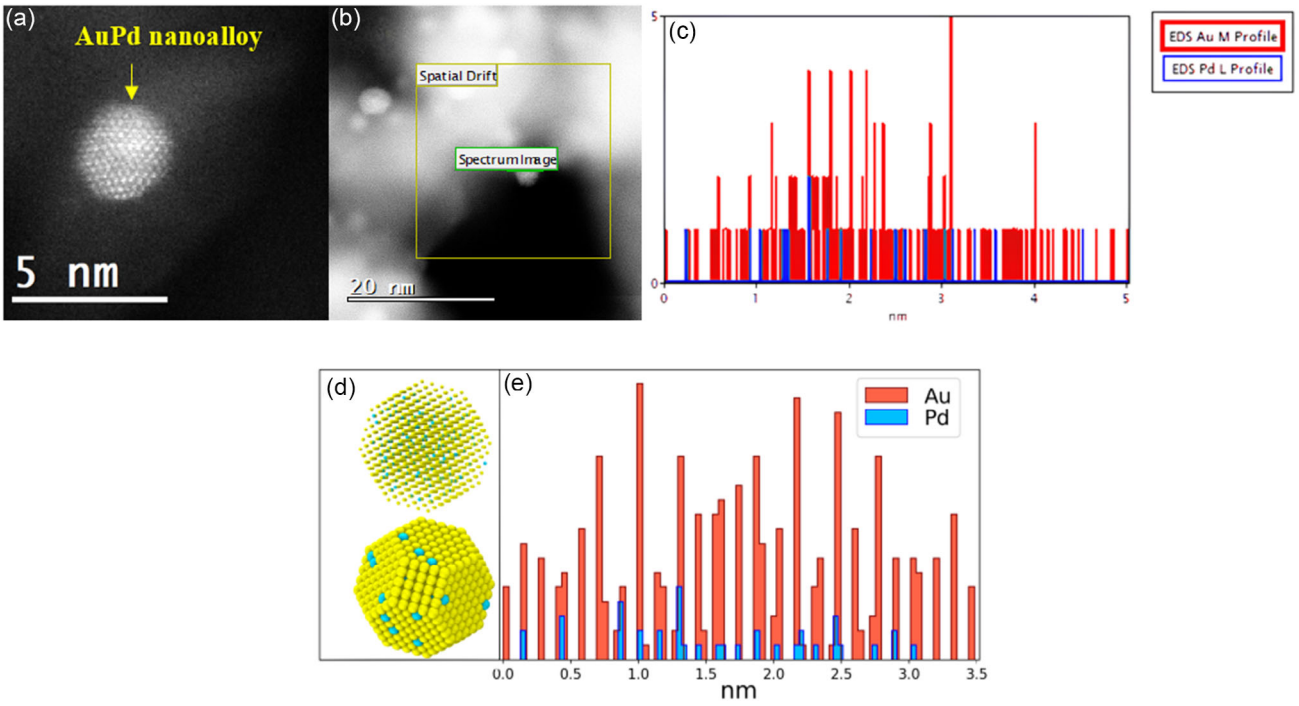


**Figure 2.** For the $Au_9Pd_1$ alloy: a) HAADF-STEM micrograph, b) spectrum image, and c) Au–M and Pd–L energy-level profiles. d) Energy optimization structure of $Au_9Pd_1$ NPs by hybrid MD–MC (Gupta) calculation for the identified size and structural shape from the experiment (a 1289 atoms cuboctahedron with ≈3.5 nm); and e) simulated line scan on this NP and orientation shown, reflecting the chemical ordering.

are shown in **Figure 4**. TRMC signals show $I_{max}$ values reached for all the samples under UV light excitation, suggesting electron migration from the VB to the CB of $TiO_2$. Then, the $I_{max}$ values decreased, and faster decays were observed for the mono- and bi-metallic photocatalysts than bare $TiO_2$. This can be explained by quick trapping by Au, Pd, and AuPd NPs of photogenerated electrons in the CB of $TiO_2$. Figure 4a shows the signals of $Au/TiO_2$ samples: the decay of the signal increases with the metal loading 0.9 wt% $Au/TiO_2$ > 0.5 wt% $Au/TiO_2$ > 0.1 wt% $Au/TiO_2$. In the case of $Pd/TiO_2$ samples (Figure 4b), the decay is not correlated with the metal loading and faster decay is obtained with 0.1 wt%. For the bimetallic photocatalysts (Figure 4c), the decay increases with 1 wt% $Au_1Pd_1/TiO_2$ > 1 wt% $Au_9Pd_1/TiO_2$ > 1 wt% $Au_1Pd_9/TiO_2$. These TRMC results indicate that the AuPd nanoalloys are efficient in electron scavenging reducing the charge-carrier recombination, which is beneficial for the photocatalytic activity.[14,35,58] At 420 nm (Figure S4, Supporting Information), no signal from mono- and bi-metallic samples was higher than the signal obtained by $TiO_2$. At 550 nm (Figure S5, Supporting Information), the gold-based photocatalysts (mono- and bi-metallic samples) show no signal, indicating that at these wavelengths no hot electrons were detected in the CB of titania after Au-LSPR excitation.

X-ray photoelectron spectroscopy (XPS) analysis was performed on the sample surface in order to get information concerning the chemical environment of Au and Pd. The obtained Au *4f* and Pd *3d* core-level spectra are presented in **Figure 5**. Both Au *4f* and Pd *3d* doublets were fitted using asymmetrical line shapes derived from metallic Au and Pd references. The binding energy scale was calibrated based on Ti $2p_{3/2}$ peak, used as internal reference, considered at 458.7 eV, which places the main O 1*s* component corresponding to O in $TiO_2$ at 530 eV.[59] As a consequence, the spin–orbit coupling doublet of Au *4f* is placed at 83.2 eV (Au $4f_{7/2}$) and 86.8 eV (Au $4f_{5/2}$) and that of Pd *3d* at 334.5 eV (Pd $3d_{5/2}$) and 339.8 eV (Pd $3d_{3/2}$). This XPS analysis confirms that AuPd NPs are in metallic states. In both cases, the binding energies of Au *4f* and Pd *3d* are shifted toward lower values from those given in the literature.[60] For instance, Au $4f_{7/2}$ reported at 84 eV shifted to 83.2 eV and Pd $3d_{5/2}$ from 335 to 334.5 eV. Two points can explain the shift toward lower binding energy values for Au *4f* and Pd *3d*, i.e., this, first, may be due to the interaction of the support ($TiO_2$) changing its electronic environment, the electron transfer from the $TiO_2$ to the AuPd NPs,[35,55] and second, may be due to a strong electronic modification and charge transfer between Au and Pd due to its nanoalloy formation.[61–63] Bimetallic AuPd nanoalloys have been reported to exhibit negative shifts in both the Au *4f* and Pd *3d* core levels.[64,65]

### 2.2. Photocatalytic Hydrogen Generation

The photocatalytic hydrogen generation for mono- and bi-metallic samples under UV–vis and visible light is shown in **Figure 6**a,b, respectively. The monometallic samples present higher hydrogen generation rates than bare $TiO_2$ under UV–vis light (Figure 6a). The hydrogen generation rate for bare $TiO_2$ was 77.5 μmol $g^{-1}$ $h^{-1}$. The hydrogen generation rates for monometallic samples 0.1, 0.5, and 0.9 wt% $Au/TiO_2$ were 482.6, 534.4,

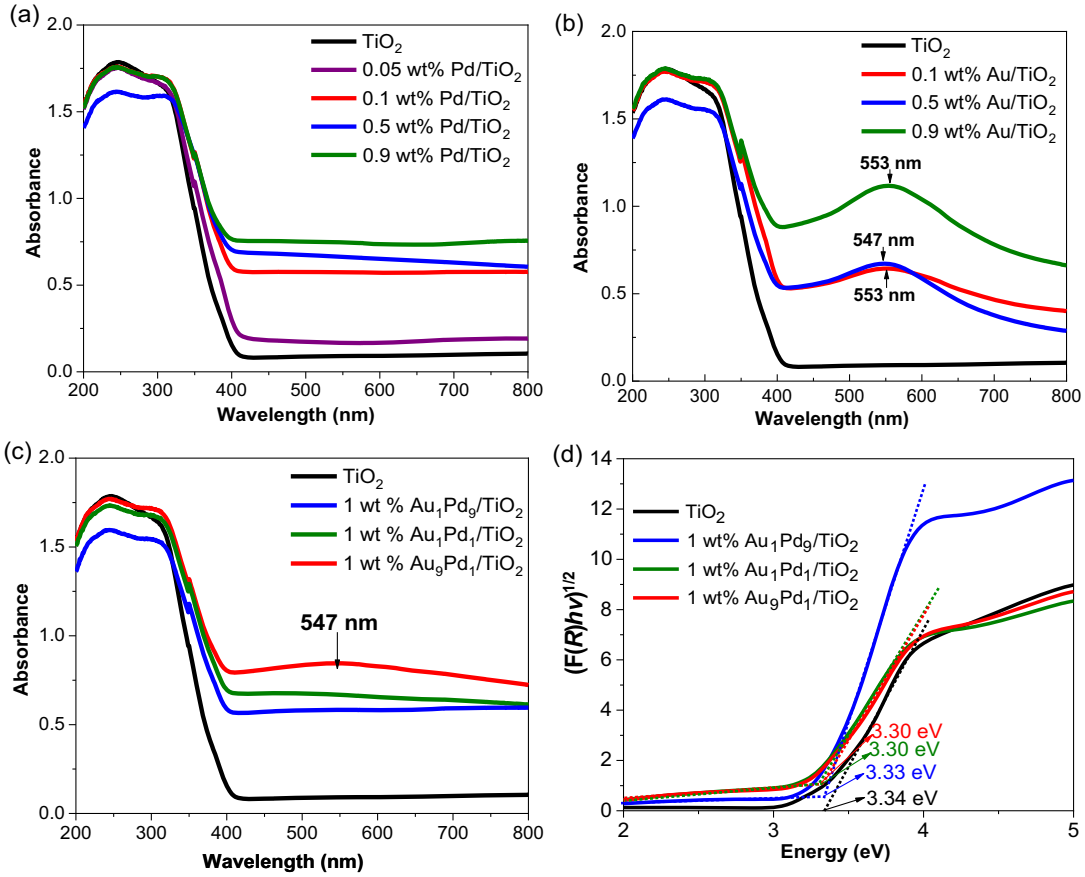


**Figure 3.** UV–vis DRS spectra of monometallic samples a) $Pd/TiO_2$ and b) $Au/TiO_2$, and bimetallic samples c) 1 wt% $AuPd/TiO_2$ and d) their corresponding Tauc plot.

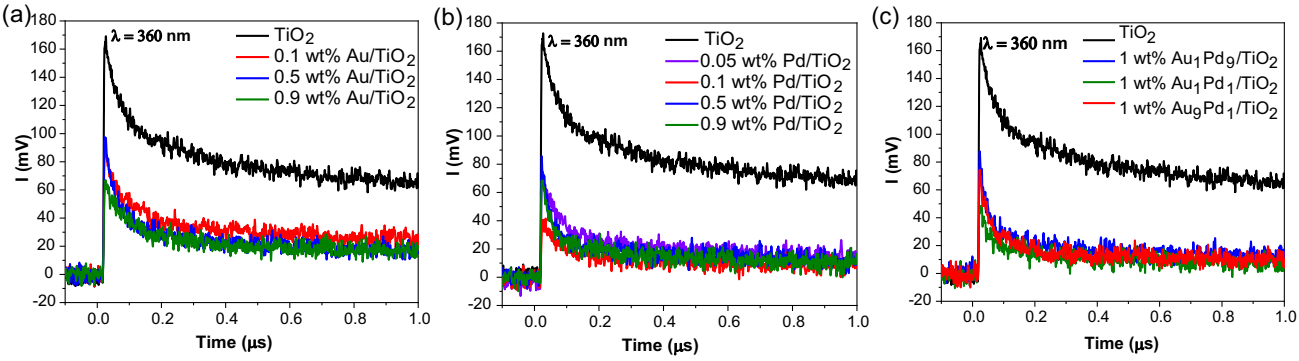


**Figure 4.** TRMC signals of monometallic photocatalysts a) $Au/TiO_2$, b) $Pd/TiO_2$, and c) bimetallic photocatalysts 1 wt% $AuPd/TiO_2$ at 360 nm with a laser energy of 1.2 mJ.

and 788.6 μmol $g^{-1}$ $h^{-1}$, respectively. For 0.05, 0.1, 0.5, and 0.9 wt% $Pd/TiO_2$ metallic samples were 182.9, 1468.2, 1142.0, and 946.4 μmol $g^{-1}$ $h^{-1}$, respectively. The higher hydrogen generation rates of monometallic samples than bare $TiO_2$ are attributed to the work function: metals with higher work functions such as Pd (5.3 eV) and Au (5.1 eV) than the electron affinity of $TiO_2$ (4.0 eV) increase the Schottky barrier effect.[66] The Schottky barrier is formed due to the interface contact between Au and Pd NPs (metallic system) and $TiO_2$ (semiconductor system).[67] The Schottky contact creates an internal electric field helping the electron–hole transfer and inhibiting the recombination process, which is confirmed by TRMC results (Figure 4a,b).

Most importantly, Figure 6a shows higher hydrogen generation rates for bimetallic samples $AuPd/TiO_2$ compared with their monometallic counterparts. The hydrogen generation rates for 1 wt% $Au_1Pd_9/TiO_2$, 1 wt% $Au_1Pd_1/TiO_2$, and 1 wt% $Au_9Pd_1/TiO_2$

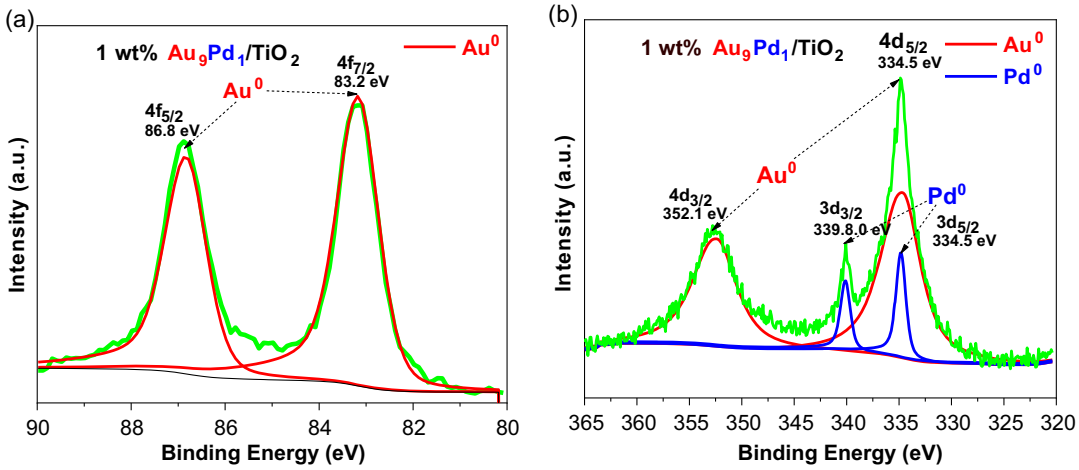


**Figure 5.** XPS spectra signals of 1 wt% $Au_9Pd_1/TiO_2$ sample: a) Au *4f* core level and b) Au *4 d* and Pd *3d* core levels.

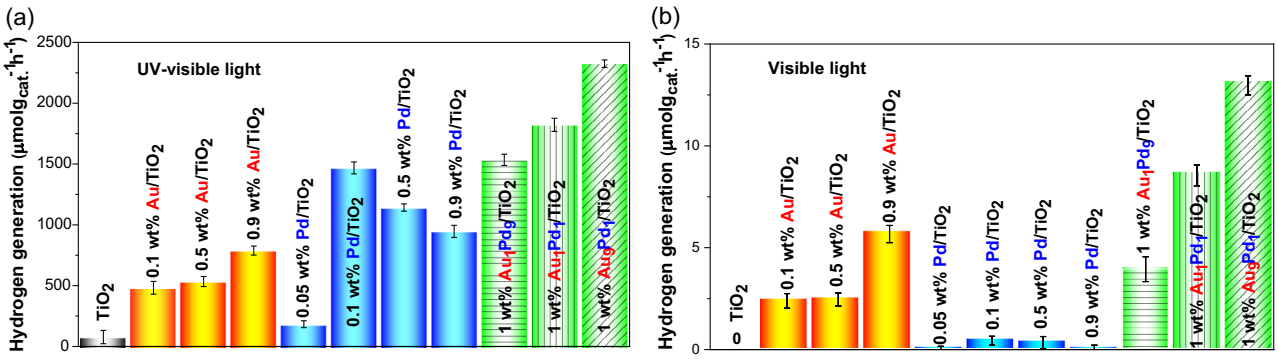


**Figure 6.** a,b) Photocatalytic hydrogen generation for mono- and bi-metallic photocatalysts and bare $TiO_2$ from 25 vol% TEOA aqueous solution under a) UV–vis and b) visible light.

were 1534.6, 1822.2, and 2325.0 $\mu mol\, g^{-1}\, h^{-1}$, respectively. The hydrogen generation increases with the Au/Pd ratio (1 wt% $Au_9Pd_1/TiO_2$ > 1 wt% $Au_1Pd_1/TiO_2$ > 1 wt% $Au_1Pd_9/TiO_2$). The sample 1 wt% $Au_9Pd_1/TiO_2$ shows the highest activity with 2325.0 $\mu mol\, g^{-1}\, h^{-1}$, which is ≈30 times higher than bare $TiO_2$ (77.5 $\mu mol\, g^{-1}\, h^{-1}$). The photocatalytic activity enhancement of the samples can be explained through their morphology, optical properties, crystallinity, and charge carrier dynamics. TEM images showed smaller AuPd NPs on $TiO_2$ surface for 1 wt% $Au_9Pd_1/TiO_2$ sample (Figure 1e) than 1 wt% $Au_1Pd_1/TiO_2$ and 1 wt% $Au_1Pd_9/TiO_2$ samples. Smaller NPs have higher work function than larger NPs improving the Schottky barrier effect and therefore reducing the charge-carrier recombination.[14,66,67] TRMC results confirm that the AuPd nanoalloys are efficient in electron scavenging reducing charge-carrier recombinations and raising the photocatalytic activity under UV light excitation (Figure 4c). The decay increases when the $TiO_2$ surface is modified with AuPd nanoalloys. The reactive surface sites are well dispersed on the titania surface scavenging electrons in the CB of $TiO_2$ (which reduce $H^+$) inhibiting the charge carrier recombination, reducing and promoting the recombination of hydrogen atoms, and therefore raising the photocatalytic activity.

The photocatalytic hydrogen generation for mono- and bi-metallic samples under visible light is shown in Figure 6b. As previously stated, $TiO_2$ is not active under visible light. $Pd/TiO_2$ samples show negligible values for hydrogen generation under visible light. Pd NPs do not modify the spectra of $TiO_2$ in the visible region due to their LSPR in the UV region (Figure 3a).[44,68] Moreover, $Au/TiO_2$ samples show photocatalytic activity under visible light due to their LSPR (Figure 3b). The hydrogen rates for 0.1, 0.5, and 0.9 wt% $Au/TiO_2$ samples were 2.4, 2.5, and 5.7 $\mu mol\, g^{-1}\, h^{-1}$, respectively. Previous studies have shown that hot electrons can be injected from Au NPs into the CB of $TiO_2$ under visible irradiation.[14] However, in our case, at 420 nm (Figure S4a, Supporting Information) no signal was higher than the signal obtained with bare $TiO_2$. At 550 nm (Figure S5a, Supporting Information), no detectable TRMC signals were obtained with $Au/TiO_2$ photocatalysts. This can be explained because the electron transfer is quite fast, and even if TRMC technique allows to obtain a signal at nanosecond scale, we cannot define the 10 first nanoseconds during the pulse.

The bimetallic samples $AuPd/TiO_2$ show higher hydrogen generation rates than the monometallic counterparts under visible light. The hydrogen generation rates for 1 wt% $Au_1Pd_9/TiO_2$, 1 wt% $Au_1Pd_1/TiO_2$, and 1 wt% $Au_9Pd_1/TiO_2$ were 3.9, 8.5, and

13.0 μmol $g^{-1}$ $h^{-1}$, respectively. The optical properties were improved with higher Au/Pd ratio (1 wt% $Au_9Pd_1/TiO_2$) showing an intense and continuous absorption over the entire visible region (Figure 3c). Nevertheless, the same case occurs for bimetallic samples, no signal was higher than the signal obtained with $TiO_2$ at 420 nm (Figure S4c, Supporting Information). At 550 nm (Figure S5c, Supporting Information), no detectable TRMC signals were found. The photocatalytic activity under visible light suggests that hot electrons from Au NPs (in $Au/TiO_2$ and $AuPd/TiO_2$ samples) were injected into the CB of $TiO_2$ due to the activation of Au-LSPR after visible excitation.

Finally, decreasing the metal loading is important for large-scale hydrogen production due to the high cost of Au and Pd. The photocatalysts 0.1, 0.2, and 0.5 wt% $AuPd/TiO_2$ with mass ratios of Au:Pd (1:9, 1:1, 9:1) were tested under UV–vis light (**Figure 7**). The samples demonstrate similar activity as 1 wt% $AuPd/TiO_2$ samples.

The hydrogen generation increases with the ratio Au/Pd ($Au_9Pd_1/TiO_2 > Au_1Pd_1/TiO_2 > Au_1Pd_9/TiO_2$) for all the metal loadings. **Figure 8** presents a comparison between our optimal sample 0.5 wt% $Au_9Pd_1/TiO_2$ and 1 wt% $Pt/TiO_2$ (our sample benchmark with high photocatalytic activity; the Pt NPs are about 1 nm size and are well dispersed on $TiO_2$ surface), revealing quite similar (or slightly lower) photocatalytic activities. As we mentioned earlier, Pt is the best cocatalyst for photocatalytic hydrogen generation. Nevertheless, because of its high cost and limited abundance, replacing it with other more abundant metals is important. Table S3, Supporting Information compares the photocatalytic hydrogen generation under UV–vis light irradiation with data from the literature. The comparison reveals notable differences in the efficiency of different catalysts under distinct conditions. However, compared to other reported studies, our work shows good photocatalytic activity under UV–vis radiation and a slight activity under visible light. Luna et al. obtained synergistic effects with bimetallic Au–Ni and Ni–Pd NPs for hydrogen generation.[26,29] Also, Su et al. reported strong synergistic effects with 1 wt% $Pd_{shell}Au_{core}/TiO_2$ for photocatalytic hydrogen generation with a specific wavelength at 365 nm (UV LED) using a variety of important feedstock chemicals. Nevertheless, they did not show any activity under visible light.[31]

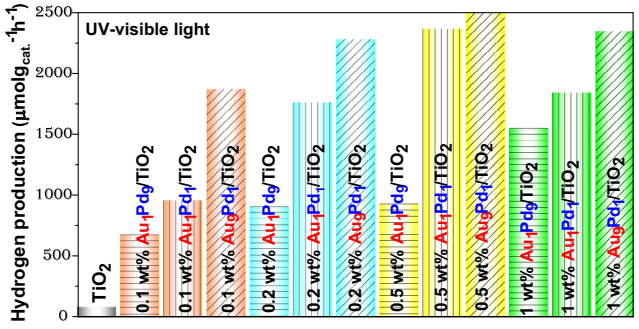


**Figure 7.** Photocatalytic hydrogen generation of bimetallic photocatalysts with metal loadings of 0.1, 0.2, 0.5, and 1 wt% $AuPd/TiO_2$ with mass ratios of Au:Pd (1:9, 1:1, 9:1) and bare $TiO_2$ from 25 vol% TEOA aqueous solution under UV–vis light irradiation.

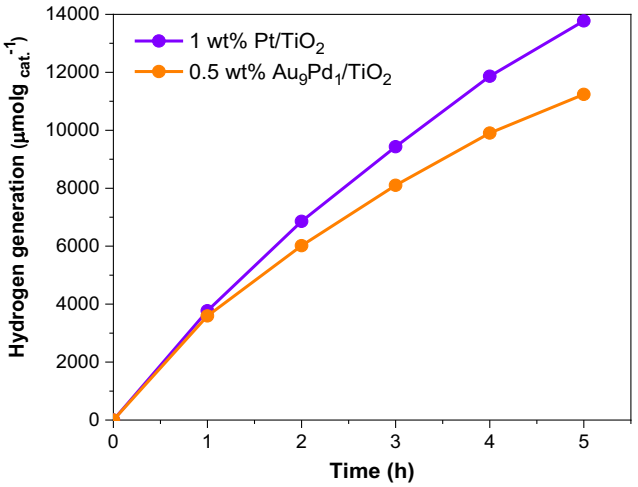


**Figure 8.** Comparison of the photocatalytic hydrogen generation of 0.5 wt% $Au_9Pd_1/TiO_2$ with 1 wt% $Pt/TiO_2$ from 25 vol% TEOA aqueous solution under UV–vis light irradiation.

### 2.3. Density Functional Theory Calculations

To improve the understanding of the higher hydrogenation rates in the case of bimetallic systems, the adsorption of two hydrogen atoms on a model of Au NP and $Au_9Pd_1$ NP was investigated at the density functional theory (DFT) and density functional tight binding (DFTB+) quantum levels (see Methods and Supporting Information for computational details). First, for DFT calculations, the optimized geometries show a different adsorption mode on the metal surface, with each H atom remaining on one Au for Au NP, and with one H atom on gold and the other H shared between the Pd and the neighboring gold atoms ("Au–H–Pd") for $Au_9Pd_1$ NP. This structural change corresponds to different bond lengths, resulting in different electronic effects (Table S5, Supporting Information). The Au–Pd and Au–Au bond lengths around the shared H in the bimetallic cluster are shorter than Au–Au distances in Au NP. In addition, the Au–H and Pd–H distances are longer in $Au_9Pd_1$ NP for the shared H atom, leading to a weaker hydrogen adsorption strength. The analysis of the electron density shows Au–H and Pd–H bonds with a valence electronic population basin of 1.7 electron and 1.6 electron for Au–H and Au–H–Pd, respectively. The strength of the bond was evaluated to be close to a single covalent bond with a Mayer bond order of 0.86 for Au–H in Au NP, and much weaker with a Mayer bond order of 0.37 for Au–H–Pd in $Au_9Pd_1$ NP. This lower hydrogen atom adsorption strength for the bimetallic system may be one explanation for the higher reactivity.

### 2.4. DFTB+ Calculations

By DFTB+ using the GFN1-xTB parameterization, we performed molecular dynamics simulations of H atoms with many different arrays (as described in Supporting Information) over the surface of optimized clusters ($N = 38$ atoms, with cuboctahedral shape) for the three $Au_9Pd_1$, $Au_1Pd_1$, and $Au_1Pd_9$ alloys. The systems

were brought to a temperature of 298 K and then left at constant temperature during 20 picoseconds, and the main results are hereby briefly presented.

The case of $Au_9Pd_1$ was the only system that led to the formation of $H_2$, while for none (among 11 systems built) of the systems in the $Au_1Pd_9$ case did the formation of $H_2$ occur. According to previous DFT results, it seems that when the amount of Pd is higher, the hydrogen atoms are strongly attracted to Pd, and thus their movement is restricted. For the case of $Au_1Pd_1$, the formation of $H_2$ also occurs for one system (among 9 built); however, we notice that the inclusion of H in these 1:1 systems seems to destabilize them (even more than the obtained structures after the energy optimization process) because most of the calculated systems end up suffering a considerable deformation of the NP. More details are given in the Supporting Information file.

### 2.5. Proposed Photocatalytic Mechanism

Charge-carrier dynamics, which is a key factor in photocatalysis, was studied by TRMC.[14,29,50,56,58,69] At 360 nm excitation, the mono- and bi-metallic systems and bare $TiO_2$ are activated meaning that electrons migrate to the CB of $TiO_2$, reaching $I_{max}$ values. Moreover, when the surface of $TiO_2$ is modified with mono- and bi-metallic NPs, the $I_{max}$ value decreases compared with bare $TiO_2$ (Figure 4). This indicates that the metal NPs act as electron traps, inhibiting the charge-carrier recombination. The electron migration from CB of $TiO_2$ to the metal NPs occurs due to the work function and Schottky junction, which creates an internal electric field helping the electron–hole transfer and inhibiting the recombination process.[70,71] **Figure 9**a shows a scheme of the photocatalytic mechanism under UV light excitation for bimetallic AuPd/$TiO_2$ sample.

$$TiO_2 \xrightarrow{h\nu > E_g} TiO_2\left(e^-_{CB} + h^+_{VB}\right) \quad (3)$$

$$H_2O + e^- \rightarrow H_2 + OH^- \quad (4)$$

$$H^+ + e^- \rightarrow H^\bullet \quad (5)$$

$$H^\bullet + H^\bullet \rightarrow H_2 \quad (6)$$

At 420 nm excitation, hot electrons are injected from AuPd nanoalloys to the CB of $TiO_2$ due to the Au-LSPR excitation.[14] Water molecules or $H^+$ are reduced on the $TiO_2$ surface by the electrons to produce $H_2$ (Figure 9b), as we mentioned before. Finally, to inhibit the oxidation reaction generated by the photogenerated holes in the VB of $TiO_2$ and AuPd NPs, an electron donor was used (TEOA in our study), which scavenges the holes to generate $H_2$ (Equation (7)–(10)).[72] TEOA can self-sustain the photocatalytic hydrogen generation process, which can be obtained from industrial organic effluents related to dry cleaning, cosmetics, shampoos, detergents, surfactants, textiles, and water repellents.[72]

$$TiO_2(h^+) + OH^- \rightarrow OH^\bullet \quad (7)$$

$$TiO_2(h^+) + H_2O \rightarrow OH^\bullet + H^+ \quad (8)$$

$$TEOA + OH^\bullet \rightarrow HCHO + NH_3 \quad (9)$$

$$HCHO + OH^\bullet \rightarrow H_2 \quad (10)$$

### 2.6. Stability with Cycling

Finally, the photocatalyst stability was investigated for the 0.5 wt % $Au_9Pd_1/TiO_2$ sample, which demonstrated a stable photocatalytic activity with a slight decrease with cycling (**Figure 10**). The dispersion of AuPd nanoalloys, morphology, size, and crystalline structure was analyzed before and after cycling (Figure S6, Supporting Information). TEM images in dark field show the AuPd NPs well dispersed on the $TiO_2$ surface before and after cycling (Figure S6a,d, Supporting Information). HAADF-STEM micrographs show that the AuPd nanoalloys are quite stable after cycling, showing brighter tiny points corresponding to Au due to its highest atomic number and less brightness tiny spots corresponding to Pd (Figure S6b,e, Supporting Information). The interplanar distance of 0.23 nm corresponds to (111) plane of Au (Figure S6c, Supporting Information)

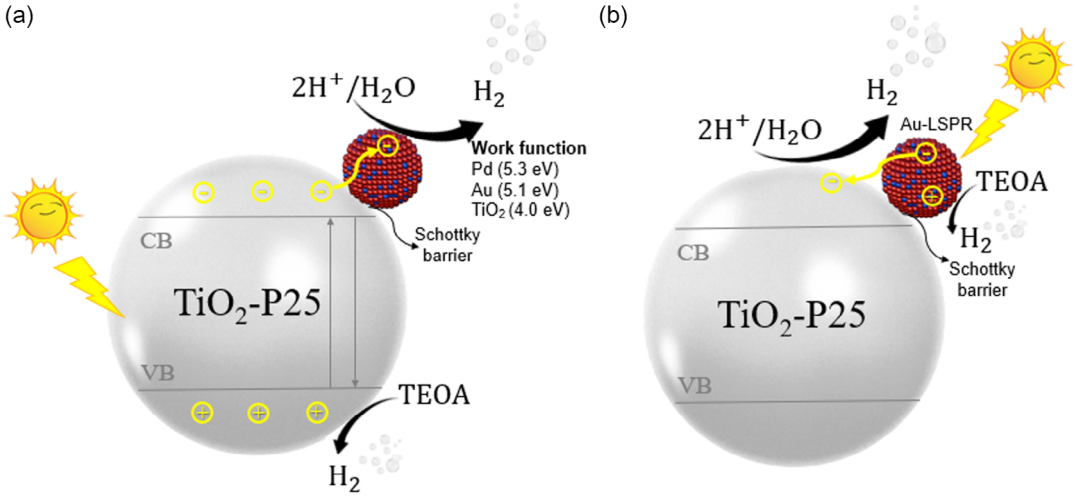


**Figure 9.** Proposed photocatalytic mechanism of bimetallic AuPd/$TiO_2$ samples under a) UV and b) visible light irradiation.

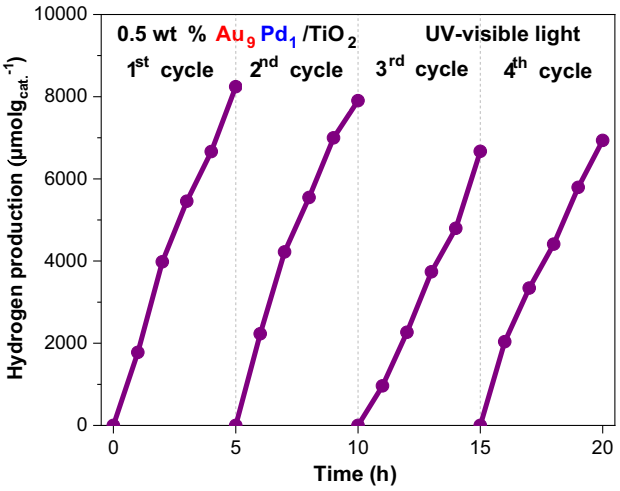


**Figure 10.** The photocatalyst stability of 0.5 wt% $Au_9Pd_1/TiO_2$ sample from 25 vol% TEOA aqueous solution under UV–vis light irradiation.

and the one of 0.2 nm corresponds to the plane (200) of Au (Figure S6f, Supporting Information). The interplanar distances of 0.18 nm (Figure S6c,f, Supporting Information) and 0.16 nm (Figure S6c, Supporting Information) can be assigned to (200) and (211) planes of the anatase phase (JCPDS No. 21-1272), respectively. However, the AuPd NPs size increases from ≈2.5–2.7 to ≈3.0–3.2 nm after cycling (Figure S6g, Supporting Information). This metal NPs' sintering probably explains the slight decrease in photocatalytic hydrogen generation due to larger NPs decreasing the work function and diminishing the Schottky barrier effect, increasing charge-carrier recombination. The surface chemical composition and oxidation states of AuPd nanoalloys on the $TiO_2$ surface were analyzed by XPS after cycling. The comparison of the XPS spectra for 0.5 wt% $AuPd/TiO_2$ sample before and after cycling for Au *4f* and Pd *3d* states is shown in Figure S6h,i, Supporting Information, respectively. After cycling, the XPS spectra are noisy compared to those before cycling. This can be attributed to metal loss after recovering the powder by centrifugation.

## 3. Conclusion

In summary, AuPd nanoalloys homogeneous in size (≈2.5–3 nm) were deposited on the $TiO_2$ surface by chemical reduction method using $NaBH_4$ at room temperature. The AuPd nanoalloys formation was confirmed by HAADF-STEM and hybrid MD–MC calculations validated this alloy structure. Synergetic effects were obtained with the AuPd nanoalloys: the bimetallic $AuPd/TiO_2$ samples show higher photocatalytic activity for $H_2$ generation under UV–vis light irradiation compared with their monometallic counterparts. The photocatalytic hydrogen generation enhancement of bimetallic samples was explained through their morphology, optical properties, crystallinity, charge carrier dynamics, electronic structure (DFT), and molecular dynamics (DFTB+) calculations. The $Au_9Pd_1/TiO_2$ sample is the most active and it is quite stable with cycling, with a slight decrease in hydrogen generation. TRMC results demonstrated that the surface modification of $TiO_2$ with bimetallic AuPd nanoalloys (electron traps) plays a role in charge-carrier separations increasing the activity under UV light irradiation. AuPd nanoalloys can be used as efficient cocatalysts for hydrogen generation with an activity comparable with that of Pt cocatalysts.

## 4. Experimental Section

*Chemical Reagents*: Commercial titanium dioxide ($TiO_2$-P25, 80% anatase, and 20% rutile, Evonik) was used as photocatalytic support. Gold (III) chloride trihydrate ($HAuCl_4{\cdot}3H_2O$, Sigma–Aldrich, 99.9%), palladium (II) chloride ($PdCl_2$, Sigma–Aldrich, 99%), and platinum (II) acetylacetonate ($Pt(C_5H_7O_2)_2$, Sigma–Aldrich, 97%) were used as metal precursors. Sodium borohydride ($NaBH_4$, Sigma–Aldrich ≥ 99%) and triethanolamine ($C_6H_{15}NO_3$, Sigma–Aldrich ≥ 99%) were used as reducing agent and hole scavenger, respectively. Deionized water (Milli-Q 18.2 MΩ) was used in all experiments.

*Photocatalysts Synthesis*: The photocatalysts were synthesized by chemical reduction using $NaBH_4$ as reducing agent at room temperature (Figure S7, Supporting Information). Mother solutions of 0.01 M $HAuCl_4$ (30 mL) and 0.01 M $PdCl_2$ (30 mL) were prepared. In a flask, 10 mL of deionized water was added to 250 mg of $TiO_2$ under vigorous stirring for 30 min. Afterward, an amount of each salt precursor solution was added to the dispersed $TiO_2$ aqueous suspension to prepare photocatalysts with different metal loadings keeping the vigorous stirring for 1 h. Immediately a fresh aqueous solution of 2 mL $NaBH_4$ 1 M was prepared in an ice-water bath because $NaBH_4$ reacts violently and quickly with water at room temperature. Freezing water slows the reaction sufficiently enough to allow the reduction of metal ions. Subsequently, 0.5 mL of $NaBH_4$ 1 M was added to the mixture, maintaining vigorous stirring for 2 h. Afterward, the photocatalysts were washed with deionized water and separated by centrifugation 3 times at 6500 rpm for 10 min to remove the non-reduced, undesired ions, and then dried at 60 °C for 48 h. The supernatants were transparent, indicating that most of the metals were deposited on the titania support. The UV–vis spectra of the supernatants were flat (Figure S8, Supporting Information) compared with the solutions of the salt precursors of $HAuCl_4$ and $PdCl_2$. The $Au^{III}$ and $Pd^{II}$ complexes were reduced by $NaBH_4$ in aqueous solutions at room temperature. The redox potentials are $E_{Au^{3+}/Au^0}$=1.5 V versus the normal hydrogen electrode (NHE), $E_{Pd^{2+}/Pd^0}$=0.83 V versus NHE,[73] and $E^0 = -1.24$ V versus NHE.[74,75] The concentration of $NaBH_4$ is a crucial factor in the synthesis; higher concentration induces the reduction of the NP size.[76]

Mono- and bi-metallic ($Au/TiO_2$, $Pd/TiO_2$, and $AuPd/TiO_2$) samples were prepared with 1 wt% metal loading for comparison (Table S4, Supporting Information). The monometallic photocatalysts containing Au and Pd were, respectively, purple and gray, and the color is more intense with the metal loading (Figure S9, Supporting Information). The bimetallic photocatalysts 1 wt% $Au_1Pd_9/TiO_2$ and 1 wt% $Au_1Pd_1/TiO_2$ were gray in color. For 1 wt% $Au_9Pd_1/TiO_2$, the color was gray-purple. Later, the bimetallic photocatalysts with total metal loading of 0.1, 0.2, and 0.5 wt% $AuPd/TiO_2$ were synthesized using the same mass ratios to study the effect of the loading on the photocatalytic activity. Finally, $Pt/TiO_2$ was synthesized (the best cocatalyst for hydrogen generation) to compare with the bimetallic samples $AuPd/TiO_2$. The 1 wt% $Pt/TiO_2$ sample was prepared by the radiolysis method. This method is very powerful to synthesize metal NPs of controlled size and shape in solution and on support.[56,77] Platinum (II) acetylacetonate was used as salt precursor and ethanol as solvent. The solution was stirred 1 h, sonicated for 5 min, degassed with Ar gas (Air Liquide), and then irradiated using a $^{60}Co$ panoramic gamma source. The dose used was 3.2 kGy, which is sufficient for complete reduction of $Pt^{II}$ complexes (at a concentration of $10^{-3}$ M) to their zerovalent state $Pt^0$. After the radiolysis process, the photocatalyst was separated by centrifugation and dried at 60 °C for 24 h to remove any remaining traces of the solvent.

*Photocatalysts Characterization*: The optical properties were analyzed by DRS with a UV–vis–NIR spectrophotometer (Cary 5000 Series, Agilent Technologies) recorded from 200 to 800 nm region. The crystal structure of the synthesized photocatalysts was investigated by XRD using a SmartLab RIGAKU with Cu Kα radiation, 40 kV, 44 mA, $\lambda = 0.15406$ nm over the $2\theta$ range from 20° to 80°, with steps of 0.01° $s^{-1}$. Transmission electron microscopy (TEM) FEI TECNAI F30 microscope equipped with a tungsten field emission gun operated at 300 keV was used to study the morphology, size, and dispersion of bimetallic AuPd NPs over the $TiO_2$ surface, equipped with an *energy-dispersive* X-ray spectroscopy (EDS) detector to identify the elemental composition of the samples. The AuPd nanoalloy formation and crystalline structure were analyzed by HAADF-STEM using a HRTEM, model JEOL 200F (200 keV). The powder samples were dissolved in 2-propanol under sonication, and then few drops of the solution were deposited on a holey carbon-coated copper grid (300 mesh). The surface elemental composition and oxidation states were studied by XPS. XPS measurements were performed on a K-alpha spectrometer from ThermoFisher, equipped with a monochromated X-ray source (Al Kα, 1486.68 eV) with a spot size of 400 µm, corresponding to an irradiated area of ≈1 $mm^2$. The samples were measured in the powder form. The base pressure was $3 \times 10^{-9}$ mbar. The hemispherical analyzer was operated in constant analyzer energy mode, with pass energy of 200 eV and a step of 1 eV for the acquisition of surveys spectra, and pass energy of 50 eV and a step of 0.1 eV for the acquisition of narrow spectra. A "dual-beam" flood gun was used to neutralize the charge buildup. The binding energies were calibrated against the neutral carbon binding energy set at 284.8 eV. The precision in binding energy is ±0.2 eV. The spectra were recorded and treated by means of Avantage software provided by Thermo Fisher. The fitting procedure implied the use of asymmetrical line shapes after the extraction of a Shirley-type background.

The photogenerated charge-carrier dynamics, which is a key factor in photocatalysis, was studied by TRMC technique for the bimetallic samples under UV and visible light excitations. A pulsed and tunable laser source (200–2000 nm) equipped with an optical parametric oscillator (EKSPLA, NT342B) was used to excite the samples, and a Gunn diode (30 GHz) was used to generate microwaves. The principle of this technique has been described in previous papers.[14,29,50,56,58,69] TRMC technique measures the relative change ($\frac{\Delta P(t)}{p}$) in microwave power reflected from a semiconductor material during its excitation by a laser pulse. This change ($\Delta\sigma(t)$) could be related to small perturbation of the sample's conductivity (Equation (11)).

$$\frac{\Delta P(t)}{p} = A\Delta\sigma(t) = Ae\mu_e\Delta n_e(t) \tag{11}$$

In $TiO_2$-based compounds, the electron mobility ($\mu_e$) is much higher than the holes. Therefore, $\Delta\sigma(t)$ is mainly due to excess electrons in the CB. $\Delta n_e(t)$ is the excess free electrons number at time *t*. *A* (sensitivity factor) is time-independent and relies on the conductivity of the semiconductor and the microwave frequency. The main data provided by the TRMC technique give the maximum value of the signal ($I_{max}$), which corresponds to the number of excess free electrons generated by the laser pulse. The signal decay $I(t)$ (denominated photoconductivity) as a function of time (in µs or ns) is owing to the decrease of excess electrons after the laser pulse by charge-carrier recombination or trapping.[14,29,50,56,58,69]

*Photocatalytic Hydrogen Generation Tests*: The photocatalytic hydrogen generation tests were performed in a closed quartz reactor. 20 mg of the photocatalyst was dispersed in 20 mL of 25 vol% of triethanolamine (TEOA) aqueous solution. TEOA was used as a sacrificial electron donor (or hole scavenger). Before irradiation, the reactor was degassed with Ar for 20 min under vigorous stirring. Afterward, the samples were irradiated for 5 h using a Peschl photoreactor and a Xenon Lamp 300 W LOT-Oriel (250–2000 nm) equipped with a water filter (a large quartz cell) between the lamp and the reactor to screen the infrared light and avoid heating of the samples. An optical filter was used to limit the irradiation to the visible ($\lambda \geq 420$ nm). The hydrogen amount was measured by gas chromatography every hour (Micro GC Fusion, INFICON). The photocatalyst stability is an essential parameter that defines the materials' commercial significance. For the photocatalyst stability, 20 mg of photocatalyst were once again dispersed in 20 mL of 25 vol% of TEOA aqueous solution. The mixture was degassed with Ar for 20 min under vigorous stirring before exposure to irradiation for 5 h in a Peschl photoreactor. The powder was recovered through centrifugation and dried at 60 °C for 24 h. Afterward, the photocatalyst was weighted and dispersed in a 25 vol% TEOA aqueous solution, maintaining a 1 mg $mL^{-1}$ ratio. This process was repeated for four cycles.

## 5. Methods

The geometry optimization calculations were carried out at the DFT level using the ORCA 5.0.3 software.[78] The general gradient approximation applying Perdew-Burke-Ernzerh of as exchange and correlation functional was used in association with dispersion corrections in the D3 framework proposed by Grimme with the addition of the Becke–Johnson damping (D3BJ).[79] The Stuttgart pseudopotential (with 19 and 18 valence electrons treated explicitly for Au and Pd atoms, respectively) and the associated basis set were used for the metal atoms, and the def2-SVP basis set was used for hydrogen atoms. The quantum chemical analyses were performed with the Multiwfn code by analyzing the electron density generated from ORCA.[80] The electron localization function was calculated to determine the valence basins.[81]

A hybrid MD–MC was used for obtaining the chemical order of the three NPs alloys concentrations, based on interatomic Gupta potential and using LAMMPS code.[82,83] For the reactivity dynamics of $H_2$ on alloys NPs, DFTB+ with the GFN1-xTB parameterization was used,[84,85] previously optimizing the structures with the hybrid MD—MC methodology. See the Supporting Information for details.

## Supporting Information

Supporting Information is available from the Wiley Online Library or from the author.

## Acknowledgements

A.A.M.-M. acknowledges CONACYT-Mexico for the financial support (grant no. 995288) and CAMPUS FRANCE for the scholarship of the French Embassy in Mexico. A.A.M.-M. acknowledges also the National Laboratory Research in Nanoscience and Nanotechnology (LINAN), IPICYT; Dr. Héctor Gabriel Silva Pereyra for TEM-EDS characterization, and M.C. Beatriz Adriana Rivera-Escoto and Dr. Ignacio Guadalupe Becerril Juárez for XRD characterization. Also, the authors acknowledge Mireille Benoit for her help at the Institut de Chimie Physique laboratory. DFT calculations were performed using computational resources from the "Mésocentre" computing center of Université Paris-Saclay, CentraleSupélec and École Normale Supérieure Paris-Saclay supported by CNRS and Région Île-de-France.

## Conflict of Interest

The authors declare no conflict of interest.

## Data Availability Statement

The data that support the findings of this study are available in the supplementary material of this article.

## Keywords

bimetallic cocatalysts, hydrogen generation, photocatalysis, solar fuels, synergetic effects

Received: February 6, 2024
Revised: March 18, 2024
Published online:

[1] H. Ahmad, S. K. Kamarudin, L. J. Minggu, M. Kassim, *Renewable Sustainable Energy Rev.* **2015**, *43*, 599.
[2] S. Protti, A. Albini, N. Serpone, *Phys. Chem. Chem. Phys.* **2014**, *16*, 19790.
[3] Y. Piña-Pérez, J. E. Samaniego-Benitez, F. Tzompantzi, L. Laurtundo-Rojas, A. Garcia-Garcia, A. Mantilla, G. Romero-Ortiz, *Mater. Lett.* **2022**, *330*, 133205.
[4] I. K. Kapdan, F. Kargi, *Enzyme Microb. Technol.* **2006**, *38*, 569.
[5] S. E. Hosseini, M. A. Wahid, *Renewable Sustainable Energy Rev.* **2016**, *57*, 850.
[6] T. N. Veziroğlu, S. Şahin, *Energy Convers. Manag.* **2008**, *49*, 1820.
[7] S. Sharma, S. K. Ghoshal, *Renewable Sustainable Energy Rev.* **2015**, *43*, 1151.
[8] B. A. Pinaud, J. D. Benck, L. C. Seitz, A. J. Forman, Z. Chen, T. G. Deutsch, B. D. James, K. N. Baum, G. N. Baum, S. Ardo, H. Wang, E. Miller, T. F. Jaramillo, *Energy Environ. Sci.* **2013**, *6*, 1983.
[9] X. Chen, S. S. Mao, *Chem. Rev.* **2007**, *107*, 2891.
[10] A. Kudo, Y. Miseki, *Chem. Soc. Rev.* **2009**, *38*, 253.
[11] H. Hennig, *Angew. Chem. Int. Ed.* **2015**, *54*, 4429.
[12] X. Yuan, D. Floresyona, P. H. Aubert, T. T. Bui, S. Remita, S. Ghosh, F. Brisset, F. Goubard, H. Remita, *Appl. Catal. B* **2019**, *242*, 284.
[13] J. Ma, J. Dai, Y. Duan, J. Zhang, L. Qiang, J. Xue, *Renewable Energy* **2020**, *156*, 1008.
[14] M. G. Méndez-Medrano, E. Kowalska, A. Lehoux, A. Herissan, B. Ohtani, S. Rau, C. Colbeau-Justin, J. L. Rodríguez-López, H. Remita, *J. Phys. Chem. C* **2016**, *120*, 25010.
[15] B. Ohtani, O. O. Prieto-Mahaney, D. Li, R. Abe, *J. Photochem. Photobiol.* **2010**, *216*, 179.
[16] J. Zhang, P. Zhou, J. Liu, J. Yu, *Phys. Chem. Chem. Phys.* **2014**, *16*, 20382.
[17] R. Ma, T. Chen, *J. Phys. Chem. C* **2019**, *123*, 19479.
[18] V. Etacheri, M. K. Seery, S. J. Hinder, S. C. Pillai, *Adv. Funct. Mater.* **2011**, *21*, 3744.
[19] A. Di Paola, G. Cufalo, M. Addamo, M. Bellardita, R. Campostrini, M. Ischia, R. Ceccato, L. Palmisano, *Colloids Surf.* **2008**, *317*, 366.
[20] E. Grabowska, A. Zaleska, S. Sorgues, M. Kunst, A. Etcheberry, C. Colbeau-Justin, H. Remita, *J. Phys. Chem. C* **2013**, *117*, 1955.
[21] M. G. Méndez-Medrano, E. Kowalska, A. Lehoux, A. Herissan, B. Ohtani, D. Bahena, V. Briois, C. Colbeau-Justin, J. L. Rodríguez-López, H. Remita, *J. Phys. Chem. C* **2016**, *120*, 5143.
[22] M. G. Méndez-Medrano, E. Kowalska, B. Ohtani, D. Bahena Uribe, C. Colbeau-Justin, S. Rau, J. L. Rodríguez-López, H. Remita, *J. Chem. Phys.* **2020**, *153*, 034705.
[23] V. Kumaravel, S. Mathew, J. Bartlett, S. C. Pillai, *Appl. Catal. B* **2019**, *244*, 1021.
[24] N. S. Ibrahim, W. L. Leaw, D. Mohamad, S. H. Alias, H. Nur, *Int. J. Hydrog. Energy* **2020**, *45*, 28553.
[25] M. Ismael, *Sol. Energy* **2020**, *211*, 522.
[26] A. L. Luna, E. Novoseltceva, E. Louarn, P. Beaunier, E. Kowalska, B. Ohtani, M. A. Valenzuela, H. Remita, C. Colbeau-Justin, *Appl. Catal. B* **2016**, *191*, 18.
[27] P. Verma, Y. Kuwahara, K. Mori, H. Yamashita, *J. Mater. Chem. A* **2016**, *4*, 10142.
[28] A. Zielińska-Jurek, *J. Nanomater.* **2014**, *2014*, 208920.
[29] A. L. Luna, D. Dragoe, K. Wang, P. Beaunier, E. K. Kowalska, B. Ohtani, D. B. Uribe, M. A. Valenzuela, H. Remita, C. Colbeau-Justin, *J. Phys. Chem. C* **2017**, *121*, 14302.
[30] M. Luo, P. Lu, W. Yao, C. Huang, Q. Xu, Q. Wu, Y. Kuwahara, H. Yamashita, *ACS Appl. Mater. Interfaces* **2016**, *8*, 20667.
[31] R. Su, R. Tiruvalam, A. J. Logsdail, Q. He, C. A. Downing, M. T. Jensen, N. Dimitratos, L. Kesavan, P. P. Wells, R. Bechstein, H. H. Jensen, S. Wendt, C. R. A. Catlow, C. J. Kiely, G. J. Hutchings, F. Besenbacher, *ACS Nano* **2014**, *8*, 3490.
[32] T. Redjala, H. Remita, G. Apostolescu, M. Mostafavi, C. Thomazeau, D. Uzio, *Oil Gas Sci. Technol.* **2006**, *61*, 789.
[33] F. Wang, Y. Jiang, D. J. Lawes, G. E. Ball, C. Zhou, Z. Liu, R. Amal, *ACS Catal.* **2015**, *5*, 3924.
[34] M. Mirdamadi-Esfahani, M. Mostafavi, B. Keita, L. Nadjo, P. Kooyman, H. Remita, *Gold Bull.* **2010**, *43*, 49.
[35] Z. Hai, N. El Kolli, D. B. Uribe, P. Beaunier, M. José-Yacaman, J. Vigneron, A. Etcheberry, S. Sorgues, C. Colbeau-Justin, J. Chen, H. Remita, *J. Mater. Chem. A* **2013**, *1*, 10829.
[36] Z. Hai, N. El Kolli, J. Chen, H. Remita, *New J. Chem.* **2014**, *38*, 5279.
[37] F. Ksar, L. Ramos, B. Keita, L. Nadjo, P. Beaunier, H. Remita, *Chem. Mater.* **2009**, *21*, 3677.
[38] F. Ksar, G. K. Sharma, F. Audonnet, P. Beaunier, H. Remita, *Nanotechnology* **2011**, *22*, 305609.
[39] F. Ksar, G. Surendran, L. Ramos, B. Keita, L. Nadjo, E. Prouzet, P. Beaunier, A. Hagège, F. Audonnet, H. Remita, *Chem. Mater.* **2009**, *21*, 1612.
[40] G. Surendran, F. Ksar, L. Ramos, B. Keita, L. Nadjo, E. Prouzet, P. Beaunier, P. Dieudonné, F. Audonnet, H. Remita, *J. Phys. Chem. C* **2008**, *112*, 10740.
[41] S. Ghosh, S. Bera, N. Karmakar, R. N. Basu, *Mater. Today: Proc.* **2018**, *5*, 9733.
[42] S. Ghosh, A. L. Teillout, D. Floresyona, P. De Oliveira, A. Hagège, H. Remita, *Int. J. Hydrogen Energy* **2015**, *40*, 4951.
[43] A. Dumas, P. Couvreur, *Chem. Sci.* **2015**, *6*, 2153.
[44] I. Sarhid, I. Abdellah, C. Martini, V. Huc, D. Dragoe, P. Beaunier, I. Lampre, H. Remita, *New J. Chem.* **2019**, *43*, 4349.
[45] D. Astruc, *Inorg. Chem.* **2007**, *46*, 1884.
[46] B. Karimi, S. Abedi, J. H. Clark, V. Budarin, *Angew. Chem. Int. Ed.* **2006**, *45*, 4776.
[47] S. K. Min, N. Kim, M. P. Cheon, S. L. Jae, Y. K. Kyung, J. Park, *Org. Lett.* **2005**, *7*, 1077.
[48] F. R. Lucci, M. T. Darby, M. F. G. Mattera, C. J. Ivimey, A. J. Therrien, A. Michaelides, M. Stamatakis, E. C. H. Sykes, *J. Phys. Chem. Lett.* **2016**, *7*, 480.
[49] N. Dimitratos, G. Vilé, S. Albonetti, F. Cavani, J. Fiorio, N. López, L. M. Rossi, R. Wojcieszak, *Nat. Rev. Chem.* **2024**, *8*, 195.
[50] A. L. Luna, F. Matter, M. Schreck, J. Wohlwend, E. Tervoort, C. Colbeau-Justin, M. Niederberger, *Appl. Catal. B* **2020**, *267*, 118660.
[51] X. Gan, D. Lei, *Coord. Chem. Rev.* **2022**, *469*, 214665.
[52] F. Berthier, B. Legrand, *J. Condens. Matter Phys.* **2020**, *32*, 354001.
[53] F. Berthier, J. Creuze, T. Gabard, B. Legrand, M. C. Marinica, C. Mottet, *Phys. Rev. B* **2019**, *32*, 014108.
[54] Y. Mi, Y. Weng, *Sci. Rep.* **2015**, *5*, 11482.
[55] J. B. Chang, C. H. Liu, J. Liu, Y. Y. Zhou, X. Gao, S. D. Wang, *Nanomicro Lett.* **2015**, *7*, 307.
[56] O. Tahiri Alaoui, A. Herissan, C. Le Quoc, M. E. M. Zekri, S. Sorgues, H. Remita, C. Colbeau-Justin, *J. Photochem. Photobiol.* **2012**, *242*, 34.
[57] S. Nishimura, N. Abrams, B. A. Lewis, L. I. Halaoui, T. E. Mallouk, K. D. Benkstein, J. van de Lagemaat, A. J. Frank, *J. Am. Chem. Soc.* **2003**, *125*, 6306.

[58] H. Remita, M. G. Méndez-Medrano, C. Colbeau-Justin, in *Visible Light-Active Photocatalysis* (Ed: S. Ghosh), Wiley-VCH, Weinheim, Germany, **2018**, pp. 129–164.
[59] M. C. Biesinger, B. P. Payne, A. P. Grosvenor, L. W. M. Lau, A. R. Gerson, R. S. C. Smart, *Appl. Surf. Sci.* **2011**, *257*, 2717.
[60] J. F. Moulder, W. F. Stickle, P. E. Sobol, K. D. Bomben, J. Chastain, in *Handbook of X-Ray Photoelectron Spectroscopy*, Perkin-Elmer, Minnesota, USA, **1992**.
[61] F. Wang, H. Zhang, Z. Zhang, Q. Ma, C. Kong, S. Min, *J. Colloid Interface Sci.* **2022**, *607*, 312.
[62] B. Liu, K. Li, Y. Luo, L. Gao, G. Duan, *J. Chem. Eng.* **2021**, *420*, 129881.
[63] J. Xu, T. White, P. Li, C. He, J. Yu, W. Yuan, Y. F. Han, *J. Am. Chem. Soc.* **2010**, *132*, 10398.
[64] É. Casey, J. D. Holmes, G. Collins, *ACS Appl. Nano Mater.* **2022**, *5*, 16196.
[65] X. Zhu, Q. Guo, Y. Sun, S. Chen, J. Q. Wang, M. Wu, W. Fu, Y. Tang, X. Duan, D. Chen, Y. Wan, *Nat. Commun.* **2019**, *10*, 1428.
[66] Y. Zhang, O. Pluchery, L. Caillard, A. F. Lamic-Humblot, S. Casale, Y. J. Chabal, M. Salmeron, *Nano Lett.* **2015**, *15*, 51.
[67] L. Lechaptois, Y. Prado, O. Pluchery, *Nanoscale* **2023**, *15*, 7510.
[68] S. de Marchi, S. Núñez-Sánchez, G. Bodelón, J. Pérez-Juste, I. Pastoriza-Santos, *Nanoscale* **2020**, *12*, 23424.
[69] C. Wang, D. Dragoe, C. Colbeau-Justin, P. Haghi-Ashtiani, M. N. Ghazzal, H. Remita, *ACS Appl. Mater. Interfaces* **2023**, *15*, 42637.
[70] H. J. Le, D. van Dao, Y. T. Yu, *J. Mater. Chem. A* **2020**, *8*, 12968.
[71] B. L. Sharma, in *Metal-Semiconductor Schottky Barrier Junctions and Their Applications*, Plenum Press, New York **1984**.
[72] P. Chowdhury, H. Gomaa, A. K. Ray, *Chemosphere* **2015**, *121*, 54.
[73] M. Sahoo, S. Mansingh, S. Subudhi, P. Mohapatra, K. Parida, *Catal. Sci. Technol.* **2019**, *9*, 4678.
[74] S. Carregal-Romero, J. Pérez-Juste, P. Hervés, L. M. Liz-Marzán, P. Mulvaney, *Langmuir* **2010**, *26*, 1271.
[75] A. M. Pasqualeti, P. Y. Olu, M. Chatenet, F. H. B. Lima, *ACS Catal.* **2015**, *5*, 2778.
[76] Q. M. Liu, D. B. Zhou, Y. Yamamoto, R. Ichino, M. Okido, *Trans. Nonferrous Met. Soc. China* **2012**, *22*, 117.
[77] P. Ray, M. Clément, C. Martini, I. Abdellah, P. Beaunier, J. L. Rodriguez-Lopez, V. Huc, H. Remita, I. Lampre, *New. J. Chem.* **2018**, *42*, 14128.
[78] F. Neese, *Wiley Interdiscip. Rev. Comput. Mol. Sci.* **2012**, *2*, 73.
[79] S. Grimme, S. Ehrlich, L. Goerigk, *J. Comput. Chem.* **2011**, *32*, 1456.
[80] T. Lu, F. Chen, *J. Comput. Chem.* **2012**, *33*, 580.
[81] A. D. Becke, K. E. A. Edgecombe, *J. Chem. Phys.* **1990**, *92*, 5397.
[82] F. Pittaway, L. O. Paz-Borbón, R. L. Johnston, H. Arslan, R. Ferrando, C. Mottet, G. Barcaro, A. Fortunelli, *J. Phys. Chem. C* **2009**, *113* 9141.
[83] A. P. Thompson, H. M. Aktulga, R. Berger, D. S. Bolintineanu, W. M. Brown, P. S. Crozier, P. J. in 't Veld, A. Kohlmeyer, S. G. Moore, T. D. Nguyen, R. Shan, M. J. Stevens, J. Tranchida, C. Trott, S. J. Plimpton, *Comput. Phys. Commun.* **2022**, *271*, 108171.
[84] B. Hourahine, B. Aradi, V. Blum, F. Bonafé, A. Buccheri, C. Camacho, C. Cevallos, M. Y. Deshaye, T. Dumitrică, A. Dominguez, S. Ehlert, M. Elstner, T. van der Heide, J. Hermann, S. Irle, J. J. Kranz, C. Köhler, T. Kowalczyk, T. Kubař, I. S. Lee, V. Lutsker, R. J. Maurer, S. K. Min, I. Mitchell, C. Negre, T. A. Niehaus, A. M. N. Niklasson, A. J. Page, A. Pecchia, G. Penazzi, et al., *J. Chem. Phys.* **2020**, *152*, 124101.
[85] S. Grimme, C. Bannwarth, P. Shushkov, *J. Chem. Theory Comput.* **2017**, *13*, 1989.